

# Thermodynamics and Phase Diagrams

**Arthur D. Pelton**  
**Centre de Recherche en Calcul Thermodynamique**  
**(CRCT)**  
**École Polytechnique de Montréal**  
**C.P. 6079, succursale Centre-ville**  
**Montréal QC Canada H3C 3A7**

**Tél :** 1-514-340-4711 (ext. 4531)  
**Fax :** 1-514-340-5840  
**E-mail :** [apelton@polymtl.ca](mailto:apelton@polymtl.ca)

(revised Aug. 10, 2011)



# 1 Introduction

An understanding of phase diagrams is fundamental and essential to the study of materials science, and an understanding of thermodynamics is fundamental to an understanding of phase diagrams. A knowledge of the equilibrium state of a system under a given set of conditions is the starting point in the description of many phenomena and processes.

A phase diagram is a graphical representation of the values of the thermodynamic variables when equilibrium is established among the phases of a system. Materials scientists are most familiar with phase diagrams which involve temperature,  $T$ , and composition as variables. Examples are  $T$ -composition phase diagrams for binary systems such as Fig. 1 for the Fe-Mo system, isothermal phase diagram sections of ternary systems such as Fig. 2 for the Zn-Mg-Al system, and isoplethal (constant composition) sections of ternary and higher-order systems such as Fig. 3a and Fig. 4.

However, many useful phase diagrams can be drawn which involve variables other than  $T$  and composition. The diagram in Fig. 5 shows the phases present at equilibrium in the Fe-Ni-O<sub>2</sub> system at 1200°C as the equilibrium oxygen partial pressure (i.e. chemical potential) is varied. The x-axis of this diagram is the overall molar metal ratio in the system. The phase diagram in Fig. 6 shows the equilibrium phases present when an equimolar Fe-Cr alloy is equilibrated at 925°C with a gas phase of varying O<sub>2</sub> and S<sub>2</sub> partial pressures. For systems at high pressure,  $P$ - $T$  phase diagrams such as the diagram for the one-component Al<sub>2</sub>SiO<sub>5</sub> system in Fig. 7a show the fields of stability of the various allotropes. When the pressure in Fig. 7a is replaced by the volume of the system as  $y$ -axis, the “corresponding”  $V$ - $T$  phase diagram of Fig. 7b results. The enthalpy of the system can also be a variable in a phase diagram. In the phase diagram in Fig. 3b, the  $y$ -axis of Fig. 3a has been replaced by the molar enthalpy difference ( $h_T - h_{25}$ ) between the system at 25°C and a temperature  $T$ . This is the heat which must be supplied or removed to heat or cool the system adiabatically between 25°C and  $T$ .

The phase diagrams in Figs. 1-7 are only a small sampling of the many possible types of phase diagram sections. These diagrams and several other useful types of phase diagrams will be discussed in this chapter. Although these diagrams appear to

have very different geometries, it will be shown that actually they all obey exactly the same geometrical rules.

The theme of this chapter is the relationship between phase diagrams and thermodynamics. To understand phase diagrams properly it has always been necessary to understand their thermodynamic basis. However, in recent years the relationship between thermodynamics and phase diagrams has taken on a new and important practical dimension. With the development of large evaluated databases of the thermodynamic properties of thousands of compound and solutions, and of software to calculate the conditions for chemical equilibrium (by minimizing the Gibbs energy), it is possible to rapidly calculate and plot desired phase diagram sections of multicomponent systems. Most of the phase diagrams shown in this chapter were calculated thermodynamically with the FactSage software and databases (see FactSage in the list of websites at the end of this chapter).

Several large integrated thermodynamic database computing systems have been developed in recent years (See list of websites at the end of this chapter.). The databases of these systems have been prepared by the following procedure. For every compound and solution phase of a system, an appropriate model is first developed giving the thermodynamic properties as functions of  $T$ ,  $P$  and composition. Next, all available thermodynamic and phase equilibrium data from the literature for the entire system are simultaneously optimized to obtain one set of critically-evaluated, self-consistent parameters of the models for all phases in 2-component, 3-component and, if data are available, higher-order subsystems. Finally, the models are used to estimate the properties of multicomponent solutions from the databases of parameters of the lower-order subsystems. The Gibbs-energy minimization software then accesses the databases and, for given sets of conditions ( $T$ ,  $P$ , composition...) calculates the compositions and amounts of all phases at equilibrium. By calculating the equilibrium state as  $T$ , composition,  $P$ , etc. are varied systematically, the software generates the phase diagram. As mentioned above, although the phase diagram sections shown in Figs. 1-7 are seemingly quite different topologically, they actually obey the same simple rules of construction and hence can all be calculated by the same algorithm.

Sec. 2 provides a review of the fundamentals of thermodynamics as required for

the interpretation and calculation of phase diagrams of all types. In Sec. 3 the Gibbs Phase Rule is developed in a general form suitable for the understanding of phase diagrams involving a wide range of variables including chemical potentials, enthalpy, volume, etc. Sec. 4 begins with a review of the thermodynamics of solutions and continues with a discussion of the thermodynamic origin of binary  $T$ -composition phase diagrams, presented in the classical manner involving common tangents to curves of Gibbs energy. A thorough discussion of all features of  $T$ -composition phase diagrams of binary systems is presented in Sec. 5, with particular stress on the relationship between the phase diagram and the thermodynamic properties of the phases. A similar discussion of  $T$ -composition phase diagrams of ternary systems is given in Sec. 6. Isothermal and isoplethal sections as well as polythermal projections are discussed.

Readers conversant in binary and ternary  $T$ -composition diagrams may wish to skip Secs. 4, 5 & 6 and pass directly to Sec. 7 where the geometry of general phase diagram sections is developed. In this section are presented: the general rules of construction of phase diagram sections; the proper choice of axis variables and constants required to give a single-valued phase diagram section with each point of the diagram representing a unique equilibrium state; and a general algorithm for calculating all such phase diagram sections.

Sec. 8 outlines the techniques used to develop large thermodynamic databases through evaluation and modeling. Sec. 9 treats the calculation of equilibrium and non-equilibrium cooling paths of multicomponent systems. In Sec. 10, order/disorder transitions and their representation on phase diagrams are discussed.

## **2      *Thermodynamics***

This section is intended to provide a review of the fundamentals of thermodynamics as required for the interpretation and calculation of phase diagrams. The development of the thermodynamics of phase diagrams will be continued in succeeding sections.

### **2.1    The First and Second Laws of Thermodynamics**

If the thermodynamic *system* under consideration is permitted to exchange both

energy and mass with its *surroundings*, the system is said to be *open*. If energy but not mass may be exchanged, the system is said to be *closed*. The state of a system is defined by *intensive properties*, such as temperature and pressure, which are independent of the mass of the system, and by *extensive properties*, such as volume and internal energy, which vary directly as the mass of the system.

### 2.1.1 Nomenclature

Extensive thermodynamic properties will be represented by upper case symbols. For example,  $G$  = Gibbs energy in J. Molar properties will be represented by lower case symbols. For example,  $g = G/n$  = molar Gibbs energy in  $\text{J mol}^{-1}$  where  $n$  is the total number of moles in the system.

### 2.1.2 The First Law

The *internal energy* of a system,  $U$ , is the total thermal and chemical bond energy stored in the system. It is an extensive state property.

Consider a closed system undergoing a change of state which involves an exchange of heat,  $dQ$ , and work,  $dW$ , with its surroundings. Since energy must be conserved:

$$dU_n = dQ + dW \quad (1)$$

This is the First Law. The convention is adopted whereby energy passing from the surroundings to the system is positive. The subscript on  $dU_n$  indicates that the system is closed (constant number of moles.)

It must be stressed that  $dQ$  and  $dW$  are not changes in state properties. For a system passing from a given initial state to a given final state,  $dU_n$  is independent of the process path since it is the change of a state property; however  $dQ$  and  $dW$  are, in general, path-dependent.

### 2.1.3 The Second Law

For a rigorous and complete development of the Second Law, the reader is referred to standard texts on thermodynamics. The *entropy* of a system,  $S$ , is an

extensive state property which is given by Boltzmann's equation as:

$$S = k_B \ln t \quad (2)$$

where  $k_B$  is Boltzmann's constant and  $t$  is the multiplicity of the system. Somewhat loosely,  $t$  is the number of possible equivalent microstates in a macrostate, that is the number of quantum states for the system which are accessible under the applicable conditions of energy, volume, etc. For example, for a system which can be described by a set of single-particle energy levels,  $t$  is the number of ways of distributing the particles over the energy levels, keeping the total internal energy constant. At low temperatures, most of the particles will be in or near the ground state. Hence,  $t$  and  $S$  will be small. As the temperature, and hence  $U$ , increase, more energy levels become occupied. Consequently  $t$  and  $S$  increase. For solutions, an additional contribution to  $t$  arises from the number of different possible ways of distributing the atoms or molecules over the lattice or quasilattice sites. (See Sec 4.1.5). Again somewhat loosely,  $S$  can be said to be a measure of the disorder of a system.

During any spontaneous process, the total entropy of the universe will increase for the simple reason that disorder is more probable than order. That is, for any spontaneous process:

$$dS_{\text{total}} = (dS + dS_{\text{surr}}) \geq 0 \quad (3)$$

where  $dS$  and  $dS_{\text{surr}}$  are the entropy changes of the system and surroundings respectively. The existence of a state property  $S$  which satisfies Eq. (3) is the essence of the Second Law.

Eq. (3) is a necessary condition for a process to occur. However, even if Eq. (3) is satisfied the process may not actually be observed if there are kinetic barriers to its occurrence. That is, the Second Law says nothing about the rate of a process which can vary from extremely rapid to infinitely slow.

It should be noted that the entropy change of the system,  $dS$ , can be negative for a spontaneous process as long as the sum  $(dS + dS_{\text{surr}})$  is positive. For example, during the solidification of a liquid, the entropy change of the system is negative in

going from the liquid to the more ordered solid state. Nevertheless, a liquid below its melting point will freeze spontaneously because the entropy change of the surroundings is sufficiently positive due to the transfer of heat from the system to the surroundings. It should also be stressed that in passing from a given initial state to a given final state, the entropy change of the system  $dS$  is independent of the process path since it is the change of a state property. However,  $dS_{surr}$  is path-dependent.

#### 2.1.4 The Fundamental Equation of Thermodynamics

Consider an open system at equilibrium with its surroundings and at internal equilibrium. That is, no spontaneous irreversible processes are taking place. Suppose that a change of state occurs in which  $S$ ,  $V$  (volume) and  $n_i$  (number of moles of component  $i$  in the system) change by  $dS$ ,  $dV$  and  $dn_i$ . Such a change of state occurring at equilibrium is called a *reversible* process, and the corresponding heat and work terms are  $dQ_{rev}$  and  $dW_{rev}$ . We may then write:

$$dU = \left(\frac{\partial U}{\partial S}\right)_{v,n} dS + \left(\frac{\partial U}{\partial V}\right)_{s,n} dV + \sum \mu_i dn_i \quad (4)$$

where:

$$\mu_i = \left(\frac{\partial U}{\partial n_i}\right)_{s,v,n_{j \neq i}} \quad (5)$$

$\mu_i$  is the chemical potential of component  $i$  which will be discussed in Sec. 2.7.

The absolute temperature is given as:

$$T = \left(\frac{\partial U}{\partial S}\right)_{v,n} \quad (6)$$

We expect that temperature should be defined such that heat flows spontaneously from high to low  $T$ . To show that  $T$  as given by Eq. (6) is, in fact, such a thermal potential, consider two closed systems, isolated from their surroundings but in thermal contact with each other, exchanging only heat at constant volume. Let the temperatures of the systems be  $T_1$  and  $T_2$  and let  $T_1 > T_2$ . Suppose that heat flows from system 1 to system 2. Then  $dU_2 = -dU_1 > 0$ . Therefore, from Eq. (6):

$$dS = dS_1 + dS_2 = dU_1 / T_1 + dU_2 / T_2 > 0 \quad (7)$$

That is, the flow of heat from high to low temperature results in an increase in total entropy and hence, from the Second Law, is spontaneous.

The second term in Eq. (4) is clearly  $(-PdV)$ , the work of reversible expansion. From Eq. (6) the first term in Eq. (4) is equal to  $TdS$ , and this is then the reversible heat:

$$T dS = dQ_{\text{rev}} \quad (8)$$

That is, in the particular case of a process which occurs reversibly,  $(dQ_{\text{rev}}/T)$  is path-independent since it is equal to the change of a state property  $dS$ . Eq. (8) is actually the definition of entropy in the classical development of the Second Law.

Eq. (4) may now be written as:

$$dU = T dS - P dV + \sum \mu_i dn_i \quad (9)$$

Eq. (9), which results from combining the First and Second Laws is called the *fundamental equation* of thermodynamics. We have assumed that the only work term is the reversible work of expansion (sometimes called “PV work”.) In general, in this chapter, this will be the case. If other types of work occur, then non-PV terms,  $dW_{\text{rev}(non-PV)}$ , must be added to Eq. (9). For example, if the process is occurring in a galvanic cell, then  $dW_{\text{rev}(non-PV)}$  is the reversible electrical work in the external circuit. Eq. (9) can thus be written more generally as:

$$dU = T dS - P dV + \sum \mu_i dn_i + dW_{\text{rev}(non-PV)} \quad (10)$$

## 2.2 Enthalpy

Enthalpy,  $H$ , is an extensive state property defined as:

$$H = U + PV \quad (11)$$

Consider a closed system undergoing a change of state which may involve irreversible processes (such as chemical reactions.) Although the overall process may be irreversible, we shall assume that any work of expansion is approximately reversible (that is, the external and internal pressures are equal) and that there is no work other

than work of expansion. Then, from Eq. (1):

$$dU_n = dQ - P dV \quad (12)$$

From Eqs (11) and (12) it follows that:

$$dH_n = dQ + V dP \quad (13)$$

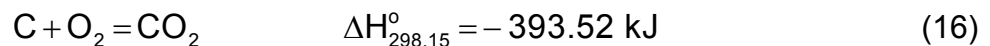
Furthermore, if the pressure remains constant throughout the process, then:

$$dH_p = dQ_p \quad (14)$$

Integrating both sides of Eq. (14) gives:

$$\Delta H_p = Q_p \quad (15)$$

That is, the enthalpy change of a closed system in passing from an initial to a final state at constant pressure is equal to the heat exchanged with the surroundings. Hence, for a process occurring at constant pressure the heat is path-independent since it is equal to the change of a state property. This is an important result. As an example, suppose that the initial state of a system consists of 1.0 mol of C and 1.0 mol of O<sub>2</sub> at 298.15 K at 1.0 bar pressure and the final state is one mole of CO<sub>2</sub> at the same temperature and pressure. The enthalpy change of this reaction is:



(where the superscript on  $\Delta H_{298.15}^{\circ}$  indicates the “standard state” reaction involving pure solid graphite, CO<sub>2</sub> and O<sub>2</sub> at 1.0 bar pressure.) Hence, an exothermic heat of -393.52 kJ will be observed, independent of the reaction path, provided only that the pressure remain constant throughout the process. For instance, during the combustion reaction the reactants and products may attain high and unknown temperatures. However, once the CO<sub>2</sub> product has cooled back to 298.15 K, the total heat which has been exchanged with the surroundings will be -393.52 kJ independent of the intermediate temperatures.

In Fig. 8 is shown the standard molar enthalpy of Fe as a function of temperature.

The y-axis,  $(h_T^o - h_{298.15}^o)$ , is the heat required to heat one mole of Fe from 298.15 K to a temperature  $T$  at constant pressure. The slope of the curve is the molar heat capacity at constant pressure:

$$c_p = (dh/dT)_p \quad (17)$$

From Eq. (17) we obtain the following expression for the heat required to heat one mole of a substance from a temperature  $T_1$  to a temperature  $T_2$  at constant  $P$  (assuming no phase changes in the interval):

$$(h_{T_2} - h_{T_1}) = \int_{T_1}^{T_2} c_p dT \quad (18)$$

The enthalpy curve can be measured by the technique of drop calorimetry, or the heat capacity can be measured directly by adiabatic calorimetry.

The standard equilibrium temperature of fusion (melting) of Fe is 1811 K as shown on Fig. 8. The fusion reaction is a *first-order phase change* since it occurs at constant temperature. The standard molar enthalpy of fusion  $\Delta h_f^o$  is 13.807 kJ mol<sup>-1</sup> as shown on Fig. 8. It can also be seen on Fig. 8 that Fe undergoes two other first-order phase changes, the first from  $\alpha$  (bcc) to  $\gamma$  (fcc) Fe at  $T_{\alpha \rightarrow \gamma}^o = 1184.8$  K and the second from  $\gamma$  to  $\delta$  (bcc) at 1667.5 K. The enthalpy changes are, respectively, 1.013 and 0.826 kJ mol<sup>-1</sup>. The Curie temperature,  $T_{\text{curie}} = 1045$  K, which is also shown on Fig. 8, will be discussed in Sec. 10.

### 2.3 Gibbs Energy

The Gibbs energy (also called the Gibbs free energy, or simply the free energy),  $G$ , is defined as:

$$G = H - TS \quad (19)$$

As in Sec. 2.2, we consider a closed system and assume that the only work term is the work of expansion and that this is reversible. From Eqs (13) and (19):

$$dG_n = dQ + V dP - T dS - S dT \quad (20)$$

Consequently, for a process occurring at constant  $T$  and  $P$  in a closed system:

$$dG_{T,P,n} = dQ_P - T dS = dH_P - T dS \quad (21)$$

Consider the case where the “surroundings” are simply a heat reservoir at a temperature equal to the temperature  $T$  of the system. That is, no irreversible processes occur in the surroundings which receive only a reversible transfer of heat ( $-dQ$ ) at constant temperature. Therefore, from Eq. (8):

$$dS_{\text{surr}} = - dQ/T \quad (22)$$

Substituting into Eq. (21) and using Eq. (3) yields:

$$dG_{T,P,n} = - T dS_{\text{surr}} - T dS = - T dS_{\text{total}} \leq 0 \quad (23)$$

Eq. (23) may be considered to be a special form of the Second Law for a process occurring in a closed system at constant  $T$  and  $P$ . From Eq. (23) such a process will be spontaneous if  $dG$  is negative.

For our purposes in this chapter Eq. (23) is the most useful form of the Second Law.

An objection might be raised that Eq. (23) applies only when the surroundings are at the same temperature  $T$  as the system. However, if the surroundings are at a different temperature, we simply postulate a hypothetical heat reservoir which is at the same temperature as the system, and which lies between the system and surroundings, and we consider the irreversible transfer of heat between the reservoir and the real surroundings as a second separate process.

Substituting Eqs (8) and (22) into Eq. (23) gives:

$$dG_{T,P,n} = (dQ - dQ_{\text{rev}}) \leq 0 \quad (24)$$

In Eq. (24),  $dQ$  is the heat of the actual process, while  $dQ_{\text{rev}}$  is the heat which would be observed were the process occurring reversibly. If the actual process is reversible, that is if the system is at equilibrium, then  $dQ = dQ_{\text{rev}}$  and  $dG = 0$ .

As an example, consider the fusion of Fe in Fig. 8. At  $T_f^0 = 1181$  K, solid and liquid are in equilibrium. That is, at this temperature melting is a reversible process. Therefore, at 1811 K:

$$dg_f^0 = dh_f^0 - Tds_f^0 = 0 \quad (25)$$

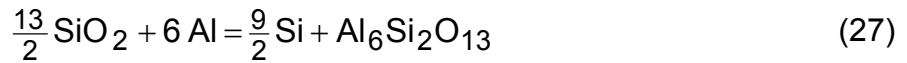
Therefore the molar entropy of fusion at 1811 K is given by:

$$\Delta s_f^0 = (\Delta h_f^0 / T) \quad \text{when } T = T_f^0 \quad (26)$$

Eq. (26) applies only at the equilibrium melting point. At temperatures below and above this temperature the liquid and solid are not in equilibrium. Above the melting point,  $\Delta g_f^0 < 0$  and melting is a spontaneous process (liquid more stable than solid). Below the melting point,  $\Delta g_f^0 > 0$  and the reverse process (solidification) is spontaneous. As the temperature deviates progressively further from the equilibrium melting point the magnitude of  $\Delta g_f^0$ , that is of the driving force, increases. We shall return to this subject in Sec. 4.2.

## 2.4 Chemical Equilibrium

Consider first the question of whether silica fibers in an aluminum matrix at 500°C will react to form mullite,  $Al_6Si_2O_{13}$ :



If the reaction proceeds with the formation of  $d\xi$  moles of mullite then, from the stoichiometry of the reaction,  $dn_{Si} = (9/2) d\xi$ ,  $dn_{Al} = -6 d\xi$ , and  $dn_{SiO_2} = -13/2 d\xi$ . Since the four substances are essentially immiscible at 500°C, their Gibbs energies are equal to their standard molar Gibbs energies,  $g_i^0$  (also known as the standard chemical potentials  $\mu_i^0$  as defined in Sec. 2.7), the standard state of a solid or liquid compound being the pure compound at  $P = 1.0$  bar. The Gibbs energy of the system then varies

as:

$$dG/d\xi = g_{\text{Al}_6\text{Si}_2\text{O}_{13}}^{\circ} + \frac{9}{2} g_{\text{Si}}^{\circ} - \frac{13}{2} g_{\text{SiO}_2}^{\circ} - 6g_{\text{Al}}^{\circ} = \Delta G^{\circ} = -830 \text{ kJ} \quad (28)$$

where  $\Delta G^{\circ}$  is called the standard Gibbs energy change of reaction (27) at 500°C.

Since  $\Delta G^{\circ} < 0$ , the formation of mullite entails a decrease in  $G$ . Hence, the reaction will proceed spontaneously so as to minimize  $G$ . Equilibrium will never be attained and the reaction will proceed to completion.

### 2.4.1 Equilibria Involving a Gaseous Phase

An *ideal gas* mixture is one which obeys the ideal gas equation of state:

$$PV = nRT \quad (29)$$

where  $n$  is the total number of moles. Further, the partial pressure of each gaseous species in the mixture is given by:

$$p_i V = n_i RT \quad (30)$$

where  $n = \sum n_i$  and  $P = \sum p_i$  (Dalton's Law for ideal gases).  $R$  is the ideal gas constant. The *standard state* of a gaseous compound is the pure compound at a pressure of 1.0 bar. It can easily be shown that the partial molar Gibbs energy  $g_i$  (also called the chemical potential  $\mu_i$  as defined in Sec. 2.7) of a species in an ideal gas mixture is given in terms of its standard molar Gibbs energy,  $g_i^{\circ}$  (also called the standard chemical potential  $\mu_i^{\circ}$ ) by:

$$g_i = g_i^{\circ} + RT \ln p_i \quad (31)$$

The final term in Eq. (31) is entropic. As a gas expands at constant temperature its entropy increases.

Consider a gaseous mixture of  $\text{H}_2$ ,  $\text{S}_2$  and  $\text{H}_2\text{S}$  with partial pressures  $p_{\text{H}_2}$ ,  $p_{\text{S}_2}$  and  $p_{\text{H}_2\text{S}}$ . The gases can react according to



If reaction (32) proceeds to the right with the formation of  $2d\xi$  moles of  $\text{H}_2\text{S}$ , then the

Gibbs energy of the system varies as:

$$\begin{aligned}
 dG/d\xi &= 2g_{\text{H}_2\text{S}} - 2g_{\text{H}_2} - g_{\text{S}_2} \\
 &= (2g_{\text{H}_2\text{S}}^\circ - 2g_{\text{H}_2}^\circ - g_{\text{S}_2}^\circ) \\
 &\quad + RT(2\ln p_{\text{H}_2\text{S}} - 2\ln p_{\text{H}_2} - \ln p_{\text{S}_2}) \\
 &= \Delta G^\circ + RT \ln(p_{\text{H}_2\text{S}}^2 p_{\text{H}_2}^{-2} p_{\text{S}_2}^{-1}) \\
 &= \Delta G
 \end{aligned} \tag{33}$$

$\Delta G$ , which is the Gibbs energy change of reaction (32), is thus a function of the partial pressures. If  $\Delta G < 0$ , then the reaction will proceed to the right so as to minimize  $G$ . In a closed system, as the reaction continues with the production of  $\text{H}_2\text{S}$ ,  $p_{\text{H}_2\text{S}}$  will increase while  $p_{\text{H}_2}$  and  $p_{\text{S}_2}$  will decrease. As a result,  $\Delta G$  will become progressively less negative. Eventually an equilibrium state will be reached when  $dG/d\xi = \Delta G = 0$ .

For the equilibrium state, therefore:

$$\begin{aligned}
 \Delta G^\circ &= -RT \ln K \\
 &= -RT \ln(p_{\text{H}_2\text{S}}^2 p_{\text{H}_2}^{-2} p_{\text{S}_2}^{-1})_{\text{equilibrium}}
 \end{aligned} \tag{34}$$

where  $K$ , the "equilibrium constant" of the reaction, is the one unique value of the ratio  $(p_{\text{H}_2\text{S}}^2 p_{\text{H}_2}^{-2} p_{\text{S}_2}^{-1})$  for which the system will be in equilibrium at the temperature  $T$ .

If the initial partial pressures are such that  $\Delta G > 0$ , then reaction (32) will proceed to the left in order to minimize  $G$  until the equilibrium condition of Eq. (34) is attained.

As a further example, consider the possible precipitation of graphite from a gaseous mixture of  $\text{CO}$  and  $\text{CO}_2$ . The reaction is:



Proceeding as above, we can write:

$$\begin{aligned}
dG/d\xi &= g_C + g_{CO_2} - 2g_{CO} \\
&= (g_C^o + g_{CO_2}^o - 2g_{CO}^o) + RT \ln (p_{CO_2} p_{CO}^{-2}) \\
&= \Delta G^o + RT \ln (p_{CO_2} p_{CO}^{-2}) \\
&= \Delta G = -RT \ln K + RT \ln (p_{CO_2} p_{CO}^{-2})
\end{aligned}
\tag{36}$$

If  $(p_{CO_2} p_{CO}^{-2})$  is less than the equilibrium constant  $K$ , then precipitation of graphite will occur in order to decrease  $G$ .

Real situations are, of course, generally more complex. To treat the deposition of solid Si from a vapour of  $Si_4$ , for example, we must consider the formation of gaseous  $I_2$ ,  $I$  and  $SiI_2$  so that three independent reaction equations must be written:



The equilibrium state, however, is still that which minimizes the total Gibbs energy of the system. This is equivalent to satisfying simultaneously the equilibrium constants of reactions (37) to (39).

Equilibria involving reactants and products which are solid or liquid solutions will be discussed in Sec. 4.1.4.

## 2.4.2 Predominance Diagrams

Predominance diagrams are a particularly simple type of phase diagram which have many applications in the fields of hot corrosion, chemical vapor deposition, etc. Furthermore, their construction clearly illustrates the principles of Gibbs energy minimization.

A predominance diagram for the  $Cu-SO_2-O_2$  system at  $700^\circ C$  is shown in Fig. 9. The axes are the logarithms of the partial pressures of  $SO_2$  and  $O_2$  in the gas phase. The diagram is divided into areas or domains of stability of the various solid compounds of Cu, S and O. For example, at point Z, where  $p_{SO_2} = 10^{-2}$  and  $p_{O_2} = 10^{-7}$  bar, the stable phase is  $Cu_2O$ . The conditions for coexistence of two and three solid phases are

indicated respectively by the lines and triple points on the diagram. For example, along the line separating the  $\text{Cu}_2\text{O}$  and  $\text{CuSO}_4$  domains the equilibrium constant  $K = p_{\text{SO}_2}^{-2} p_{\text{O}_2}^{-3/2}$  of the following reaction is satisfied:



Hence, along this line:

$$\log K = -\Delta G^\circ / RT = -2 \log p_{\text{SO}_2} - 3/2 \log p_{\text{O}_2} = \text{constant} \quad (41)$$

This line is thus straight with slope  $(-3/2)/2 = -3/4$ .

We can construct Fig. 9 following the procedure of Bale et al. (1986). We formulate a reaction for the formation of each solid phase, always from one mole of Cu, and involving the gaseous species whose pressures are used as the axes ( $\text{SO}_2$  and  $\text{O}_2$  in this example):



and similarly for the formation of  $\text{Cu}_2\text{S}$ ,  $\text{Cu}_2\text{SO}_4$  and  $\text{Cu}_2\text{SO}_5$ .

The values of  $\Delta G^\circ$  are obtained from tables of thermodynamic properties. For any given values of  $p_{\text{SO}_2}$  and  $p_{\text{O}_2}$ ,  $\Delta G$  for each formation reaction can then be calculated. The stable compound is simply the one with the most negative  $\Delta G$ . If all the  $\Delta G$  values are positive, then pure Cu is the stable compound.

By reformulating Eqs. (42) to (45) in terms of, for example,  $\text{S}_2$  and  $\text{O}_2$  rather than  $\text{SO}_2$  and  $\text{O}_2$ , a predominance diagram with  $\log p_{\text{S}_2}$  and  $\log p_{\text{O}_2}$  as axes can be constructed. Logarithms of ratios or products of partial pressures can also be used as axes.

Along the curve shown by the crosses on Fig. 9 the total pressure is 1.0 bar. That is, the gas consists not only of  $\text{SO}_2$  and  $\text{O}_2$ , but of other species such as  $\text{S}_2$  whose

equilibrium partial pressures can be calculated. Above this line the total pressure is greater than 1.0 bar even though the sum of the partial pressures of SO<sub>2</sub> and O<sub>2</sub> may be less than 1.0 bar.

A similar phase diagram of  $RT \ln p_{O_2}$  versus  $T$  for the Cu-O<sub>2</sub> system is shown in Fig. 10. For the formation reaction:



we can write:

$$\Delta G^\circ = -RT \ln K = RT \ln (p_{O_2})_{\text{equilibrium}} = \Delta H^\circ - T\Delta S^\circ \quad (47)$$

The line between the Cu and Cu<sub>2</sub>O domains in Fig. 10 is thus a plot of the standard Gibbs energy of formation of Cu<sub>2</sub>O versus  $T$ . The temperatures indicated by the symbols M and  $\boxed{M}$  are the melting points of Cu and Cu<sub>2</sub>O respectively. This line is thus simply a line taken from the well-known *Ellingham diagram* or  $\Delta G^\circ$  vs.  $T$  diagram for the formation of oxides. However, by drawing vertical lines at the melting points of Cu and Cu<sub>2</sub>O as shown in Fig. 10, we convert the Ellingham diagram to a phase diagram. Stability domains for Cu(sol), Cu(liq), Cu<sub>2</sub>O(sol), Cu<sub>2</sub>O(liq) and CuO(sol) are shown as functions of  $T$  and of the imposed equilibrium  $p_{O_2}$ . The lines and triple points indicate conditions for two- and three-phase equilibria.

## 2.5 Measuring Gibbs Energy, Enthalpy and Entropy

### 2.5.1 Measuring Gibbs Energy Change

In general, the Gibbs energy change of a process can be determined by performing measurements under equilibrium conditions. Consider reaction (35) for example. Experimentally, equilibrium is first established between solid C and the gas phase and the equilibrium constant is then found by measuring the partial pressures of CO and CO<sub>2</sub>. Eq. (36) is then used to calculate  $\Delta G^\circ$ .

Another common technique of establishing equilibrium is by means of an electrochemical cell. A galvanic cell is designed so that a reaction (the cell reaction) can occur only with the passage of an electric current through an external circuit. An

external voltage is applied which is equal in magnitude but opposite in sign to the cell potential,  $E$ (volts), such that no current flows. The system is then at equilibrium. With the passage of  $dz$  coulombs through the external circuit,  $Edz$  joules of work are performed. Since the process occurs at equilibrium, this is the reversible non-PV work,  $dW_{rev(non-PV)}$ . Substituting Eq. (11) into Eq. (19), differentiating, and substituting Eq. (10) gives:

$$dG = V dP - S dT + \sum \mu_i dn_i + dW_{rev(non-PV)} \quad (48)$$

For a closed system at constant  $T$  and  $P$ :

$$dG_{T,P,n} = dW_{rev(non-PV)} \quad (49)$$

If the cell reaction is formulated such that the advancement of the reaction by  $d\xi$  moles is associated with the passage of  $dz$  coulombs through the external circuit, then from Eq. (49):

$$\Delta G d\xi = - E dz \quad (50)$$

Hence: 
$$\Delta G = - FE \quad (51)$$

where  $\Delta G$  is the Gibbs energy change of the cell reaction,  $F = dz/d\xi = 96500 \text{ coulombs mol}^{-1}$  is the Faraday constant, which is the number of coulombs in a mole of electrons, and the negative sign follows the usual electrochemical sign convention. Hence, by measuring the open-circuit voltage  $E$ , one can determine  $\Delta G$  of the cell reaction.

### 2.5.2 Measuring Enthalpy Change

The enthalpy change,  $\Delta H$ , of a process may be measured directly by calorimetry. Alternatively, if  $\Delta G$  is measured by an equilibration technique as in Sec. 2.5.1, then  $\Delta H$  can be determined from the measured temperature dependence of  $\Delta G$ . From Eq. (48), for a process in a closed system with no non-PV work at constant pressure:

$$(dG/dT)_{P,n} = -S \quad (52)$$

Substitution of Eq. (19) into Eq. (52) gives:

$$(d(G/T)/d(1/T))_{P,n} = H \quad (53)$$

Eqs. (52) and (53) apply to both the initial and final states of a process. Hence:

$$(d(\Delta G)/dT)_{P,n} = -\Delta S \quad (54)$$

$$(d(\Delta G/T)d(1/T))_{P,n} = \Delta H \quad (55)$$

Eqs. (52) to (55) are various forms of the *Gibbs-Helmholtz equation*.

### 2.5.3 Measuring Entropy

As is the case with the enthalpy,  $\Delta S$  of a process can be determined from the measured temperature dependence of  $\Delta G$  by means of Eq. (54). This is known as the “second law method” of measuring entropy.

Another method of measuring entropy involves the *Third Law* of thermodynamics which states that the entropy of a perfect crystal of a pure substance at internal equilibrium at a temperature of 0 K is zero. This follows from Eq. (2) and the concept of entropy as disorder. For a perfectly ordered system at absolute zero,  $t = 1$  and  $S = 0$ .

Let us first derive an expression for the change in entropy as a substance is heated. Combining Eqs (52) and (53) gives:

$$(dH/dT)_{P,n} = T(dS/dT)_{P,n} \quad (56)$$

Substituting Eq. (18) into Eq. (56) and integrating then gives the following expression for the entropy change as one mole of a substance is heated at constant  $P$  from  $T_1$  to  $T_2$ :

$$(s_{T_2} - s_{T_1}) = \int_{T_1}^{T_2} (c_p/T) dT \quad (57)$$

The similarity to Eq. (18) is evident, and a plot of  $(s_{T_2} - s_{T_1})$  versus  $T$  is similar in appearance to Fig. 8.

Setting  $T_1 = 0$  in Eq. (57) and using the Third Law gives:

$$s_{T_2} = \int_0^{T_2} (c_p/T) dT \quad (58)$$

Hence, if  $c_p$  has been measured down to temperatures sufficiently close to 0 K, Eq. (58) can be used to calculate the absolute entropy. This is known as the “third law method” of measuring entropy.

#### 2.5.4 Zero Entropy and Zero Enthalpy

The third law method permits the measurement of the absolute entropy of a substance, whereas the second law method permits the measurement only of entropy changes,  $\Delta S$ .

The Third Law is not a convention. It provides a natural zero for entropy. On the other hand, no such natural zero exists for the enthalpy since there is no simple natural zero for the internal energy. However, by convention the absolute enthalpy of a pure element in its stable state at  $P = 1.0$  bar and  $T = 298.15$  K is usually set to zero. Therefore, the absolute enthalpy of a compound is, by convention, equal to its standard enthalpy of formation from the pure elements in their stable standard states at 298.15 K.

## 2.6 Auxiliary Functions

It was shown in Sec. 2.3 that Eq. (23) is a special form of the Second Law for a process occurring at constant  $T$  and  $P$ . Other special forms of the Second Law can be derived in a similar manner.

It follows directly from Eqs. (3,12 & 22), for a process at constant  $V$  and  $S$ , that:

$$dU_{V,S,n} = - T dS_{\text{total}} \leq 0 \quad (59)$$

Similarly, from Eqs. (3, 13 & 22):

$$dH_{P,S,n} = - T dS_{\text{total}} \leq 0 \quad (60)$$

Eqs. (59) and (60) are not of direct practical use since there is no simple means of maintaining the entropy of a system constant during a change of state. A more useful function is the *Helmholtz energy*,  $A$ , defined as:

$$A = U - TS \quad (61)$$

From Eqs. (12) and (40):

$$dA_n = dQ - P dV - T dS - S dT \quad (62)$$

Then, from Eqs. (3) and (22), for processes at constant  $T$  and  $V$ :

$$dA_{T,V,n} = -T dS_{\text{total}} \leq 0 \quad (63)$$

Eqs. (23, 59, 60 & 63) are special forms of the Second Law for closed systems. In this regard,  $H$ ,  $A$  and  $G$  are sometimes called *auxiliary functions*. If we consider open systems, then many other auxiliary functions can be defined as will be shown in Sec. 2.8.2.

In Sec. 2.3 the very important result was derived that the equilibrium state of a system corresponds to a minimum of the Gibbs energy  $G$ . This is used as the basis of nearly all algorithms for calculating chemical equilibria and phase diagrams. An objection might be raised that Eq. (23) only applies at constant  $T$  and  $P$ . What if equilibrium were approached at constant  $T$  and  $V$  for instance? Should we not then minimize  $A$  as in Eq. (63)? The response is that the restrictions on Eqs. (23) and (63) only apply to the paths followed during the approach to equilibrium. However, for a system at an equilibrium temperature, pressure and volume, it clearly does not matter along which hypothetical path the approach to equilibrium was calculated. The reason that most algorithms minimize  $G$  rather than other auxiliary functions is simply that it is generally easiest and most convenient to express thermodynamic properties in terms of the independent variables  $T$ ,  $P$  and  $n_i$ .

## 2.7 The Chemical Potential

The chemical potential was defined in Eq. (5). However, this equation is not particularly useful directly since it is difficult to see how  $S$  can be held constant.

Substituting Eq. (11) into Eq. (19), differentiating and substituting Eq. (9) gives:

$$dG = V dP - S dT + \sum \mu_i dn_i \quad (64)$$

from which it can be seen that  $\mu_i$  is also given by:

$$\mu_i = (\partial G / \partial n_i)_{T,P,n_j \neq i} \quad (65)$$

Differentiating Eq. (11) with substitution of Eq. (9) gives:

$$dH = T dS + V dP + \sum \mu_i dn_i \quad (66)$$

whence: 
$$\mu_i = (\partial H / \partial n_i)_{T, V, n_j \neq i} \quad (67)$$

Similarly it can be shown that:

$$\mu_i = (\partial A / \partial n_i)_{T, V, n_j \neq i} \quad (68)$$

Of these equations for  $\mu_i$ , the most useful is Eq. (65). The chemical potential of a component  $i$  of a system is given by the increase in Gibbs energy as the component is added to the system at constant  $T$  and  $P$  while keeping the numbers of moles of all other components of the system constant.

The chemical potentials of its components are intensive properties of a system; for a system at a given  $T$ ,  $P$  and composition, the chemical potentials are independent of the mass of the system. That is, with reference to Eq. (65), adding  $dn_i$  moles of component  $i$  to a solution of a fixed composition will result in a change in Gibbs energy  $dG$  which is independent of the total mass of the solution.

The reason that this property is called a chemical potential is illustrated by the following thought experiment. Imagine two systems, I and II, at the same temperature and pressure and separated by a membrane that permits the passage of only one component, say component 1. The chemical potentials of component 1 in systems I and II are  $\mu_1^I = \partial G^I / \partial n_1^I$  and  $\mu_1^{II} = \partial G^{II} / \partial n_1^{II}$ . Component 1 is transferred across the membrane with  $dn_1^I = -dn_1^{II}$ . The change in the total Gibbs energy accompanying this transfer is then:

$$dG = d(G^I + dG^{II}) = -(\mu_1^I - \mu_1^{II}) dn_1^{II} \quad (69)$$

If  $\mu_1^I > \mu_1^{II}$ , then  $d(G^I + dG^{II})$  is negative when  $dn_1^{II}$  is positive. That is, the total Gibbs energy is decreased by a transfer of component 1 from system I to system II. Hence, component 1 is transferred spontaneously from a system of higher  $\mu_1$  to a system of lower  $\mu_1$ . For this reason,  $\mu_1$  is called the chemical potential of component 1.

Similarly, by using the appropriate auxiliary functions, it can be shown that  $\mu_i$  is the

potential for the transfer of component  $i$  at constant  $T$  and  $V$ , at constant  $S$  and  $V$ , etc.

An important principle of phase equilibrium can now be stated. *When two or more phases are in equilibrium, the chemical potential of any component is the same in all phases.* This criterion for phase equilibrium is thus equivalent to the criterion of minimizing  $G$ . This will be discussed further in Sec.4.2.

## 2.8 Some Other Useful Thermodynamic Equations

In this section some other useful thermodynamic relations are derived. Consider an open system which is initially empty. That is, initially  $S$ ,  $V$  and  $n$  are all equal to zero. We now “fill up” the system by adding a previously equilibrated mixture. The addition is made at constant  $T$ ,  $P$  and composition. Hence, it is also made at constant  $\mu_i$  (of every component), since  $\mu_i$  is an intensive property. The addition is continued until the entropy, volume and numbers of moles of the components in the system are  $S$ ,  $V$  and  $n_i$ . Integrating Eq. (9) from the initial (empty) to the final state then gives:

$$U = TS - PV + \sum n_i \mu_i \quad (70)$$

It then follows that:

$$H = TS + \sum n_i \mu_i \quad (71)$$

$$A = -PV + \sum n_i \mu_i \quad (72)$$

and most importantly:

$$G = \sum n_i \mu_i \quad (73)$$

### 2.8.1 The Gibbs-Duhem Equation

By differentiation of Eq. (70):

$$dU = T dS + S dT - P dV - V dP + \sum n_i d\mu_i + \sum \mu_i dn_i \quad (74)$$

By comparison of Eqs (9) and (74) it follows that:

$$S dT - V dP + \sum n_i d\mu_i = 0 \quad (75)$$

This is the general Gibbs-Duhem equation.

### 2.8.2 General Auxiliary Functions

It was stated in Sec. 2.6 that many auxiliary functions can be defined for open systems. Consider for example the auxiliary function:

$$\begin{aligned} G' &= U - (-PV) - TS - \sum_1^k n_i \mu_i \\ &= G - \sum_1^k n_i \mu_i \end{aligned} \quad (76)$$

Differentiating Eq. (76) with substitution of Eq. (64) gives:

$$dG' = V dP - S dT - \sum_1^k n_i d\mu_i + \sum_{k+1}^C \mu_i dn_i \quad (77)$$

where  $C$  is the number of components in the system. It then follows that:

$$dG'_{T,P,\mu_i (1 \leq i \leq k), n_i (k+1 \leq i \leq C)} \leq 0 \quad (78)$$

is the criterion for a spontaneous process at constant  $T$ ,  $P$ ,  $\mu_i$  (for  $1 \leq i \leq k$ ) and  $n_i$  (for  $k+1 \leq i \leq C$ ) and that equilibrium is achieved when  $dG' = 0$ . The chemical potential of a component may be held constant, for example, by equilibration with a gas phase as, for example, by fixing the partial pressure of  $O_2$ ,  $SO_2$ , etc.

Finally, it also follows that the chemical potential may be defined very generally as:

$$\mu_i = \left( \frac{\partial G'}{\partial n_i} \right)_{T,P,\mu_i (1 \leq i \leq k), n_i (k+1 \leq i \leq C)} \quad (79)$$

The discussion of the generalized auxiliary functions will be continued in Sec. 7.7.

## 3 The Gibbs Phase Rule

The geometry of all types of phase diagrams is governed by the *Gibbs Phase Rule*

which applies to any system at equilibrium:

$$F = C - P + 2 \quad (80)$$

The Phase Rule will be derived in this section in a general form along with several examples. Further examples will be presented in later sections.

In Eq. (80),  $C$  is the number of *components* in the system. This is the minimum number of substances required to describe the elemental composition of every phase present. As an example, for pure  $\text{H}_2\text{O}$  at  $25^\circ\text{C}$  and 1.0 bar pressure,  $C = 1$ . For a gaseous mixture of  $\text{H}_2$ ,  $\text{O}_2$  and  $\text{H}_2\text{O}$  at high temperature,  $C = 2$ . (Although there are many species present in the gas including  $\text{O}_2$ ,  $\text{H}_2$ ,  $\text{H}_2\text{O}$ ,  $\text{O}_3$ , etc., these species are all at equilibrium with each other. At a given  $T$  and  $P$  it is sufficient to know the overall elemental composition in order to be able to calculate the concentration of every species. Hence,  $C = 2$ .  $C$  can never exceed the number of elements in the system).

For the systems shown in Figs. 1 to 7 respectively,  $C = 2, 3, 3, 4, 3, 4$  and 1.

There is generally more than one way to specify the components of a system. For example, the Fe-Si-O system could also be described as the FeO-Fe<sub>2</sub>O<sub>3</sub>-SiO<sub>2</sub> system, or the FeO-SiO<sub>2</sub>-O<sub>2</sub> system, etc. The formulation of a phase diagram can often be simplified by a judicious definition of the components as will be discussed in Sec. 7.5.

In Eq. (80),  $P$  is the number of *phases* present at equilibrium at a given point on the phase diagram. For example, in Fig. 1 at any point within the region labeled "Liquid + bcc",  $P = 2$ . At any point in the region labeled "Liquid",  $P = 1$ .

In Eq. (80),  $F$  is the *number of degrees of freedom* or the *variance* of the system at a given point on the phase diagram. It is the number of variables which must be specified in order to completely specify the state of the system. Let us number the components as 1, 2, 3,.....,  $C$  and designate the phases as  $\alpha$ ,  $\beta$ ,  $\gamma$ , ..... In most derivations of the Phase Rule, the only variables considered are  $T$ ,  $P$  and the compositions of the phases. Since we also want to treat more general phase diagrams in which chemical potentials, volumes, enthalpies, etc. can also be variables, we shall extend the list of variables as follows:

$T, P$

$(X_1^\alpha, X_2^\alpha, \dots, X_{C-1}^\alpha), (X_1^\beta, X_2^\beta, \dots, X_{C-1}^\beta), \dots$

$\mu_1, \mu_2, \mu_3, \dots$

$V^\alpha, V^\beta, V^\gamma, \dots$

$S^\alpha, S^\beta, S^\gamma, \dots$

where  $X_i^\alpha$  is the mole fraction of component  $i$  in phase  $\alpha$ ,  $\mu_i$  is the chemical potential of component  $i$ , and  $V^\alpha$  and  $S^\alpha$  are the volume and entropy of phase  $\alpha$ . Alternatively, we may substitute mass fractions for mole fractions and enthalpies  $H^\alpha, H^\beta, \dots$  for  $S^\alpha, S^\beta, \dots$

It must be stressed that the overall composition of the system is not a variable in the sense of the Phase Rule. The composition variables are the compositions of the individual phases.

The total number of variables is thus equal to  $(2 + P(C-1) + C + 2P)$ .

(Only  $(C-1)$  independent composition variables  $X_i$  are required for each phase since the sum of the mole fractions is unity.)

At equilibrium the chemical potential  $\mu_i$  of each component  $i$  is the same in all phases (see Sec.2.7) as are  $T$  and  $P$ .  $\mu_i$  is an intensive variable (see Sec. 2.7) which is a function of  $T, P$  and composition. Hence:

$$\mu_i^\alpha(T, P, X_1^\alpha, X_2^\alpha, \dots) = \mu_i^\beta(T, P, X_1^\beta, X_2^\beta, \dots) = \dots = \mu_i \quad (81)$$

This yields  $PC$  equations relating the variables. Furthermore, the volume of each phase is a function of  $T, P$  and composition,  $V^\alpha = (T, P, X_1^\alpha, X_2^\alpha, \dots)$ , as is the entropy of the phase (or, alternatively, the enthalpy). This yields an additional  $2P$  equations relating the variables.

$F$  is then equal to the number of variables minus the number of equations relating the variables at equilibrium:

$$F = (2 + P(C-1) + C + 2P) - PC - 2P = C - P + 2 \quad (82)$$

Eq. (80) is thereby derived.

### 3.1 The Phase Rule and Binary Temperature-Composition Phase Diagrams

As a first example of the application of the Phase Rule, consider the temperature-composition ( $T$ - $X$ ) phase diagram of the Bi-Sb system at a constant applied pressure of 1.0 bar in Fig. 11. The abscissa of Fig. 11 is the composition, expressed as mole fraction of Sb,  $X_{Sb}$ . Note that  $X_{Bi} = 1 - X_{Sb}$ . Phase diagrams are also often drawn with the composition axis expressed as weight percent.

At all compositions and temperatures in the area above the line labelled “liquidus”, a single-phase liquid solution will be observed, while at all compositions and temperatures below the line labelled “solidus”, there will be a single-phase solid solution. A sample at equilibrium at a temperature and overall composition between these two curves will consist of a mixture of solid and liquid phases, the compositions of which are given by the liquidus and solidus compositions at that temperature. For example, a sample of overall composition  $X_{Sb} = 0.60$  at  $T=450^\circ\text{C}$  (at point  $R$  in Fig. 11) will consist, at equilibrium, of a mixture of a liquid of composition  $X_{Sb} = 0.37$  (point  $P$ ) and solid of composition  $X_{Sb} = 0.80$  (point  $Q$ ). The line  $PQ$  is called a *tie-line* or *conode*.

Binary temperature-composition phase diagrams are generally plotted at a fixed pressure, usually 1.0 bar. This eliminates one degree of freedom. In a binary system,  $C = 2$ . Hence, for binary isobaric  $T$ - $X$  diagrams the phase rule reduces to:

$$F = 3 - P \quad (83)$$

Binary  $T$ - $X$  diagrams contain single-phase areas and two-phase areas. In the single-phase areas,  $F = 3 - 1 = 2$ . That is, temperature and composition can be specified independently. These regions are thus called *bivariant*. In two-phase regions,  $F = 3 - 2 = 1$ . If, say,  $T$  is specified, then the compositions of both phases are determined by the ends of the tie-lines. Two-phase regions are thus termed *univariant*. Note that although the overall composition can vary over a range within a two-phase region at constant  $T$ , the overall composition is not a parameter in the sense of the phase rule. Rather, it is the compositions of the individual phases at equilibrium that are the parameters to be considered in counting the number of degrees of freedom.

As the overall composition is varied at 450°C between points  $P$  and  $Q$ , the compositions of the liquid and solid phases remain fixed at  $P$  and  $Q$ , and only the relative proportions of the two phases change. From a simple mass balance, we can derive the *lever rule* for binary systems: (moles of liquid)/(moles of solid) =  $QR/PR$  where  $QR$  and  $PR$  are the lengths of the line segments. Hence, at 450°C a sample with overall composition  $X_{Sb} = 0.60$  consists of liquid and solid phases in the molar ratio  $(0.80-0.60)/(0.60-0.37) = 0.87$ . Were the composition axis expressed as weight percent, then the lever rule would give the weight ratio of the two phases.

Suppose that a liquid Bi - Sb solution with composition  $X_{Sb} = 0.60$  is cooled very slowly from an initial temperature above 526°C. When the temperature has decreased to the liquidus temperature 526°C (point  $A$ ), the first solid appears, with a composition at point  $B$  ( $X_{Sb} = 0.89$ ). As the temperature is decreased further, solid continues to precipitate with the compositions of the two phases at any temperature being given by the liquidus and solidus compositions at that temperature and with their relative proportions being given by the lever rule. Solidification is complete at 349°C, the last liquid to solidify having composition  $X_{Sb} = 0.16$  (point  $C$ ).

The process just described is known as *equilibrium cooling*. At any temperature during equilibrium cooling the solid phase has a uniform (homogeneous) composition. In the preceding example, the composition of the solid phase during cooling varies along the line  $BQD$ . Hence, in order for the solid grains to have a uniform composition at any temperature, diffusion of Sb from the center to the surface of the growing grains must occur. Since solid-state diffusion is a relatively slow process, equilibrium cooling conditions are only approached if the temperature is decreased very slowly. If a sample of composition  $X_{Sb} = 0.60$  is cooled rapidly from the liquid, concentration gradients will be observed in the solid grains, with the concentration of Sb decreasing towards the surface from a maximum of  $X_{Sb} = 0.89$  (point  $B$ ). Furthermore, in this case solidification will not be complete at 349°C since at 349°C the average concentration of Sb in the solid grains will be greater than  $X_{Sb} = 0.60$ . These considerations are discussed more fully in Sec. 9 and in Chapter 7 of this volume.

At  $X_{Sb} = 0$  and  $X_{Sb} = 1$  in Fig. 11, the liquidus and solidus curves meet at the equilibrium melting points, or *temperatures of fusion* of Bi and Sb, which are

$T_{f(Bi)}^{\circ} = 271.4^{\circ}\text{C}$  and  $T_{f(Sb)}^{\circ} = 630.6^{\circ}\text{C}$ . At these two points the number of components is reduced to 1. Hence, from the Phase Rule the two-phase region becomes invariant ( $F = 0$ ) and solid and liquid co-exist at the same temperature.

The phase diagram is influenced by the total pressure,  $P$ . Unless otherwise stated,  $T$ - $X$  diagrams are usually presented for  $P = \text{constant} = 1.0 \text{ bar}$ . For equilibria involving only solid and liquid phases, the phase boundaries are typically shifted only by the order of a few hundredths of a degree per bar change in  $P$ . Hence, the effect of pressure upon the phase diagram is generally negligible unless the pressure is of the order of hundreds of bars. On the other hand, if gaseous phases are involved the effect of pressure is very important. The effect of pressure will be discussed in Sec. 4.3.

### 3.1.1 Three-phase Invariants in Binary Temperature-Composition Phase Diagrams

When three phases are at equilibrium in a binary system at constant pressure, then from Eq. (83),  $F = 0$ . Hence, the compositions of all three phases as well as  $T$  are fixed and the system is said to be *invariant*. An example is the line  $PQR$  in Fig. 1 in the  $T$ - $X$  diagram of the Fe-Mo system. At any overall composition of the system lying between points  $P$  and  $R$  at  $1612^{\circ}\text{C}$ , three phases will be in equilibrium: liquid, sigma and bcc, with compositions at points  $P$ ,  $Q$  and  $R$  respectively. Several other invariants can also be seen in Fig. 1. Binary  $T$ - $X$  diagrams and invariant reactions will be discussed in detail in Sec. 5.

## 3.2 Other Examples of Applications of the Phase Rule

Despite its apparent simplicity, the Phase Rule is frequently misunderstood and incorrectly applied. In this section a few additional illustrative examples of the application of the Phase Rule will be briefly presented. These examples will be elaborated upon in subsequent sections.

In the single-component  $\text{Al}_2\text{SiO}_5$  system ( $C = 1$ ) shown Fig. 7, the Phase Rule reduces to:

$$F = 3 - P \quad (84)$$

Three allotropes of  $\text{Al}_2\text{SiO}_5$  are shown in the figure. In the single-phase regions,  $F = 2$ ;

in these bivariant regions, both  $P$  and  $T$  (Fig. 7a) or both  $V$  and  $T$  (Fig. 7b) can be specified independently. When two phases are in equilibrium,  $F = 1$ . Two-phase equilibrium is therefore represented by the univariant lines in the  $P$ - $T$  phase diagram in Fig. 7a; when two phases are in equilibrium,  $T$  and  $P$  cannot be specified independently. When all three allotropes are in equilibrium,  $F = 0$ . Three-phase equilibrium can thus only occur at the invariant *triple point* (530°C, 3859 bar) in Fig. 7a.

The invariant triple point in Fig. 7a becomes the invariant line  $PQR$  at  $T = 530^\circ\text{C}$  in the  $V$ - $T$  phase diagram in Fig. 7b. When the three phases are in equilibrium, the total molar volume of the system can lie anywhere on this line depending upon the relative amounts of the three phases present. However, the molar volumes of the individual allotropes are fixed at points  $P$ ,  $Q$  and  $R$ . It is the molar volumes of the individual phases which are the system variables in the sense of the Phase Rule. Similarly, the two-phase univariant lines in Fig. 7a become the two-phase univariant areas in Fig. 7b. The lever rule can be applied in these regions to give the ratio of the volumes of the two phases at equilibrium.

As another example, consider the phase diagram section for the ternary ( $C = 3$ ) Zn-Mg-Al system shown in Fig. 3a. Since the total pressure is constant, one degree of freedom is eliminated. Consequently:

$$F = 4 - P \quad (85)$$

Although the diagram is plotted at constant 10 mol % Zn, this is a composition variable of the entire system, not of any individual phase. That is, it is not a variable in the sense of the Phase Rule, and setting it constant does not reduce the number of degrees of freedom. Hence, for example, the three-phase regions in Fig. 3a are univariant ( $F = 1$ ); at any given  $T$ , the compositions of all three phases are fixed, but the three-phase region extends over a range of temperature. Ternary temperature-composition phase diagrams will be discussed in detail in Sec. 6.

Finally we shall examine some diagrams with chemical potentials as variables. As a first example, the phase diagram of the Fe-Ni-O<sub>2</sub> system in Fig. 5 is a plot of the equilibrium oxygen pressure (fixed, for example, by equilibrating the solid phases with a gas phase of fixed  $p_{\text{O}_2}$ ) versus the molar ratio Ni/(Fe+Ni) at constant  $T$  and constant

total hydrostatic pressure. For an ideal gas, it follows from Eq. (31) and the definition of chemical potential (Sec. 2.7) that:

$$\mu_i = \mu_i^\circ + RT \ln p_i \quad (86)$$

where  $\mu_i^\circ$  is the standard-state (at  $p_i = 1.0$  bar) chemical potential of the pure gas at temperature  $T$ . Hence, if  $T$  is constant,  $\mu_i$  varies directly as  $\ln p_i$ . The y-axis in Fig. 5 thus varies directly as  $\mu_{O_2}$ . Fixing  $T$  and hydrostatic pressure eliminates two degrees of freedom. Hence,  $F = 3 - P$ . Therefore, Fig. 5 has the same topology as a binary  $T$ - $X$  diagram like Fig. 1, with single-phase bivariant areas, two-phase univariant areas with tie-lines, and three-phase invariant lines at fixed  $\log p_{O_2}$  and fixed compositions of the three phases.

As a second example, in the isothermal predominance diagram of the Cu-SO<sub>2</sub>-O<sub>2</sub> system in Fig. 9, the x- and y-axis variables vary as  $\mu_{S_2}$  and  $\mu_{O_2}$ . Since  $C = 3$  and  $T$  is constant:

$$F = 4 - P \quad (87)$$

The diagram has a topology similar to the  $P$ - $T$  phase diagram of a one-component system as in Fig. 7a. Along the lines of the diagram two solid phases are in equilibrium and at the triple points three solid phases co-exist. However, a gas phase is also present everywhere. Hence, at the triple points there are really four phases present at equilibrium, while the lines represent three-phase equilibria. Hence, the diagram is consistent with Eq. (87).

It is instructive to look at Fig. 9 in another way. Suppose that we fix a constant hydrostatic pressure of 1.0 bar (for example, by placing the system in a cylinder fitted with a piston). This removes one further degree of freedom, so that now  $F = 3 - P$ . However, as long as the total equilibrium gas pressure is less than 1.0 bar there will be no gas phase present, and so the diagram is consistent with the Phase Rule. On the other hand, above the 1.0 bar curve shown by the line of crosses on Fig. 9, the total gas pressure exceeds 1.0 bar. Hence the phase diagram calculated at a total hydrostatic pressure of 1.0 bar must terminate at this curve.

The Phase Rule may be applied to the four-component isothermal Fe-Cr-S<sub>2</sub>-O<sub>2</sub> phase diagram in Fig. 10 in a similar way. Remember that fixing the molar ratio Cr/(Fe+Cr) equal to 0.5 does not eliminate a degree of freedom since this composition variable applies to the entire system, not to any individual phase.

## 4 Thermodynamic Origin of Binary Phase Diagrams

### 4.1 Thermodynamics of Solutions

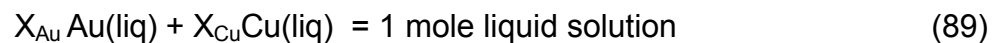
#### 4.1.1 Gibbs Energy of Mixing

Liquid gold and copper are completely miscible at all compositions. The Gibbs energy of one mole of liquid solution,  $g^l$  at 1100°C is drawn in Fig. 12 as a function of composition expressed as *mole fraction*,  $X_{Cu}$ , of copper. Note that  $X_{Au} = 1 - X_{Cu}$ . The curve of  $g^l$  varies between the standard molar Gibbs energies of pure liquid Au and Cu,  $g_{Au}^o$  and  $g_{Cu}^o$ . From Eq. (65) it follows that, for a pure component,  $g_i^o$  and  $\mu_i^o$  are identical.

The function  $\Delta g_m^l$  shown on Fig. 12 is called the molar *Gibbs energy of mixing* of the liquid solution. It is defined as:

$$\Delta g_m^l = g^l - (X_{Au} \mu_{Au}^o + X_{Cu} \mu_{Cu}^o) \quad (88)$$

It can be seen that  $\Delta g_m^l$  is the Gibbs energy change associated with the isothermal mixing of  $X_{Au}$  moles of pure liquid Au and  $X_{Cu}$  moles of pure liquid Cu to form one mole of solution according to the reaction:



Note that for the solution to be stable it is necessary that  $\Delta g_m^l$  be negative.

#### 4.1.2 Tangent Construction

An important construction is illustrated in Fig. 12. If a tangent is drawn to the curve of  $g^l$  at a certain composition ( $X_{Cu} = 0.4$  in Fig.12), then the intercepts of this tangent on the axes at  $X_{Au} = 1$  and  $X_{Cu} = 1$  are equal to  $\mu_{Au}$  and  $\mu_{Cu}$  respectively at this composition.

To prove this, divide Eqs. (64) and (73) by  $(n_{Au} + n_{Cu})$  at constant  $T$  and  $P$  to obtain

expressions for the molar Gibbs energy and its derivative:

$$g^l = X_{\text{Au}}\mu_{\text{Au}} + X_{\text{Cu}}\mu_{\text{Cu}} \quad (90)$$

and

$$dg^l = \mu_{\text{Au}} dX_{\text{Au}} + \mu_{\text{Cu}} dX_{\text{Cu}} \quad (91)$$

Since  $dX_{\text{Au}} = -dX_{\text{Cu}}$ , it can be seen that Eqs. (90) and (91) are equivalent to the tangent construction shown in Fig. 12.

These equations may also be rearranged to give the following useful expression for a binary system:

$$\mu_i = g + (1 - X_i) dg/dX_i \quad (92)$$

#### 4.1.3 Relative Partial Properties

The difference between the chemical potential  $\mu_i$  (also called the partial Gibbs energy  $g_i$ ) of a component in solution and the chemical potential  $\mu_i^{\circ}$  (or  $g_i^{\circ}$ ) of the same component in a *standard state* is called the *relative chemical potential* (or *relative partial Gibbs energy*),  $\Delta\mu_i$  (or  $\Delta g_i$ ). It is usual to choose, as standard state, the pure component in the same phase at the same temperature. *The activity  $a_i$  of the component relative to the chosen standard state* is then defined in terms of  $\Delta\mu_i$  by the following equation, as illustrated in Fig. 12.

$$\Delta\mu_i = \mu_i - \mu_i^{\circ} = RT \ln a_i \quad (93)$$

From Fig. 12, it can be seen that:

$$\Delta g_m = X_{\text{Au}}\Delta\mu_{\text{Au}} + X_{\text{Cu}}\Delta\mu_{\text{Cu}} = RT (X_{\text{Au}} \ln a_{\text{Au}} + X_{\text{Cu}} \ln a_{\text{Cu}}) \quad (94)$$

The isothermal Gibbs energy of mixing can be divided into enthalpy and entropy terms, as can the relative chemical potentials:

$$\Delta g_m = \Delta h_m - T\Delta s_m \quad (95)$$

$$\Delta\mu_i = \Delta h_i - T\Delta s_i \quad (96)$$

where  $\Delta h_m$  and  $\Delta s_m$  are the enthalpy and entropy change associated with the isothermal mixing reaction (89). It follows from Eqs.(94) to (96) that:

$$\Delta h_m = X_{Au}\Delta h_{Au} + X_{Cu}\Delta h_{Cu} \quad (97)$$

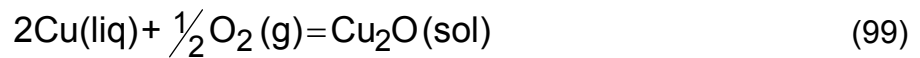
$$\Delta s_m = X_{Au}\Delta s_{Au} + X_{Cu}\Delta s_{Cu} \quad (98)$$

and so tangent constructions similar to that of Fig. 12 can be used to relate the *relative partial enthalpies and entropies*  $\Delta h_i$  and  $\Delta s_i$  to the *integral molar enthalpy of mixing*  $\Delta h_m$  and *integral molar entropy of mixing*  $\Delta s_m$  respectively.

#### 4.1.4 Activity

The activity of a component in a solution was defined by Eq. (93). Since  $a_i$  varies monotonically with  $\mu_i$  it follows that *when two or more phases are in equilibrium the activity of any component is the same in all phases*, provided that the activity in every phase is expressed with respect to the same standard state.

The use of activities in calculations of chemical equilibrium conditions is illustrated by the following example. A liquid solution of Au and Cu at 1100°C with  $X_{Cu} = 0.6$  is exposed to an atmosphere in which the oxygen partial pressure is  $p_{O_2} = 10^{-3}$  bar. Will  $Cu_2O$  be formed? The reaction is:



where the Cu(liq) is in solution. If the reaction proceeds with the formation of  $dn$  moles of  $Cu_2O$ , then  $2dn$  moles of Cu are consumed, and the Gibbs energy of the Au-Cu solution changes by  $-2(dG^I/dn_{Cu})dn$ . The total Gibbs energy then varies as:

$$\begin{aligned} dG/dn &= \mu_{Cu_2O}^{\circ} - \frac{1}{2}\mu_{O_2} - 2\left(dG^I/dn_{Cu}\right) \\ &= \mu_{Cu_2O}^{\circ} - \frac{1}{2}\mu_{O_2} - 2\mu_{Cu} \\ &= \left(\mu_{Cu_2O}^{\circ} - \frac{1}{2}\mu_{O_2}^{\circ} - 2\mu_{Cu}^{\circ}\right) - \frac{1}{2}RT \ln p_{O_2} - 2RT \ln a_{Cu} \\ &= \Delta G^{\circ} + RT \ln \left(p_{O_2}^{-\frac{1}{2}} a_{Cu}^{-2}\right) = \Delta G \end{aligned} \quad (100)$$

where Eqs. (65, 86, 93) have been used.

For reaction (99) at 1100°C,  $\Delta G^\circ = -68.73$  kJ (from FactSage - see list of websites at end of chapter). The activity of Cu in the liquid alloy at  $X_{Cu} = 0.6$  is  $a_{Cu} = 0.385$  (from FactSage). Substitution into Eq. (100) with  $p_{O_2} = 10^{-3}$  bar gives:

$$dG/dn = \Delta G = -7.50 \text{ kJ} \quad (101)$$

Hence under these conditions the reaction entails a decrease in the total Gibbs energy and so the copper will be oxidized.

#### 4.1.5 Ideal Raoultian Solutions

An *ideal solution* or *Raoultian solution* is usually defined as one in which the activity of a component is equal to its mole fraction:

$$a_i^{\text{ideal}} = X_i \quad (102)$$

(With a judicious choice of standard state, this definition can also encompass ideal Henrian solutions, as discussed in Sec. 5.8).

This Raoultian definition of ideality is generally only applicable to simple substitutional solutions. There are more useful definitions for other types of solutions such as interstitial solutions, ionic solutions, solutions of defects, polymer solutions, etc. That is, the most convenient definition of ideality depends upon the solution model. Solution models are discussed in Sec. 8.2. In the present section, Eq. (102) for an ideal substitutional solution will be developed with the Au-Cu solution as example.

In the ideal substitutional solution model it is assumed that Au and Cu atoms are nearly alike, with nearly identical radii and electronic structures. This being the case, there will be no change in bonding energy or volume upon mixing, so that the enthalpy of mixing is zero:

$$\Delta h_m^{\text{ideal}} = 0 \quad (103)$$

Furthermore, and for the same reason, the Au and Cu atoms will be randomly distributed over the lattice sites. (In the case of a liquid solution we can think of the lattice sites as the instantaneous atomic positions.) For a random distribution of  $N_{Au}$  gold atoms and  $N_{Cu}$  copper atoms over  $(N_{Au} + N_{Cu})$  sites, Boltzmann's equation (2) can be used to calculate the configurational entropy of the solution. This is the entropy associated with

the spatial distribution of the particles:

$$S^{\text{config}} = k_B \ln(N_{\text{Au}} + N_{\text{Cu}})! / N_{\text{Au}}! N_{\text{Cu}}! \quad (104)$$

The configurational entropies of pure Au and Cu are zero. Hence the configurational entropy of mixing,  $\Delta S_m^{\text{config}}$ , will be equal to  $S^{\text{config}}$ . Furthermore, because of the assumed close similarity of Au and Cu, there will be no non-configurational contribution to the entropy of mixing. Hence, the entropy of mixing will be equal to  $S^{\text{config}}$ . Applying Stirling's approximation, which states that  $\ln N! \approx [(N \ln N) - N]$  if  $N$  is large, yields:

$$\Delta S_m^{\text{ideal}} = S^{\text{config}} = -k_B \left[ N_{\text{Au}} \ln \frac{N_{\text{Au}}}{N_{\text{Au}} + N_{\text{Cu}}} + N_{\text{Cu}} \ln \frac{N_{\text{Cu}}}{N_{\text{Au}} + N_{\text{Cu}}} \right] \quad (105)$$

For one mole of solution,  $(N_{\text{Au}} + N_{\text{Cu}}) = N^\circ$  where  $N^\circ =$  Avogadro's number. We also note that  $(k_B N^\circ)$  is equal to the ideal gas constant  $R$ . Hence:

$$\Delta S_m^{\text{ideal}} = -R \left( X_{\text{Au}} \ln X_{\text{Au}} + X_{\text{Cu}} \ln X_{\text{Cu}} \right) \quad (106)$$

Therefore, since the ideal enthalpy of mixing is zero:

$$\Delta g_m^{\text{ideal}} = RT \left( X_{\text{Au}} \ln X_{\text{Au}} + X_{\text{Cu}} \ln X_{\text{Cu}} \right) \quad (107)$$

By comparing Eqs. (94) and (107) we obtain:

$$\Delta \mu_i^{\text{ideal}} = RT \ln a_i^{\text{ideal}} = RT \ln X_i \quad (108)$$

Hence Eq. (102) has been demonstrated for an ideal substitutional solution.

#### 4.1.6 Excess Properties

In reality, Au and Cu atoms are not identical, and so Au-Cu solutions are not perfectly ideal. The difference between a solution property and its value in an ideal solution is called an *excess property*. The *excess Gibbs energy*, for example, is defined as:

$$g^E = \Delta g_m - \Delta g_m^{\text{ideal}} \quad (109)$$

Since the ideal enthalpy of mixing is zero, the excess enthalpy is equal to the enthalpy of mixing:

$$h^E = \Delta h_m - \Delta h_m^{ideal} = \Delta h_m \quad (110)$$

Hence:

$$g^E = h^E - Ts^E = \Delta h_m - Ts^E \quad (111)$$

Excess partial properties are defined similarly:

$$\mu_i^E = \Delta\mu_i - \Delta\mu_i^{ideal} = RT \ln a_i - RT \ln X_i \quad (112)$$

$$s_i^E = \Delta s_i - \Delta s_i^{ideal} = \Delta s_i + R \ln X_i \quad (113)$$

(where  $\mu_i^E$  is equivalent to  $g_i^E$ ). Also:

$$\mu_i^E = h_i^E - Ts_i^E = \Delta h_i - Ts_i^E \quad (114)$$

Equations analogous to Eqs. (94), (97) and (98) relate the integral and partial excess properties. For example, in Au-Cu solutions:

$$g^E = X_{Au} \mu_{Au}^E + X_{Cu} \mu_{Cu}^E \quad \text{and} \quad s^E = X_{Au} s_{Au}^E + X_{Cu} s_{Cu}^E \quad (115)$$

Tangent constructions similar to that of Fig. 12 can thus also be employed for excess properties, and an equation analogous to Eq. (92) can be written:

$$\mu_i^E = g^E + (1 - X_i) dg^E / dX_i \quad (116)$$

The Gibbs-Duhem equation (75) also applies to excess properties. At constant  $T$  and  $P$ :

$$X_{Au} d\mu_{Au}^E + X_{Cu} d\mu_{Cu}^E = 0 \quad (117)$$

In Au-Cu alloys,  $g^E$  is negative. That is,  $\Delta g_m$  is more negative than  $\Delta g_m^{ideal}$  and so the solution is thermodynamically more stable than an ideal solution. We thus say that Au-

Cu solutions exhibit *negative deviations from ideality*. If  $g^E > 0$ , then a solution is less stable than an ideal solution and is said to exhibit *positive deviations*.

#### 4.1.7 Activity Coefficients

The *activity coefficient* of a component in a solution is defined as:

$$\gamma_i = a_i / X_i \quad (118)$$

Hence, from Eq. (112):

$$\mu_i^E = RT \ln \gamma_i \quad (119)$$

In an ideal solution  $\gamma_i = 1$  and  $\mu_i^E = 0$  for all components. If  $\gamma_i < 1$  then  $\mu_i^E < 0$  and from Eq. (112),  $\Delta\mu_i < \Delta\mu_i^{ideal}$ . That is, the component  $i$  is more stable in the solution than it would be in an ideal solution of the same composition. If  $\gamma_i > 1$ , then  $\mu_i^E > 0$  and the driving force for the component to enter into solution is less than in the case of an ideal solution.

#### 4.1.8 Multicomponent Solutions

The equations of this section were derived with a binary solution as an example. However, the equations apply equally to systems of any number of components. For instance, in a solution of components A-B-C-D ..., Eq. (94) becomes:

$$\Delta g_m = X_A \Delta\mu_A + X_B \Delta\mu_B + X_C \Delta\mu_C + \dots \quad (120)$$

## 4.2 Binary Temperature-Composition Phase Diagrams

In this section we first consider the thermodynamic origin of simple "lens-shaped" phase diagrams in binary systems with complete liquid and solid miscibility. An example of such a diagram was given in Fig. 11. Another example is the Ge-Si phase diagram in the lowest panel of Fig. 13. In the upper three panels of Fig. 13 the molar Gibbs energies of the solid and liquid phases,  $g^s$  and  $g^l$  at three temperatures are shown to scale. As illustrated in the top panel,  $g^s$  varies with composition between the standard chemical potentials of pure solid Ge and of pure solid Si,  $\mu_{Ge}^{o(s)}$  and  $\mu_{Si}^{o(s)}$ , while  $g^l$  varies between

the standard chemical potentials of the pure liquid components,  $\mu_{\text{Ge}}^{o(l)}$  and  $\mu_{\text{Si}}^{o(l)}$ . The difference between  $\mu_{\text{Ge}}^{o(l)}$  and  $\mu_{\text{Ge}}^{o(s)}$  is equal to the standard molar Gibbs energy of fusion (melting) of pure Ge,  $\Delta g_{f(\text{Ge})}^o = (\mu_{\text{Ge}}^{o(l)} - \mu_{\text{Ge}}^{o(s)})$ . Similarly for Si,  $\Delta g_{f(\text{Si})}^o = (\mu_{\text{Si}}^{o(l)} - \mu_{\text{Si}}^{o(s)})$ . The Gibbs energy of fusion of a pure component may be written as:

$$\Delta g_f^o = \Delta h_f^o - T\Delta s_f^o \quad (121)$$

where  $\Delta h_f^o$  and  $\Delta s_f^o$  are the standard molar enthalpy and entropy of fusion.

Since, to a first approximation,  $\Delta h_f^o$  and  $\Delta s_f^o$  are independent of  $T$ ,  $\Delta g_f^o$  is approximately a linear function of  $T$ . If  $T > T_f^o$ , then  $\Delta g_f^o$  is negative. If  $T < T_f^o$ , then  $\Delta g_f^o$  is positive. Hence, as seen in Fig. 13, as  $T$  decreases, the  $g^s$  curve descends relative to  $g^l$ . At 1500°C,  $g^l < g^s$  at all compositions. Therefore, by the principle that a system always seeks the state of minimum Gibbs energy at constant  $T$  and  $P$ , the liquid phase is stable at all compositions at 1500°C.

At 1300°C, the curves of  $g^s$  and  $g^l$  cross. The line  $P_1Q_1$  which is the *common tangent* to the two curves, divides the composition range into three sections. For compositions between pure Ge and  $P_1$  a single-phase liquid is the state of minimum Gibbs energy. For compositions between  $Q_1$  and pure Si, a single-phase solid solution is the stable state. Between  $P_1$  and  $Q_1$ , a total Gibbs energy lying on the tangent line  $P_1Q_1$  may be realized if the system adopts a state consisting of two phases with compositions at  $P_1$  and  $Q_1$  with relative proportions given by the lever rule (Sec. 3.1). Since the tangent line  $P_1Q_1$  lies below both  $g^s$  and  $g^l$ , this two-phase state is more stable than either phase alone. Furthermore, no other line joining any point on the  $g^l$  curve to any point on the  $g^s$  curve lies below the line  $P_1Q_1$ . Hence, this line represents the true equilibrium state of the system, and the compositions  $P_1$  and  $Q_1$  are the liquidus and solidus compositions at 1300°C.

As  $T$  is decreased to 1100°C, the points of common tangency are displaced to higher concentrations of Ge. For  $T < 937^\circ\text{C}$ ,  $g^s < g^l$  at all compositions.

It was shown in Fig. 12 that if a tangent is drawn to a Gibbs energy curve, then the intercept of this tangent on the axis at  $X_i = 1$  is equal to the chemical potential  $\mu_i$  of

component  $i$ . The *common tangent construction* of Fig. 13 thus ensures that the chemical potentials of Ge and Si are equal in the solid and liquid phases at equilibrium. That is:

$$\mu_{\text{Ge}}^{\text{l}} = \mu_{\text{Ge}}^{\text{s}} \quad (122)$$

$$\mu_{\text{Si}}^{\text{l}} = \mu_{\text{Si}}^{\text{s}} \quad (123)$$

This equality of chemical potentials was shown in Sec. 2.7 to be the criterion for phase equilibrium. That is, the common tangent construction simultaneously minimizes the total Gibbs energy and ensures the equality of the chemical potentials, thereby showing that these are equivalent criteria for equilibrium between phases as was discussed in Sec. 2.7.

If we rearrange Eq. (122), subtracting the Gibbs energy of fusion of pure Ge,  $\Delta g_{f(\text{Ge})}^{\circ} = (\mu_{\text{Ge}}^{\circ(\text{l})} - \mu_{\text{Ge}}^{\circ(\text{s})})$  from each side, we obtain:

$$(\mu_{\text{Ge}}^{\text{l}} - \mu_{\text{Ge}}^{\circ(\text{l})}) - (\mu_{\text{Ge}}^{\text{s}} - \mu_{\text{Ge}}^{\circ(\text{s})}) = -(\mu_{\text{Ge}}^{\circ(\text{l})} - \mu_{\text{Ge}}^{\circ(\text{s})}) \quad (124)$$

Using Eq. (93), we can write Eq. (124) as:

$$\Delta \mu_{\text{Ge}}^{\text{l}} - \Delta \mu_{\text{Ge}}^{\text{s}} = -\Delta g_{f(\text{Ge})}^{\circ} \quad (125)$$

or

$$RT \ln a_{\text{Ge}}^{\text{l}} - RT \ln a_{\text{Ge}}^{\text{s}} = -\Delta g_{f(\text{Ge})}^{\circ} \quad (126)$$

where  $a_{\text{Ge}}^{\text{l}}$  is the activity of Ge (with respect to pure liquid Ge as standard state) in the liquid solution on the liquidus, and  $a_{\text{Ge}}^{\text{s}}$  is the activity of Ge (with respect to pure solid Ge as standard state) in the solid solution on the solidus. Starting with Eq. (123), we can derive a similar expression for the other component:

$$RT \ln a_{\text{Si}}^{\text{l}} - RT \ln a_{\text{Si}}^{\text{s}} = -\Delta g_{f(\text{Si})}^{\circ} \quad (127)$$

Eqs. (126) and (127) are equivalent to the common tangent construction.

It should be noted that absolute values of chemical potentials cannot be defined. Hence, the relative positions of  $\mu_{\text{Ge}}^{\circ(\text{l})}$  and  $\mu_{\text{Si}}^{\circ(\text{l})}$  in Fig. 13 are arbitrary. However, this is

immaterial for the preceding discussion, since displacing both  $\mu_{Si}^{o(l)}$  and  $\mu_{Si}^{o(s)}$  by the same arbitrary amount relative to  $\mu_{Ge}^{o(l)}$  and  $\mu_{Ge}^{o(s)}$  will not alter the compositions of the points of common tangency.

The shape of the two-phase (solid + liquid) "lens" on the phase diagram is determined by the Gibbs energies of fusion,  $\Delta g_f^o$ , of the components and by the mixing terms,  $\Delta g^s$  and  $\Delta g^l$ . In order to observe how the shape is influenced by varying  $\Delta g_f^o$ , let us consider a hypothetical system A-B in which  $\Delta g^s$  and  $\Delta g^l$  are ideal Raoultian (Eq. (107)). Let  $T_{f(A)}^o = 800$  K and  $T_{f(B)}^o = 1200$  K. Furthermore, assume that the entropies of fusion of A and B are equal and temperature-independent. The enthalpies of fusion are then given from Eq. (121) by the expression  $\Delta h_f^o = T_f^o \Delta s_f^o$  since  $\Delta g_f^o = 0$  when  $T = T_f^o$  (See Sec. 2.3). Calculated phase diagrams for  $\Delta s_f^o = 3, 10$  and  $30$  J mol<sup>-1</sup>K<sup>-1</sup> are shown in Fig. 14. A value of  $\Delta s_f^o \approx 10$  J mol<sup>-1</sup>K<sup>-1</sup> is typical of most metals. When the components are ionic compounds such as ionic oxides, halides, etc.,  $\Delta s_f^o$  can be significantly larger since there are several ions per formula unit. Hence, two-phase "lenses" in binary ionic salt or oxide phase diagrams tend to be wider than those encountered in alloy systems. If we are considering vapor-liquid equilibria rather than solid-liquid equilibria, then the shape is determined by the entropy of vaporization,  $\Delta s_v^o$ . Since  $\Delta s_v^o$  is usually an order of magnitude larger than  $\Delta s_f^o$ , two-phase (liquid + vapor) lenses tend to be very wide. For equilibria between two solid solutions of different crystal structure, the shape is determined by the entropy of solid-solid transformation, which is usually smaller than the entropy of fusion by approximately an order of magnitude. Therefore two-phase (solid + solid) lenses tend to be narrow.

#### 4.2.1 Effect of Grain Size and Strain Energy

The foregoing phase diagram calculations have assumed that the grain size of the solid phases is sufficiently large so that surface (interfacial) energy contributions to the Gibbs energy can be neglected. It has also been assumed that strain energy is negligible. For very fine grain sizes in the sub-micron range, however, the interfacial

energy can be appreciable and can have an influence on the phase diagram. This effect can be important with the development of materials with grain sizes in the nanometer range.

Interfacial and strain energies increase the Gibbs energy of a phase and hence decrease its thermodynamic stability. In particular, the liquidus temperature of a fine-grained solid will be lowered. If a suitable estimate can be made for the grain boundary or strain energies, then this can simply be added to the Gibbs energy expression of the phase for purposes of calculating phase diagrams.

### 4.3 Binary Pressure-Composition Phase Diagrams

Let us consider liquid-vapor equilibrium in a system with complete liquid miscibility, using as example the Zn-Mg system. Curves of  $g^v$  and  $g^l$  can be drawn at any given  $T$  and  $P$ , as in the upper panel of Fig. 15, and the common tangent construction then gives the equilibrium vapor and liquid compositions. The phase diagram depends upon the Gibbs energies of vaporization of the pure components  $\Delta g_{v(Zn)}^o = (\mu_{Zn}^v - \mu_{Zn}^{o(l)})$  and  $\Delta g_{v(Mg)}^o = (\mu_{Mg}^v - \mu_{Mg}^{o(l)})$  as shown in Fig. 15.

To generate the isothermal pressure-composition ( $P$ - $X$ ) phase diagram in the lower panel of Fig. 15 we require the Gibbs energies of vaporization as functions of  $P$ . Assuming monatomic ideal vapors and assuming that pressure has negligible effect upon the Gibbs energy of the liquid, we can write, using Eq. (86):

$$\Delta g_{v(i)} = \Delta g_{v(i)}^o + RT \ln P \quad (128)$$

where  $\Delta g_{v(i)}^o$  is the standard Gibbs energy of vaporization (when  $P = 1.0$  bar), which is given by:

$$\Delta g_{v(i)}^o = \Delta h_{v(i)}^o - T \Delta s_{v(i)}^o \quad (129)$$

For example, the standard enthalpy of vaporization of Zn is  $115310 \text{ J mol}^{-1}$  at its normal boiling point of  $1180 \text{ K}$  (see FactSage). Assuming that  $\Delta h_{v(Zn)}^o$  is independent of  $T$ , we calculate from Eq. (129) that  $\Delta s_{v(Zn)}^o = 115310/1180 = 97.71 \text{ J mol}^{-1}\text{K}^{-1}$ . From

Eq.(128),  $\Delta g_{v(Zn)}$  at any  $T$  and  $P$  is thus given by:

$$\Delta g_{v(Zn)} = (115310 - 97.71 T) + RT \ln P \quad (130)$$

A similar expression can be derived for the other component, Mg.

At constant temperature then, the curve of  $g^v$  in Fig. 15 descends relative to  $g^l$  as the pressure is lowered, and the  $P$ - $X$  phase diagram is generated by the common tangent construction. The diagram at  $977^\circ\text{C}$  in Fig. 15 was calculated under the assumption of ideal liquid and vapor mixing ( $g^{E(l)} = 0$ ,  $g^{E(v)} = 0$ ).

$P$ - $X$  phase diagrams involving liquid-solid and solid-solid equilibria can be calculated in a similar fashion through the following general equation, which follows from Eq. (64) and which gives the effect of pressure upon the Gibbs energy change for the transformation of one mole of pure component  $i$  from an  $\alpha$ -phase to a  $\beta$ -phase at constant  $T$ :

$$\Delta g_{\alpha \rightarrow \beta} = \Delta g_{\alpha \rightarrow \beta}^{\circ} + \int_{P=1}^P (v_i^{\beta} - v_i^{\alpha}) dP \quad (131)$$

where  $\Delta g_{\alpha \rightarrow \beta}^{\circ}$  is the standard ( $P = 1.0$  bar) Gibbs energy of transformation, and  $v_i^{\beta}$  and  $v_i^{\alpha}$  are the molar volumes.

## 5 Binary Temperature-Composition Phase Diagrams

### 5.1 Systems with Complete Solid and Liquid Miscibility

Examples of phase diagrams of such systems were given in Figs. 11 and 13 and discussed in Secs. 3.1 and 4.2 .

### 5.2 Minima and Maxima in Two-Phase Regions

As discussed in Sec. 4.1.6, the Gibbs energy of mixing  $\Delta g_m$  may be expressed as the sum of an ideal term  $\Delta g_m^{ideal}$  and an excess term  $g^E$ . As was shown in Sec. 4.2 , if the solid and liquid phases are both ideal, or close to ideal, a "lens-shaped" two-phase region results. However in most systems even approximately ideal behavior is the

exception rather than the rule.

Curves of  $g^s$  and  $g^l$  for a hypothetical system A-B are shown schematically in Fig. 16 at a constant temperature (below the melting points of pure A and B) such that the solid state is the stable state for both pure components. However, in this system  $g^{E(l)} < g^{E(s)}$  so that  $g^s$  presents a flatter curve than does  $g^l$  and there exists a central composition region in which  $g^l < g^s$ . Hence, there are two common tangent lines,  $P_1Q_1$  and  $P_2Q_2$ . Such a situation gives rise to a phase diagram with a minimum in the two-phase region, as observed in the quasibinary  $\text{Na}_2\text{CO}_3\text{-K}_2\text{CO}_3$  system shown in Fig. 17. At a composition and temperature corresponding to the minimum point, liquid and solid of the same composition exist in equilibrium.

A two-phase region with a minimum point as in Fig. 17 may be thought of as a two-phase "lens" which has been "pushed down" by virtue of the fact that the liquid is relatively more stable than the solid. Thermodynamically, this relative stability is expressed as  $g^{E(l)} < g^{E(s)}$ .

Conversely, if  $g^{E(l)} > g^{E(s)}$  to a sufficient extent, then a two-phase region with a maximum will result. Such maxima in (liquid + solid) or (solid + solid) two-phase regions are nearly always associated with the existence of an intermediate phase, as will be discussed in Sec. 5.7.

### 5.3 Miscibility Gaps

If  $g^E > 0$  then the solution is thermodynamically less stable than an ideal solution. This can result from a large difference in size of the component atoms, ions or molecules; or from differences in bond types, valencies, electronic structure; or from many other factors.

In the Au-Ni system,  $g^E$  is positive in the solid phase. In the top panel of Fig. 18,  $g^{E(s)}$  is plotted at 1200 K (Hultgren et al, 1973) and the ideal Gibbs energy of mixing,  $\Delta g_m^{ideal}$ , is also plotted at 1200 K. The sum of these two terms is the Gibbs energy of mixing of the solid solution,  $\Delta g_m^s$ , which is plotted at 1200 K as well as at other temperatures in the central panel of Fig. 18. Now, from Eq. (107),  $\Delta g_m^{ideal}$  is always negative and varies directly with  $T$ , whereas  $g^E$  generally varies less rapidly with

temperature. As a result, the sum  $\Delta g_m^s = \Delta g_m^{ideal} + g^E$  becomes less negative as  $T$  decreases. However, the limiting slopes to the  $\Delta g_m^{ideal}$  curve at  $X_{Au} = 1$  and  $X_{Ni} = 1$  are both infinite, whereas the limiting slopes of  $g^E$  are always finite (Henry's Law). Hence,  $\Delta g_m^s$  will always be negative as  $X_{Au} \rightarrow 1$  and  $X_{Ni} \rightarrow 1$  no matter how low the temperature. As a result, below a certain temperature the curve of  $\Delta g_m^s$  will exhibit two negative "humps". Common tangent lines  $P_1Q_1$ ,  $P_2Q_2$ ,  $P_3Q_3$  to the two humps at different temperatures define the ends of tie-lines of a two-phase solid-solid *miscibility gap* in the Au-Ni phase diagram, which is shown in the lower panel in Fig.18 (Hultgren et al., 1973). The peak of the gap occurs at the *critical* or *consolute* temperature and composition,  $T_c$  and  $X_c$ .

An example of a miscibility gap in a liquid phase will be given in Fig. 21.

When  $g^{E(s)}$  is positive for the solid phase in a system it is usually also the case that  $g^{E(l)} < g^{E(s)}$  since the unfavorable factors (such as a difference in atomic dimensions) which cause  $g^{E(s)}$  to be positive will have less of an effect upon  $g^{E(l)}$  in the liquid phase owing to the greater flexibility of the liquid structure to accommodate different atomic sizes, valencies, etc. Hence, a solid-solid miscibility gap is often associated with a minimum in the two-phase (solid + liquid) region, as is the case in the Au-Ni system.

Below the critical temperature the curve of  $\Delta g_m^s$  exhibits two inflection points, indicated by the letter  $s$  in Fig.18. These are known as the *spinodal points*. On the phase diagram their locus traces out the *spinodal curve*. The spinodal curve is not part of the equilibrium phase diagram, but it is important in the kinetics of phase separation, as discussed in Chapter 8 of this volume.

## 5.4 Simple Eutectic Systems

The more positive  $g^E$  is in a system, the higher is  $T_c$  and the wider is the miscibility gap at any temperature. Suppose that  $g^{E(s)}$  is so positive that  $T_c$  is higher than the minimum in the (solid + liquid) region. The result will be a phase diagram such as that of the Ag-Cu system shown in Fig.19. The upper panel of Fig.19 shows the Gibbs energy curves at 850°C. The two common tangents define two two-phase regions. As the temperature is decreased below 850°C, the  $g^s$  curve descends relative to  $g^l$  and the two points of tangency  $P_1$  and  $P_2$  approach each other until, at  $T = 780^\circ\text{C}$ ,  $P_1$  and  $P_2$

become coincident at the composition  $E$ . That is, at  $T = 780^\circ\text{C}$  there is just one common tangent line contacting the two portions of the  $g^s$  curve at compositions  $A$  and  $B$  and contacting the  $g^l$  curve at  $E$ . This temperature is known as the *eutectic temperature*,  $T_E$ , and the composition  $E$  is the *eutectic composition*. For temperatures below  $T_E$ ,  $g^l$  lies completely above the common tangent to the two portions of the  $g^s$  curve and so for  $T < T_E$  a solid-solid miscibility gap is observed. The phase boundaries of this two-phase region are called the *solvus* lines. The word eutectic is from the Greek for "to melt well", since the eutectic composition  $E$  is a minimum melting temperature.

This description of the thermodynamic origin of simple eutectic phase diagrams is strictly correct only if the pure solid components  $A$  and  $B$  have the same crystal structure. Otherwise, a curve for  $g^s$  which is continuous at all compositions cannot be drawn. In this case, each terminal solid solution ( $\alpha$  and  $\beta$ ) must have its own Gibbs energy curve ( $g^\alpha$  and  $g^\beta$ ) which do not join up with each other. However, a simple eutectic phase diagram as in Fig. 19 still results.

Suppose a liquid Ag-Cu solution of composition  $X_{Cu} = 0.22$  (composition  $P_1$ ) is cooled from the liquid state very slowly under equilibrium conditions. At  $850^\circ\text{C}$  the first solid appears with composition  $Q_1$ . As  $T$  decreases further, solidification continues with the liquid composition following the liquidus curve from  $P_1$  to  $E$  and the composition of the solid phase following the solidus curve from  $Q_1$  to  $A$ . The relative proportions of the two phases at any  $T$  are given by the lever rule (Sec. 3.1). At a temperature just above  $T_E$ , two phases are observed: a solid of composition  $A$  and a liquid of composition  $E$ . At a temperature just below  $T_E$ , two solids with compositions  $A$  and  $B$  are observed. Therefore, at  $T_E$ , during cooling, the following *binary eutectic reaction* occurs:



Under equilibrium conditions the temperature will remain constant at  $T = T_E$  until all the liquid has solidified, and during the reaction the compositions of the three phases will remain fixed at  $A$ ,  $B$  and  $E$ . For this reason the eutectic reaction is called an *invariant* reaction as was discussed in Sec.3.1.1. More on eutectic solidification may be found in Chapter 7 of this volume.

## 5.5 Regular Solution Theory

Many years ago Van Laar (1908) showed that the thermodynamic origin of a great many of the observed features of binary phase diagrams can be illustrated at least qualitatively by simple regular solution theory. A simple *regular solution* of components A and B is one for which:

$$g^E = X_A X_B (\omega - \eta T) \quad (133)$$

where  $\omega$  and  $\eta$  are parameters independent of temperature and composition. Substituting Eq. (133) into Eq. (116) yields, for the partial properties:

$$\mu_A^E = X_B^2 (\omega - \eta T), \quad \mu_B^E = X_A^2 (\omega - \eta T) \quad (134)$$

Several liquid and solid solutions conform approximately to regular solution behavior, particularly if  $g^E$  is small. Examples may be found for alloys, molecular solutions, and ionic solutions such as molten salts and oxides, among others. (The very low values of  $g^E$  observed for gaseous solutions generally conform very closely to Eq. (133)).

To understand why this should be so, we need only a very simple model. Suppose that the atoms or molecules of the components A and B mix substitutionally. If the atomic (or molecular) sizes and electronic structures of A and B are similar, then the distribution will be nearly random, and the configurational entropy will be nearly ideal as in Eq. (106). That is:

$$g^E = \Delta h_m - T s^{E(\text{non-config})} \quad (135)$$

Assuming that the bond energies  $\epsilon_{AA}$ ,  $\epsilon_{BB}$  and  $\epsilon_{AB}$  of first-nearest-neighbor pairs are independent of temperature and composition and that the average nearest-neighbor coordination number,  $Z$ , is also constant, we calculate the enthalpy of mixing resulting from the change in the total energy of first-nearest-neighbor pair bonds as follows.

In one mole of solution there are  $(N^\circ Z/2)$  nearest-neighbor pair bonds, where  $N^\circ$  is Avogadro's number. Since the distribution is assumed to be random, the probability that a given bond is an A-A bond is equal to  $X_A^2$ . The probabilities of B-B and A-B bonds are, respectively,  $X_B^2$  and  $2X_A X_B$ . The contribution to the molar enthalpy of

mixing resulting from the change in total energy of first-nearest-neighbor bonds is then equal to the sum of the energies of the first-nearest-neighbor bonds in one mole of solution, minus the energy of the A-A bonds in  $X_A$  moles of pure A and the energy of the B-B bonds in  $X_B$  moles of pure B:

$$\begin{aligned}
 \Delta h^{\text{FNN}} &= (N^{\circ} Z/2) (X_A^2 \varepsilon_{AA} + X_B^2 \varepsilon_{BB} + 2 X_A X_B \varepsilon_{AB}) \\
 &\quad - (N^{\circ} Z/2) (X_A \varepsilon_{AA} + X_B \varepsilon_{BB}) \\
 &= (N^{\circ} Z) \left[ \varepsilon_{AB} - (\varepsilon_{AA} + \varepsilon_{BB})/2 \right] X_A X_B \\
 &= C_1 X_A X_B
 \end{aligned} \tag{136}$$

where  $C_1$  is a constant.

With exactly the same assumptions and arguments we can derive equations for the enthalpy of mixing contributions resulting from the change in total energy of second-nearest-neighbor,  $\Delta h^{\text{SNN}}$ , third-nearest-neighbor,  $\Delta h^{\text{TNN}}$ , etc. pair bonds. These are clearly all of the same form,  $C_i X_A X_B$ . If we now assume that the actual observed enthalpy of mixing,  $\Delta h_m$ , results mainly from these changes in the total energy of all pair bonds, then:

$$\Delta h_m = \omega X_A X_B \tag{137}$$

where  $\omega = C_1 + C_2 + C_3 + \dots$

If we now define  $\sigma_{AA}$ ,  $\sigma_{BB}$ , and  $\sigma_{AB}$  as the vibrational entropies of pair bonds and follow an identical argument to that just presented for the pair bond energies we obtain:

$$s^{\text{E(non-config)}} = (N^{\circ} Z/2) \left[ \sigma_{AB} - (\sigma_{AA} + \sigma_{BB}/2) \right] = \eta X_A X_B \tag{138}$$

Eq. (133) has thus been derived. If A-B bonds are stronger than A-A and B-B bonds, then  $(\varepsilon_{AB} - \eta_{AB} T) < \left[ (\varepsilon_{AA} + \eta_{AA} T)/2 + (\varepsilon_{BB} + \eta_{BB} T)/2 \right]$  so that  $(\omega - \eta T) < 0$  and  $g^E < 0$ . That is, the solution is rendered more stable. If the A-B bonds are relatively weaker, then the solution is rendered less stable,  $(\omega - \eta T) > 0$  and  $g^E > 0$ .

Simple non-polar molecular solutions and simple ionic solutions such as molten salts often exhibit approximately regular behavior. The assumption of additivity of the energy of pair bonds is probably reasonably realistic for van der Waals or coulombic

forces. For metallic alloys, the concept of a pair bond is, at best, vague, and metallic solutions tend to exhibit larger deviations from regular behavior.

In several solutions it is found that  $|\eta T| < |\omega|$  in Eq. (133). That is,  $g^E \approx \Delta h_m = \omega X_A X_B$ , and so to a first approximation  $g^E$  is independent of  $T$ . This is more often the case in non-metallic solutions than in metallic solutions.

### 5.5.1 Thermodynamic Origin of Simple Phase Diagrams Illustrated by Regular Solution Theory

Figure 20 shows several phase diagrams calculated for a hypothetical system A-B containing a solid and a liquid phase with melting points of  $T_{f(A)}^o = 800$  K and  $T_{f(B)}^o = 1200$  K and with entropies of fusion of both A and B set to  $10 \text{ J mol}^{-1} \text{ K}^{-1}$  which is a typical value for metals. The solid and liquid phases are both regular with temperature-independent excess Gibbs energies

$$g^{E(s)} = \omega^s X_A X_B \quad \text{and} \quad g^{E(l)} = \omega^l X_A X_B \quad (139)$$

The parameters  $\omega^s$  and  $\omega^l$  have been varied systematically to generate the various panels of Fig. 20.

In panel (n) both phases are ideal. Panels (l) to (r) exhibit minima or maxima depending upon the sign and magnitude of  $(g^{E(l)} - g^{E(s)})$ , as has been discussed in Sec. 5.2. In panel (h) the liquid is ideal but positive deviations in the solid give rise to a solid-solid miscibility gap as discussed in Sec. 5.4. On passing from panel (h) to panel (c), an increase in  $g^{E(s)}$  results in a widening of the miscibility gap so that the solubilities of A in solid B and of B in solid A decrease. Panels (a) to (c) illustrate that negative deviations in the liquid cause a relative stabilization of the liquid with resultant lowering of the eutectic temperature. Panels (d) and (e) are discussed in Sec. 5.6.

## 5.6 Immiscibility - Montectics

In Fig. 20e positive deviations in the liquid have given rise to a *liquid-liquid miscibility* gap. The quasibinary CaO-SiO<sub>2</sub> system, shown in Fig. 21, exhibits such a feature. Suppose that a liquid of composition  $X_{\text{SiO}_2} = 0.8$  is cooled slowly from high

temperatures. At  $T = 1830^\circ\text{C}$  the miscibility gap boundary is crossed and a second liquid layer appears with a composition of  $X_{\text{SiO}_2} = 0.96$ . As the temperature is lowered further, the composition of each liquid phase follows its respective phase boundary until, at  $1689^\circ\text{C}$ , the  $\text{SiO}_2$ -rich liquid has a composition of  $X_{\text{SiO}_2} = 0.988$  (point  $B$ ), and in the  $\text{CaO}$ -rich liquid  $X_{\text{SiO}_2} = 0.72$  (point  $A$ ). At any temperature, the relative amounts of the two phases are given by the lever rule.

At  $1689^\circ\text{C}$  the following invariant *binary monotectic reaction* occurs upon cooling:



The temperature remains constant at  $1689^\circ\text{C}$  and the compositions of the phases remain constant until all of liquid  $B$  is consumed. Cooling then continues with precipitation of solid  $\text{SiO}_2$  with the equilibrium liquid composition following the liquidus from point  $A$  to the eutectic  $E$ .

Returning to Fig. 20, we see in panel (d) that the positive deviations in the liquid in this case are not large enough to produce immiscibility, but they do result in a flattening of the liquidus, which indicates a "tendency to immiscibility". If the nucleation of the solid phases can be suppressed by sufficiently rapid cooling, then a *metastable liquid-liquid miscibility gap* is observed as shown in Fig. 20d. For example, in the  $\text{Na}_2\text{O}-\text{SiO}_2$  system the flattened (or "S-shaped")  $\text{SiO}_2$ -liquidus heralds the existence of a metastable miscibility gap of importance in glass technology.

## 5.7 Intermediate Phases

The phase diagram of the  $\text{Ag}-\text{Mg}$  system (Hultgren et al., 1973) is shown in Fig. 22d. An intermetallic phase,  $\beta'$ , is seen centered approximately about the composition  $X_{\text{Mg}} = 0.5$ . The Gibbs energy curve at 1050 K for such an intermetallic phase has the form shown schematically in Fig. 22a. The curve  $g^{\beta'}$  rises quite rapidly on either side of its minimum, which occurs near  $X_{\text{Mg}} = 0.5$ . As a result, the single-phase  $\beta'$  region appears on the phase diagram only over a limited composition range. This form of the Gibbs energy curve results from the fact that when  $X_{\text{Ag}} \approx X_{\text{Mg}}$  a particularly stable crystal structure exists in which  $\text{Ag}$  and  $\text{Mg}$  atoms preferentially occupy different sites. The two

common tangents  $P_1Q_1$  and  $P_2Q_2$  give rise to a maximum in the two-phase ( $\beta'$  + liquid) region of the phase diagram. (Although the maximum is observed very near  $X_{Mg} = 0.5$ , there is no thermodynamic reason for the maximum to occur exactly at this composition.)

Another intermetallic phase, the  $\varepsilon$  phase, is also observed in the Ag-Mg system, Fig. 22d. The phase is associated with a *peritectic* invariant  $ABC$  at 744 K. The Gibbs energy curves are shown schematically at the peritectic temperature in Fig. 22c. One common tangent line can be drawn to  $g^l$ ,  $g^{\beta'}$  and  $g^\varepsilon$  at 744 K.

Suppose that a liquid alloy of composition  $X_{Mg} = 0.7$  is cooled very slowly from the liquid state. At a temperature just above 744 K a liquid phase of composition  $C$  and a  $\beta'$  phase of composition  $A$  are observed at equilibrium. At a temperature just below 744 K the two phases at equilibrium are  $\beta'$  of composition  $A$  and  $\varepsilon$  of composition  $B$ . The following invariant *binary peritectic reaction* thus occurs upon cooling:



This reaction occurs isothermally at 744 K with all three phases at fixed compositions (at points  $A$ ,  $B$  and  $C$ ). For an alloy with overall composition between points  $A$  and  $B$  the reaction proceeds until all the liquid has been consumed. In the case of an alloy with overall composition between  $B$  and  $C$ , the  $\beta'$  phase will be the first to be completely consumed.

Peritectic reactions occur upon cooling generally with formation of the product solid ( $\varepsilon$  in this example) on the surface of the reactant solid ( $\beta'$ ), thereby forming a coating which can reduce or prevent further contact between the reactant solid and liquid. Further reaction may thus be greatly retarded so that equilibrium conditions can only be achieved by extremely slow cooling.

The Gibbs energy curve for the  $\varepsilon$  phase,  $g^\varepsilon$ , in Fig. 22c rises more rapidly on either side of its minimum than does the Gibbs energy  $g^{\beta'}$  of the  $\beta'$  phase. Consequently, the width of the single-phase region over which the  $\varepsilon$  phase exists (sometimes called its *range of stoichiometry* or *homogeneity range*) is narrower than that of the  $\beta'$  phase.

In the upper panel of Fig. 21 for the CaO-SiO<sub>2</sub> system, Gibbs energy curves at 1500°C for the liquid and CaSiO<sub>3</sub> phases are shown schematically.  $g_{0.5(\text{CaSiO}_3)}$  rises

extremely rapidly on either side of its minimum. (We write  $g_{0.5(\text{CaSiO}_3)}$  for 0.5 moles of the compound in order to normalize to a basis of one mole of components CaO and SiO<sub>2</sub>.) As a result, the points of tangency  $Q_1$  and  $Q_2$  of the common tangents  $P_1Q_1$  and  $P_2Q_2$  nearly (although not exactly) coincide. Hence, the range of stoichiometry of the CaSiO<sub>3</sub> phase is very narrow (although never zero). The two-phase regions labelled (liquid + CaSiO<sub>3</sub>) in Fig. 21 are the two sides of a two-phase region that passes through a maximum at 1540°C just as the ( $\beta'$  + liquid) region passes through a maximum in Fig. 22d. Because the CaSiO<sub>3</sub> single-phase region is extremely narrow (although always of finite width), we refer to CaSiO<sub>3</sub> as a *stoichiometric compound*. Any deviation in composition from the stoichiometric 1:1 ratio of CaO to SiO<sub>2</sub> results in a very large increase in its Gibbs energy.

The  $\varepsilon$  phase in Fig. 22 is based on the stoichiometry AgMg<sub>3</sub>. The Gibbs energy curve, Fig. 22c, rises extremely rapidly on the Ag side of the minimum, but somewhat less steeply on the Mg side. As a result, Ag is virtually insoluble in AgMg<sub>3</sub>, while Mg is sparingly soluble. Such a phase with a narrow range of homogeneity is often called a *non-stoichiometric compound*. At low temperatures the  $\beta'$  phase exhibits a relatively narrow range of stoichiometry about the 1:1 AgMg composition and can properly be called a compound. However, at higher temperatures it is debatable whether a phase with such a wide range of composition should be called a "compound".

From Fig. 21 it can be seen that if stoichiometric CaSiO<sub>3</sub> is heated it will melt isothermally at 1540°C to form a liquid of the same composition. Such a compound is called *congruently melting* or simply a *congruent compound*. The compound Ca<sub>2</sub>SiO<sub>4</sub> in Fig. 21 is also congruently melting. The  $\beta'$  phase in Fig. 22 is also congruently melting at the composition of the liquidus/solidus maximum.

It should be noted with regard to congruent melting that the limiting slopes  $dT/dX$  of both branches of the liquidus at the congruent melting point (that is, at the maximum of the two-phase region) are zero since we are dealing with a maximum in a two-phase region (similar to the minimum in the two-phase region in Fig. 17).

The AgMg<sub>3</sub> ( $\varepsilon$ ) compound in Fig. 22 is said to *melt incongruently*. If solid AgMg<sub>3</sub> is heated it will melt isothermally at 744 K by the reverse of the peritectic reaction (141), to form a liquid of composition C and another solid phase,  $\beta'$ , of composition A.

Another example of an *incongruently melting compound* is  $\text{Ca}_3\text{Si}_2\text{O}_7$  in Fig. 21, which melts incongruently (or peritectically) to form liquid and  $\text{Ca}_2\text{SiO}_4$  at the peritectic temperature of  $1464^\circ\text{C}$ .

An incongruently melting compound is always associated with a peritectic. However, the converse is not necessarily true. A peritectic is not always associated with an intermediate phase. See, for example, Fig. 20i.

For purposes of phase diagram calculations involving stoichiometric compounds such as  $\text{CaSiO}_3$ , we may, to a good approximation, consider the Gibbs energy curve,  $g_{0.5(\text{CaSiO}_3)}$  in the upper panel of Fig. 21 to have zero width. All that is then required is the value of  $g_{0.5(\text{CaSiO}_3)}$  at the minimum. This value is usually expressed in terms of the *Gibbs energy of fusion* of the compound,  $\Delta g_{f(0.5\text{CaSiO}_3)}$  or of the *Gibbs energy of formation*  $\Delta g_{\text{form}(0.5\text{CaSiO}_3)}$  of the compound from the pure solid components  $\text{CaO}$  and  $\text{SiO}_2$  according to the reaction:  $0.5 \text{CaO (sol)} + 0.5 \text{SiO}_2(\text{sol}) = 0.5 \text{CaSiO}_3(\text{sol})$ . Both these quantities are interpreted graphically in Fig. 21.

## 5.8 Limited Mutual Solubility – Ideal Henrian Solutions

In Sec. 5.4, the region of two solids in the Ag-Cu phase diagram of Fig. 19 was described as a miscibility gap. That is, only one continuous  $g^s$  curve was assumed. If, somehow, the appearance of the liquid phase could be suppressed, the two solvus lines in Fig. 19, when projected upwards, would meet at a critical point, above which one continuous solid solution would exist at all compositions.

Such a description is justifiable only if the pure solid components have the same crystal structure, as is the case for Ag and Cu. However, consider the Ag-Mg system, Fig. 22, in which the terminal (Ag) solid solution is face-centered-cubic and the terminal (Mg) solid solution is hexagonal-close-packed. In this case, one continuous curve for  $g^s$  cannot be drawn. Each solid phase must have its own separate Gibbs energy curve, as shown schematically in Fig. 22b at 800 K. In this figure,  $\mu_{\text{Mg}}^{o(\text{hcp})}$  and  $\mu_{\text{Ag}}^{o(\text{fcc})}$  are the standard molar Gibbs energies of pure hcp Mg and pure fcc Ag, while  $\mu_{\text{Ag}}^{o(\text{hcp-Mg})}$  is the standard molar Gibbs energy of pure (hypothetical) hcp Ag in the hcp-Mg phase.

Since the solubility of Ag in the hcp-Mg phase is limited we can, to a good

approximation, describe it as a *Henrian ideal solution*. That is, when a solution is sufficiently dilute in one component, we can approximate  $\mu_{solute}^E = RT \ln \gamma_{solute}$  by its value in an infinitely dilute solution. That is, if  $X_{solute}$  is small we set  $\gamma_{solute} = \gamma_{solute}^o$  where  $\gamma_{solute}^o$  is the *Henrian activity coefficient* at  $X_{solute} = 0$ . Thus, for sufficiently dilute solutions we assume that  $\gamma_{solute}$  is independent of composition. Physically, this means that in a very dilute solution there is negligible interaction among solute particles because they are so far apart. Hence, each additional solute particle added to the solution makes the same contribution to the excess Gibbs energy of the solution and so  $\mu_{solute}^E = dG^E/dn_{solute} =$  constant.

From the Gibbs-Duhem equation (117), if  $d\mu_{solute}^E = 0$ , then  $d\mu_{solvent}^E = 0$ . Hence, in a Henrian solution  $\gamma_{solvent}$  is also constant and equal to its value in an infinitely dilute solution. That is,  $\gamma_{solvent} = 1$  and the solvent behaves ideally. In summary then, for dilute solutions ( $X_{solvent} \approx 1$ ) *Henry's Law* applies:

$$\begin{aligned} \gamma_{solvent} &\approx 1 \\ \gamma_{solute} &\approx \gamma_{solute}^o = \text{constant} \end{aligned} \quad (142)$$

(Care must be exercised for solutions other than simple substitutional solutions. Henry's Law applies only if the ideal activity is defined correctly for the applicable solution model. Solution models are discussed in Sec. 8.2)

Henrian activity coefficients can usually be expressed as functions of temperature:

$$RT \ln \gamma_i^o = a - bT \quad (143)$$

where  $a$  and  $b$  are constants. If data are limited, it can further be assumed that  $b \approx 0$  so that  $RT \ln \gamma_i^o \approx \text{constant}$ .

Treating the hcp-Mg phase in the Ag-Mg system (Fig. 22b) as a Henrian solution we write:

$$\begin{aligned}
g^{\text{hcp}} &= (X_{\text{Ag}}\mu_{\text{Ag}}^{\text{o(fcc)}} + X_{\text{Mg}}\mu_{\text{Mg}}^{\text{o(hcp)}}) + RT(X_{\text{Ag}} \ln a_{\text{Ag}} + X_{\text{Mg}} \ln a_{\text{Mg}}) \\
&= (X_{\text{Ag}}\mu_{\text{Ag}}^{\text{o(fcc)}} + X_{\text{Mg}}\mu_{\text{Mg}}^{\text{o(hcp)}}) + RT(X_{\text{Ag}} \ln(\gamma_{\text{Ag}}^{\text{o}} X_{\text{Ag}}) + X_{\text{Mg}} \ln X_{\text{Mg}})
\end{aligned} \tag{144}$$

where  $a_{\text{Ag}}$  and  $\gamma_{\text{Ag}}^{\text{o}}$  are the activity and activity coefficient of silver with respect to pure fcc silver as standard state. Let us now combine terms as follows:

$$\begin{aligned}
g^{\text{hcp}} &= \left[ X_{\text{Ag}} (\mu_{\text{Ag}}^{\text{o(fcc)}} + RT \ln \gamma_{\text{Ag}}^{\text{o}}) + X_{\text{Mg}} \mu_{\text{Mg}}^{\text{o(hcp)}} \right] \\
&\quad + RT(X_{\text{Ag}} \ln X_{\text{Ag}} + X_{\text{Mg}} \ln X_{\text{Mg}})
\end{aligned} \tag{145}$$

Since  $\gamma_{\text{Ag}}^{\text{o}}$  is independent of composition, let us define:

$$\mu_{\text{Ag}}^{\text{o(hcp-Mg)}} = \mu_{\text{Ag}}^{\text{o(fcc)}} + RT \ln \gamma_{\text{Ag}}^{\text{o}} \tag{146}$$

From Eqs. (145) and (146) it can be seen that, relative to  $\mu_{\text{Mg}}^{\text{o(hcp)}}$  and to the hypothetical standard state  $\mu_{\text{Ag}}^{\text{o(hcp-Mg)}}$  defined in this way, the hcp solution is ideal. Eqs. (145) and (146) are illustrated in Fig. 22b. It can be seen that as  $\gamma_{\text{Ag}}^{\text{o}}$  becomes larger, the point of tangency  $N$  moves to higher Mg concentrations. That is, as  $(\mu_{\text{Ag}}^{\text{o(hcp-Mg)}} - \mu_{\text{Ag}}^{\text{o(fcc)}})$  becomes more positive, the solubility of Ag in hcp-Mg decreases.

It must be stressed that  $\mu_{\text{Ag}}^{\text{o(hcp-Mg)}}$  as defined by Eq. (146) is solvent-dependent. That is,  $\mu_{\text{Ag}}^{\text{o(hcp-Mg)}}$  is not the same as, for example,  $\mu_{\text{Ag}}^{\text{o(hcp-Cd)}}$  for Ag in dilute hcp-Cd solutions. However, for purposes of developing consistent thermodynamic databases for multicomponent solution phases, it is generally considered advantageous to select a set of values for the chemical potentials of pure elements and compounds in metastable or unstable crystal structures, such as  $\mu_{\text{Ag}}^{\text{o(hcp)}}$ , which are independent of the solvent. Such values may be obtained (i) from measurements at high pressures if the structure is stable at high pressure, (ii) as averages of the values for several solvents, or (iii) from first-principles quantum mechanical or molecular dynamics calculations. Tables

(Dinsdale, 1991) of such values for many elements in metastable or unstable states have been prepared and agreed upon by the international community working in the field of phase diagram evaluation and thermodynamic database optimization. (See Sec. 8.) The use of such solvent-independent values, of course, means that even in dilute solutions non-zero excess Gibbs energy terms are usually required.

## 5.9 Geometry of Binary Temperature-Composition Phase Diagrams

In Sec. 3.1.1 it was shown that when three phases are at equilibrium in a binary system at constant pressure, the system is invariant ( $F = 0$ ). There are two general types of three-phase *invariants* in binary phase diagrams. These are the *eutectic-type* and *peritectic-type* invariants as illustrated in Fig. 23. Let the three phases concerned be called  $\alpha$ ,  $\beta$  and  $\gamma$ , with  $\beta$  as the central phase as shown in Fig. 23. The phases  $\alpha$ ,  $\beta$  and  $\gamma$  can be solid, liquid or gaseous. At a eutectic-type invariant, the following invariant reaction occurs isothermally as the system is cooled:



while at a peritectic-type invariant the invariant reaction upon cooling is:



Some examples of eutectic-type invariants are: (i) *eutectics* (Fig. 19) in which  $\alpha = \text{solid}_1$ ,  $\beta = \text{liquid}$ ,  $\gamma = \text{solid}_2$ ; the eutectic reaction is  $\text{liq} \rightarrow \text{s}_1 + \text{s}_2$ ; (ii) *monotectics* (Fig. 21) in which  $\alpha = \text{liquid}_1$ ,  $\beta = \text{liquid}_2$ ,  $\gamma = \text{solid}$ ; the monotectic reaction is  $\text{liq}_2 \rightarrow \text{liq}_1 + \text{s}$ ; (iii) *eutectoids* in which  $\alpha = \text{solid}_1$ ,  $\beta = \text{solid}_2$ ,  $\gamma = \text{solid}_3$ ; the eutectoid reaction is  $\text{s}_2 \rightarrow \text{s}_1 + \text{s}_3$ ; (iv) *catatectics* in which  $\alpha = \text{liquid}$ ,  $\beta = \text{solid}_1$ ,  $\gamma = \text{solid}_2$ ; the catatectic reaction is  $\text{s}_1 \rightarrow \text{liq} + \text{s}_2$ .

Some examples of peritectic-type invariants are: (i) *peritectics* (Fig. 22) in which  $\alpha = \text{liquid}$ ,  $\beta = \text{solid}_1$ ,  $\gamma = \text{solid}_2$ . The peritectic reaction is  $\text{liq} + \text{s}_2 \rightarrow \text{s}_1$ ; (ii) *syntectics* (Fig. 20 k) in which  $\alpha = \text{liquid}_1$ ,  $\beta = \text{solid}$ ,  $\gamma = \text{liquid}_2$ . The syntectic reaction is  $\text{liq}_1 + \text{liq}_2 \rightarrow \text{s}$ . (iii) *peritectoids* in which  $\alpha = \text{solid}_1$ ,  $\beta = \text{solid}_2$ ,  $\gamma = \text{solid}_3$ . The peritectoid reaction is  $\text{s}_1 + \text{s}_3 \rightarrow \text{s}_2$ .

An important rule of construction which applies to invariants in binary phase dia-

grams is illustrated in Fig. 23. This *extension rule* states that at an invariant the extension of a boundary of a two-phase region must pass into the adjacent two-phase region and not into a single-phase region. Examples of both correct and incorrect constructions are given in Fig. 23. To understand why the "incorrect extension" shown is not correct consider that the  $(\alpha + \gamma)/\gamma$  phase boundary line indicates the composition of the  $\gamma$ -phase in equilibrium with the  $\alpha$ -phase, as determined by the common tangent to the Gibbs energy curves. Since there is no reason for the Gibbs energy curves or their derivatives to change discontinuously at the invariant temperature, the extension of the  $(\alpha + \gamma)/\gamma$  phase boundary also represents the stable phase boundary under equilibrium conditions. Hence, for this line to extend into a region labeled as single-phase  $\gamma$  is incorrect. This extension rule is a particular case of the general Schreinemakers' rule. (See Secs 7.4 and 7.7.1)

Two-phase regions in binary phase diagrams can terminate: (i) on the pure component axes (at  $X_A = 1$  or  $X_B = 1$ ) at a transformation point of pure A or B; (ii) at a critical point of a miscibility gap; (iii) at an invariant. Two-phase regions can also exhibit maxima or minima. In this case, both phase boundaries must pass through their maximum or minimum at the same point as shown in Fig. 23.

All the *geometrical units* of construction of binary phase diagrams have now been discussed. The phase diagram of a binary alloy system will usually exhibit several of these units. As an example, the Fe-Mo phase diagram was shown in Fig. 1. The invariants in this system are peritectics at 1612, 1498 and 1453°C; eutectoids at 1240, 1233 and 308°C; and peritectoids at 1368 and 1250°C. The two-phase (liquid + bcc) region passes through a minimum at  $X_{Mo} = 0.2$ .

Between 910°C and 1390°C is a two-phase  $(\alpha + \gamma)$   *$\gamma$ -loop*. Pure Fe adopts the fcc  $\gamma$  structure between these two temperatures but exists as the bcc  $\alpha$  phase at higher and lower temperatures. Mo, on the other hand, is more soluble in the bcc than in the fcc structure. That is  $\mu_{Mo}^{o(bcc-Fe)} < \mu_{Mo}^{o(fcc-Fe)}$  as discussed in Sec. 5.8. Therefore, small additions of Mo stabilize the bcc structure.

In the CaO-SiO<sub>2</sub> phase diagram, Fig. 21, we observe eutectics at 1437, 1463 and 2017°C; a monotectic at 1689°C; and a peritectic at 1464°C. The compound

$\text{Ca}_3\text{SiO}_5$  dissociates upon heating to  $\text{CaO}$  and  $\text{Ca}_2\text{SiO}_4$  by a peritectoid reaction at  $1799^\circ\text{C}$  and dissociates upon cooling to  $\text{CaO}$  and  $\text{Ca}_2\text{SiO}_4$  by a eutectoid reaction at  $1300^\circ\text{C}$ . Maxima are observed at  $2154$  and  $1540^\circ\text{C}$ . At  $1465^\circ\text{C}$  there is an invariant associated with the tridymite  $\rightarrow$  cristobalite transition of  $\text{SiO}_2$ . This is either a peritectic or a catatectic depending upon the relative solubility of  $\text{CaO}$  in tridymite and cristobalite. However, these solubilities are very small and unknown. At  $1437^\circ\text{C}$ ,  $\text{Ca}_2\text{SiO}_4$  undergoes an allotropic transformation. This gives rise to two invariants, one involving  $\text{Ca}_2\text{SiO}_4(\alpha)$ ,  $\text{Ca}_2\text{SiO}_4(\beta)$  and  $\text{Ca}_3\text{SiO}_5$ , and the other  $\text{Ca}_2\text{SiO}_4(\alpha)$ ,  $\text{Ca}_2\text{SiO}_4(\beta)$  and  $\text{Ca}_3\text{Si}_2\text{O}_7$ . Since the compounds are all essentially stoichiometric, these two invariants are observed at almost exactly the same temperature of  $1437^\circ\text{C}$  and it is not possible to distinguish whether they are of the eutectoid or peritectoid type.

## **6 Ternary Temperature-Composition Phase Diagrams**

### **6.1 The Ternary Composition Triangle**

In a ternary system with components A-B-C, the sum of the mole fractions is unity,  $(X_A+X_B+X_C) = 1$ . Hence, there are two independent composition variables. A representation of composition, symmetrical with respect to all three components, may be obtained with the equilateral "composition triangle" as shown in Fig. 24 for the Bi-Sn-Cd system. Compositions at the corners of the triangle correspond to the pure components. Compositions along the edges of the triangle correspond to the three binary subsystems Bi-Sn, Sn-Cd and Cd-Bi. Lines of constant mole fraction  $X_{Bi}$  are parallel to the Sn-Cd edge, while lines of constant  $X_{Sn}$  and  $X_{Cd}$  are parallel to the Cd-Bi and Bi-Sn edges respectively. For example, at point a in Fig. 24,  $X_{Bi} = 0.05$ ,  $X_{Sn} = 0.45$  and  $X_{Cd} = 0.50$ .

Similar equilateral composition triangles can be drawn with coordinates in terms of weight % of the three components.

### **6.2 Ternary Space Model**

A ternary temperature-composition phase diagram at constant total pressure may be plotted as a three-dimensional "space model" within a right triangular prism with the equilateral composition triangle as base and temperature as vertical axis. Such a space

model for a simple eutectic ternary system A-B-C is illustrated in Fig. 25. On the three vertical faces of the prism are found the phase diagrams of the three binary subsystems, A-B, B-C and C-A which, in this example, are all simple eutectic binary systems. The binary eutectic points are  $e_1$ ,  $e_2$  and  $e_3$ . Within the prism we see three *liquidus surfaces* descending from the melting points of pure A, B and C. Compositions on these surfaces correspond to compositions of liquid in equilibrium with A-, B- and C-rich solid phases.

In a ternary system at constant pressure, the Gibbs Phase Rule, Eq. (80), becomes:

$$F = 4 - P \quad (149)$$

When the liquid and one solid phase are in equilibrium  $P = 2$ . Hence  $F = 2$  and the system is bivariant. A ternary liquidus is thus a two-dimensional surface. We may choose two variables, say  $T$  and one composition coordinate of the liquid, but then the other liquid composition coordinate and the composition of the solid are fixed.

The A- and B-liquidus surfaces in Fig. 25 intersect along the line  $e_1E$ . Liquids with compositions along this line are therefore in equilibrium with A-rich and B-rich solid phases simultaneously. That is,  $P = 3$  and so  $F = 1$ . Such "valleys" are thus called *univariant lines*. The three univariant lines meet at the *ternary eutectic point E* at which  $P = 4$  and  $F = 0$ . This is an invariant point since the temperature and the compositions of all four phases in equilibrium are fixed.

### 6.3 Polythermal Projections of Liquidus Surfaces

A two-dimensional representation of the ternary liquidus surface may be obtained as an orthogonal projection upon the base composition triangle. Such a *polythermal projection* of the liquidus of the Bi-Sn-Cd system (Bray et al., 1961-62) is shown in Fig. 24. This is a simple eutectic ternary system with a space model like that shown in Fig. 25. The constant temperature lines on Fig, 24 are called *liquidus isotherms*. The univariant valleys are shown as heavier lines. By convention, the large arrows indicate the directions of decreasing temperature along these lines.

Let us consider the sequence of events occurring during the equilibrium cooling from the liquid of an alloy of overall composition  $a$  in Fig. 24. Point  $a$  lies within the field of *primary crystallization* of Cd. That is, it lies within the composition region in Fig. 24 in

which Cd-rich solid will be the first solid to precipitate upon cooling. As the liquid alloy is cooled, the Cd-liquidus surface is reached at  $T \approx 465$  K (slightly below the 473 K isotherm). A solid Cd-rich phase begins to precipitate at this temperature. Now, in this particular system, Bi and Sn are nearly insoluble in solid Cd, so that the solid phase is virtually pure Cd. (Note that this fact cannot be deduced from Fig. 24 alone.) Therefore, as solidification proceeds the liquid becomes depleted in Cd, but the ratio  $X_{Sn}/X_{Bi}$  in the liquid remains constant. Hence, the composition path followed by the liquid (its *crystallization path*) is a straight line passing through point *a* and projecting to the Cd-corner of the triangle. This crystallization path is shown on Fig. 24 as the line *ab*.

In the general case in which a solid solution rather than a pure component or stoichiometric compound is precipitating, the crystallization path will not be a straight line. However, for equilibrium cooling, a straight line joining a point on the crystallization path at any  $T$  to the overall composition point *a* will extend through the composition, on the solidus surface, of the solid phase in equilibrium with the liquid at that temperature. That is, the compositions of the two equilibrium phases and the overall system composition always lie on the same tie-line as is required by mass balance considerations.

When the composition of the liquid has reached point *b* in Fig. 24 at  $T \approx 435$  K, the relative proportions of the solid Cd and liquid phases at equilibrium are given by the *lever rule* applied to the *tie-line dab*: (moles of liquid)/(moles of Cd) =  $da/ab$  where *da* and *ab* are the lengths of the line segments. Upon further cooling, the liquid composition follows the univariant valley from *b* to *E* while Cd and Sn-rich solids co-precipitate as a binary eutectic mixture. When the liquidus composition attains the ternary eutectic composition *E* at  $T \approx 380$  K the invariant *ternary eutectic reaction* occurs:



where  $s_1$ ,  $s_2$  and  $s_3$  are the three solid phases and where the compositions of all four phases (as well as  $T$ ) remain fixed until all liquid has solidified.

In order to illustrate several of the features of polythermal projections of liquidus surfaces, a projection of the liquidus surface of a hypothetical system A-B-C is shown in Fig. 26. For the sake of simplicity, isotherms are not shown; only the univariant lines are

shown, with arrows to show the directions of decreasing temperature. The binary subsystems A-B and C-A are simple eutectic systems, while the binary subsystem B-C contains one congruently melting binary phase,  $\varepsilon$ , and one incongruently melting binary phase,  $\delta$ , as shown in the insert in Fig. 26. The letters  $e$  and  $p$  indicate binary eutectic and peritectic points. The  $\delta$  and  $\varepsilon$  phases are called *binary compounds* since they have compositions within a binary subsystem. Two *ternary compounds*,  $\eta$  and  $\zeta$ , with compositions within the ternary triangle, as indicated in Fig. 26, are also found in this system. All compounds, as well as pure solid A, B and C (the  $\alpha$ ,  $\beta$  and  $\gamma$  phases), are assumed to be stoichiometric (i.e., there is no solid solubility). The fields of primary crystallization of all the solids are indicated in parentheses in Fig. 26. The composition of the  $\varepsilon$  phase lies within its field, since it is a congruently melting compound, while the composition of the  $\delta$  phase lies outside of its field since it is an incongruently melting compound. Similarly for the ternary compounds,  $\eta$  is a congruently melting compound while  $\zeta$  is incongruently melting. For the congruent compound  $\eta$ , the highest temperature on the  $\eta$ -liquidus occurs at the composition of  $\eta$

The univariant lines meet at a number of *ternary eutectics*  $E$  (three arrows converging on the point), a *ternary peritectic*  $P$  (one arrow entering, two arrows leaving the point), and several *ternary quasi-peritectics*  $P'$  (two arrows entering, one arrow leaving). Two *saddle points*  $s$  are also shown. These are points of maximum  $T$  along the univariant line but of minimum  $T$  on the liquidus surface along a section joining the compositions of the two solids. For example,  $s_1$  is a maximum point along the univariant  $E_1P'_3$ , but is a minimum point on the liquidus along the straight line  $\zeta s_1 \eta$ .

Let us consider the events occurring during equilibrium cooling from the liquid of an alloy of overall composition  $a$  in Fig. 26. The primary crystallization product will be the  $\varepsilon$  phase. Since this is a pure stoichiometric solid the crystallization path of the liquid will be along a straight line passing through  $a$  and extending to the composition of  $\varepsilon$  as shown in the figure.

Solidification of  $\varepsilon$  continues until the liquid attains a composition on the univariant valley. Thereafter the liquid composition descends along the valley towards the point  $P'_1$

in co-existence with  $\varepsilon$  and  $\zeta$ . At point  $P'_1$  the invariant *ternary quasi-peritectic reaction* occurs isothermally:



Since there are two reactants, there are two possible outcomes: (i) the liquid is completely consumed before the  $\varepsilon$  phase and solidification will be complete at the point  $P'_1$ ; (ii)  $\varepsilon$  is completely consumed before the liquid and solidification will continue with decreasing  $T$  along the univariant line  $P_1E_1$  with co-precipitation of  $\delta$  and  $\zeta$  until, at  $E_1$ , the liquid will solidify eutectically (liquid  $\rightarrow \delta + \zeta + \eta$ ). To determine whether outcome (i) or (ii) occurs, we use the mass balance criterion that, for three-phase equilibrium, the overall composition  $a$  must always lie within the *tie-triangle* formed by the compositions of the three phases. Now the triangle joining the compositions of  $\delta$ ,  $\varepsilon$  and  $\zeta$ , does not contain the point  $a$ , but the triangle joining the compositions of  $\delta$ ,  $\zeta$  and liquid at  $P'_1$  does contain the point  $a$ . Hence, outcome (ii) occurs.

An alloy of overall composition  $b$  in Fig. 26 solidifies with  $\varepsilon$  as primary crystallization product until the liquid composition contacts the univariant line. Thereafter, co-precipitation of  $\varepsilon$  and  $\beta$  occurs with the liquid composition following the univariant valley until the liquid reaches the peritectic composition  $P$ . The invariant *ternary peritectic reaction* then occurs isothermally: .



Since there are three reactants, there are three possible outcomes: (i) the liquid is consumed before either  $\varepsilon$  or  $\beta$  and solidification terminates at  $P$ ; (ii)  $\varepsilon$  is consumed first and solidification then continues along the path  $PP'_3$ ; or (iii)  $\beta$  is consumed first and solidification continues along the path  $PP'_1$ . Which outcome actually occurs depends on whether the overall composition  $b$  lies within the tie-triangle (i)  $\varepsilon\beta\zeta$ , (ii)  $\beta\zeta P$ , or (iii)  $\varepsilon\zeta P$ . In the example shown, outcome (i) will occur.

A polythermal projection of the liquidus surface of the Zn-Mg-Al system is shown in Fig. 27. There are eleven primary crystallization fields of nine binary solid solutions (with limited solubility of the third component) and of two ternary solid solutions. There

are three ternary eutectic points, two saddle points, four ternary peritectic points and four ternary quasi-peritectic points.

## 6.4 Ternary Isothermal Sections

Isothermal projections of the liquidus surface do not provide information on the compositions of the solid phases at equilibrium. However, this information can be presented at any one temperature on an *isothermal section* such as that shown for the Bi-Sn-Cd system at 423 K in Fig. 28. This phase diagram is a constant temperature slice through the space model of Fig. 25.

The liquidus lines bordering the one-phase liquid region of Fig. 28 are identical to the 423 K isotherms of the projection in Fig. 24. Point *c* in Fig. 28 is point *c* on the univariant line in Fig. 24. An alloy with overall composition in the one-phase liquid region of Fig. 28 at 423 K will consist of a single liquid phase. If the overall composition lies within one of the two-phase regions, then the compositions of the two phases are given by the ends of the *tie-line* which passes through the overall composition. For example, a sample with overall composition *p* in Fig. 28 will consist of a liquid of composition *q* on the liquidus and a solid Bi-rich alloy of composition *r* on the solidus. The relative proportions of the two phases are given by the lever rule:

(moles of liquid)/(moles of solid) =  $pr/pq$ , where *pr* and *pq* are the lengths of the tie-line segments.

In the case of solid Cd, the solid phase is nearly pure Cd, so all tie-lines of the (Cd + liquid) region converge nearly to the corner of the triangle. In the case of the Bi- and Sn-rich solids, some solid solubility is observed. (The actual extent of this solubility is exaggerated in Fig. 28 for the sake of clarity of presentation.) Alloys with overall compositions rich enough in Bi or Sn to lie within the single-phase (Sn) or (Bi) regions of Fig. 28 will consist at 423 K of single-phase solid solutions. Alloys with overall compositions at 423 K in the two-phase (Cd + Sn) region will consist of two solid phases.

Alloys with overall compositions within the three-phase triangle *dcf* will, at 423 K, consist of three phases: Cd- and Sn-rich solids with compositions at *d* and *f* and liquid of composition *c*. To understand this better, consider an alloy of composition *a* in

Fig. 28, which is the same composition as the point *a* in Fig. 24. In Sec. 6.3 we saw that when an alloy of this composition is cooled, the liquid follows the path *ab* in Fig. 24 with primary precipitation of Cd and then follows the univariant line with coprecipitation of Cd and Sn so that at 423 K the liquid is at the composition point *c*, and two solid phases are in equilibrium with the liquid.

#### 6.4.1 Topology of Ternary Isothermal Sections

At constant temperature the Gibbs energy of each phase in a ternary system is represented as a function of composition by a surface plotted in a right triangular prism with Gibbs energy as vertical axis and the composition triangle as base. Just as the compositions of phases at equilibrium in binary systems are determined by the points of contact of a common tangent line to their isothermal Gibbs energy curves (Fig. 13), so the compositions of phases at equilibrium in a ternary system are given by the points of contact of a common tangent plane to their isothermal Gibbs energy surfaces (or, equivalently as discussed in Sec. 4.2, by minimizing the total Gibbs energy of the system.) A common tangent plane can contact two Gibbs energy surfaces at an infinite number of pairs of points, thereby generating an infinite number of tie-lines within a two-phase region on an isothermal section. A common tangent plane to three Gibbs energy surfaces contacts each surface at a unique point, thereby generating a three-phase tie-triangle.

Hence, the principal topological units of construction of an isothermal ternary phase diagram are three-phase ( $\alpha + \beta + \gamma$ ) tie-triangles as in Fig. 29 with their accompanying two-phase and single-phase areas. Each corner of the tie-triangle contacts a single-phase region, and from each edge of the triangle there extends a two-phase region. The edge of the triangle is a limiting tie-line of the two-phase region.

For overall compositions within the tie-triangle, the compositions of the three phases at equilibrium are fixed at the corners of the triangle. The relative proportions of the three phases are given by the *lever rule of tie-triangles*, which can be derived from mass balance considerations. At an overall composition *q* in Fig. 29 for example, the relative proportion of the  $\gamma$  phase is given by projecting a straight line from the  $\gamma$ -corner of the triangle (point *c*) through the overall composition *q* to the opposite side of the

triangle, point  $p$ . Then: (moles of  $\gamma$ )/(total moles) =  $qp/cp$  if compositions are expressed as mole fractions, or (weight of  $\gamma$ )/(total weight) =  $qp/cp$  if compositions are in weight percent.

Isothermal ternary phase diagrams are generally composed of a number of these topological units. An example for the Zn-Mg-Al system at 25°C is shown in Fig. 2. At 25°C, hcp-Mg, hcp-Zn and  $Mg_2Zn_{11}$  are nearly stoichiometric compounds, while Mg and Zn have very limited solubility in fcc-Al. The gamma and  $\beta$ AlMg phases are binary compounds which exhibit very narrow ranges of stoichiometry in the Mg-Al binary system and in which Zn is very sparingly soluble. The Laves,  $Mg_2Zn_3$  and MgZn phases are virtually stoichiometric binary compounds in which Al is soluble to a few percent. Their ranges of stoichiometry are thus shown on Fig. 2 as very narrow lines. The Tau phase is a ternary phase with a small single-phase region of stoichiometry as shown. An examination of Fig. 2 will show that it is composed of the topological units of Fig. 29.

An *extension rule*, a particular case of *Schreinemakers' Rule* (See Sec. 7.4 and 7.7.1), for ternary tie-triangles is illustrated in Fig. 29 at points  $a$  and  $b$ . At each corner, the extension of the boundaries of the single-phase regions, indicated by the broken lines, must either both project into the triangle as at point  $a$ , or must both project outside the triangle as at point  $b$ . Furthermore, the angle between the boundaries must not be greater than 180°.

Another important rule of construction, whose derivation is evident, is that within any two-phase region tie-lines must never cross one another.

## 6.5 Ternary Isopleths (Constant Composition Sections)

A vertical *isopleth*, or constant composition section, through the space model of the Bi-Sn-Cd system, is shown in Fig. 30. The section follows the line  $AB$  in Fig. 24.

The phase fields on Fig. 30 indicate which phases are present when an alloy with an overall composition on the line  $AB$  is equilibrated at any temperature. For example, consider the cooling, from the liquid state, of an alloy of composition  $a$  which is on the line  $AB$  (See Fig. 24). At  $T \approx 465$  K, precipitation of the solid (Cd) phase begins at point  $a$  in Fig. 30. At  $T \approx 435$  K (point  $b$  in Figs. 24 and 30) the solid (Sn) phase begins to appear. Finally, at the eutectic temperature  $T_E$ , the ternary reaction occurs, leaving solid

(Cd) + (Bi) + (Sn) at lower temperatures. The intersection of the isopleth with the univariant lines on Fig. 24 occurs at points *f* and *g* which are also indicated on Fig. 30. The intersection of this isopleth with the isothermal section at 423 K is shown in Fig. 28. The points *s*, *t*, *u* and *v* of Fig. 28 are also shown on Fig. 30.

It is important to note that on an isopleth the tie-lines do not, in general, lie in the plane of the diagram. Therefore, the diagram provides information only on which phases are present, not on their compositions or relative proportions. The boundary lines on an isopleth do not in general indicate the phase compositions or relative proportions, only the temperature at which a phase appears or disappears for a given overall composition. The lever-rule cannot be applied on an isoplethal section.

An isoplethal section of the Zn-Mg-Al system at 10 mol % Zn was shown in Fig. 3a. The liquidus surface of the diagram may be compared to the liquidus surface along the line where  $X_{Zn} = 0.1$  in Fig. 27 and to the section at  $X_{Zn} = 0.1$  in the isothermal section at 25°C in Fig. 2. Point *p* on the two-phase (Tau + Gamma) field on Fig. 3a at 25°C corresponds to point *p* on Fig. 2 where the equilibrium compositions of the Gamma and Tau phases are given by the ends of the tie-line. These individual phase compositions cannot be read from Fig. 3a.

The geometrical rules which apply to isoplethal sections will be discussed in Sec. 7.

### 6.5.1 Quasibinary Phase Diagrams

The binary CaO-SiO<sub>2</sub> phase diagram in Fig. 21 is actually an isopleth of the ternary Ca-Si-O system along the line  $n_O = (n_{Ca} + 2n_{Si})$ . However all tie-lines in Fig. 21 lie within (or virtually within) the plane of the diagram because  $n_O = (n_{Ca} + 2n_{Si})$  in every phase. Therefore, the diagram is called a *quasibinary* phase diagram. Similarly, the K<sub>2</sub>CO<sub>3</sub>-Na<sub>2</sub>CO<sub>3</sub> phase diagram in Fig. 17 is a quasibinary isoplethal section of the quaternary K-Na-C-O system.

## 7 General Phase Diagram Sections

Phase diagrams involving temperature and composition as variables have been discussed in Secs. 5 and 6 for binary and ternary systems. In the present section we

shall discuss the geometry of general phase diagram sections involving these and other variables such as total pressure, chemical potentials, volume, enthalpy, etc. for systems of any number of components. A few examples of such diagrams have already been shown in Figs. 4-7, 9 and 10. It will now be shown that all these phase diagrams, although seemingly quite different geometrically, actually all obey one simple set of geometrical rules.

The rules which will be developed apply to two-dimensional phase diagram sections in which two thermodynamic variables are plotted as axes while other variables are held constant. We shall develop a set of sufficient conditions for the choice of axis variables and constants which ensure that the phase diagram section is single-valued, with each point on the diagram representing a unique equilibrium state. Although these rules do not apply directly to phase diagram projections such as in Figs. 24, 26 and 27, such diagrams can be considered to consist of portions of several phase diagram sections projected onto a common plane. Some geometrical rules specific to projections will be given in Sec. 7.13. Finally, since all single-valued phase diagram sections obey the same set of geometrical rules, one single algorithm can be used for their calculation as will be demonstrated in Sec. 7.4.1.

In Secs. 7.1 to 7.6 we shall first present the geometrical rules governing general phase diagram sections without giving detailed proofs. Rigorous proofs will follow in Secs. 7.7 and 7.9.

## 7.1 Corresponding Potentials and Extensive Variables

In a system with  $C$  components, we select the following  $(C + 2)$  *thermodynamic potentials* (intensive variables):  $T, P, \mu_1, \mu_2, \dots, \mu_C$ . For each potential  $\phi_i$  there is a *corresponding extensive variable*  $q_i$  related by the equation:

$$\phi_i = \left( \partial \mathbf{U} / \partial \mathbf{q}_i \right)_{\mathbf{q}_j (j \neq i)} \quad (153)$$

The corresponding pairs of potentials and extensive variables are listed in Table 1. The corresponding pairs are found together in the terms of the fundamental equation (9) and in the Gibbs-Duhem equation (75).

When a system is at equilibrium, the potential variables are the same for all

phases (all phases are at the same  $T, P, \mu_1, \mu_2, \dots$ ) but the extensive variables can differ from one phase to the next (the phases can all have different volumes, entropies and compositions). In this regard it is important to note the following. If the only variables which are held constant are potential variables, then the compositions of all phases will lie in the plane of the phase diagram section and the lever rule may be applied. Some examples are found in Figs. 1, 2 and 5. However, if an extensive variable such as composition is held constant, then this is no longer necessarily true as was discussed for example in Sec. 6.5 regarding isoplethal sections such as Figs. 3, 4 and 30.

## 7.2 The Law of Adjoining Phase Regions

The following *Law of Adjoining Phase Regions* (Palatnik and Landau, 1956) applies to all single-valued phase diagram sections: “As a phase boundary line is crossed, one and only one phase either appears or disappears.”

This law is clearly obeyed in any phase diagram section in which both axis variables are extensive variables such as Figs. 2, 3b, 4 and 28. When one axis variable is a potential, however, it may at first glance appear the the law is not obeyed for invariant lines. For instance, as the eutectic line is crossed in the binary  $T$ -composition phase diagram in Fig. 19, one phase disappears and another appears. However, the eutectic line in this figure is not a simple phase boundary, but rather an infinitely narrow three-phase region. This is illustrated schematically in Fig. 31 where the three-phase region has been “opened up” to show that the region is enclosed by upper and lower phase boundaries which are coincident. In passing from the  $(\beta + L)$  to the  $(\alpha + \beta)$  region, for example, we first pass through the  $(\alpha + \beta + L)$  region. Hence the Law of Adjoining Phase Regions is obeyed. The three-phase region is infinitely narrow because all three phases at equilibrium must be at the same temperature. Another example is seen in the isoplethal section in Fig. 30. At the ternary eutectic temperature,  $T_E$ , there is an infinitely narrow horizontal four-phase invariant region ( $L + (\text{Bi}) + (\text{Cd}) + (\text{Sn})$ ). As yet another example, the y-axis of Fig. 5 is the chemical potential of oxygen which is the same in all phases at equilibrium. This diagram exhibits two infinitely narrow horizontal three-phase invariant regions.

Similarly, if both axis variables are potentials, there may be several infinitely narrow univariant phase regions. For example, in the  $P$ - $T$  diagram of Fig. 7a all lines are infinitely narrow two-phase regions bounded on either side by coincident phase boundaries as shown schematically in Fig. 32 where all two-phase regions have been “opened up.” The three-phase invariant triple point is then seen to be a degenerate three-phase triangle. Other examples of diagrams in which both axis variables are potentials are seen in Figs. 6, 9 and 10. All lines on Figs. 9 and 10 are infinitely narrow two-phase univariant regions. In Fig. 6 some lines are infinitely narrow three-phase univariant regions while others are simple phase boundaries.

### 7.3 Nodes in Phase Diagram Sections

All phase boundary lines in any single-valued phase diagram section meet at nodes where exactly four lines converge as illustrated in Fig. 33.  $N$  phases ( $\alpha_1, \alpha_2, \dots, \alpha_N$ ), where  $N \geq 1$ , are common to all four regions. Two additional phases,  $\beta$  and  $\gamma$ , are disposed as shown in Fig. 33, giving rise to two  $(N+1)$ -phase regions and one  $(N+2)$ -phase region. At every node, the generalized *Schreinemakers' Rule* requires that the extensions of the boundaries of the  $N$ -phase region must either both lie within the  $(N+1)$ -phase regions as in Fig. 33, or they must both lie within the  $(N+2)$ -phase region.

Schreinemakers' Rule will be proven in Sec. 7.7.1.

An examination of Fig. 4 for example will reveal that all nodes involve exactly four boundary lines. Schreinemakers' Rule is illustrated on this figure by the dashed extensions of the phase boundaries at the nodes labeled  $a$ ,  $b$  and  $c$  and on Fig. 30 by the dashed extension lines at nodes  $f$  and  $g$ .

For phase diagrams in which one or both axis variables are potentials it might at first glance seem that fewer than four boundaries converge at some nodes. However, all nodes can still be seen to involve exactly four phase boundary lines when all infinitely narrow phase regions are “opened up” as in Figs. 31 and 32.

The extension rule illustrated in Fig. 29 for tie-triangles in ternary isothermal sections can be seen to be a particular case of Schreinemakers' Rule, as can the extension rules shown in Fig. 23 for binary  $T$ -composition phase diagrams. Finally, an

extension rule for triple points on  $P$ - $T$  phase diagrams is illustrated in Fig. 7a; the extension of each univariant line must pass into the opposite bivariant region. This rule, which can be seen to apply to Figs. 9 and 10 as well, is also a particular case of Schreinemakers' Rule.

An objection might be raised that a minimum or a maximum in a two-phase region in a binary temperature-composition phase diagram, as in Figs. 17, 21 and 22 represents an exception to Schrelnemakers' Rule. However, the extremum in such cases is not actually a node where four phase boundaries converge, but rather a point where two boundaries touch. Such extrema in which two phase boundaries touch with zero slope may occur for a  $C$ -phase region in a phase diagram of a  $C$ -component system when one axis is a potential. For example, in an isobaric temperature-composition phase diagram of a four-component system, we may observe a maximum or a minimum in a four-phase region separating two three-phase regions. A similar maximum or minimum in a  $(C-n)$ -phase region, where  $n > 0$ , may also occur along particular composition paths. This will be discussed in more detail in Sec. 9.4.

Other apparent exceptions to Schreinemakers' Rule (such as five boundaries meeting at a node) can occur in special limiting cases, as for example if an isoplethal section of a ternary system passes exactly through the ternary eutectic composition.

## 7.4 Zero Phase Fraction Lines

All phase boundaries on any single-valued phase diagram section are *Zero Phase Fraction (ZPF) Lines*, an extremely useful concept introduced by Gupta, Morral and Nowotny (1986), which is a direct consequence of the Law of Adjoining Phase Regions. There is a ZPF line associated with each phase. On one side of its ZPF line the phase occurs, while on the other side it does not, as illustrated by the colored lines on Fig. 4. There is a ZPF line for each of the five phases in Fig. 4. The five ZPF lines account for all the phase boundaries on the two-dimensional section. Phase diagram sections plotted on triangular coordinates as in Figs. 2 and 28 similarly consist of one ZPF line for each phase.

With reference to Fig. 33, it can be seen that at every node, two ZPF lines cross each other.

In the case of phase diagrams in which one or both axis variables are potentials, certain phase boundaries may be coincident as was discussed in Sec. 7.2. Hence, ZPF lines for two different phases may be coincident over part of their lengths as is illustrated in Fig. 34. In Figs. 9 and 10, every line on the diagram is actually two coincident ZPF lines.

#### **7.4.1 General Algorithm to Calculate Any Phase Diagram Section**

Since all single-valued phase diagram sections obey the same geometrical rules described in Secs. 7.1 to 7.3, one general algorithm can be used to calculate any phase diagram section thermodynamically. As discussed in Sec 2.3, the equilibrium state of a system (that is, the amount and composition of every phase) can be calculated for a given set of conditions ( $T$ ,  $P$ , overall composition, chemical potentials, etc.) by software which minimizes the total Gibbs energy of the system, retrieving the thermodynamic data for each phase from databases. To calculate any phase diagram section, one first specifies the desired axis variables and their limits as well as the constants of the diagram. The software then scans the four edges of the diagram, using Gibbs energy minimization to find the ends of each ZPF line. Next, each ZPF line is calculated from one end to the other using Gibbs energy minimization to determine the series of points at which the phase is just on the verge of appearing. Should a ZPF line not intersect any edge of the diagram it will be discovered by the program while it is tracing one of the other ZPF lines. When ZPF lines for all phases have been drawn, the diagram is complete. This is the algorithm used by the FactSage system software which has been used to calculate most of the phase diagrams shown in this Chapter (see FactSage).

### **7.5 Choice of Variables to Ensure That Phase Diagram Sections are Single-Valued**

In a system of  $C$  components, a two-dimensional phase diagram section is obtained by choosing two axis variables and holding  $(C-1)$  other variables constant. However, not every choice of variables will result in a single-valued phase diagram with a unique equilibrium state at every point. For example on the  $P$ - $V$  diagram for  $H_2O$  shown schematically in Fig. 35, at any point in the area where the  $(S + L)$  and

(L + G) regions overlap there are two possible equilibrium states of the system. Similarly, the diagram of S<sub>2</sub> pressure versus the mole fraction of Ni at constant T and P in the Cu-Ni-S<sub>2</sub> system in Fig. 36 exhibits a region in which there are two possible equilibrium states.

In order to ensure that a phase diagram section is single-valued at every point, the following procedure for the choice of variables is sufficient:

- (1) From each corresponding pair ( $\phi_i$ ,  $q_i$ ) in Table 1, select either  $\phi_i$  or  $q_i$ , but not both. At least one of the selected variables must be an extensive variable  $q_i$ .
- (2) Define the size of the system as some function of the selected extensive variables. (Examples:  $(n_1 + n_2) = \text{constant}$ ;  $n_2 = \text{constant}$ ;  $V = \text{constant}$ ; etc.) and then normalize the chosen extensive variables.
- (3) The chosen potentials and normalized extensive variables are then the (C + 1) independent phase diagram variables. Two of these are selected as axes and the others are held constant.

Note that this procedure constitutes a set of sufficient (but not necessary) conditions for the diagram to be single-valued. That is, a diagram which violates these conditions may still be single-valued, but there is no assurance that this will be the case.

The procedure is illustrated by the following examples. In each example the selected variables, one from each conjugate pair, are underlined.

System Fe-Mo (Fig. 1):

$\phi_i$ : T    P     $\mu_{\text{Fe}}$      $\mu_{\text{Mo}}$

$q_i$ :    S    -V     $n_{\text{Fe}}$      $n_{\text{Mo}}$

Size :  $(n_{\text{Fe}} + n_{\text{Mo}})$

Phase diagram variables: T, P,  $n_{\text{Mo}}/(n_{\text{Fe}} + n_{\text{Mo}}) = X_{\text{Mo}}$

System Fe-Cr-S<sub>2</sub>-O<sub>2</sub> (Fig. 6):

$$\phi_i : \underline{T} \quad \underline{P} \quad \mu_{\text{Fe}} \quad \mu_{\text{Cu}} \quad \underline{\mu_{\text{S}_2}} \quad \underline{\mu_{\text{O}_2}}$$

$$q_i : \underline{S} \quad -V \quad \underline{n_{\text{Fe}}} \quad \underline{n_{\text{Cu}}} \quad n_{\text{S}_2} \quad n_{\text{O}_2}$$

$$\text{Size} : (n_{\text{Fe}} + n_{\text{Cu}})$$

$$\text{Phase diagram variables: } T, P, \mu_{\text{O}_2}, \mu_{\text{S}_2}, n_{\text{Cr}} / (n_{\text{Fe}} + n_{\text{Cr}})$$

System Zn-Mg-Al isopleth (Fig. 3a):

$$\phi_i : \underline{T} \quad \underline{P} \quad \mu_{\text{Zn}} \quad \mu_{\text{Mg}} \quad \mu_{\text{Al}}$$

$$q_i : \underline{S} \quad -V \quad \underline{n_{\text{Zn}}} \quad \underline{n_{\text{Mg}}} \quad \underline{n_{\text{Al}}}$$

$$\text{Size} : (n_{\text{Mg}} + n_{\text{Al}})$$

$$\text{Phase diagram variables: } T, P, n_{\text{Al}} / (n_{\text{Mg}} + n_{\text{Al}}), n_{\text{Zn}} / (n_{\text{Mg}} + n_{\text{Al}}) = X_{\text{Zn}} / (1 - X_{\text{Zn}})$$

System Al<sub>2</sub>SiO<sub>5</sub> (Fig. 7b):

$$\phi_i : \underline{T} \quad \underline{P} \quad \mu_{\text{Al}_2\text{SiO}_5}$$

$$q_i : \underline{S} \quad -V \quad \underline{n_{\text{Al}_2\text{SiO}_5}}$$

$$\text{Size} : n_{\text{Al}_2\text{SiO}_5}$$

$$\text{Phase diagram variables: } T, V / n_{\text{Al}_2\text{SiO}_5}$$

System Cu-Ni-S<sub>2</sub> (Fig. 37):

$$\phi_i : \underline{T} \quad \underline{P} \quad \mu_{\text{Cu}} \quad \mu_{\text{Ni}} \quad \underline{\mu_{\text{S}_2}}$$

$$q_i : \underline{S} \quad -V \quad \underline{n_{\text{Cu}}} \quad \underline{n_{\text{Ni}}} \quad n_{\text{S}_2}$$

$$\text{Size} : (n_{\text{Cu}} + n_{\text{Ni}})$$

$$\text{Phase diagram variables: } T, P, \mu_{\text{S}_2}, n_{\text{Ni}} / (n_{\text{Cu}} + n_{\text{Ni}})$$

This choice of variables for the Cu-Ni-S<sub>2</sub> system gives the single-valued phase diagram in Fig. 37. For the same system in Fig. 36 an incorrect choice of variables was made, leading to a diagram which is not single-valued. The x-axis variable of Fig. 36 contains the term  $n_{\text{S}_2}$ . That is, both variables ( $\mu_{\text{S}_2}, n_{\text{S}_2}$ ) of the same corresponding pair were

selected, thereby violating the first selection rule. Similarly, the selection of both variables ( $P$ ,  $-V$ ) from the same corresponding pair results in the diagram of Fig. 35 which is not single-valued. Similar examples of phase diagrams which are not single-valued have been shown by Hillert (1997).

Other examples of applying the procedure for choosing variables will be given in Secs. 7.8 to 7.10.

In several of the phase diagrams in this chapter,  $\log p_i$  or  $RT \ln p_i$  is substituted for  $\mu_i$  as an axis variable or constant. From Eq. (86), this substitution can clearly be made if  $T$  is constant. However, even when  $T$  is an axis variable of the phase diagram as in Fig. 10 this substitution is still permissible since  $\mu_i^\circ$  is a monotonic function of  $T$ . The substitution of  $\log p_i$  or  $RT \ln p_i$  for  $\mu_i$  results in a progressive expansion and displacement of the axis with increasing  $T$  that preserves the overall geometry of the diagram.

## 7.6 Corresponding Phase Diagrams

If a potential axis,  $\phi_i$ , of a phase diagram section is replaced by its normalized conjugate variable  $q_i$ , then the new diagram and the original diagram may be said to be *corresponding phase diagrams*. An example is seen in Fig. 7, where the  $P$ -axis of Fig. 7a is replaced by the  $V$ -axis of Fig. 7b. Another example is shown in Fig. 38 for the Fe-O system. Placing corresponding diagrams beside each other as in Figs. 7 and 38 is useful because the information contained in the two diagrams is complementary. Note how the invariant triple points of one diagram of each pair correspond to the invariant lines of the other. Note also that as  $\phi_i$  increases,  $q_i$  increases. That is, in passing from left to right at constant  $T$  across the two diagrams in Fig. 38, the same sequence of phase regions is encountered. This is a general result of the thermodynamic stability criterion which will be discussed in Sec. 7.7.

A set of corresponding phase diagrams for a multicomponent system with components 1,2,3,...,C is shown in Fig. 39. The potentials  $\phi_4, \phi_5, \dots, \phi_{C+2}$  are held constant. The size of the system (in the sense of Sec. 7.5) is  $q_3$ . The invariant triple points of Fig. 39b correspond to the invariant lines of Figs. 39a & d and to the invariant

tie-triangles of Fig. 39c. The *critical points* of Fig. 39b where the two-phase regions terminate correspond to the critical points of the “miscibility gaps” in Figs. 39b,c & d.

A set of corresponding phase diagrams for the Fe-Cr-O<sub>2</sub> system at  $T = 1300^{\circ}\text{C}$  is shown in Fig. 40. Fig. 40b is a plot of  $\mu_{\text{Cr}}$  versus  $\mu_{\text{O}_2}$ . Fig. 40a is similar to Fig. 5. Fig. 40c is a plot of  $n_{\text{O}}/(n_{\text{Fe}} + n_{\text{Cr}})$  versus  $n_{\text{Cr}}/(n_{\text{Fe}} + n_{\text{Cr}})$  where the size of the system is defined by  $(n_{\text{Fe}} + n_{\text{Cr}})$ . The coordinates of Fig. 40c are known as *Jänecke coordinates*. Fig. 40c may be “folded up” to give the more familiar isothermal ternary section of Fig. 40d plotted on the equilateral composition triangle.

### 7.6.1 Enthalpy-Composition Phase Diagrams

The  $T$ -composition phase diagram of the Mg-Si system is shown in Fig. 41a. A corresponding phase diagram could be constructed by replacing the  $T$ -axis by the molar entropy because  $(T,S)$  is a corresponding pair, although such a diagram would not be of much practical interest. However, just as  $(dS/dT) > 0$  at constant  $P$  and composition, so also is  $(dH/dT) > 0$ . Hence, an  $H$ -composition phase diagram will have the same geometry as an  $S$ -composition diagram. (This will be demonstrated more rigorously in Sec. 7.12.)

Fig. 41b is the enthalpy-composition phase diagram corresponding to the  $T$ -composition diagram of Fig. 41a. The  $y$ -axis is  $(h - h_{25})$  where  $h_{25}$  is the molar enthalpy of the system in equilibrium at  $25^{\circ}\text{C}$ . Referencing the enthalpy to  $h_{25}$  slightly distorts the geometry of the diagram because  $h_{25}$  is a function of composition. In particular, the tie-lines are no longer necessarily perfectly straight lines. However, this choice of reference renders the diagram more practically useful since the  $y$ -axis variable then directly gives the heat which must be added, or removed, to heat, or cool, the system between  $25^{\circ}\text{C}$  and any temperature  $T$ . The isothermal lines shown on Fig. 41b are not part of the phase diagram but have been calculated and plotted to make the diagram more useful. It should be stressed that Fig. 41b is a phase diagram section obeying all the geometrical rules of phase diagram sections discussed in Secs. 7.1 to 7.4. It consists of ZPF lines and can be calculated using the same algorithm as for any other phase diagram section as discussed in Sec. 7.4.1. Note that the three-phase tie-triangles are isothermal.

Another  $H$ -composition phase diagram is shown in Fig. 3b for the Zn-Mg-Al system along the isoplethal section where  $X_{Zn} = 0.1$ .

## 7.7 The Thermodynamics of General Phase Diagram Sections

This section provides a more rigorous derivation of the geometry of general phase diagram sections which was discussed in Secs. 7.2 to 7.6.

In Sec. 2.8.2, a general auxiliary function  $G'$  was introduced. Let us now define an even more general auxiliary function,  $B$ , as follows:

$$B = U - \sum_{i=1}^m \phi_i q_i \quad 0 \leq m \leq (C+2) \quad (154)$$

where the  $\phi_i$  and  $q_i$  include all corresponding pairs in Table 1. (If  $m = 0$ , then  $B = U$ ). Following the same reasoning as in Sec. 2.8.2, we obtain for a system at equilibrium:

$$dB = - \sum_1^m q_i d\phi_i + \sum_{m+1}^{C+2} \phi_i dq_i \quad (155)$$

and the equilibrium state at constant  $\phi_i$  ( $0 \leq i \leq m$ ) and  $q_i$  ( $m+1 \leq i \leq C+2$ ) is approached by minimizing  $B$ :

$$dB_{\phi_i(0 \leq i \leq m), q_i(m+1 \leq i \leq C+2)} \leq 0 \quad (156)$$

Fig. 42 is a plot of the  $\phi_1$ - $\phi_2$ - $\phi_3$  surfaces of two phases,  $\alpha$  and  $\beta$ , in a  $C$ -component system when  $\phi_4, \phi_5, \dots, \phi_{C+2}$  are all held constant. For example, in a one-component system, Fig. 42 would be a plot of the  $P$ - $T$ - $\mu$  surfaces. Let us now choose a pair of values  $\phi_1$  and  $\phi_2$  and derive the condition for equilibrium. Since all potentials except  $\phi_3$  are now fixed, the appropriate auxiliary function, from Eqs. (154) and (70), is  $B = q_3 \phi_3$ . Furthermore, let us fix the size of the system by setting  $q_3$  constant. Then, from Eq. (156) the equilibrium state for any given pair of values of  $\phi_1$  and  $\phi_2$  is given by setting  $dB = q_3 d\phi_3 = 0$ , that is by minimizing  $\phi_3$ . This is illustrated on Fig. 42 where the base plane of the figure is the  $\phi_1$ - $\phi_2$  phase diagram of the system at constant  $\phi_4, \phi_5, \dots, \phi_{C+2}$ . For example, in a one-component system if  $\phi_1, \phi_2, \phi_3$  are  $P, T, \mu$  respectively, then the  $P$ - $T$  phase diagram is given by minimizing  $\mu$ , the molar Gibbs

energy of the system. Clearly therefore, a  $\phi_1$ - $\phi_2$  diagram at constant  $\phi_4, \phi_5, \dots, \phi_{C+2}$  is single-valued.

As another example, consider the  $T - \mu_{O_2}$  phase diagram of the Fe-O system at constant hydrostatic pressure in Fig. 38. The potentials of the system are  $T, P, \mu_{O_2}$  and  $\mu_{Fe}$ . At constant  $P$ , and for any given values of  $T$  and  $\mu_{O_2}$ , the equilibrium state of the system is given by minimizing  $\mu_{Fe}$ . Similarly, the predominance diagram of the Cu-SO<sub>2</sub>-O<sub>2</sub> system in Fig. 9 can be calculated by minimizing  $\mu_{Cu}$  which can be shown to be equivalent to the procedure described in Sec. 2.4.2.

A general  $\phi_1$ - $\phi_2$  phase diagram at constant  $\phi_4, \phi_5, \dots, \phi_{C+2}$  was shown in Fig. 39b. The size of the system is defined by fixing  $q_3$ . We wish now to show that, when Fig. 39b is “opened up” by replacing  $\phi_2$  by  $q_2$  to give the corresponding phase diagram in Fig. 39a, the sequence of phase regions encountered in moving horizontally across Fig. 39a is the same as in Fig. 39b. For example, when the two-phase ( $\alpha+\beta$ ) line in Fig. 39b is “opened” up to form the two-phase ( $\alpha+\beta$ ) region in Fig. 39a, the  $\alpha$  and  $\beta$  phases remain on the left and right sides respectively of the two-phase region.

We first derive the general *thermodynamic stability criterion* for a single phase region. Imagine two bordering microscopic regions, I and II, within a homogeneous phase and suppose that a local fluctuation occurs in which an amount  $dq_n > 0$  of the extensive property  $q_n$  is transferred from region I to region II at constant  $\phi_i (0 \leq i \leq m)$  and constant  $q_i (m+1 \leq i \leq C+2)$  where  $i \neq n$ . Suppose that, as a result of the transfer,  $\phi_n$  increases in region I and decreases in region II, that is that  $(d\phi_n/dq_n) < 0$ . A potential gradient is thus set up with  $\phi_n^I > \phi_n^{II}$ . From Eq.(155), further transfer of  $q_n$  from region I to II then results in a decrease in B:  $dB = (\phi_n^{II} - \phi_n^I) dq_n < 0$ . From Eq. (156), equilibrium is approached by minimizing B. Hence, the fluctuation grows, with continual transfer from region I to II. That is, the phase is unstable. Therefore, the criterion for a phase to be thermodynamically stable is:

$$d\phi_n/dq_n > 0 \quad (157)$$

for any choice of constant  $\phi_i$  or  $q_i$  constraints ( $i \neq n$ ). Since  $\phi_n = (\partial B / \partial q_n)$ , the stability criterion can also be written as:

$$\left(\partial^2 B / \partial q_n^2\right) \phi_{i(0 \leq i \leq m)}, q_{i(m+1 \leq i \leq C+2); i \neq n} > 0 \quad (158)$$

An important example is illustrated in Fig. 18 for the solid phase of the Au-Ni system. In this case, the appropriate auxiliary function is the Gibbs energy,  $G$ . In the central composition regions of the Gibbs energy curves in Fig. 18, between the spinodal points indicated by the letter  $s$ ,  $\left(\partial^2 G / \partial n_{Ni}^2\right)_{T, P, n_{Fe}} < 0$ . Hence, at compositions between the spinodal points, microscopic composition fluctuations will grow since this leads to a decrease in the total Gibbs energy of the system. Hence, the phase is unstable and phase separation can occur by spinodal decomposition as discussed in Chapter 7 of this volume. Other well-known examples of the stability criterion are  $(dT/dS) > 0$  (entropy increases with temperature), and  $(dP/d(-V)) > 0$  (pressure increases with decreasing volume).

Returning now to Fig. 39, it can be seen from Eq.(157) that moving horizontally across a single-phase region in Fig. 39b corresponds to moving in the same direction across the same region in Fig. 39a. Furthermore, in the two-phase ( $\alpha+\beta$ ) region, suppose that  $\phi_2$  is increased by an amount  $d\phi_2 > 0$  keeping all other potentials except  $\phi_3$  constant thereby displacing the system into the single-phase  $\beta$  region. From the Gibbs-Duhem equation (75):

$$d\phi_3^\alpha = -\left(q_2/q_3\right)^\alpha d\phi_2 \quad \text{and} \quad d\phi_3^\beta = -\left(q_2/q_3\right)^\beta d\phi_2 \quad (159)$$

Where  $(q_2/q_3)^\alpha$  and  $(q_2/q_3)^\beta$  are the values at the boundaries of the two-phase region.

Since, as has just been shown, the equilibrium state is given by minimizing  $\phi_3$ , it follows that:

$$d(\phi_3^\beta - \phi_3^\alpha) / d\phi_2 = (q_2/q_3)^\alpha - (q_2/q_3)^\beta < 0 \quad (160)$$

Hence, the  $\alpha$ -phase and  $\beta$ -phase region lie to the left and right respectively of the ( $\alpha + \beta$ ) region in Fig. 39a, and Fig. 39a is single-valued.

Since the stability criterion also applies when extensive variables are held constant, it can similarly be shown that when Fig. 39a is “opened up” by replacing the  $\phi_1$  axis by  $q_1/q_3$  to give Fig. 39c, the sequence of the phase regions encountered as the diagram is traversed vertically is the same as in Fig. 39a, and that Fig. 39c is single-valued. Finally, it can be shown that the phase diagrams will remain single-valued if a constant  $\phi_4$  is replaced by  $q_4/q_3$ . Fig. 39a, for example, is a section at constant  $q_4$  through a three-dimensional  $\phi_1$ - $\phi_4$ - $(q_2/q_3)$  diagram which may be “opened up” by replacing  $\phi_4$  by  $(q_4/q_3)$  to give a  $\phi_1$ - $(q_4/q_3)$ - $(q_2/q_3)$  diagram which is necessarily single-valued because of the stability criterion. Hence, sections through this diagram at constant  $(q_4/q_3)$  will also be single-valued.

Consider now the node in a general phase diagram section shown in Fig. 33. At any point on either phase boundary of the  $(\alpha_1 + \alpha_2 + \dots + \alpha_N)$  region, one additional phase,  $\beta$  or  $\gamma$ , becomes stable. Since there is no thermodynamic reason why more than one additional phase should become stable at exactly the same point, the Law of Adjoining Phase Regions is evident. These phase boundaries intersect at the node below which there must clearly be a region in which  $\beta$  and  $\gamma$  are simultaneously stable. If the x-axis of the diagram is an extensive variable, then this region will have a finite width since there is no thermodynamic reason for the  $\beta$ -phase to become unstable at exactly the same point as the  $\gamma$ -phase becomes stable. It then follows that exactly four boundaries meet at a node. Of course, if the x-axis is a potential variable, then the two phase boundaries of the  $(\alpha_1 + \alpha_2 + \dots + \alpha_N + \beta + \gamma)$  region will necessarily be coincident.

### 7.7.1 Schreinemakers' Rule

Schreinemakers' Rule (Schreinemakers, 1915; Pelton 1995), which was discussed in Sec. 7.4, will now be proven for the general case. Consider the point  $p$  on Fig. 33 which lies in the  $(\alpha_1 + \alpha_2 + \dots + \alpha_N + \gamma)$  region arbitrarily close to the node. If precipitation of  $\gamma$  were prohibited by kinetic constraints, point  $p$  would lie in the  $(\alpha_1 + \alpha_2 + \dots + \alpha_N + \beta)$  region since it lies below the dashed extension of the phase boundary line as shown on the figure. Let  $B$  be the appropriate auxiliary function. If

precipitation of  $\gamma$  is prohibited, then  $dB/dn^\beta$ , where  $dn^\beta$  is the amount of  $\beta$ -phase (of fixed composition) which precipitates. That is, precipitation of  $\beta$  decreases  $B$ . If  $\gamma$  is permitted to precipitate, then precipitation of  $\beta$  is prevented. Therefore:

$$\frac{d}{dn^\gamma} \left( \frac{dB}{dn^\beta} \right) > 0 \quad (161)$$

Since the order of differentiation does not matter:

$$\frac{d}{dn^\beta} \left( \frac{dB}{dn^\gamma} \right) > 0 \quad (162)$$

Hence, the extension of the other boundary of the  $(\alpha_1 + \alpha_2 + \dots + \alpha_N)$  region must pass into the  $(\alpha_1 + \alpha_2 + \dots + \alpha_N + \beta)$  region as shown on Fig. 33. Similarly it can be shown that if the extension of one boundary of the  $(\alpha_1 + \alpha_2 + \dots + \alpha_N)$  region passes into the  $(\alpha_1 + \alpha_2 + \dots + \alpha_N + \beta + \gamma)$  region then so must the extension of the other (Pelton, 1995).

## 7.8 Interpreting Oxide Phase Diagrams

Three phase diagrams for the Fe-Si-O<sub>2</sub> system are shown in Figs. 43 to 45. Diagrams of these types are often a source of confusion.

Fig. 43 is often called the “phase diagram of the Fe<sub>3</sub>O<sub>4</sub>-SiO<sub>2</sub> system”. However, it is not a binary phase diagram, nor is it a quasibinary phase diagram. Rather, it is an isoplethal section across the Fe<sub>3</sub>O<sub>4</sub>-SiO<sub>2</sub> join of the Fe-Si-O<sub>2</sub> composition triangle. As with any isoplethal section, tie-lines in Fig. 43 do not necessarily lie in the plane of the diagram. That is, the x-axis gives only the overall composition of the system, not the compositions of individual phases. The lever rule does not apply. In the scheme of Sec. 7.5, Fig. 43 is described as follows:

$$\phi_i: \quad \underline{T} \quad \underline{P} \quad \mu_{\text{Fe}_3\text{O}_4} \quad \mu_{\text{SiO}_2} \quad \mu_{\text{O}_2}$$

$$q_i: \quad \underline{S} \quad -V \quad \underline{n_{\text{Fe}_3\text{O}_4}} \quad \underline{n_{\text{SiO}_2}} \quad \underline{n_{\text{O}_2}}$$

$$\text{Size: } (n_{\text{Fe}_3\text{O}_4} + n_{\text{SiO}_2})$$

$$\text{Phase diagram variables: } T, P, n_{\text{SiO}_2} / (n_{\text{Fe}_3\text{O}_4} + n_{\text{SiO}_2}), n_{\text{O}_2} / (n_{\text{Fe}_3\text{O}_4} + n_{\text{SiO}_2})$$

with  $n_{\text{O}_2} / (n_{\text{Fe}_3\text{O}_4} + n_{\text{SiO}_2}) = 0$ . The components have been defined judiciously as  $\text{Fe}_3\text{O}_4\text{-SiO}_2\text{-O}_2$  rather than  $\text{Fe-Si-O}_2$ . While this is not necessary, it clearly simplifies the description.

Fig. 44 is often called the “ $\text{Fe}_2\text{O}_3\text{-SiO}_2$  phase diagram at constant  $p_{\text{O}_2}$ .” This diagram is actually a ternary section along a constant  $p_{\text{O}_2}$  line as shown schematically in Fig. 46. Note that the position of this line for any give  $p_{\text{O}_2}$  will vary with temperature. At lower temperatures the line approaches the  $\text{Fe}_2\text{O}_3\text{-SiO}_2$  join. Since  $p_{\text{O}_2}$  is the same in all phases at equilibrium, the compositions of all phases, as well as the overall composition, lie along the constant  $p_{\text{O}_2}$  line. Hence, Fig. 44 has the same topology as binary  $T$ -composition phase diagrams. All tie-lines lie in the plane of the diagram as illustrated on Fig. 46, and the lever rule applies. In the scheme of Sec. 7.5, Fig. 44 is described as:

$$\phi_i: \quad \underline{T} \quad \underline{P} \quad \mu_{\text{Fe}_2\text{O}_3} \quad \mu_{\text{SiO}_2} \quad \underline{\mu_{\text{O}_2}}$$

$$q_i: \quad \underline{S} \quad \underline{P} \quad \underline{n_{\text{Fe}_2\text{O}_3}} \quad \underline{n_{\text{SiO}_2}} \quad n_{\text{O}_2}$$

$$\text{Size: } (n_{\text{Fe}_2\text{O}_3} + n_{\text{SiO}_2})$$

$$\text{Phase diagram variables: } T, P, n_{\text{SiO}_2} / (n_{\text{Fe}_2\text{O}_3} + n_{\text{SiO}_2}), \mu_{\text{O}_2}$$

The phase boundary lines in Fig. 44 give the ratio  $n_{\text{SiO}_2} / (n_{\text{Fe}_2\text{O}_3} + n_{\text{SiO}_2})$  in the individual phases of the  $\text{Fe}_2\text{O}_3\text{-SiO}_2\text{-O}_2$  system at equilibrium. However they do not give the total composition of the phases which may be deficient in oxygen. That is, some of the Fe may be present in a phase as FeO. The diagram may also be visualized as a projection of the equilibrium phase boundaries from the  $\text{O}_2$ -corner of the composition triangle onto the  $\text{Fe}_2\text{O}_3\text{-SiO}_2$  join as illustrated in Fig. 46. From an experimental standpoint, the x-axis represents the relative amounts of an initial mixture

of Fe<sub>2</sub>O<sub>3</sub> and SiO<sub>2</sub> which was charged into the apparatus at room temperature and which was subsequently equilibrated with air at higher temperatures.

Fig. 45 is often called the “FeO-SiO<sub>2</sub> phase diagram at Fe saturation.” Usually this diagram is drawn without indicating the presence of Fe in each phase field, although metallic Fe is always present as a separate phase. The horizontal lines on Fig. 45 which indicate the allotropic transformation temperatures and melting point of Fe are also generally not drawn. Diagrams such as Fig. 45 are best regarded and calculated as isoplethal sections with excess Fe. Fig. 45 was calculated by the following scheme:

$$\phi_i : \underline{T} \quad \underline{P} \quad \mu_{\text{FeO}} \quad \mu_{\text{SiO}_2} \quad \mu_{\text{Fe}}$$

$$q_i : \underline{S} \quad -V \quad \underline{n_{\text{FeO}}} \quad \underline{n_{\text{SiO}_2}} \quad \underline{n_{\text{Fe}}}$$

$$\text{Size: } (n_{\text{FeO}} + n_{\text{SiO}_2})$$

$$\text{Phase diagram variables : } T, P, n_{\text{SiO}_2} / (n_{\text{FeO}} + n_{\text{SiO}_2}), n_{\text{Fe}} / (n_{\text{FeO}} + n_{\text{SiO}_2})$$

with  $n_{\text{Fe}} / (n_{\text{FeO}} + n_{\text{SiO}_2}) = 0.0001$ . That is, the components of the system have been defined as FeO, SiO<sub>2</sub> and O<sub>2</sub> with a sufficient excess of Fe so as to always give a metallic phase at equilibrium. Note that the phase boundary compositions in Fig. 45 give only the ratio  $n_{\text{SiO}_2} / (n_{\text{FeO}} + n_{\text{SiO}_2})$  in each phase but not the total compositions of the phases which may contain an excess or a deficit of iron relative to the FeO-SiO<sub>2</sub> join. In this system the solubility of Si in Fe is very small, and so has a negligible effect on the phase diagram. However, in other systems such as Fe-Zn-O<sub>2</sub>, the equilibrium metal phase could actually contain more Zn than Fe, depending upon the conditions.

## 7.9 Choice of Components and Choice of Variables

As was discussed in Sec. 3, the components of a given system may be defined in different ways. A judicious selection can simplify the choice of variables for a phase diagram as has just been illustrated in Sec. 7.8. As another example, the selection of variables for the isothermal  $\log p_{\text{SO}_2} - \log p_{\text{O}_2}$  phase diagram of the Cu-SO<sub>2</sub>-O<sub>2</sub> system in Fig. 9 according to the scheme of Sec. 7.5 is clearly simplified if the components are formally selected as Cu-SO<sub>2</sub>-O<sub>2</sub> rather than, for example, as Cu-S-O.

In certain cases, different choices of variables can result in different phase

diagrams. For the same system as in Fig. 9 suppose that we wish to plot an isothermal predominance diagram with  $\log p_{\text{SO}_2}$  as y-axis but with  $\log a_{\text{Cu}}$  as the x-axis. The gas phase will consist principally of  $\text{O}_2$ ,  $\text{S}_2$  and  $\text{SO}_2$  species. As the composition of the gas phase varies at constant total pressure from pure  $\text{O}_2$  to pure  $\text{S}_2$ , the partial pressure of  $\text{SO}_2$  passes through a maximum where the gas phase consists mainly of  $\text{SO}_2$ . Therefore, for the phase diagram to be single-valued, the  $\log p_{\text{SO}_2}$  axis must encompass gaseous mixtures which consist either mainly of  $(\text{O}_2 + \text{SO}_2)$  or of  $(\text{SO}_2 + \text{S}_2)$ , but not both. Let us define the components as  $\text{Cu-SO}_2\text{-O}_2$  and choose the phase diagram variables as follows:

$$\begin{aligned} \phi_i &: \underline{T} \quad \underline{P} \quad \underline{\mu_{\text{Cu}}} \quad \underline{\mu_{\text{SO}_2}} \quad \underline{\mu_{\text{O}_2}} \\ q_i &: \underline{S} \quad -\underline{V} \quad \underline{n_{\text{Cu}}} \quad \underline{n_{\text{SO}_2}} \quad \underline{n_{\text{O}_2}} \end{aligned}$$

Size:  $n_{\text{O}_2}$

Phase diagram variables:  $T, P, \mu_{\text{Cu}}, \mu_{\text{SO}_2}, n_{\text{O}_2}$

As  $p_{\text{SO}_2}$  increases at constant  $T, P$  and  $n_{\text{O}_2}$ ,  $p_{\text{O}_2}$  decreases while  $p_{\text{S}_2}$  always remains small. The phase diagram then essentially encompasses only the  $\text{Cu-SO}_2\text{-O}_2$  subsystem of the  $\text{Cu-S}_2\text{-O}_2$  system. A phase field for  $\text{Cu}_2\text{O}$  will appear on the diagram, for example, but there will be no field for  $\text{Cu}_2\text{S}$ . If, on the other hand, we choose the components as  $\text{Cu-SO}_2\text{-S}_2$  with the size of the system defined as  $n_{\text{S}_2} = \text{constant}$ , then  $p_{\text{S}_2}$  varies along the  $p_{\text{SO}_2}$  axis while  $p_{\text{O}_2}$  always remains small. The phase diagram then encompasses only the  $\text{Cu-SO}_2\text{-S}_2$  subsystem. A phase field for  $\text{Cu}_2\text{S}$  appears, but there will be no field for  $\text{Cu}_2\text{O}$ .

This example serves to illustrate again how the procedure for choosing variables given in Sec. 7.5 provides sufficient conditions for a phase diagram to be single-valued.

## 7.10 Phase Diagrams of Reciprocal Systems

A section at  $T = 750^\circ\text{C}$  and  $P = 1.0$  bar of the *reciprocal salt system*  $\text{NaCl-CaCl}_2\text{-NaF-CaF}_2$  is shown in Fig. 47. A reciprocal salt system is one consisting of two or more cations and two or more anions. Since excess  $\text{Na}, \text{Ca}, \text{F}$  and  $\text{Cl}$  are virtually insoluble

in the ionic salts, this system is, to a very close approximation, a quasi-ternary isoplethal section of the Na-Ca-Cl-F system in which:

$$(n_F + n_{Cl}) = (2n_{Ca} + n_{Na}) \quad (163)$$

That is, the total cationic charge is equal to the total anionic charge. The compositions of all phases lie in the plane of the diagram and the lever rule applies.

The corners of the composition square in Fig. 47 represent the pure salts, while the edges of the square represent compositions in common-ion quasi-binary systems. The choice of phase diagram variables is most simply formulated, using the procedure of Sec. 7.5, as follows:

$$\begin{array}{l} \phi_i: \quad \underline{T} \quad \underline{P} \quad \mu_{Na} \quad \mu_{Ca} \quad \mu_F \quad \mu_{Cl} \\ q_i: \quad \underline{S} \quad -V \quad \underline{n_{Na}} \quad \underline{n_{Ca}} \quad \underline{n_F} \quad \underline{n_{Cl}} \end{array}$$

$$\text{Size: } (n_F + n_{Cl}) = (2n_{Ca} + n_{Na})$$

Phase diagram variables :

$$T, P, n_F/(n_F + n_{Cl}), 2n_{Ca}/(2n_{Ca} + n_{Na}), (2n_{Ca} + n_{Na})/(n_F + n_{Cl}) = 1$$

The axis variables of Fig. 47 are sometimes called “equivalent ionic fractions” in which the number of moles of each ion is weighted by its absolute charge. (Note that if Na, Ca, F or Cl were actually significantly soluble in the salts, the diagram could still be plotted as in Fig. 47, but it would then no longer be a quasi-ternary section and tie-lines would not necessarily lie in the plane of the diagram, nor would the lever rule apply).

## 7.11 Choice of Variables to Ensure Straight Tie-lines

Fig. 47 could be drawn with the axis variables chosen instead as  $n_F/(n_F + n_{Cl})$  and  $n_{Ca}/(n_{Ca} + n_{Na})$ , that is as molar ionic fractions rather than equivalent ionic fractions.

In this case, the diagram would be a distorted version of Fig. 47, but would still be a valid phase diagram obeying all the geometrical rules. However, tie-lines in two-phase regions would no longer be straight lines. That is, a straight line joining the compositions of two phases at equilibrium would not pass through the overall composition of the system. It is clearly desirable from a practical standpoint that tie-lines be straight.

It can be shown, through simple mass balance considerations (Pelton and

Thompson, 1975) that the tie-lines of a phase diagram in which both axes are composition variables will only be straight lines if the denominators of the two composition variable ratios are the same. This is the case in Fig. 47 where the denominators are the same because of the condition of Eq.(163). For another example, see Fig. 39c, d. It can thus be appreciated that the procedure of Sec. 7.5 provides a sufficient condition for tie-lines to be straight by the stratagem of normalizing all composition variables with respect to the same system “size.”

It can also be shown (Pelton and Thompson, 1975) that ternary phase diagram sections plotted on a composition triangle always have straight tie-lines.

## 7.12 Other Sets of Corresponding Variable Pairs

The set of corresponding variable pairs in Table 1, Sec. 7.1 is only one of several possible sets.

Substituting  $S$  from Eq. (71) into the Gibbs-Duhem equation (75) and rearranging terms yields:

$$-Hd(1/T) - (V/T)dP + \sum n_i d(\mu_i / T) = 0 \quad (164)$$

Hence, another set of corresponding variable pairs is that given in Table 2.

With this set of conjugate variable pairs replacing those in Table 1, the same procedure as described in Sec. 7.5 can be used to choose variables to construct single-valued phase diagrams. For example, the procedure for the  $H$ -composition phase diagram in Fig. 41b is as follows:

$$\begin{array}{l} \phi_i : \quad 1/T \quad P \quad \mu_{Mg} / T \quad \mu_{Si} / T \\ q_i : \quad \underline{-H} \quad \underline{-V/T} \quad \underline{n_{Mg}} \quad \underline{n_{Si}} \end{array}$$

$$\text{Size: } (n_{Mg} + n_{Si})$$

Phase diagram variables:  $H, P, n_{Mg} / (n_{Mg} + n_{Si})$

This demonstrates that Fig. 41b is, in fact, a single-valued phase diagram. Although in this particular case an  $S$ -composition phase diagram would also be single-valued, and very similar in form to Fig. 41b,  $H$  cannot simply be substituted for  $S$  in Table 1 in all

cases.

Many other sets of conjugate variable pairs can be obtained through appropriate thermodynamic manipulation. The set shown in Table 2 and many other such sets have been discussed by Hillert (1997). For example,  $(-A/T, T/P), (-TU/P, 1/T), (\mu_i/T, n_i)$  is one such set. In conjunction with the selection rules of Sec. 7.5, all these sets of conjugate pairs can be used to construct single-valued phase diagram sections. However, these diagrams would probably be of very limited practical utility.

### **7.13 Extension Rules for Polythermal Projections**

An extension rule for the univariant lines on polythermal projections is illustrated on Fig. 27 at point A. At any intersection point of three univariant lines, the extension of each univariant line passes between the other two. The proof, although straightforward, is rather lengthy and so will not be reproduced here.

## **8 *Thermodynamic Databases for the Computer Calculation of Phase Diagrams***

As discussed in Sec. 1, the last 25 years have witnessed a rapid development of large evaluated optimized thermodynamic databases and of software which accesses these databases to calculate phase diagrams by Gibbs energy minimization.

The databases for multicomponent solution phases are prepared by first developing an appropriate mathematical model, based upon the structure of the solution, which gives the thermodynamic properties as functions of temperature and composition for every phase of a system. Next, all available thermodynamic data (calorimetric data, activity measurements, etc.) and phase equilibrium data from the literature for the entire system are evaluated and simultaneously “optimized” to obtain one set of critically-evaluated self-consistent parameters of the models for all phases in two-component, three-component and, if available, higher-order systems. Finally, the models are used to estimate the properties of multicomponent solutions from the databases of parameters of lower-order subsystems. Recently, experimental data are being supplemented by “virtual data” from first principles calculations. For a review, see Turchi et al, 2007.

The optimized model equations are consistent with thermodynamic principles and with theories of solutions. The phase diagrams can be calculated from these thermodynamic equations, and so one set of self-consistent equations describes simultaneously all the thermodynamic properties and the phase diagrams. This technique of analysis greatly reduces the amount of experimental data needed to fully characterize a system. All data can be tested for internal consistency. The data can be interpolated and extrapolated more accurately. All the thermodynamic properties and the phase diagram can be represented and stored by means of a relatively small set of coefficients.

This technique permits the estimation of phase diagrams of multicomponent systems based only upon data from lower-order subsystems and allows any desired phase diagram section or projection to be calculated and displayed rapidly. In Fig. 48 is a calculated phase diagram section for a 6-component system which might be of interest in the design of new Mg alloys. This diagram was calculated on a laptop computer in approximately 2 minutes. Hence, many sections of a multicomponent system can be quickly generated for study.

The computer calculation of phase diagrams present many advantages. For example, metastable phase boundaries can be readily calculated by simply removing one or more stable phases from the calculation. An example is shown in Fig. 49 where the metastable liquid miscibility gap was calculated. Other metastable phase boundaries such as the extension of a liquidus below the eutectic temperature can be calculated similarly. Another advantage is the possibility of calculating phase compositions at points on an isoplethal section. For instance, compositions of individual phases at equilibrium cannot be read directly from Fig. 48. However, with the calculated diagram on the computer screen, and with appropriate software (see FactSage), one can simply place the cursor at any desired point on the diagram and “click” in order to calculate the amounts and compositions of all phases in equilibrium at that point. Other software can follow the course of equilibrium cooling or of non-equilibrium “Scheil-Gulliver cooling” as will be discussed in Sec 9. And, of course, the thermodynamic databases permit the calculation of chemical potentials which are essential for calculating kinetic phenomena such as diffusion. Coupling thermodynamic

databases and software with databases of diffusion coefficients and software for calculating diffusion (as with the DICTRA program of ThermoCalc (see ThermoCalc)) provides a powerful tool for the study of the heat treatment of alloys for instance.

Among the largest integrated database computing systems with applications in metallurgy and material science are ThermoCalc, FactSage, MTDATA and Pandat. (see list of websites). These systems all combine large evaluated and optimized databases with advanced Gibbs energy minimization software. As well, the SGTE group (See SGTE) has developed a large database for metallic systems.

All these databases are extensive. For example, the SGTE alloy database contains optimized data for 78 components, involving hundreds of solution phases and stoichiometric compounds, 350 completely assessed and optimized binary systems and 120 optimized ternary systems. Equally extensive optimized databases have been developed for systems of oxides, salts, etc.

It is beyond the scope of this chapter to give a detailed account of the techniques of thermodynamic evaluation, optimization and modeling. The following sections are intended only to provide a general idea of what is involved in order to permit an appreciation of the advantages of the technique and of its limitations.

## 8.1 Thermodynamic/Phase Diagram Optimization of a Binary System

As a simple example of the optimization/evaluation of a binary system, we shall consider the Cd-Na system. The phase diagram, with points measured by several authors (Mathewson, 1906; Kurnakow and Kusnetzow, 1907; Weeks and Davies, 1964) is shown in Fig. 49. From electromotive force measurements on alloy concentration cells, several authors have measured the activity coefficient of Na in liquid alloys. The data are shown in Fig. 50 at 400°C. From the temperature dependence of  $\mu_{Na}^E = RT \ln \gamma_{Na}$ , the partial enthalpy of Na in the liquid was obtained via Eq. (114). The results are shown in Fig. 51. Also,  $h^E$  of the liquid has been measured by Kleinstuber (1961) by direct calorimetry.

The system contains four solid phases, Cd, Na, Cd<sub>11</sub>Na<sub>2</sub> and Cd<sub>2</sub>Na, which are all assumed to be stoichiometric compounds. We seek expressions for the Gibbs energy of

every solid phase and the liquid phase as functions of  $T$  and, in the case of the liquid, of composition. An expression for the Gibbs energy of a phase as a function of  $T$  and composition constitutes a complete thermodynamic description of the phase, since all other thermodynamic properties can be calculated from  $G$  by taking the appropriate derivatives.

For pure solid elemental Cd,  $h_{298}^{\circ} = 0.0$  by convention. From third law measurements (see Sec 2.5.3)  $s_{298}^{\circ} = 51.800 \text{ J mol}^{-1}\text{K}^{-1}$  (see SGTE). The heat capacity has been measured as a function of  $T$  and can be represented by the empirical equation:

$$c_p = 22.044 + 0.012548 T + 0.139 (10^5) T^{-2} \quad \text{J mol}^{-1}\text{K}^{-1} \quad (165)$$

Hence, from Eqs.(18, 19, 57), the following expression is obtained for the molar Gibbs energy of solid Cd:

$$\mu_{\text{Cd}}^{o(s)} = -7083 + 99.506 T - 6.274(10^{-3})T^2 - 6966 T^{-1} - 22.044 T \ln T \quad \text{J mol}^{-1} \quad (166)$$

(where  $T$  is in kelvins). A similar expression is obtained for  $\mu_{\text{Na}}^{o(s)}$ . The Gibbs energies of  $\text{Cd}_{11}\text{Na}_2$  and  $\text{Cd}_2\text{Na}$  have not been measured and are obtained from the optimization procedure.

We now require an expression for the Gibbs energy of the liquid phase. From Eqs. (88, 107, 111):

$$g^l = X_{\text{Cd}} \mu_{\text{Cd}}^{o(l)} + X_{\text{Na}} \mu_{\text{Na}}^{o(l)} + RT(X_{\text{Cd}} \ln X_{\text{Cd}} + X_{\text{Na}} \ln X_{\text{Na}}) + (h^E - Ts^E) \quad (167)$$

Expressions similar to Eq. (166) can be obtained for  $\mu_{\text{Cd}}^{o(l)}$  and  $\mu_{\text{Na}}^{o(l)}$  from measurements of the melting points, enthalpies of fusion and heat capacities of the liquid phase of the pure elements. For many simple binary substitutional solutions, good representations of  $h^E$  and  $s^E$  are obtained by expanding the functions as polynomials in the mole fractions  $X_A$  and  $X_B$  of the components:

$$h^E = X_A X_B [h_0 + h_1(X_B - X_A) + h_2(X_B - X_A)^2 + h_3(X_B - X_A)^3 + \dots] \quad (168)$$

$$s^E = X_A X_B [s_0 + s_1(X_B - X_A) + s_2(X_B - X_A)^2 + s_3(X_B - X_A)^3 + \dots] \quad (169)$$

where the  $h_i$  and  $s_i$  are empirical parameters to be obtained during optimization. As many parameters are used as are required to represent the data in a given solution. For

most solutions it is a good approximation to assume that the coefficients  $h_i$  and  $s_i$  are independent of temperature.

If the series are truncated after the first term, then:

$$g^E = h^E - Ts^E = X_A X_B (h_0 - Ts_0) \quad (170)$$

This is the equation for a regular solution discussed in Sec. 5.5. Hence, the polynomial representation can be considered to be an extension of regular solution theory. When the expansions are written in terms of the composition variable  $(X_B - X_A)$ , as in Eqs. (168) and (169), they are said to be in *Redlich-Kister form*.

Differentiation of Eqs. (168) and (169) and substitution into Eqs (116) and (114) yields the following expansions for the partial excess enthalpies and entropies:

$$h_A^E = X_B^2 \sum_{i=0} h_i \left[ (X_B - X_A)^i - 2iX_A (X_B - X_A)^{i-1} \right] \quad (171)$$

$$h_B^E = X_A^2 \sum_{i=0} h_i \left[ (X_B - X_A)^i + 2iX_B (X_B - X_A)^{i-1} \right] \quad (172)$$

$$s_A^E = X_B^2 \sum_{i=0} s_i \left[ (X_B - X_A)^i - 2iX_A (X_B - X_A)^{i-1} \right] \quad (173)$$

$$s_B^E = X_A^2 \sum_{i=0} s_i \left[ (X_B - X_A)^i + 2iX_B (X_B - X_A)^{i-1} \right] \quad (174)$$

Eqs. (168), (169) and (171) to (174) are linear in terms of the coefficients. Through the use of these equations, all integral and partial excess properties ( $g^E$ ,  $h^E$ ,  $s^E$ ,  $\mu_i^E$ ,  $h_i^E$ ,  $s_i^E$ ) can be expressed by linear equations in terms of the one set of coefficients  $\{h_i, s_i\}$ . It is thus possible to include all available experimental data for a binary phase in one simultaneous linear optimization.

Several algorithms have been developed to perform such optimizations using least-squares, Bayesian, and other techniques. See, for example, Bale and Pelton (1983), Lukas et al (1977), Dörner et al (1980) and Königsberger and Eriksson (1995).

All the data points shown in Fig. 49 to 51 along with the enthalpy of mixing data for the liquid (Kleinstuber, 1961) were optimized in one simultaneous operation

(Pelton, 1988) to obtain the following expressions for  $h^E$  and  $s^E$  of the liquid:

$$h^{E(l)} = X_{\text{Cd}}X_{\text{Na}} \left[ -12508 + 20316(X_{\text{Na}} - X_{\text{Cd}}) - 8714(X_{\text{Na}} - X_{\text{Cd}})^2 \right] \text{ J mol}^{-1} \quad (175)$$

$$s^{E(l)} = X_{\text{Cd}}X_{\text{Na}} \left[ \begin{array}{l} -15.452 + 15.186(X_{\text{Na}} - X_{\text{Cd}}) \\ -10.062(X_{\text{Na}} - X_{\text{Cd}})^2 - 1.122(X_{\text{Na}} - X_{\text{Cd}})^3 \end{array} \right] \text{ J mol}^{-1} \text{ K}^{-1} \quad (176)$$

During the same simultaneous optimization procedure the optimized Gibbs energies of fusion of the two compounds were determined:

$$\Delta g_{f(1/13 \text{ Cd}_{11}\text{Na}_2)}^{\circ} = 6816 - 10.724T \quad \text{J mol}^{-1} \quad (177)$$

$$\Delta g_{f(1/3 \text{ Cd}_2\text{Na})}^{\circ} = 8368 - 12.737T \quad \text{J mol}^{-1} \quad (178)$$

The above equations can be combined to give the Gibbs energies of formation of the two compounds from the solid elements. (See Fig. 21 for an illustration of the relation between the Gibbs energy of formation and the Gibbs energy of fusion of a compound.)

Eq. (175) reproduces the calorimetric data within  $200 \text{ J mol}^{-1}$ . Eqs. (114), (119), (172) and (174) can be used to calculate  $h_{\text{Na}}^E$  and  $\gamma_{\text{Na}}$ . The calculated curves are compared to the measured points in Figs. 50 and 51. The optimized enthalpies of fusion of the compounds of  $6816$  and  $8368 \text{ J mol}^{-1}$  agree within error limits with the values of  $6987$  and  $7878 \text{ J mol}^{-1}$  measured by Roos (1916).

The phase diagram in Fig. 49 was calculated from the optimized thermodynamic expressions. Complete details of the analysis of the Cd-Na system are given by Pelton (1988).

It can thus be seen that one simple set of equations can simultaneously and self-consistently describe all the thermodynamic properties and the phase diagram of a binary system.

The exact optimization procedure will vary from system to system depending upon the type and accuracy of the available data, the number of phases present, the extent of solid solubility, etc. A large number of optimizations have been published since 1977 in the *Calphad Journal* (Pergamon).

## 8.2 Solution Models

As discussed in Sec. 8.1, the polynomial model, Eqs. (168, 169), is an extension of regular solution theory (Sec. 5.5). Hence, the polynomial model can be expected to provide an acceptable description of the properties of a solution only if the physical assumptions of regular solution theory are approximately valid, that is if the solution is approximately a random substitutional solution of atoms or molecules on a single sublattice with relatively weak interactions.

### 8.2.1 Short-Range-Ordering (sro) and the Quasichemical Model

Consider a binary solution of components A-B with a single sublattice (or quasilattice in the case of a liquid) and consider the formation of two nearest-neighbor A-B pairs from an A-A and a B-B pair by the following “quasichemical reaction”:



Let the molar Gibbs energy change for this reaction be  $(\omega - \eta T)$ . This term has essentially the same interpretation in terms of bond energies as the regular solution parameter as in Eqs (136) to (138).

If  $(\omega - \eta T)$  is negative, then reaction (179) is displaced to the right, and at equilibrium the fraction of (A – B) pairs will be greater than in an ideal randomly mixed solution. Conversely, if  $(\omega - \eta T)$  is positive, reaction (179) is shifted to the left and clustering of A and B particles occurs; if it is sufficiently positive, a miscibility gap will be observed. This short-range-ordering (sro) can be modeled by the quasichemical model in the pair approximation (Guggenheim, 1935; Fowler and Guggenheim, 1939) which has been modified by Pelton and Blander (1984) and Blander and Pelton (1987). For the most recent and complete development of the modified quasichemical model (MQM) in the pair approximation, see Pelton et al. (2000) and Pelton and Chartrand (2001a).

In the MQM, expressions for the enthalpy and entropy of a solution are written in terms of the numbers of (A – A), (B – B) and (A – B) pairs. The expression for the entropy is obtained via the Helmholtz equation (2) by randomly distributing the pairs over pairs of lattice sites rather than by distributing the atoms or molecules over lattice

sites as in the regular solution theory. The parameter of the model,  $(\omega - \eta T)$ , can be expanded as an empirical polynomial in the component mole fractions similar to Eqs. (168, 169) or as a polynomial in the pair fractions. The numbers of each type of pair at equilibrium are then obtained by minimizing the Gibbs energy. This results in an equilibrium constant for the quasichemical reaction (179). In the limit as  $(\omega - \eta T)$  approaches zero, the MQM and the polynomial model become identical (Pelton et al, 2000). When  $(\omega - \eta T)$  differs significantly from zero, the shapes of the curves of  $h^E$  and  $s^E$  versus composition predicted by the MQM differ significantly from the approximately parabolic shape (Eq. (133)) predicted by the polynomial model, and generally correspond more closely to experimental data. The MQM has been used successfully (see FactSage) to model a large number of solutions, particularly liquid solutions, of metals, salts, sulfides and oxides.

Quasichemical theory has been further extended beyond the pair approximation to account for clusters of more than two particles. This model is known as the Cluster Variation Method (CVM). For a review of the CVM, see Inden (2001). A somewhat simplified version of the CVM, which is mathematically more tractable, is the Cluster Site Approximation (CSA) proposed by Oates and Wenzl (1996); see also Inden (2001).

### **8.2.2 Long-Range-Ordering (lro) and Sublattice Models**

Long-range-ordering (lro) is generally treated by models which involve two or more sublattices. Ionic salts, for example, are modeled with one sublattice for cations and another for anions. As another example, in the spinel structure of certain ceramic oxides, the oxygen ions occupy one sublattice while some metal ions are distributed on a second sublattice with tetrahedral coordination and other metal ions are distributed on a third sublattice with octahedral coordination. Intermetallic solutions, such as Laves phases, are described by sublattice models. Interstitial solutions are modeled by introducing an interstitial sublattice on which some sites are occupied while others are vacant. Non-stoichiometric compounds  $A_xB_y$  with a range of homogeneity, as for example the compounds  $\beta'$  and  $\varepsilon$  in Fig. 22, are modeled as containing point defects such as substitutional defects (some A atoms on B-sublattice sites and B atoms on A-

sublattice sites), interstitial atoms, or vacancies on one or more sublattices.

The simplest implementation of sublattice modeling is the Compound Energy Formalism (CEF) (Barry et al., 1992; Hillert, 2008) in which species are distributed randomly over each sublattice. The parameters of the model are, essentially, the site energies for the species on the different sublattices and the interaction energies between pairs of species on different sublattices and on the same sublattice. The equilibrium distribution of species among the sublattices is calculated as that which minimizes the Gibbs energy of the solution. The CEF has been applied successfully to model a very large number of solutions of metals, salts, oxides, sulfides, etc.

The CEF model accounts for lro, but not for sro. In some solutions a satisfactory representation of the properties can only be obtained by modeling both lro and sro simultaneously. The CVM and CSA models permit this, as does an extension of the MQM to systems with two sublattices (Pelton and Chartrand, 2001b). An approximate correction term for relatively small degrees of sro can also be added to the CEF equations (Hillert, 2008).

### **8.3 Estimating Thermodynamic Properties of Ternary and Multicomponent Solutions**

Among 70 metallic elements,  $70!/3!67! = 54740$  ternary systems and 916895 quaternary systems are formed. In view of the amount of work involved in measuring even one isothermal section of a relatively simple ternary phase diagram, it is very important to have a means of estimating ternary and higher-order phase diagrams.

For a solution phase in a ternary system with components A-B-C, one first performs evaluations/optimizations on the three binary subsystems A-B, B-C and C-A as discussed in Sec. 8.1 in order to obtain the binary model parameters. Next, the model is used, along with reasonable assumptions, to estimate the thermodynamic properties of the ternary solution.

Suppose that a phase, such as a liquid phase or an fcc phase, has been modeled in all three binary subsystems with the simple polynomial model of Eqs. (168, 169). The Gibbs energy of the ternary solution could then be estimated by the following equation

first suggested by Kohler (1960):

$$g^E = (1-X_A)^2 g_{B/C}^E + (1-X_B)^2 g_{C/A}^E + (1-X_C)^2 g_{A/B}^E \quad (180)$$

In this equation,  $g^E$  is the excess molar Gibbs energy at a composition point in the ternary liquid phase and  $g_{B/C}^E$ ,  $g_{C/A}^E$  and  $g_{A/B}^E$  are the excess Gibbs energies in the three binary systems at the same ratios  $X_B/X_C$ ,  $X_C/X_A$  and  $X_A/X_B$  as at the ternary point. If the ternary liquid phase as well as the three binary liquid phases are all regular solutions, then Eq. (180) is exact. In the general case, a physical interpretation of Eq. (180) is that the contribution to  $g^E$  from pair interactions between A and B species is constant at a constant ratio  $X_A/X_B$ , apart from the dilutive effect of the C species which is accounted for by the term  $(1-X_C)^2$  taken from regular solution theory.

Ternary phase diagrams estimated in this way are often quite acceptable. The agreement between the experimental and calculated diagrams can be markedly improved by the inclusion of one or more "ternary terms" with adjustable parameters in the interpolation equations for  $g^E$ . For example, ternary terms  $a_{ijk} X_A^i X_B^j X_C^k$  ( $i \geq 1$ ,  $j \geq 1$ ,  $k \geq 1$ ,) which are zero in all three binary subsystems, could be added to Eq. (180) and the values of the parameters  $a_{ijk}$  which gives the "best" fit to experimental ternary thermodynamic or phase equilibrium data could be found by optimization. This, of course, requires that ternary measurements be made, but only a few experimental points will generally suffice rather than the large number of measurements usually required for a fully experimental determination. In this way, the coupling of the thermodynamic approach with a few well chosen experimental measurements greatly reduces the experimental effort involved in determining multicomponent phase diagrams.

Other equations, similar to the Kohler equation (180) are often used to estimate the thermodynamic properties of ternary solutions from the model parameters of the binary subsystems when the polynomial model is used. For a discussion, and for extensions to estimating the thermodynamic properties of multicomponent solutions from binary and ternary model parameters, see Pelton (2001b). These equations, like

the Kohler equation, are based on the polynomial model which is an extension of regular solution theory, and they can only be expected to yield good estimates when the physical assumptions of the model are valid; that is when the solution can reasonably be approximated as a random substitutional solution on a single sublattice with relatively weak interactions. For more complex solutions, involving sro or lro, a good estimate can only be expected when a proper physical model is employed. Therefore, if the solution in question is a liquid with appreciable sro, a model which takes sro into account must be used for the multicomponent solution, including all three binary subsystems, even though it might be possible to force fit a binary solution with a simpler model such as the polynomial model. If the solution exhibits lro, then an appropriate sublattice model must be used. As an example of the prediction of ternary phase diagrams from optimized model parameters for the binary subsystems, the liquid phase of the Zn-Mg-Al system was modeled using the MQM, and binary model parameters were obtained by evaluation/optimization of the three binary subsystems (see FactSage). The thermodynamic properties of the ternary liquid phase were then estimated with the MQM by assuming that the binary parameters remain constant in the ternary solution along lines of constant  $X_{Zn}/X_{Mg}$ ,  $X_{Mg}/X_{Al}$  and  $X_{Al}/X_{Zn}$ . When the ternary liquidus projection was then calculated, based only on the binary parameters, a liquidus surface was calculated which deviates from that shown in Fig. 27 by no more than  $8^\circ$  and 2 mol %. Since experimental data are available for this system, they were used to evaluate one small ternary model parameter. The resultant calculated diagram in Fig. 27 agrees with the available experimental data within the experimental error limits.

Such agreement is not exceptional. Phase diagrams calculated from the best thermodynamic databases generally agree with experimental measurements within or nearly within experimental error limits. In this regard, it may be noted that estimating the properties of a  $C$ -component system from the optimized parameters of its  $(C - 1)$  component subsystems becomes increasingly more exact as  $C$  becomes larger. For example, if all the ternary subsystems of a four-component system have been experimentally investigated and optimized ternary model parameters have been obtained, then the estimation of the properties of the four-component solution are generally good.

For a general discussion of many solution models see Hillert (2008). A great many models and their applications have been published since 1977 in the *Calphad Journal* (Pergamon).

## 9 ***Equilibrium and Non-Equilibrium Solidification***

### 9.1 **Equilibrium Solidification**

The course of equilibrium solidification can be followed through the use of isoplethal sections, such as that for the 6-component Mg alloy shown in Fig. 48. Polythermal liquidus projections are also useful in this respect. Consider an alloy with composition 85 mol% Mg, 15 % Al and 5 % Zn at point *B* in Fig. 27. As this alloy is cooled at equilibrium, solid hcp Mg begins to precipitate at the liquidus temperature which is just below 500°C. The liquid composition then follows the crystallization path shown on Fig. 27 until it attains a composition on the univariant line. The liquid composition then follows the univariant line towards the point *P'* with co-precipitation of hcp and the gamma phase. (For a discussion of equilibrium crystallization paths, see Sec. 6.3.) At point *P'* a quasi-peritectic reaction occurs. All the foregoing information can be deduced from Fig. 27. However, from this diagram alone it is not possible to determine the amounts and compositions of the various phases at equilibrium because the extent of the solid solutions are not shown nor, for the same reason, is it possible to determine whether solidification is complete at the point *P'* or whether the liquid persists to lower temperatures.

However, with thermodynamic calculations, this information is readily obtained. Software is available, with tabular or graphical display, to calculate the amounts and compositions of every phase during equilibrium solidification as well as to display the sequence of reactions during solidification. In the current example, the reaction sequence, calculated using the FactSage software and databases is:

Liq. → hcp (498° to 405°C; bivariant)

Liq. → hcp +  $\gamma$  (405° to 364°C; univariant)



The solidification is calculated to terminate at  $364^{\circ}\text{C}$  with complete consumption of the liquid by the quasi-peritectic reaction. A graphical display of the calculated amounts of all phases during equilibrium cooling is shown in Fig. 52.

## 9.2 Non-Equilibrium Scheil-Gulliver Solidification

Throughout equilibrium cooling, every solid solution phase remains homogeneous with no concentration gradients. As was described in Sec. 3.1, during the equilibrium cooling of a Bi-Sb alloy (Fig. 11) with  $X_{\text{Sb}} = 0.6$ , the first solid precipitate appears at  $526^{\circ}\text{C}$  with a composition  $X_{\text{Sb}} = 0.89$ . As cooling continues, the composition of the solid phase follows the solidus to point  $D$  at which its composition is  $X_{\text{Sb}} = 0.60$ , and solidification terminates at  $349^{\circ}\text{C}$ . For all this to happen, diffusion must continually occur in the solid grains in order for their composition to remain uniform. Since solid state diffusion is a relatively slow process, equilibrium cooling conditions are realized only for very slow cooling rates.

Consider now the limiting case of extremely rapid cooling such that no diffusion whatsoever takes place in the solid phase. However, the liquid is still assumed to be homogeneous, and equilibrium is assumed at the solid/liquid interface. Consequently there will be a concentration gradient within the grains, with the concentration of Sb decreasing from a maximum of  $X_{\text{Sb}} = 0.89$  at the points of initial nucleation. When the temperature has decreased to  $349^{\circ}\text{C}$ , the concentration of Sb at the surface of the solid grains will be  $X_{\text{Sb}} = 0.60$ , but the average composition of the solid will lie between  $X_{\text{Sb}} = 0.60$  and  $X_{\text{Sb}} = 0.89$ . Hence, a liquid phase is still present at  $349^{\circ}\text{C}$  and will, in fact, persist down to the melting point of pure Bi,  $271.4^{\circ}\text{C}$ .

This limiting case is called *Scheil-Gulliver cooling*. As another example, consider the cooling of the hypothetical ternary liquid with composition at point  $b$  in Fig. 26. As discussed in Sec. 6.3, under equilibrium cooling conditions solidification terminates at point  $P$  where the liquid is completely consumed in the ternary peritectic reaction:



reactions (or any reactions involving solid reactants) cannot occur. Hence, the liquid continues to lower temperatures, its composition following the univariant lines past point  $P'_3$  to the ternary eutectic composition  $E_3$  where it is finally consumed in the ternary eutectic reaction. (The liquid does not follow the other path from  $P$  to  $P'_1$ , because tie-triangles  $\varepsilon\zeta X$ , where  $X$  is any point on the line  $PP'_1$ , do not contain the liquid composition at point  $P$ . That is,  $\varepsilon$  and  $\zeta$  cannot coprecipitate from a liquid of composition  $P$  because of mass balance considerations.)

Similarly, for the Zn-Mg-Al system it was shown in Sec. 9.1 that a liquid of initial composition at point  $B$  on Fig. 27, when cooled under equilibrium conditions, is completely consumed by the quasi-peritectic reaction at point  $P'$ . Under Scheil-Gulliver cooling conditions on the other hand, the liquid will continue to lower temperatures, following the univariant lines to the eutectic point  $E$ . The path followed by the composition of the liquid along the liquidus during precipitation of the primary hcp phase (shown by the small arrows on Fig. 27) will be different in the cases of equilibrium and Scheil-Gulliver cooling, as will the compositions and relative amounts of the phases at any temperature. The course of Scheil-Gulliver cooling is easily followed through thermodynamic calculations using the following algorithm. The temperature is reduced from the initial liquid state in incremental steps, typically of the order of  $1^\circ$  to  $10^\circ$ . At each step the equilibrium state is calculated and then all solid phases are removed from the calculation, leaving only the liquid which is then cooled by another incremental step and the process is repeated. At any temperature the amount and average composition of every phase can thereby be calculated and presented in tabular or graphical form similar to Fig. 52. The calculated (FactSage) reaction sequence in the present example is:

Liq.  $\rightarrow$  hcp (498° to 405°C; bivariant)

Liq.  $\rightarrow$  hcp +  $\gamma$  (405° to 364°C; univariant)

Liq.  $\rightarrow$  hcp + Phi (364° to 343°C; univariant)

Liq.  $\rightarrow$  hcp + Tau (343° to 341°C; univariant)

Liq.  $\rightarrow$  hcp + Tau + MgZn (341°C; invariant)

This reaction sequence may be compared to that given in Sec. 9.1 for equilibrium cooling of the same alloy.

### 9.3 General Nomenclature for Invariant and Other Reactions

As discussed in Sec. 5.9, in a binary isobaric temperature-composition phase diagram there are two possible types of invariant reactions: "eutectic-type" ( $\beta \rightarrow \alpha + \gamma$ ) and "peritectic type" ( $\alpha + \gamma \rightarrow \beta$ ). In a ternary system, there are "eutectic-type" ( $\alpha \rightarrow \beta + \gamma + \delta$ ), "peritectic-type" ( $\alpha + \beta + \gamma \rightarrow \delta$ ), and "quasi-peritectic-type" ( $\alpha + \beta \rightarrow \gamma + \delta$ ) invariants (Sec. 6.3). In a system of  $C$  components, the number of types of isobaric invariant reactions is equal to  $C$ . A reaction with one reactant, such as ( $\alpha \rightarrow \beta + \gamma + \delta$ ) is clearly a "eutectic-type" invariant reaction but in general there is no standard terminology. These reactions may be conveniently described according to the numbers of reactants and products (in the direction which occurs upon cooling). Hence the reaction ( $\alpha + \beta \rightarrow \gamma + \delta + \epsilon$ ) is a  $2 \rightarrow 3$  reaction; the reaction ( $\alpha \rightarrow \beta + \gamma + \delta$ ) is a  $1 \rightarrow 3$  reaction; and so on.

A similar terminology can be used for univariant, bivariant, etc. isobaric reactions. For example, a  $1 \rightarrow 2$  reaction ( $\alpha \rightarrow \beta + \gamma$ ) is invariant in a binary system, but univariant in a ternary system. The ternary peritectic-type  $3 \rightarrow 1$  reaction ( $\alpha + \beta + \gamma \rightarrow \delta$ ) is invariant in a ternary system, univariant in a quaternary system, bivariant in a quinary system, etc.

### 9.4 Quasi-Invariant Reactions

According to the Phase Rule, an invariant reaction occurs in a  $C$ -component system when  $(C + 1)$  phases are at equilibrium at constant pressure. Apparent exceptions are observed where an isothermal reaction occurs even though fewer than  $(C + 1)$  phases are present. However, these are just limiting cases.

An example was shown in Fig. 17. A liquid with a composition exactly at the

liquidus/solidus minimum in a binary system will solidify isothermally to give a single solid phase of the same composition. Similarly, at a maximum in a two-phase region in a binary system the liquid solidifies isothermally to give a single solid phase, as for example at the congruent melting points of the  $\beta'$  phase in Fig. 22 and of the  $\text{Ca}_2\text{SiO}_4$  and  $\text{CaSiO}_3$  compounds in Fig. 21. Such maxima are also associated with congruently melting compounds in ternary and higher-order systems as, for example, the compound  $\eta$  in Fig. 26.

In a ternary system, a minimum point may be observed on a univariant line as shown in Fig. 53. In this hypothetical system there are two solid phases, pure stoichiometric A and a solid solution of B and C in which A is only slightly soluble. The A-B and C-A binary subsystems thus have simple eutectic phase diagrams, while the B-C system resembles Fig. 11. A liquid with a composition at the minimum point  $m$  on the univariant line joining the two binary eutectic points  $e_1$  and  $e_2$  will solidify isothermally to give solid A and a solid solution of composition at point  $p$ . Point  $m$  is a local liquidus minimum, but the isothermal solidification at point  $m$  is not a ternary eutectic reaction since the latter involves three solid phases. Similar quasi-invariant reactions can also occur at liquidus minima in higher-order systems.

At point  $m$  in Fig. 53 the eutectic quasi-invariant reaction  $\text{Liq} \rightarrow \alpha + \beta$  occurs. A line joining two binary peritectic points  $p_1$  and  $p_2$  in a ternary system can also pass through a minimum at which a peritectic quasi-invariant reaction occurs:  $\text{Liq} + \alpha \rightarrow \beta$ .

Another example of a quasi-invariant reaction is that which occurs at saddle points such as the points  $s$  in Figs. 26 and 27. Saddle points occur at maxima on univariant lines. A ternary liquid with a composition exactly at a saddle point will solidify isothermally, at constant composition, to give the two solid phases with which it is in equilibrium. Higher-order saddle points can be found in systems where  $C \geq 4$ .

## 10 ***Second-Order and Higher-Order Transitions***

All the transitions discussed until now have been *first-order transitions*. When a first-order phase boundary is crossed, a new phase appears with extensive properties which are discontinuous with the other phases.

An example of a transition which is not first-order is the ferromagnetic to

paramagnetic transition of Fe, Co, Ni and other ferromagnetic materials which contain unpaired electron spins. Below its Curie temperature,  $T_{curie} = 1043$  K, Fe is ferromagnetic since its spins tend to be aligned parallel to one another. This alignment occurs because it lowers the internal energy of the system. At 0 K at equilibrium the spins are fully aligned. As the temperature increases, the spins become progressively less aligned, since this disordering increases the entropy of the system, until at  $T_{curie}$  the disordering is complete and the material becomes paramagnetic. There is never a two-phase region and no abrupt change occurs at  $T_{curie}$  which is simply the temperature at which the disordering becomes complete.

The following model is vastly oversimplified and is presented only as the simplest possible model illustrating the essential features of a second-order phase transition. Suppose that we may speak of localized spins and, furthermore, that a spin is oriented either “up” or “down”. Let the fraction of “up” and “down” spins be  $\xi$  and  $(1 - \xi)$ . Suppose further that when two neighboring spins are aligned a stabilizing internal energy contribution  $\varepsilon < 0$  results. Assuming that the spins are randomly distributed, the probability of two “up” spins being aligned is  $\xi^2$  and of two “down” spins being aligned is  $(1 - \xi)^2$ . The resultant contribution to the molar Gibbs energy is:

$$g = RT(\xi \ln \xi + (1 - \xi) \ln (1 - \xi)) + [\xi^2 + (1 - \xi)^2] \varepsilon \quad (181)$$

The equilibrium value of  $\xi$  is that which minimizes  $g$ . Setting  $dg/d\xi = 0$  gives:

$$\xi/(1-\xi) = \exp(2(1-2\xi)\varepsilon/RT) \quad (182)$$

At  $T = 0$  K,  $\xi = 0$  (or, equivalently,  $\xi = 1$ .) That is, the spins are completely aligned. A plot of  $\xi$  versus  $T$  from Eq. (182) shows that  $\xi$  increases with  $T$ , attaining the value  $\xi = 1/2$  when  $T = -\varepsilon/R$ . At all higher temperatures,  $\xi = 1/2$  which is the only solution of Eq. (182) above  $T_{curie} = -\varepsilon/R$ . As the spins become disordered with increasing temperature, energy is absorbed, thereby increasing the heat capacity. Most of the disordering occurs over a fairly small range of temperature below  $T_{curie}$ . This can be seen in Fig. 8 where the slope of the enthalpy curve increases up to  $T_{curie}$  and then quite abruptly decreases at this temperature.

In this extremely simple model there is a discontinuity in the slope  $c_P = dh/dT$  at  $T_{curie}$ , that is a discontinuity in the second derivative of the Gibbs energy. Such a transition is called a *second-order transition*.

For proper models of magnetism, see Chapter 19. In reality, some ordering persists above  $T_{curie}$ , and the transformation is not exactly second-order. Transitions involving discontinuities in the third, fourth, etc. derivatives of  $G$  are called third-order, fourth-order, etc. transitions.

The  $T$ -composition phase diagram of the Fe-Ni system is shown in Fig. 54. The Curie temperature varies with composition as it traverses the bcc phase field as a line. Nickel also undergoes a magnetic transition at its Curie temperature of 360°C. The second-order transition line crosses the fcc phase field as shown.

At point  $P$  on Fig. 54, the second-order transition line widens into a two-phase miscibility gap and the transition becomes first order. Point  $P$  is called a *tri-critical point*. (Other versions of the Fe-Ni phase diagram do not show a tri-critical point (Massalski et al. 2001).)

The magnetic transition is an example of an *order-disorder transition*. Another important type of order-disorder transition involves an ordering of the crystal structure. An example is seen in the Al-Fe system in Fig. 55. At low temperatures the body-centered phase exhibits long-range-ordering (lro). Two sublattices can be distinguished, one consisting of the corner sites of the unit cells and the other of the body-centered sites. The Al atoms preferentially occupy one sublattice while the Fe atoms preferentially occupy the other. This is the ordered B2 (CsCl) structure. As the temperature increases the phase becomes progressively disordered, with more and more Al atoms moving to the Fe-sublattice and *vice-versa* until, at the transition line, the disordering becomes complete with the Al and Fe atoms distributed equally over both sublattices. At this point the two sublattices become indistinguishable, the lro disappears, and the structure becomes the A2 (bcc) structure. As with the magnetic transition, there is no two-phase region and no abrupt change at the transition line which is simply the temperature at which the disordering becomes complete. As with the magnetic transition, most of the disordering takes place over a fairly small range of temperature below the transition line. The heat capacity thus increases as the transition

line is approached from below and then decreases sharply as the line is crossed. The transition is thus second-order, or approximately second-order.

The B2/A2 transition line may terminate at a tri-critical point like point *P* of Fig. 54. Although it is not shown on Fig. 55, there is most likely a tri-critical point near 660°C..

Order-disorder transitions need not necessarily be of second- or higher-order. In Fig. 54 the L12 phase has an ordered face-centered structure with the Ni atoms preferentially occupying the face-centered sites of the unit cells and the Fe atoms the corner sites. This structure transforms to the disordered fcc (A1) structure by a first-order transition with a discontinuous increase in enthalpy at the congruent point (504°C). There is also some controversy as to whether or not many reported second-order transition lines may actually be very narrow two-phase regions.

Although there is no Iro in the high-temperature disordered structures, appreciable short-range-ordering remains. For example, in the disordered A2 phase in the Al-Fe system, nearest-neighbor (Fe-Al) pairs are still preferred as in reaction (179). Modeling of ordered phases and the order-disorder transition is a complex subject with a large literature. The CEF (Sec. 8.2.2) has been used with some success, but only through the introduction of a large number of adjustable parameters. A quantitative model most likely requires that the coupling of sro and Iro be taken into account; the CVM and CSA models (Sec. 8.2.2) have been applied to this end. Ordered phases and order-disorder transitions are treated in Chapter 8 of this volume. See also Inden (2001).

## **11 Bibliography**

### **11.1 Phase Diagram Compilations**

From 1979 to the early 1990s, the American Society for Metals undertook a project to evaluate critically all binary and ternary alloy phase diagrams. All available literature on phase equilibria, crystal structures and, often, thermodynamic properties were critically evaluated in detail by international experts. Many evaluations have appeared in the *Journal of Phase Equilibria* (formerly *Bulletin of Alloy Phase Diagrams*), (ASM Intl., Materials Park, OH), which continues to publish phase diagram evaluations. Condensed critical evaluations of 4700 binary alloy phase diagrams have been published in three volumes (Massalski et al, 2001). The ternary phase diagrams of 7380 alloy systems

have also been published in a 10-volume compilation (Villars et al., 1995). Both binary and ternary phase diagrams from these compilations are available on the website of the ASM alloy phase diagram center. Many of the evaluations have also been published by ASM as monographs on phase diagrams involving a particular metal as a component.

The SGTE (Scientific Group Thermodata Europe) group has produced several subvolumes within volume 19 of the Landolt-Börnstein series (SGTE, 1999-2007) of compilations of thermodynamic data for inorganic materials and of phase diagrams and integral and partial thermodynamic quantities of binary alloys.

Phase diagrams for over 9000 binary, ternary and multicomponent ceramic systems (including oxides, halides, carbonates, sulfates, etc.) have been compiled in the 14-volume series, *Phase Diagrams for Ceramists* (Levin et al, 1964-2005). Earlier volumes were non-critical compilations. However, recent volumes have included critical commentaries.

Hundreds of critically evaluated and optimized phase diagrams of metallic, oxide, salt and sulfide systems may be downloaded from the FactSage website.

## 11.2 Further Reading

A recent text by Hillert (2008) provides a thorough thermodynamic treatment of phase equilibria as well as solution modeling and thermodynamic/phase diagram optimization.

A classical discussion of phase diagrams in metallurgy was given by Rhines (1956). Prince (1966) presents a detailed treatment of the geometry of multicomponent phase diagrams. A series of five volumes edited by Alper (1970-1978) discusses many aspects of phase diagrams in materials science. Bergeron and Risbud (1984) give an introduction to phase diagrams, with particular attention to applications in ceramic systems.

In the *Calphad Journal*, (Pergamon) and in the *Journal of Phase Equilibria*, (ASM Intl., Materials Park, OH) are to be found many articles on the relationships between thermodynamics and phase diagrams.

The SGTE Casebook (Hack, 2008) illustrates, through many examples, how thermodynamic calculations can be used as a basic tool in the development and

optimization of materials and processes of many different types.

## **12 Acknowledgements**

It would have been impossible to write this chapter without the FactSage software. I am indebted to my colleagues Chris Bale, Gunnar Eriksson and Patrice Chatrand. Financial assistance over many years from the Natural Sciences and Engineering Research Council of Canada is gratefully acknowledged.

### **List of Websites**

American Society for Metals, alloy phase diagram center,

<[www1.asminternational.org/asmenterprise/apd/](http://www1.asminternational.org/asmenterprise/apd/)>

FactSage, Montreal, <[www.factsage.com](http://www.factsage.com)>

NPL-MTDATA,

<[www.npl.co.uk/advancedmaterials/measurement-techniques/modelling/mtdata](http://www.npl.co.uk/advancedmaterials/measurement-techniques/modelling/mtdata)>

Pandat, <[www.compuetherm.com/pandat.html](http://www.compuetherm.com/pandat.html)>

SGTE, Scientific Group Thermodata Europe, <[www.sgte.org](http://www.sgte.org)>

Thermocalc, Stockholm, <[www.thermocalc.com](http://www.thermocalc.com)>

## References

- Alabyshev, A. F., Morachevskii, A. G. (1957), *Z Neorg. Khim.* **2**, 669.
- Alper, A. M. (Ed.) (1970-1978), *Phase Diagrams –J. Materials Science and Technology*, Vols, 1-5. New York: Academic.
- Bale, C. W., Pelton, A. D. (1983), *Metall Trans.* **B 14**,77.
- Bale, C. W., Pelton, A. D., Thompson W. T. (1986), *Canad. Metall. Quart.* **25**, 107
- Barry, T. I., Dinsdale, A. T., Gisby, J. A., Hallstedt, B., Hillert, M., Jansson, B., Jonsson, J., Sundman, B., Taylor, J. R. (1992), *J. Phase Equilib.* **13**, 459.
- Bartlett, H. E. Neethling, A. J., Crowther, P. (1970), *J. Chem. Thermo.* **2**, 523.
- Bergeron, C. J., Risbud, S. H. (1984), *Introduction to Phase Equilibria in Ceramics*. Columbus, Ohio: Amer. Ceramic Soc,
- Blander, M., Pelton, A. D. (1987), *Geochim. et Cosmochim. Acta* **51**, 85.
- Bray, H. F., Bell, F. D., Harris, S. J. (1961-1962), *J. Inst. Metals* **90**, 24.
- Dinsdale, A.T. (1991), *Calphad Journal*, **15**, 317.
- Dörner, P., Henig, E.-Th., Krieg, H., Lucas, H. L., Petzow, G. (1980), *Calphad Journal* **4**, 241.
- Fowler, R. H., Guggenheim, E. A. (1939), *Statistical Thermodynamics*. Cambridge: Cambridge Univ. Press, p. 350.
- Guggenheim, E. A. (1935), *Proc. Roy. Soc.* **A148**, 304.
- Gupta, H., Morral, J. E., Nowotny, H. (1986), *Scripta Metall.* **20**, 889.
- Hack, K. (ed.) (2008), *SGTE Casebook-Thermodynamics at Work*, 2<sup>nd</sup> ed., Boca Raton FL: CRC Press.
- Hansen, M. (1958), *Constitution of Binary Alloys*, 2nd ed. New York: McGraw-Hill.
- Hauffe, K. (1940), *Z. Elektrochem.* **46**, 348.
- Hillert, M. (1997), *J. Phase Equilib.* **18**, 249.
- Hillert, M. (2008), *Phase Equilibria, Phase Diagrams and Phase Transformations–Their Thermodynamic Basis*, 2<sup>nd</sup> ed., Cambridge: Cambridge Univ. Press.
- Hultgren, R., Desai, P. D., Hawkins, D. T., Gleiser, M., Kelly, K. K., Wagman, D. D. (1973), *Selected Values of the Thermodynamic Properties of the Elements and Binary Alloys*. Metals Park, Ohio: Am. Soc. Metals.
- Inden, G (2001), Atomic ordering, in G. Kostorz (ed.), *Phase Transformations in Materials*, ch. 8. Weinheim: Wiley-VCH.
- Kleinstuber, T. (1961), Ph.D. Thesis, Univ. Munich, Germany.
- Kohler, F. (1960), *Monatsh. Chemie* **91**, 738.
- Köningsberger, E., Eriksson, G. (1995), A new optimization routine for ChemSage, *CALPHAD Journal*, **19**, 207-214.
- Kurnakow, N. S., Kusnetzow, A. N. (1907), *Z. Anorg. Chem.* **52**, 173.
- Lantratov, M. R., Mikhailova, A. G. (1971), *Zh. Prikl. Khimii* **44**, 1778.
- Levin, E. M., Robbins, C. R., McMurdie, H. F. (1964), and 13 supplements to (2005), *Phase Diagrams for Ceramists*: Columbus, Ohio: Am. Ceramic Soc.
- Lukas, H. L., Henig, E.-Th., Zimmermann, B. (1977), *Calphad Journal* **1**, 225.

- Maierova, E. A., Morachevskii, A. G., Kovalenko, S. G. (1976), *Elektrokhimiya* **12**, 313.
- Massalski, T. B., Okamoto, H., Subramanian, P. R., Kacprzak, L. (2001), *Binary Alloy Phase Diagrams*, 2nd ed. Metals Park, OH: Am. Soc. Metals.
- Mathewson, C. H. (1906), *Z. Ang. Chem.* **50**, 180.
- Muan, A., and Osborn, F. (1965), *Phase Equilibria Among Oxides in Steelmaking*. Reading, MA.: Addison Wesley.
- Oates, W.A., Wenzl, H. (1996) *Scripta Mater.*, **35**, 623.
- Palatnik, L.S., Landau, A.I. (1956), *Zh. Fiz. Khim.*, **30**, 2399.
- Pelton, A. D. (1988), *Bull. Alloy Phase Diag.* **9**, 41.
- Pelton, A. D. (1995), *J. Phase Equilib.* **16**, 501.
- Pelton, A.D. (2001a), Thermodynamics and Phase Diagrams of Materials, in G. Kostorz (ed.) *Phase Transformations in Materials*, ch. 1. Weinheim: Wiley-VCH.
- Pelton, A.D. (2001b), A general geometric thermodynamic model for multicomponent solutions, *Calphad Journal*, **25**, 319-328.
- Pelton, A. D., Blander, M. (1984), *Proc. AIME Symp. on Molten Salts and Slags*. Warrendale, Pa.: The Metall. Soc.AIME, p. 281.
- Pelton, A.D., Chartrand, P. (2001a), The modified quasichemical model II – multicomponent solutions, *Met. & Mat. Trans.*, **32A**, 1355-60.
- Pelton, A.D., Chartrand, P. (2001b), The modified quasichemical model IV – Two sublattice quadruplet approximation, *Met & Mat. Trans.*, **32A**, 1409-16.
- Pelton, A.D., Degterov, S.A., Eriksson, G., Robelin, C., Dessureault, Y., The modified quasichemical model I binary solutions, *Met. & Mat. Trans.* **31B**, 651-60.
- Pelton, A. D., Schmalzried, H. (1973), *Metall. Trans.* **4**, 1395-1403.
- Pelton, A. D., Thompson, W. T. (1975), *Prog. Solid State Chem.* **10**, part 3, 119.
- Prince, A. (1966), *Alloy Phase Equilibria*. Amsterdam: Elsevier.
- Rhines, F. N. (1956), *Phase Diagrams in Metallurgy*. New York: McGraw-Hill.
- Roos, G. D. (1916), *Z Anorg. Chem.* **94**, 329.
- Schreinemakers, F. A. H. (1915), *Proc. K. Akad. Wetenschappen. Amsterdam (Section of Sciences)* **18**, 116.
- SGTE group (1999-2007), ed. Lehrstuhl für Werkstoffchemie, RWTH, Aachen, *Thermodynamic Properties of Inorganic Materials*, Landolt-Börnstein Group IV, vol. 19, Berlin: Springer.
- Turchi, P.E., Abrikosov, I.A., Burton, B., Fries, S.G., Grimvall, G., Kaufman, L., Korzhavyi, P., Manga, V.R., Ohno, M., Pisch, A., Scott, A., Zhang, W. (2007), Interface between quantum-mechanical-based approaches, experiments, and CALPHAD methodology, *Calphad Journal*, **31**, 4-27.
- Van Laar, J. J. (1908), *Z. Phys. Chem.* **63**, 216; **64**, 257.
- Villars, R, Prince, A., Okamoto, H. (1995), *Handbook of Ternary Alloy Phase Diagrams*. Metals Park, OH: Am. Soc. Metals.
- Weeks, J. R., Davies, H. A. (1964), AEC Report, Conf. 660712-1, BNL-10372.

## Tables

Table 1. Corresponding pairs of potentials  $\phi_i$  and extensive variables  $q_i$ .

$\phi_i$ :	T	P	$\mu_1$	$\mu_2 \dots$	$\mu_C$
$q_i$	S	-V	$n_1$	$n_2 \dots$	$n_C$

Table 2. Corresponding pairs of potentials  $\phi_i$  and extensive variables  $q_i$ .

$\phi_i$ :	1/T	P	$\mu_i/T$	$\mu_2/T$	....	$\mu_C/T$
$q_i$ :	-H	-V/T	$n_1$	$n_2$	....	$n_C$

## Figure Captions

Figure 1. Temperature-composition phase diagram at  $P = 1$  bar of the Fe-Mo system (see FactSage).

Figure 2. Isothermal section at  $25^{\circ}\text{C}$  and  $P = 1$  bar of the Zn-Mg-Al system (see FactSage)

Figure 3. Isoplethal phase diagram section at  $X_{\text{Zn}} = 0.1$  and  $P = 1$  bar of the Zn-Mg-Al system. (a) temperature vs. composition; (b) enthalpy vs. composition. (see FactSage).

Figure 4. Phase diagram section of the Fe-Cr-V-C system at  $850^{\circ}\text{C}$ , 0.3 wt. % C and  $P = 1$  bar (see FactSage; SGTE).

Figure 5. Phase diagram of the Fe-Ni- $\text{O}_2$  system at  $1200^{\circ}\text{C}$  showing equilibrium oxygen pressure vs. overall metal ratio (see FactSage).

Figure 6. Phase diagram of the Fe-Cr- $\text{S}_2$ - $\text{O}_2$  system at  $925^{\circ}\text{C}$  showing equilibrium  $\text{S}_2$  and  $\text{O}_2$  partial pressures at constant molar ratio  $\text{Cr}/(\text{Cr} + \text{Fe}) = 0.5$  (see FactSage).

Figure 7. (a)  $P$ - $T$  and (b)  $V$ - $T$  phase diagrams of  $\text{Al}_2\text{SiO}_5$  (see FactSage).

Figure 8. Standard molar enthalpy of Fe (see FactSage).

Figure 9. "Predominance" phase diagram of the Cu- $\text{SO}_2$ - $\text{O}_2$  system at  $700^{\circ}\text{C}$  showing the solid phases at equilibrium as a function of the equilibrium  $\text{SO}_2$  and  $\text{O}_2$  partial pressures (see FactSage).

Figure 10. Predominance phase diagram (also known as a Gibbs energy –  $T$  diagram or an Ellingham diagram) for the Cu- $\text{O}_2$  system. Points M and M are the melting points of Cu and  $\text{Cu}_2\text{O}$  respectively (see FactSage).

Figure 11. Temperature-composition phase diagram at  $P = 1$  bar of the Bi-Sb system (see FactSage; SGTE).

Figure 12. Molar Gibbs energy of liquid Au-Cu alloys at  $1100^{\circ}\text{C}$  illustrating the tangent construction (see FactSage).

Figure 13. Ge-Si phase diagram at  $P = 1$  bar (after Hansen, 1958) and Gibbs energy curves at three temperatures, illustrating the common tangent construction.

Figure 14. Phase diagram of a system A-B with ideal solid and liquid solutions. Melting points of A and B are 800 and 1200 K respectively. Diagrams calculated for entropies of fusion  $\Delta s_{f(A)}^{\circ} = \Delta s_{f(B)}^{\circ} = 3, 10$  and  $30 \text{ J mol}^{-1}\text{K}^{-1}$ .

Figure 15. Pressure-composition phase diagram of the Zn-Mg system at  $977^{\circ}\text{C}$

calculated for ideal vapor and liquid solutions. Upper panel illustrates common tangent construction at a constant pressure.

Figure 16. Isothermal Gibbs energy curves for solid and liquid phases in a system A-B in which  $g^{E(l)} < g^{E(s)}$ . A phase diagram of the type of Fig. 17 results.

Figure 17. Temperature-composition phase diagram of the  $K_2CO_3$ - $Na_2CO_3$  system at  $P = 1$  bar (see FactSage).

Figure 18. Phase diagram (after Hultgren et al., 1973) and Gibbs energy curves of solid solutions for the Au-Ni system at  $P = 1$  bar. Letters *s* indicate spinodal points.

Figure 19. Temperature-composition phase diagram at  $P = 1$  bar and Gibbs energy curves at  $850^\circ C$  for the Ag-Cu system. Solid Ag and Cu have the same (fcc) crystal structure (see FactSage; SGTE).

Figure 20. Topological changes in the phase diagram for a system A-B with regular solid and liquid phases brought about by systematic changes in the regular solution parameters  $\omega^s$  and  $\omega^l$ . Melting points of pure A and B are 800 K and 1200 K. Entropies of fusion of both A and B are  $10.0 \text{ J mol}^{-1}K^{-1}$  (Pelton and Thompson, 1975). Dashed curve in panel (d) is a metastable liquid miscibility gap.

Figure 21.  $CaO$ - $SiO_2$  phase diagram at  $P = 1$  bar and Gibbs energy curves at  $1500^\circ C$  illustrating Gibbs energies of fusion and formation of the compound  $CaSiO_3$  (see FactSage) (reprinted with permission from Pelton, 2001a). The temperature difference between the peritectic at  $1464^\circ C$  and the eutectic at  $1463^\circ C$  has been exaggerated for the sake of clarity.

Figure 22. Ag-Mg phase diagram at  $P = 1$  bar (after Hultgren et al., 1973) and Gibbs energy curves at three temperatures.

Figure 23. Geometrical units of binary phase diagrams, illustrating rules of construction.

Figure 24. Projection of the liquidus surface of the Bi-Sn-Cd system onto the ternary composition triangle (after Bray et al., 1961-1962.) Small arrows show the crystallization path of an alloy of overall composition at point *a*. ( $P = 1$  bar).

Figure 25. Perspective view of ternary space model of a simple eutectic ternary system.  $e_1$ ,  $e_2$  and  $e_3$  are the binary eutectics and  $E$  is the ternary eutectic. The base of the prism is the equilateral composition triangle (pressure = constant).

Figure 26. Projection of the liquidus surface of a system A-B-C. The binary subsystems A-B and C-A are simple eutectic systems. The binary phase diagram B-C is shown in the insert. All solid phases are assumed pure stoichiometric components or compounds. Small arrows show crystallization paths of alloys of compositions at points *a* and *b*.

Figure 27. Polythermal projection of the liquidus surface of the Zn-Mg-Al system at

$P = 1$  bar (see FactSage).

Figure 28. Isothermal section of the Bi-Sn-Cd system at 423 K at  $P = 1$  bar (after Bray et al., 1961-1962). Extents of solid solubility in Bi and Sn have been exaggerated for clarity of presentation.

Figure 29. A tie-triangle in a ternary isothermal (and isobaric) section illustrating the lever rule and the extension rule (Schreinemakers' rule).

Figure 30. Isopleth (constant composition section) of the Bi-Sn-Cd system at  $P = 1$  bar following the line  $AB$  of Fig. 24. (Extents of solid solubility in the terminal solid solutions have been exaggerated for clarity of presentation.)

Figure 31. An isobaric temperature-composition phase diagram with the eutectic "opened up" to show that it is an infinitely narrow three-phase region (reprinted with permission from Pelton, 2001a).

Figure 32. A  $P$ - $T$  diagram in a one-component system "opened up" to show that the two-phase lines are infinitely narrow two-phase regions (reprinted with permission from Pelton, 2001a).

Figure 33. A node in a general phase diagram section. Schreinemakers' Rule is obeyed. Red and blue lines are Zero Phase Fraction (ZPF) lines of the  $\beta$  and  $\gamma$  phases respectively (reprinted with permission from Pelton, 2001a).

Figure 34. Binary  $T$ -composition phase diagram at  $P = 1$  bar of the MgO-CaO system showing Zero Phase Fraction (ZPF) lines of the phases (see FactSage).

Figure 35. Schematic  $P$ - $V$  diagram for  $H_2O$ . This is not a single-valued phase diagram section (reprinted with permission from Pelton, 2001a).

Figure 36. Equilibrium  $S_2$  pressure versus mole fraction of Ni in the Cu-Ni- $S_2$  system at 427°C. This is not a single-valued phase diagram (see FactSage).

Figure 37. Equilibrium  $S_2$  pressure versus molar ratio  $n_{Ni}/(n_{Cu} + n_{Ni})$  in the Cu-Ni- $S_2$  system at 427°C. This is a single-valued phase diagram (see FactSage).

Figure 38. Corresponding  $T$ - $X_O$  and  $T - (\mu_{O_2} - \mu_{O_2}^o)$  phase diagrams of the Fe-O system (after Muan and Osborn, 1965).

Figure 39. A corresponding set of phase diagrams for a C-component system when the potentials  $\phi_4, \phi_5, \dots, \phi_{C+2}$  are constant (Pelton and Schmalzried, 1973).

Figure 40. Corresponding phase diagrams of the Fe-Cr- $O_2$  system at 1300°C (Pelton and Schmalzried, 1973).

Figure 41. Corresponding  $T$ -composition and enthalpy-composition phase diagrams of

the Mg-Si system at  $P = 1$  bar. The enthalpy axis is referred to the enthalpy of the system at equilibrium at  $25^\circ\text{C}$  (see FactSage).

Figure 42.  $\phi_1$ - $\phi_2$ - $\phi_3$  surfaces of  $\alpha$  and  $\beta$  phases in a C-component system when  $\phi_4, \phi_5, \dots, \phi_{C+2}$  are constant (reprinted with permission from Hillert, 2008).

Figure 43. Isolethal section across the  $\text{Fe}_3\text{O}_4$ - $\text{SiO}_2$  join of the Fe-Si- $\text{O}_2$  system. ( $P = 1$  bar) (see FactSage).

Figure 44. “ $\text{Fe}_2\text{O}_3$ - $\text{SiO}_2$  phase diagram in air ( $p_{\text{O}_2} = 0.21$  bar)” (see FactSage).

Figure 45. “FeO- $\text{SiO}_2$  phase diagram at Fe saturation” (see FactSage).

Figure 46. Constant  $p_{\text{O}_2}$  line in the Fe-Si- $\text{O}_2$  system illustrating the construction and interpretation Figure 44.

Figure 47. Phase diagram at  $T = 750^\circ\text{C}$  and  $P = 1$  bar of the reciprocal system NaCl- $\text{CaCl}_2$ -NaF- $\text{CaF}_2$  (see FactSage).

Figure 48. Isolethal section of the Mg-Al-Ce-Mn-Y-Zn system at 0.05% Ce, 0.5% Mn, 0.1% Y and 1.0% Zn (weight %) at  $P = 1$  bar (see FactSage).

Figure 49. Cd-Na phase diagram at  $P = 1$  bar calculated from optimized thermodynamic parameters showing experimental data points.  $\circ$  Kurnakow and Kusnetzow (1907),  $\triangle$  Mathewson (1906),  $\times$  Weeks and Davies (1964).

Figure 50. Sodium activity coefficient in liquid Cd-Na alloys at  $400^\circ\text{C}$ . Line is calculated from optimized thermodynamic parameters.  $\square$  Hauffe (1940),  $\bullet$  Lantratov and Mikhailova (1971),  $\triangle$  Maiorova et al. (1976),  $\blacktriangledown$  Alabyshev and Morachevskii (1957),  $\circ$  Bartlett et al. (1970).

Figure 51. Partial excess enthalpy of sodium in liquid Cd-Na alloys. Line is calculated from optimized thermodynamic parameters.  $\bullet$  Lantratov and Mikhailova (1971),  $\triangle$  Maiorova et al. (1976),  $\circ$  Bartlett et al. (1970).

Figure 52. Calculated amounts of phases present during equilibrium cooling of an alloy of composition 85 mol% Mg, 15% Al, 5% Zn (point B on Fig. 27) (see FactSage).

Figure 53. Liquidus projection of a system A-B-C with a minimum on the univariant line joining the binary eutectic points  $e_1$  and  $e_2$ . Solid phases are stoichiometric A and a binary solid solution B-C.

Figure 54. Temperature-composition phase diagram of the Fe-Ni system at  $P = 1$  bar showing the magnetic transformations (see FactSage; SGTE; Massalski et al., 2001).

Figure 55. Temperature-composition phase diagram of the Al-Fe system at  $P = 1$  bar showing the B2→A2 order-disorder transition (see FactSage; SGTE).

Figure 1. Temperature-composition phase diagram at  $P = 1$  bar of the Fe-Mo system (see FactSage).

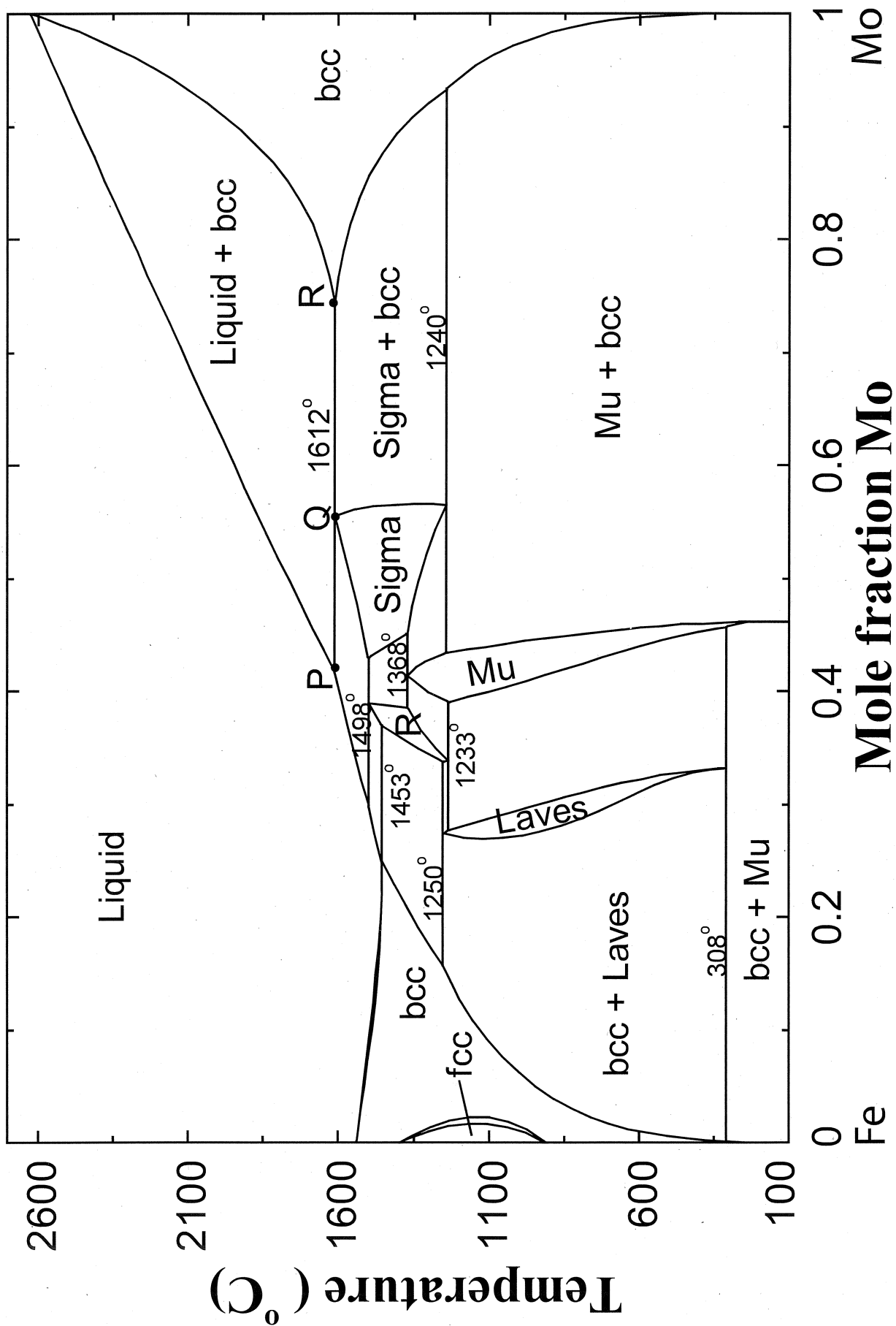


Figure 2. Isothermal section at 25°C and P = 1 bar of the Zn-Mg-Al system (see FactSage)

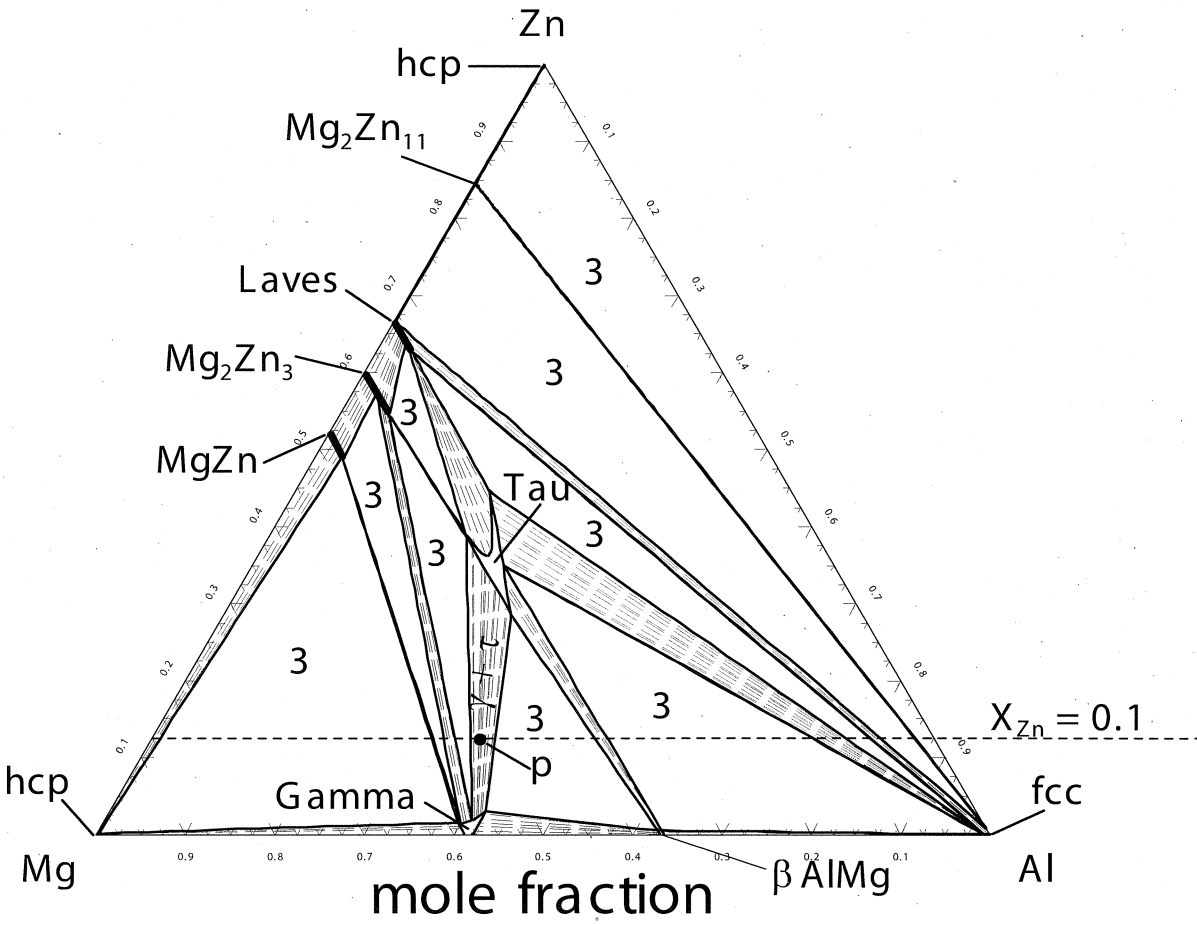


Figure 3. Isolethal phase diagram section at  $X_{Zn} = 0.1$  and  $P = 1$  bar of the Zn-Mg-Al system. (a) temperature vs. composition; (b) enthalpy vs. composition. (see FactSage).

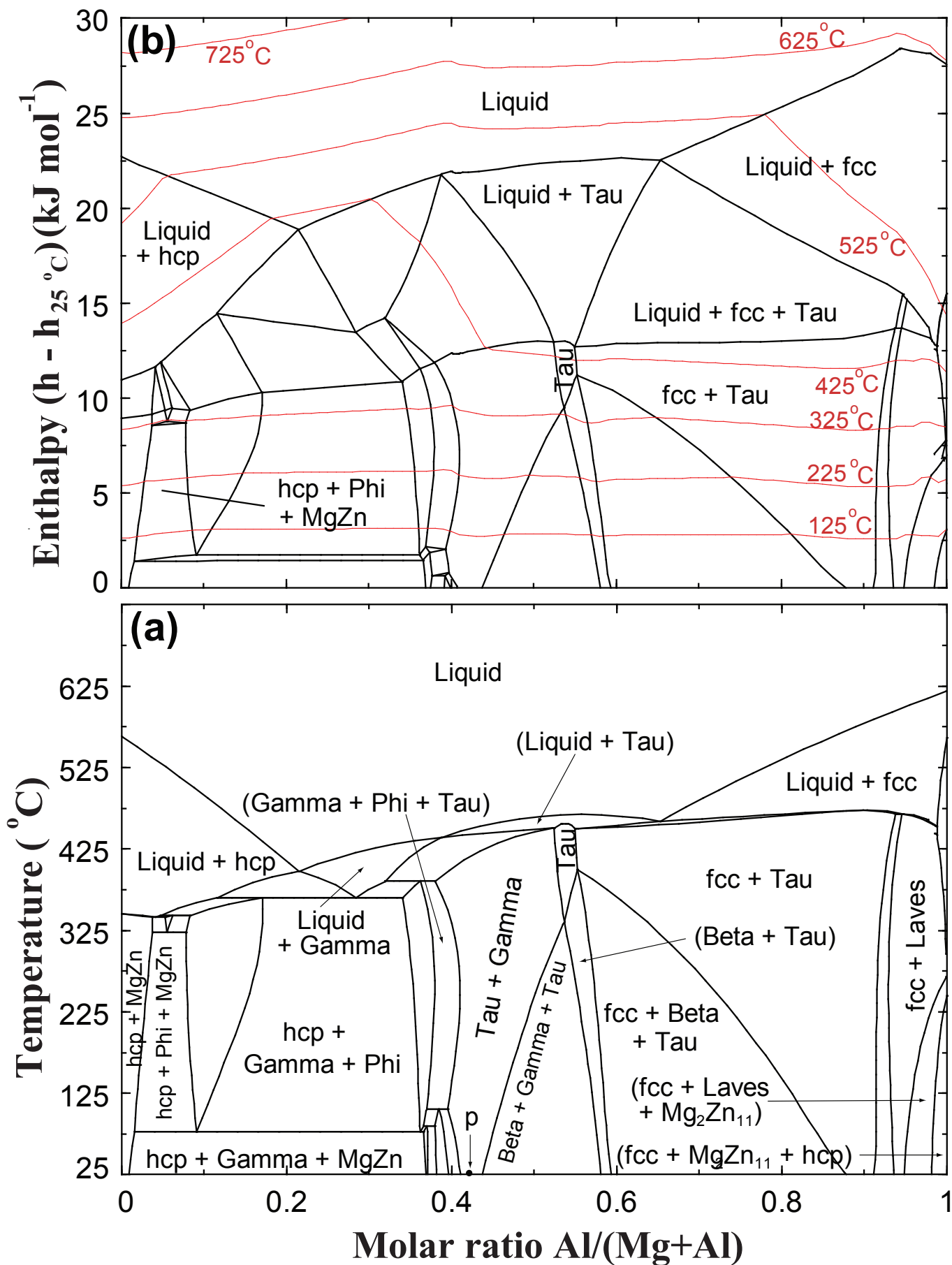


Figure 4. Phase diagram section of the Fe-Cr-V-C system at 850° C, 0.3 wt. % C and P = 1 bar (see FactSage; SGTE).

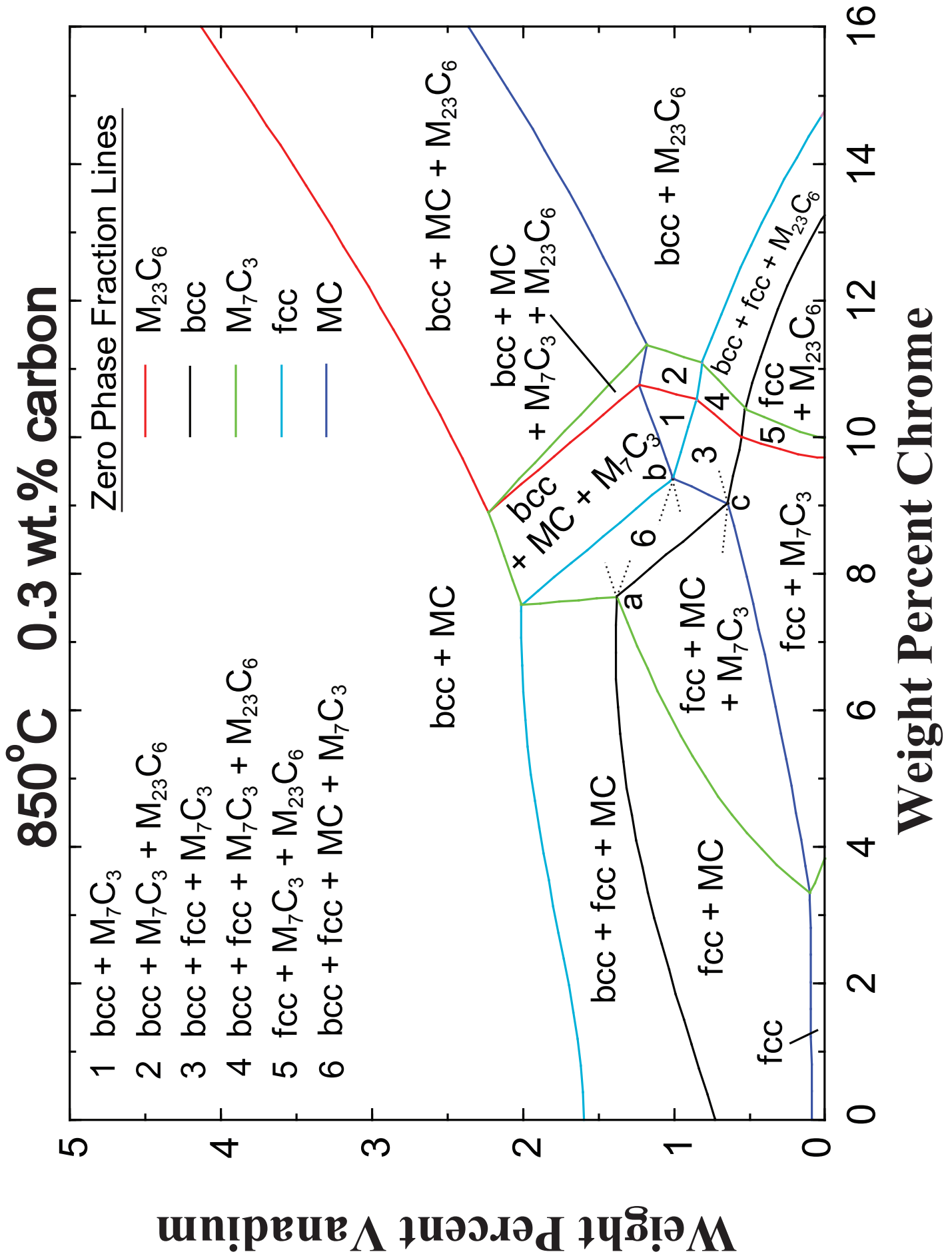


Figure 5. Phase diagram of the Fe-Ni-O<sub>2</sub> system at 1200° C showing equilibrium oxygen pressure vs. overall metal ratio (see FactSage).

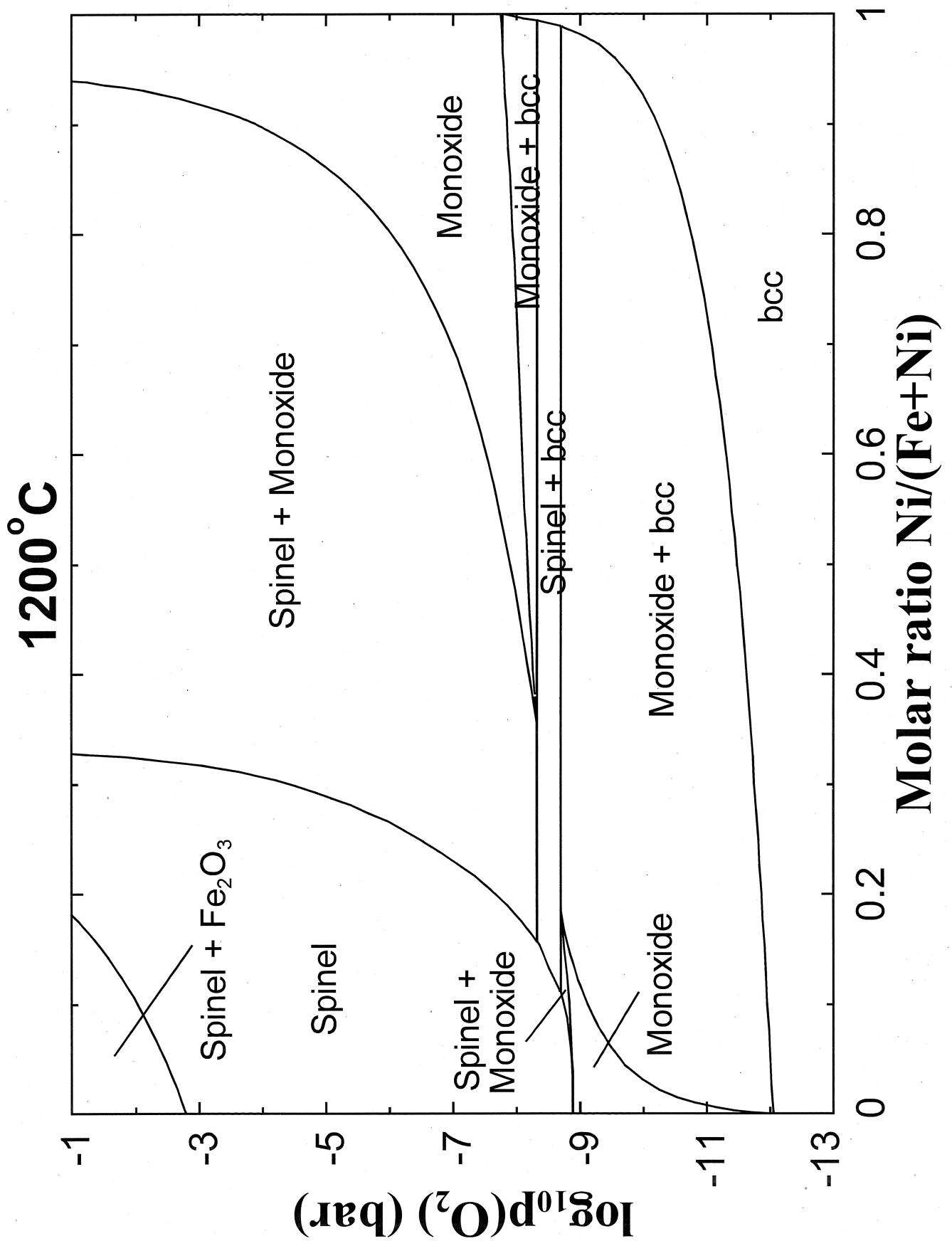


Figure 6. Phase diagram of the Fe-Cr-S<sub>2</sub>-O<sub>2</sub> system at 925° C showing equilibrium S<sub>2</sub> and O<sub>2</sub> partial pressures at constant molar ratio Cr/(Cr + Fe) = 0.5 (see FactSage).

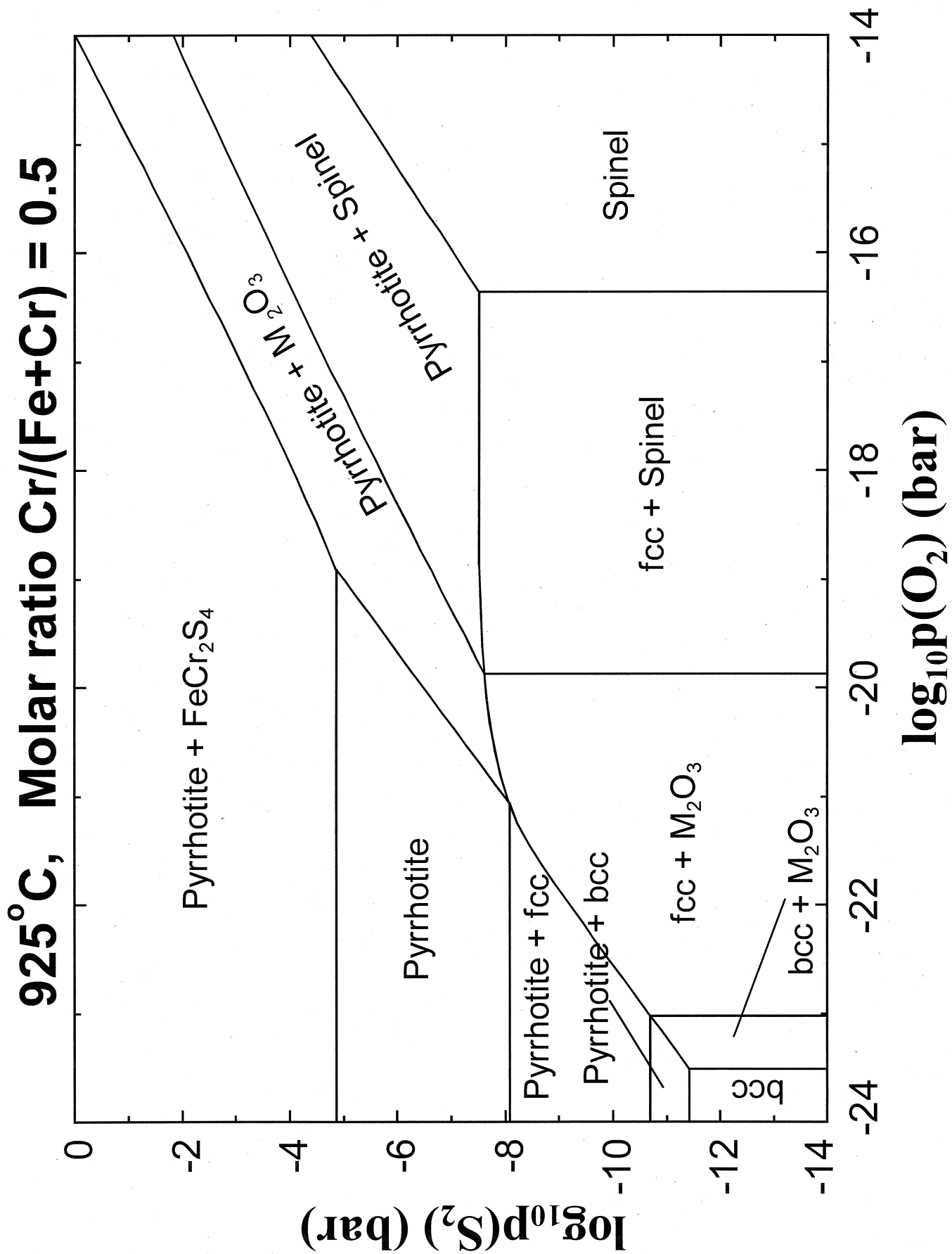


Figure 7. (a)  $P$ - $T$  and (b)  $V$ - $T$  phase diagrams of  $\text{Al}_2\text{SiO}_5$  (see FactSage).

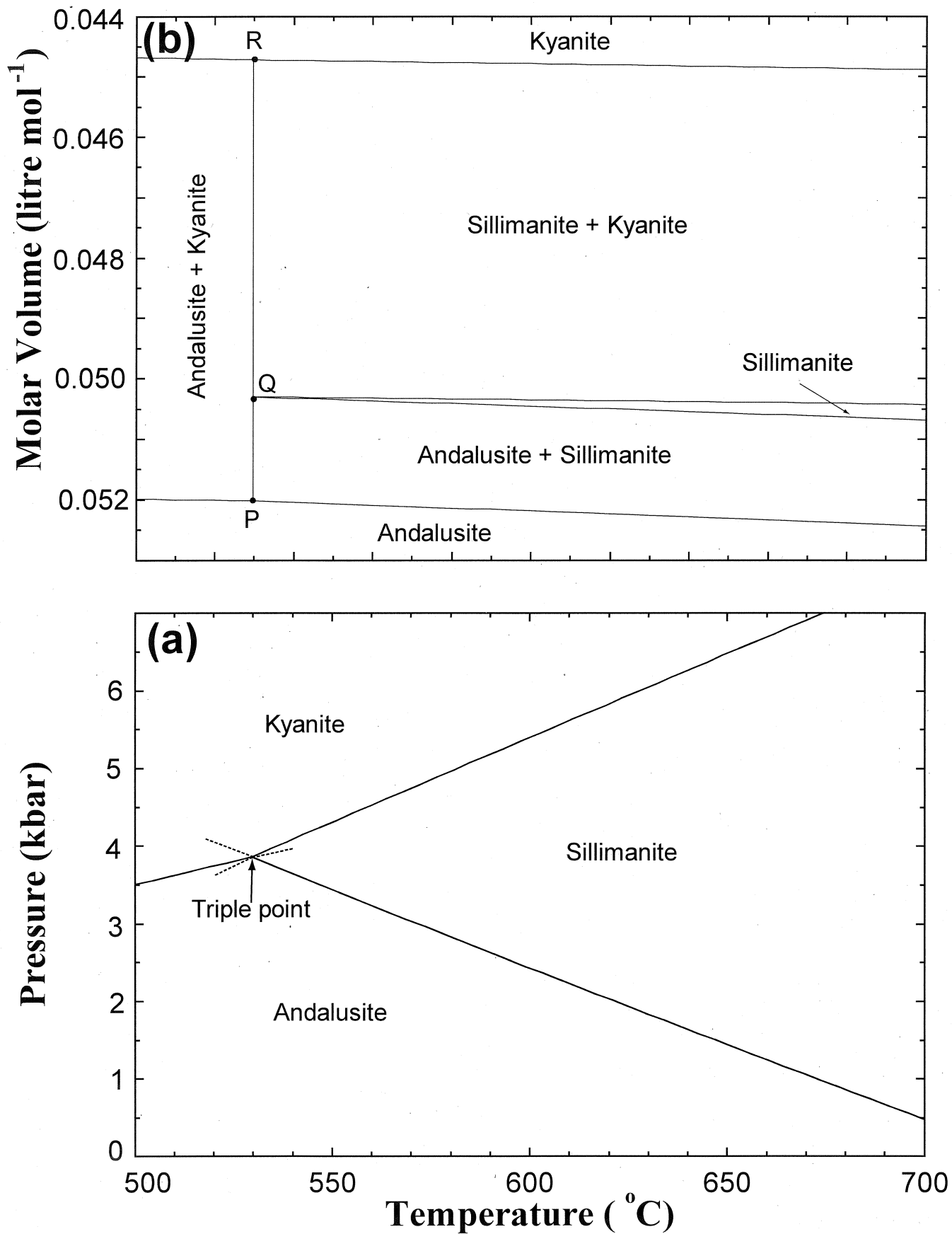


Figure 8. Standard molar enthalpy of Fe (see FactSage).

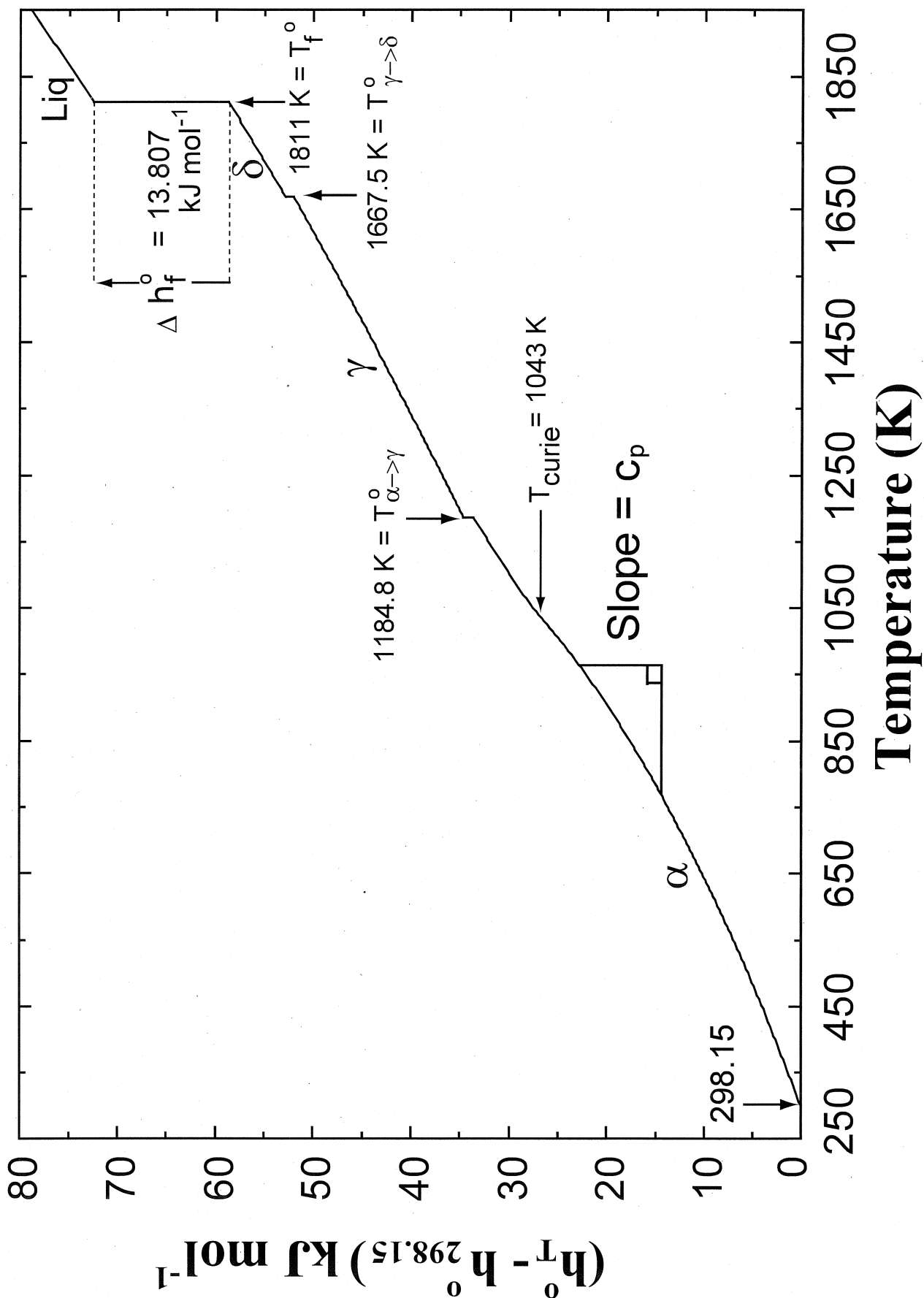


Figure 9. "Predominance" phase diagram of the Cu-SO<sub>2</sub>-O<sub>2</sub> system at 700°C showing the solid phases at equilibrium as a function of the equilibrium SO<sub>2</sub> and O<sub>2</sub> partial pressures (see FactSage).

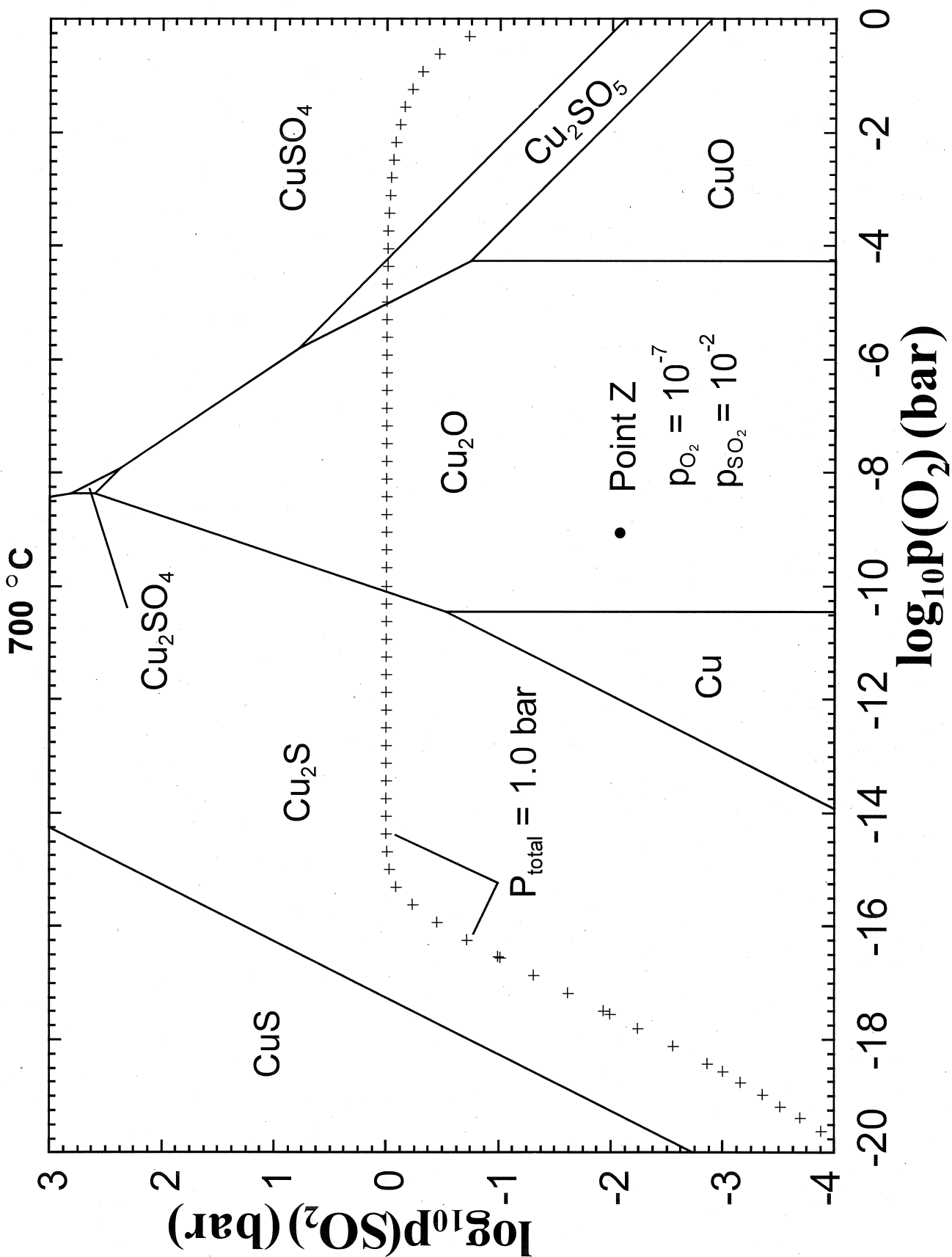


Figure 10. Predominance phase diagram (also known as a Gibbs energy –  $T$  diagram or an Ellingham diagram) for the Cu-O<sub>2</sub> system. Points M and  $\overline{M}$  are the melting points of Cu and Cu<sub>2</sub>O respectively (see FactSage).

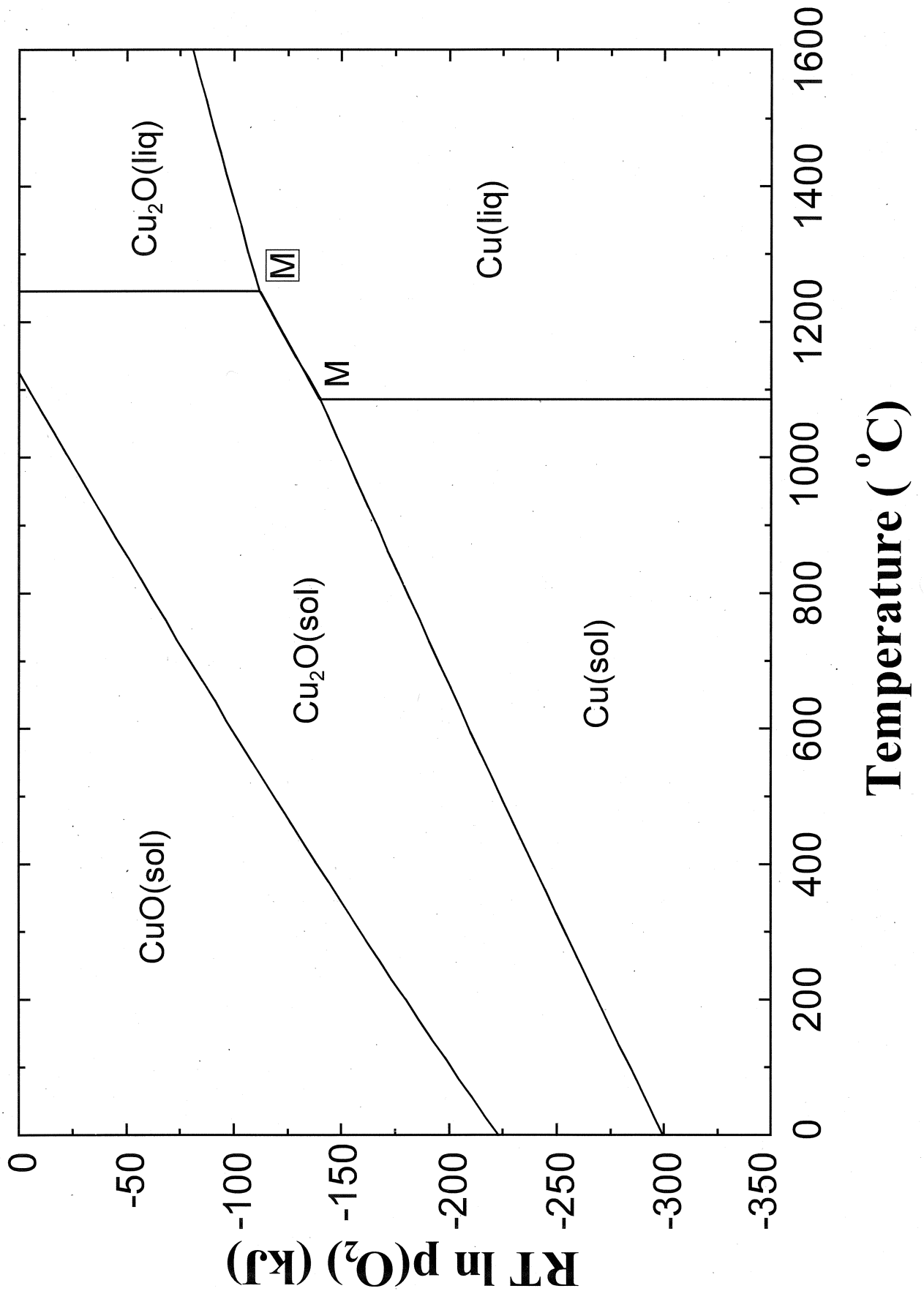


Figure 11. Temperature-composition phase diagram at  $P = 1$  bar of the Bi-Sb system (see FactSage; SGTE).

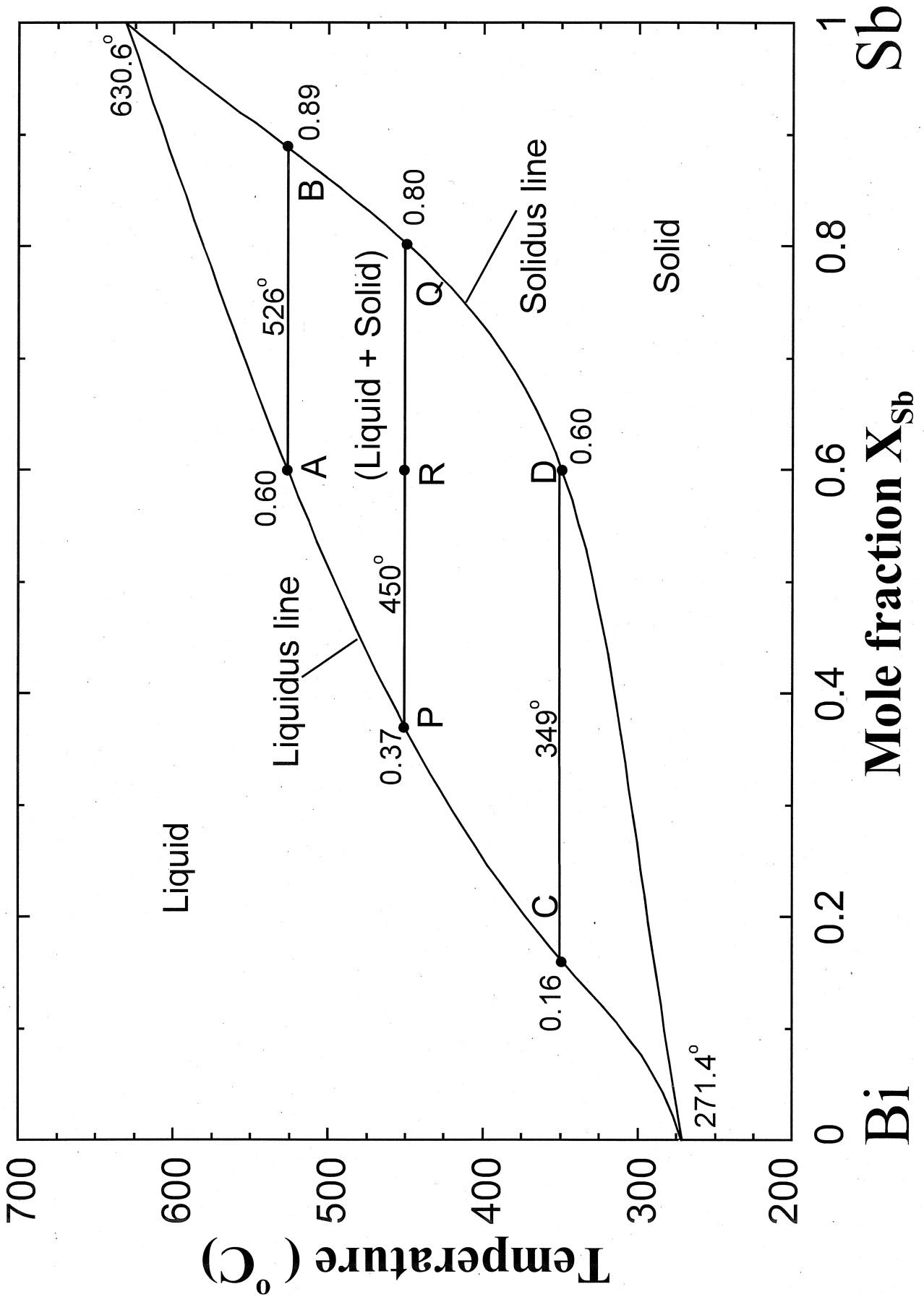


Figure 12. Molar Gibbs energy of liquid Au-Cu alloys at 1100°C illustrating the tangent construction (see FactSage).

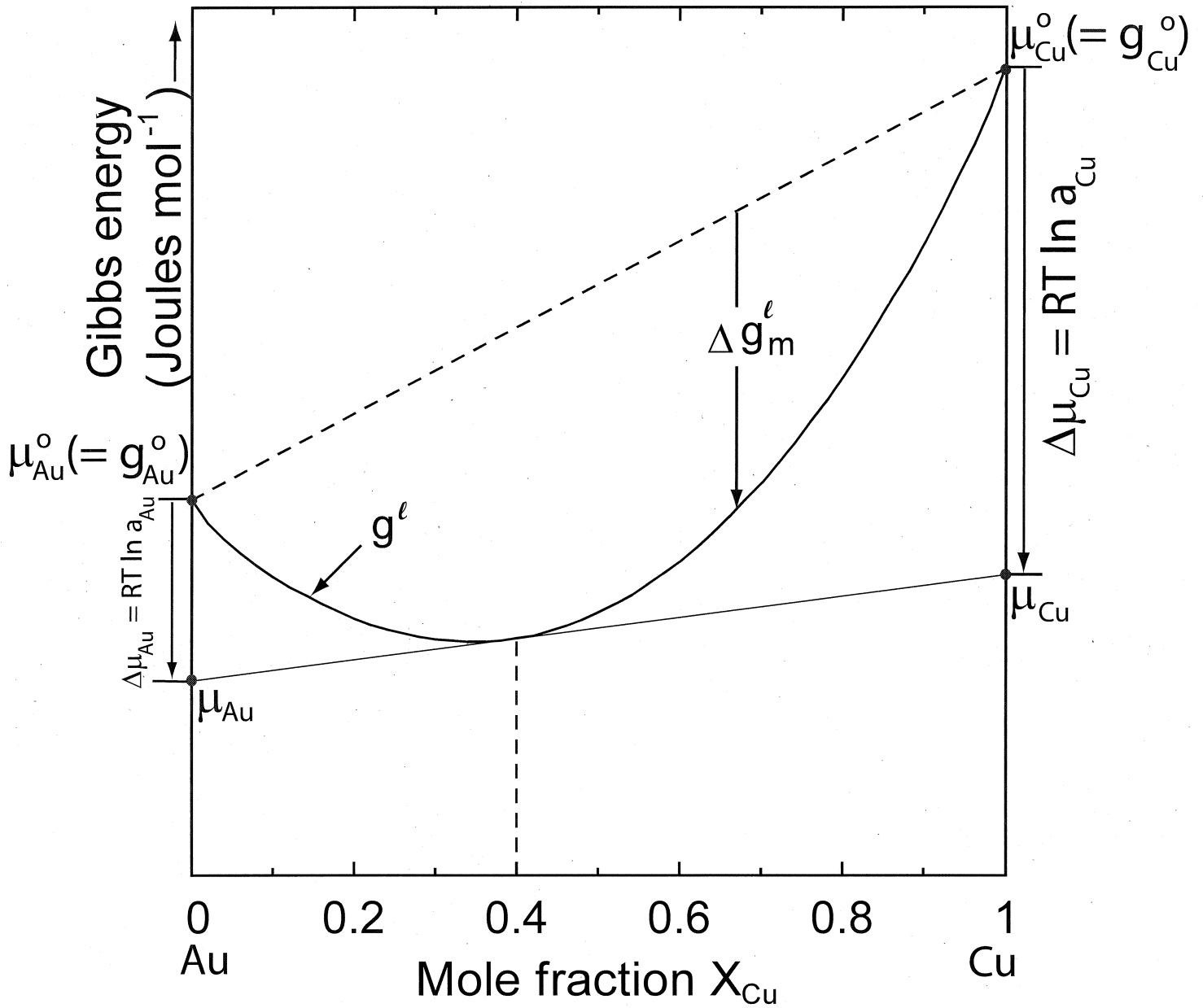




Figure 14. Phase diagram of a system A-B with ideal solid and liquid solutions. Melting points of A and B are 800 and 1200 K respectively. Diagrams calculated for entropies of fusion  $\Delta s_{f(A)}^{\circ} = \Delta s_{f(B)}^{\circ} = 3, 10$  and  $30 \text{ J mol}^{-1} \text{ K}^{-1}$ .

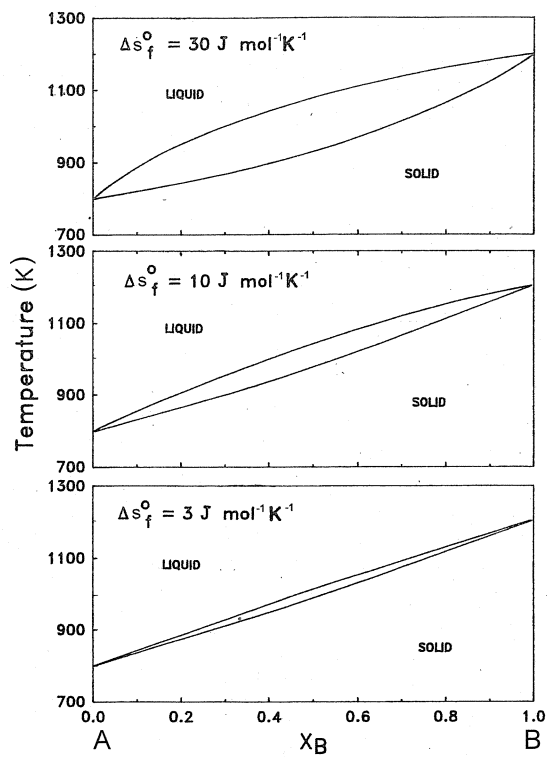


Figure 15. Pressure-composition phase diagram of the Zn-Mg system at 977°C calculated for ideal vapor and liquid solutions. Upper panel illustrates common tangent construction at a constant pressure.

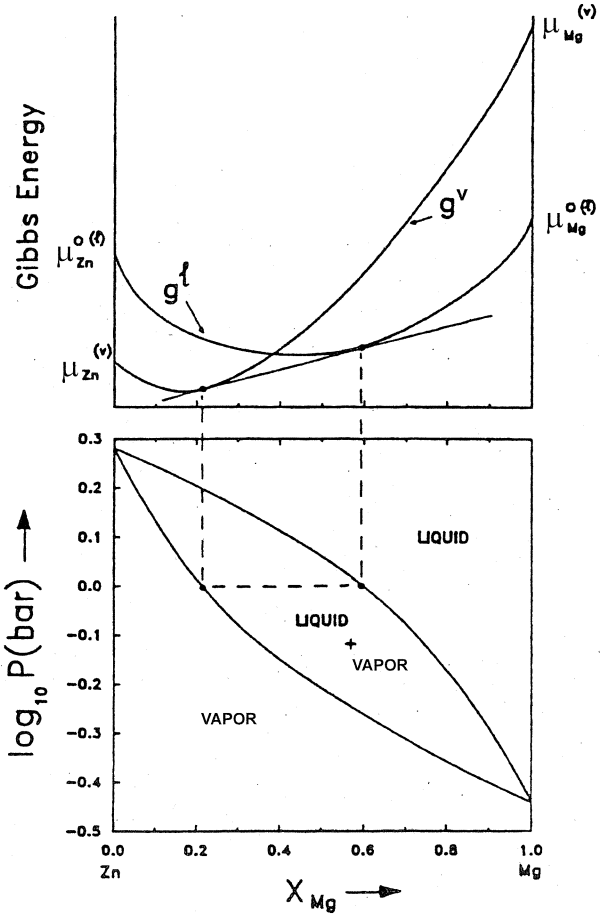


Figure 16. Isothermal Gibbs energy curves for solid and liquid phases in a system A-B in which  $g^{E(l)} < g^{E(s)}$ . A phase diagram of the type of Fig. 17 results.

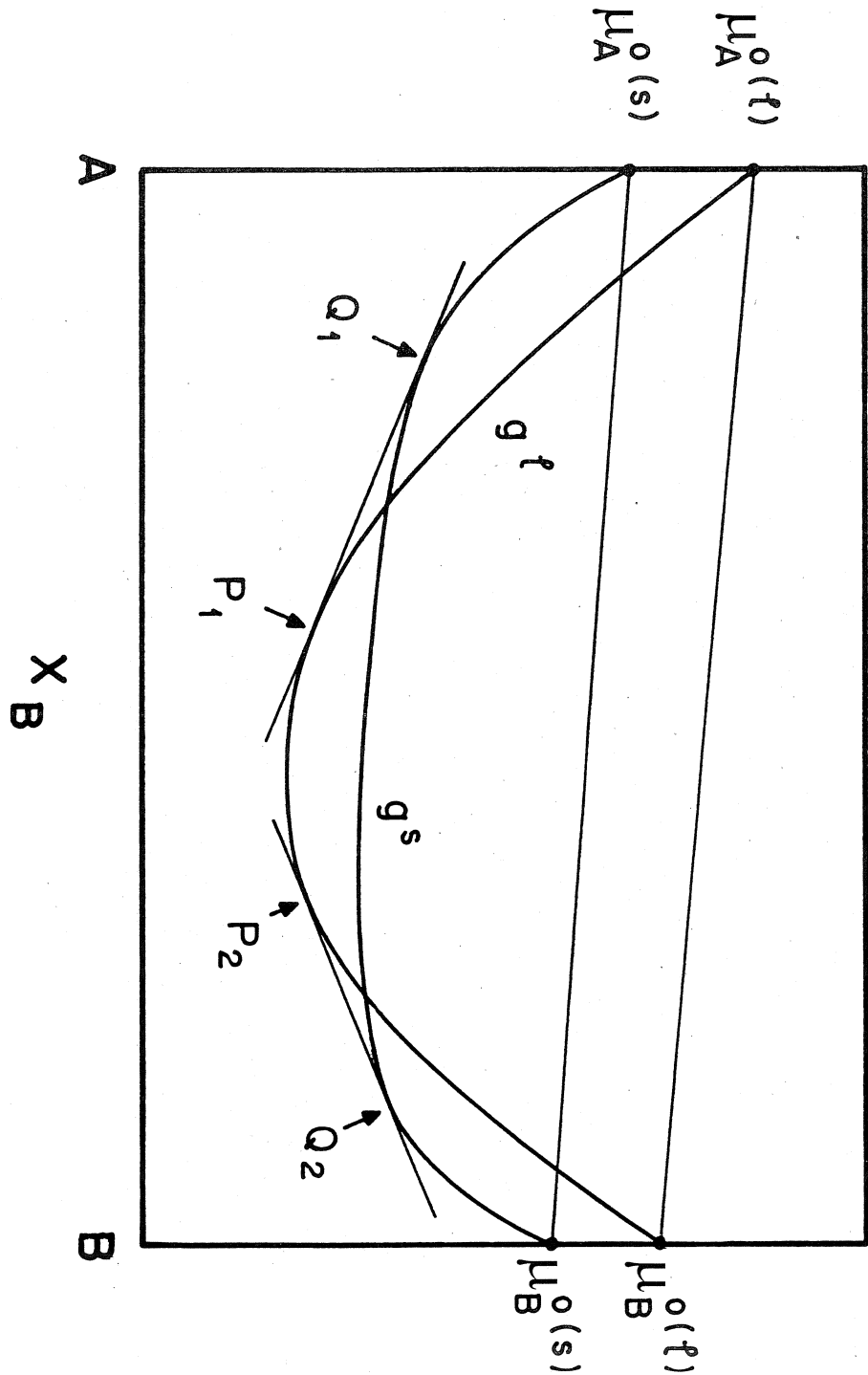


Figure 17. Temperature-composition phase diagram of the  $K_2CO_3$ - $Na_2CO_3$  system at  $P = 1$  bar (see FactSage).

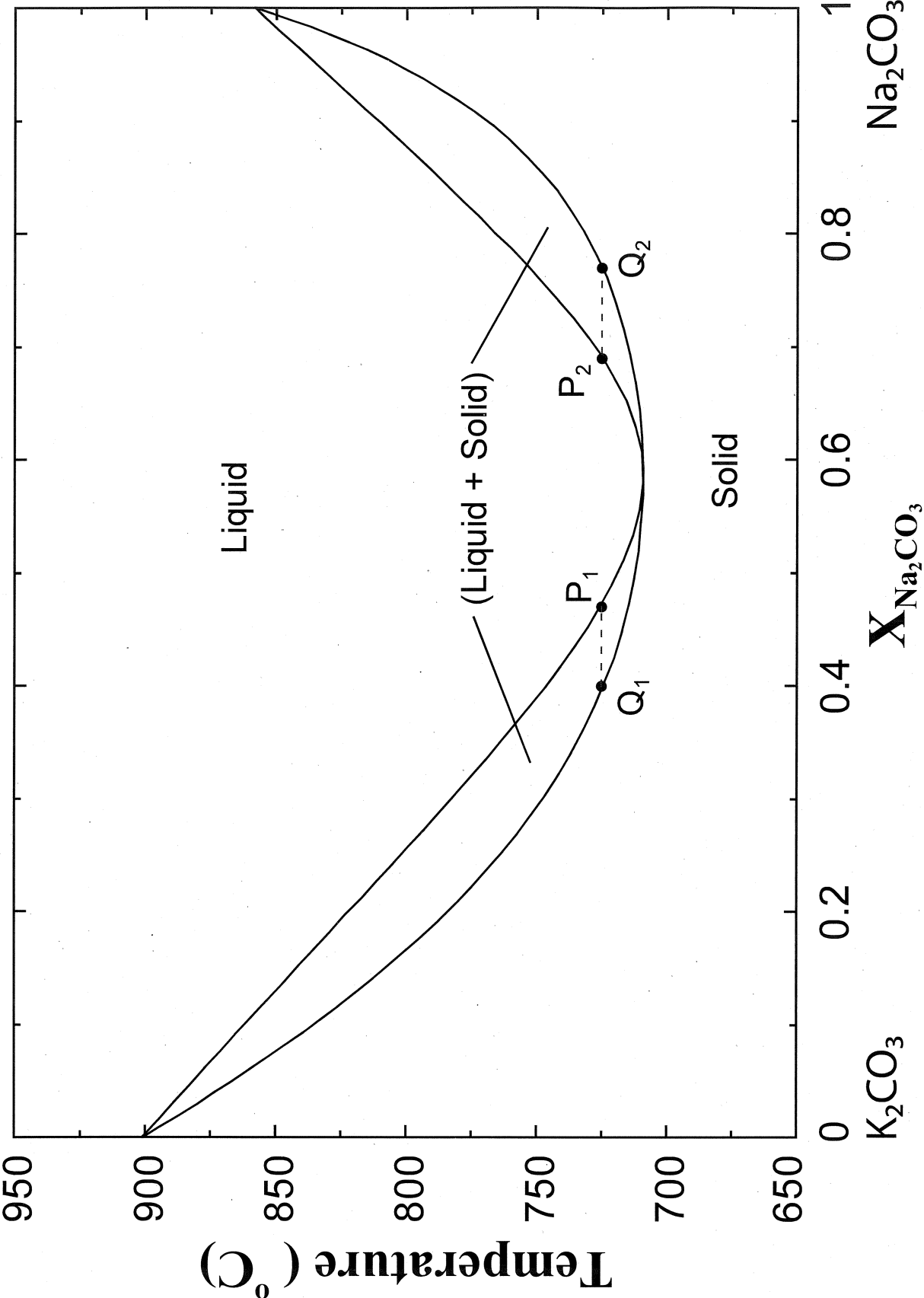


Figure 18. Phase diagram (after Hultgren et al., 1973) and Gibbs energy curves of solid solutions for the Au-Ni system at  $P = 1$  bar. Letters s indicate spinodal points.

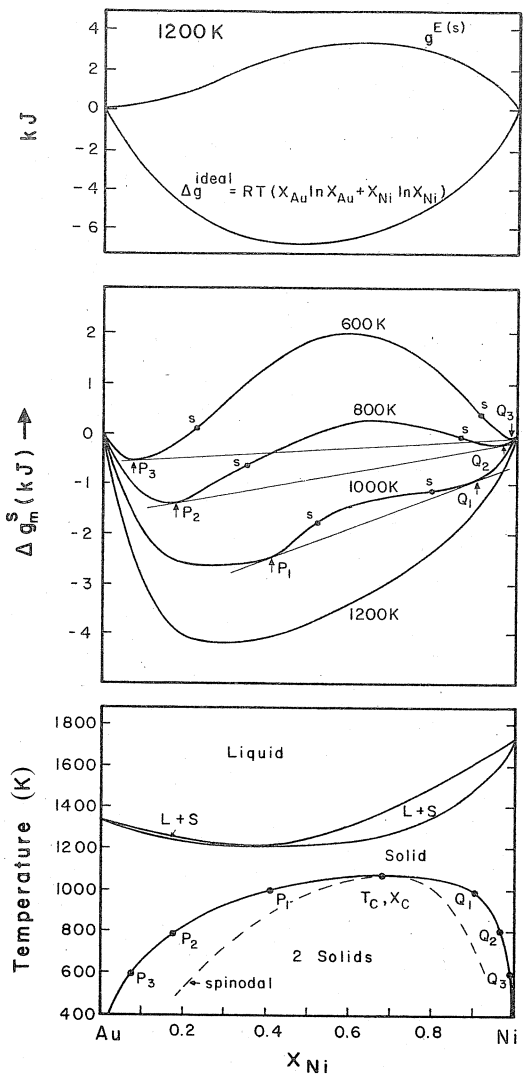


Figure 19. Temperature-composition phase diagram at  $P = 1$  bar and Gibbs energy curves at  $850^\circ\text{C}$  for the Ag-Cu system. Solid Ag and Cu have the same (fcc) crystal structure (see FactSage; SGTE).

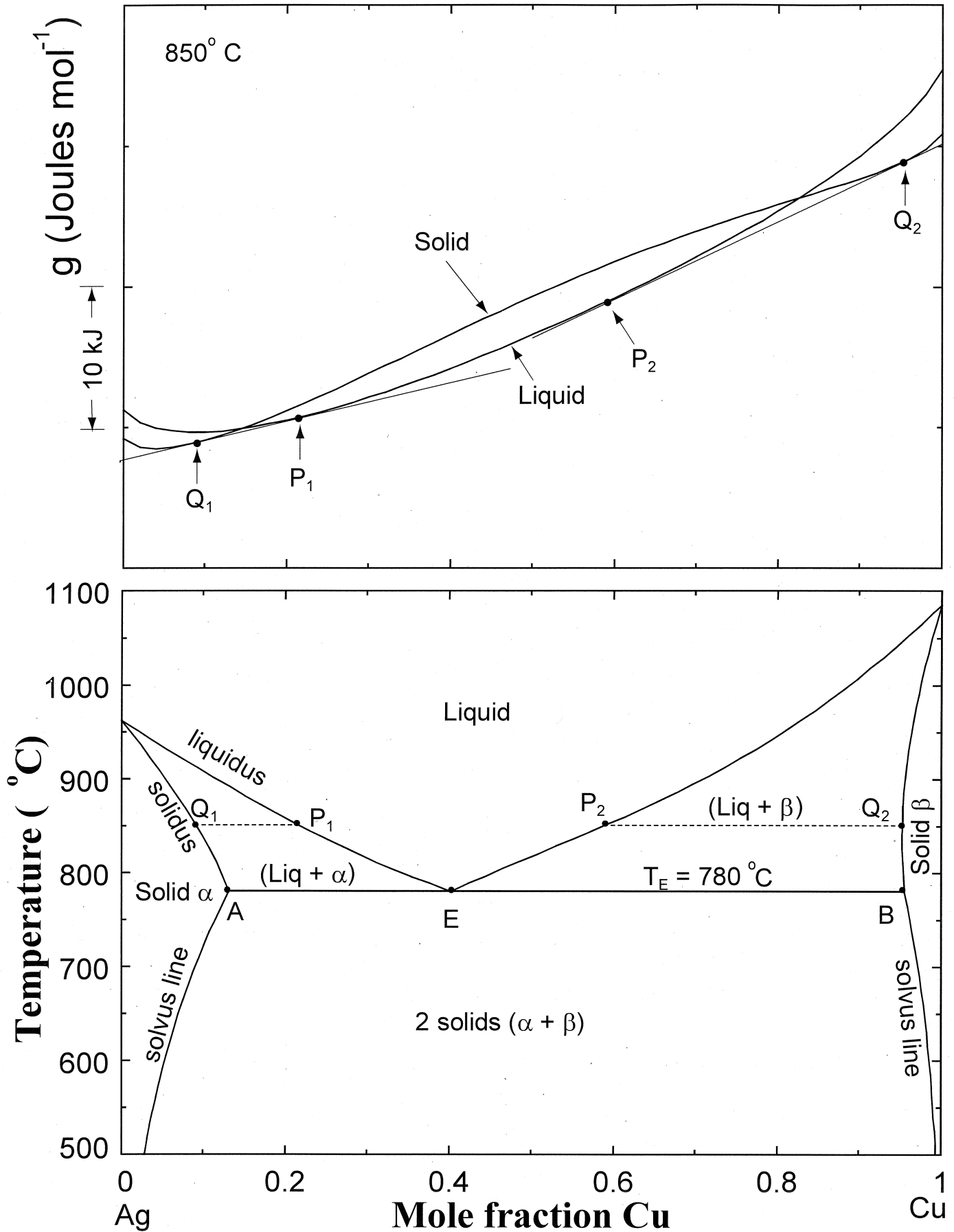


Figure 20. Topological changes in the phase diagram for a system A-B with regular solid and liquid phases brought about by systematic changes in the regular solution parameters  $\omega^S$  and  $\omega^L$ . Melting points of pure A and B are 800 K and 1200 K. Entropies of fusion of both A and B are  $10.0 \text{ J mol}^{-1}\text{K}^{-1}$  (Pelton and Thompson, 1975). Dashed curve in panel (d) is a metastable liquid miscibility gap.

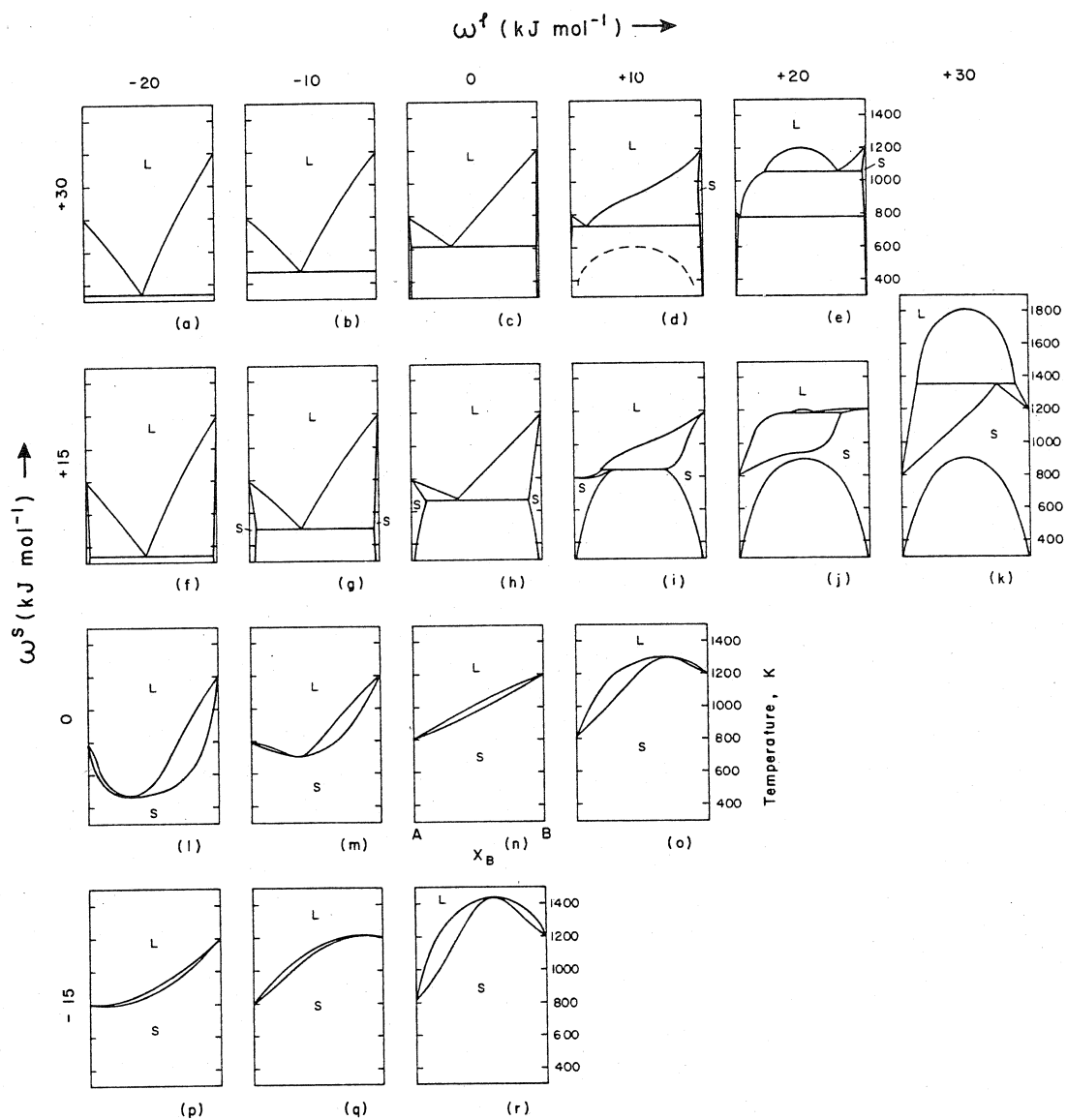


Figure 21. CaO-SiO<sub>2</sub> phase diagram at  $P = 1$  bar and Gibbs energy curves at 1500°C illustrating Gibbs energies of fusion and formation of the compound CaSiO<sub>3</sub> (see FactSage) (reprinted with permission from Pelton, 2001a). The temperature difference between the peritectic at 1464°C and the eutectic at 1463°C has been exaggerated for the sake of clarity.

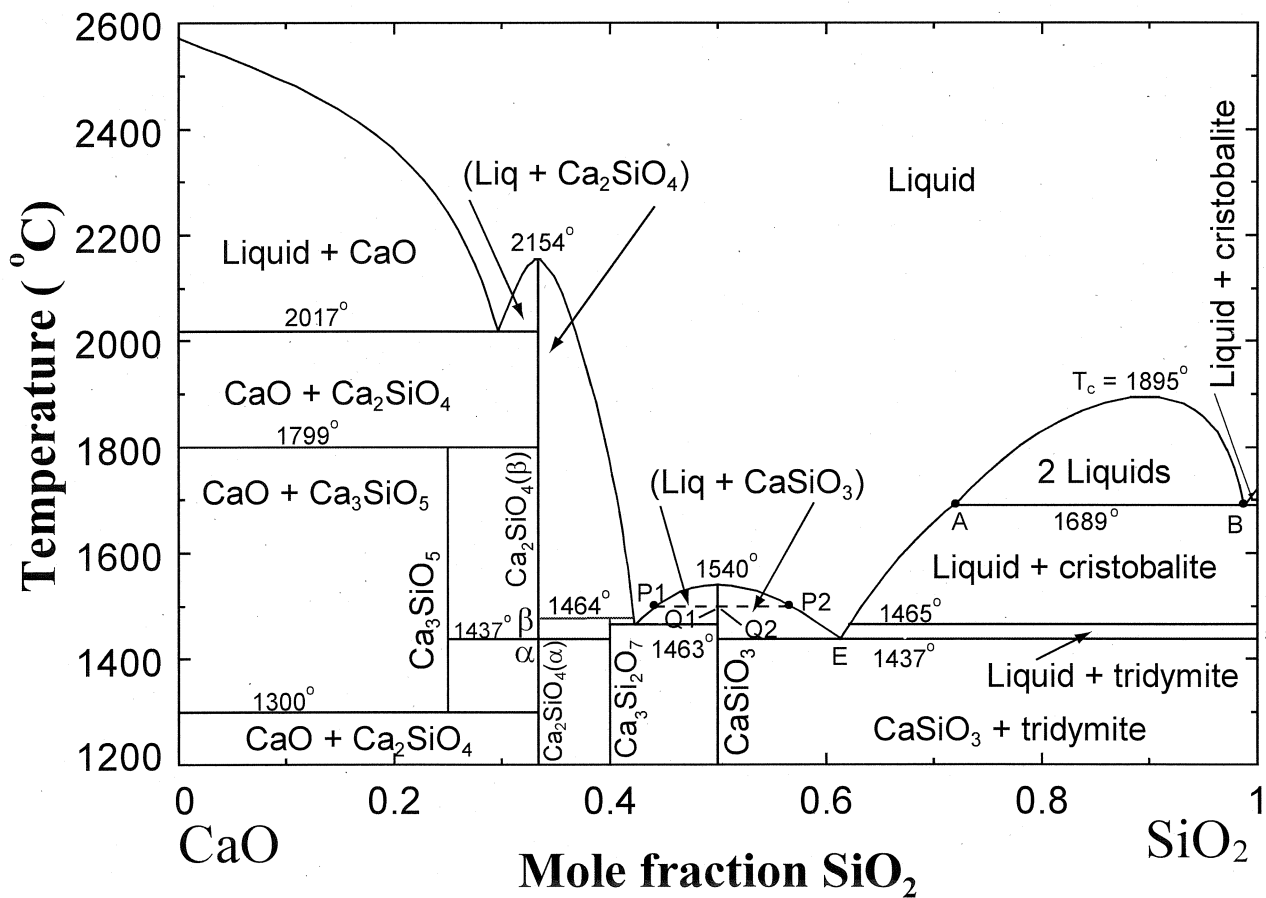
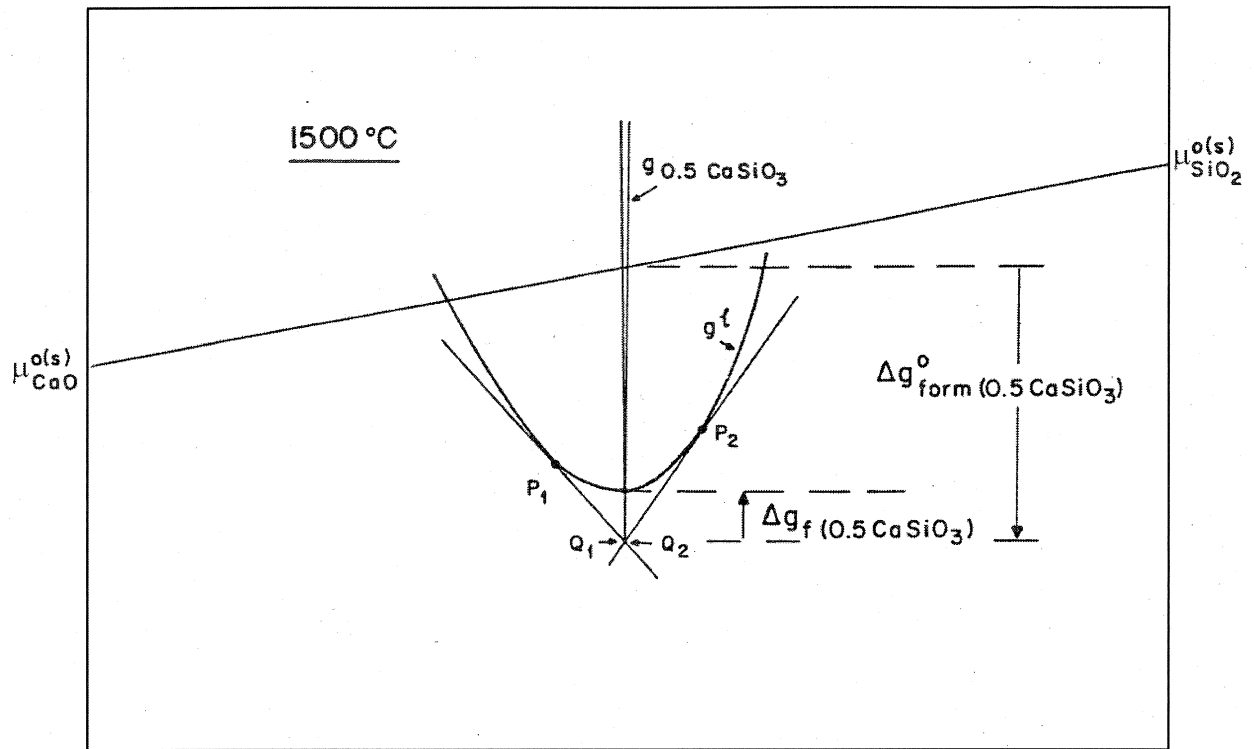


Figure 22. Ag-Mg phase diagram at  $P = 1$  bar (after Hultgren et al., 1973) and Gibbs energy curves at three temperatures.

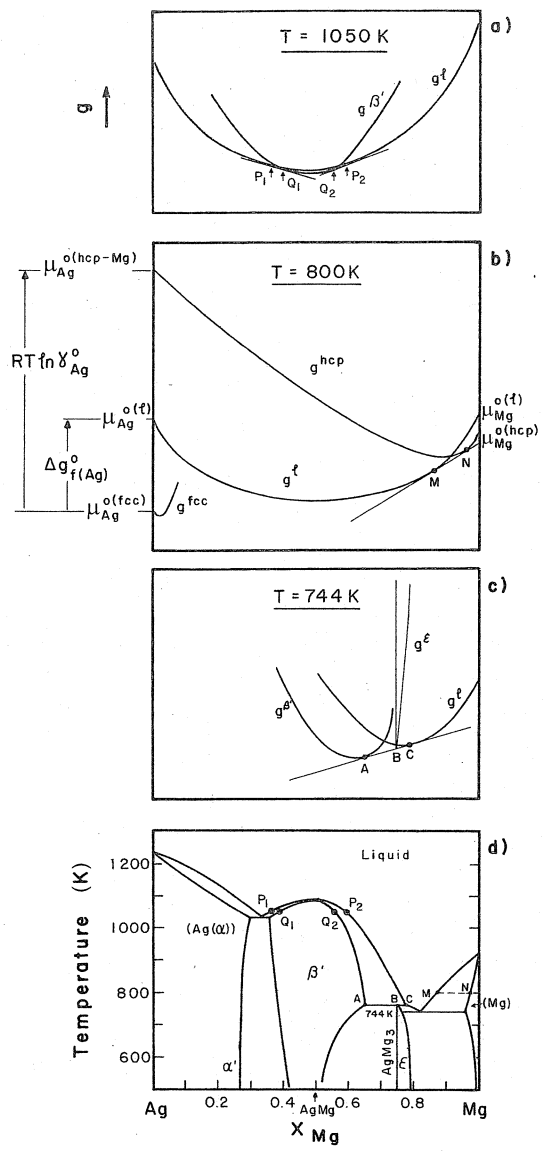


Figure 23. Geometrical units of binary phase diagrams, illustrating rules of construction.

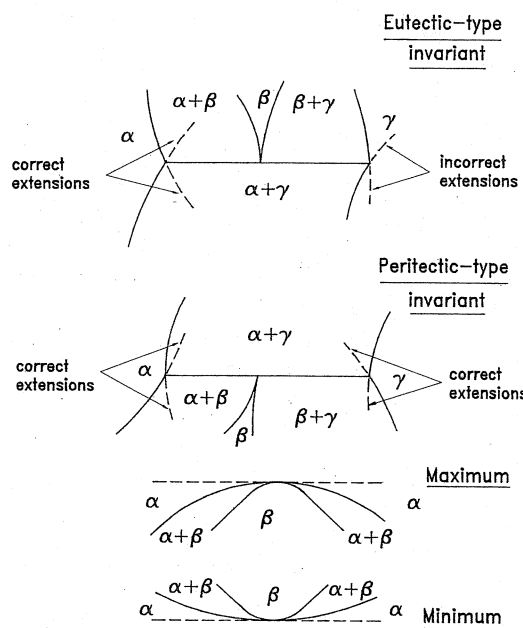


Figure 24. Projection of the liquidus surface of the Bi-Sn-Cd system onto the ternary composition triangle (after Bray et al., 1961-1962.) Small arrows show the crystallization path of an alloy of overall composition at point a. ( $P = 1$  bar).

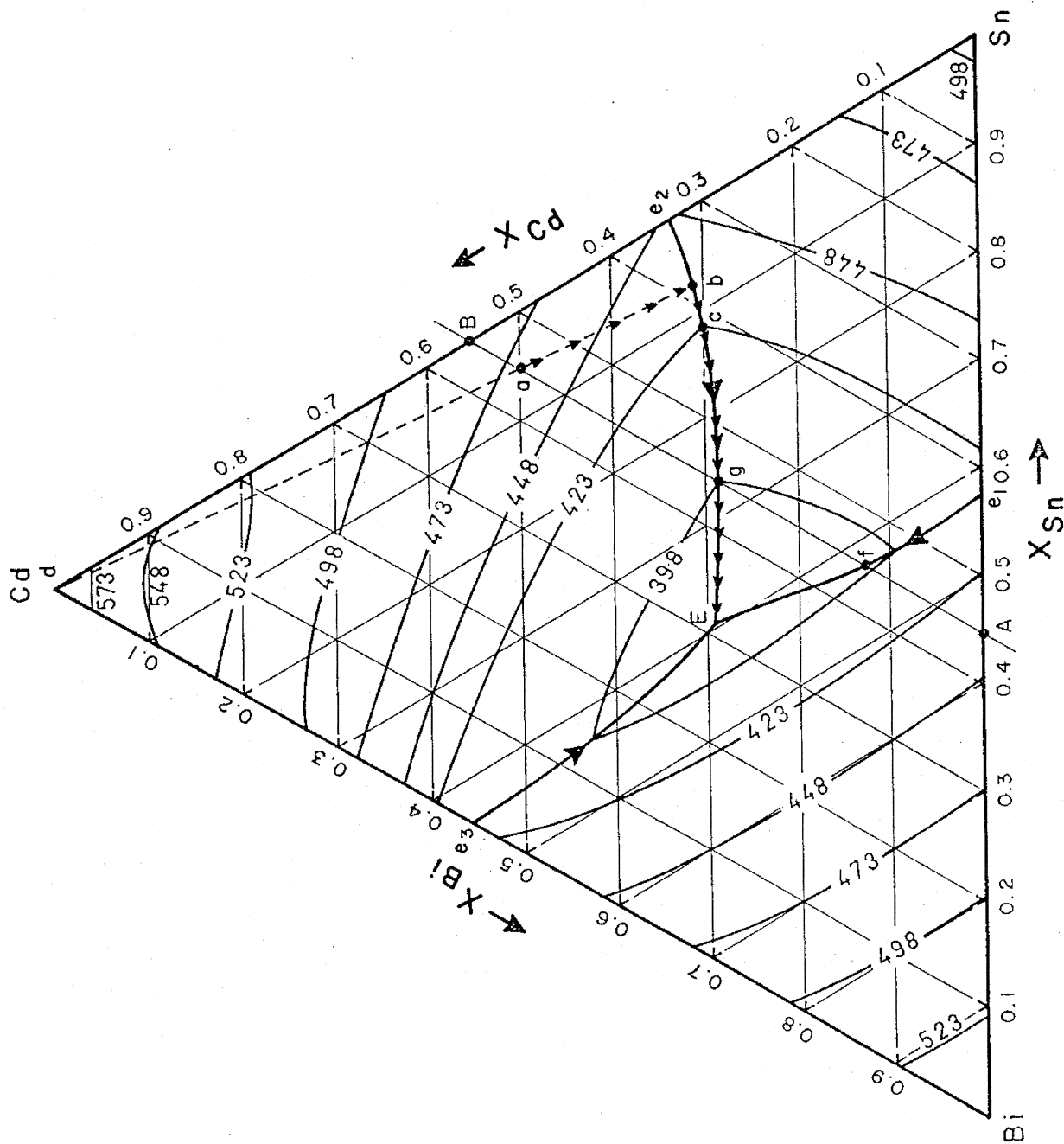


Figure 25. Perspective view of ternary space model of a simple eutectic ternary system.  $e_1$ ,  $e_2$  and  $e_3$  are the binary eutectics and  $E$  is the ternary eutectic. The base of the prism is the equilateral composition triangle (pressure = constant).

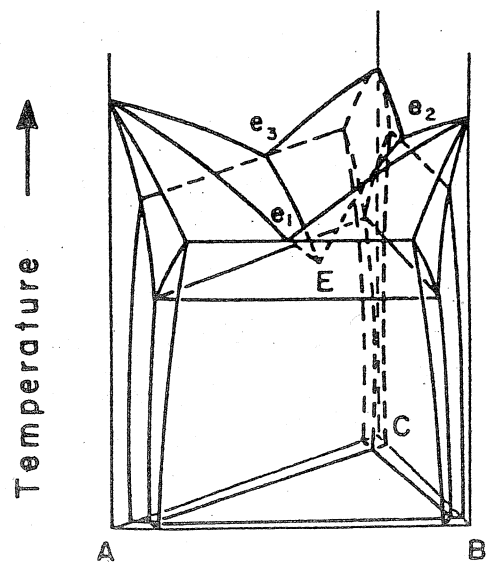


Figure 26. Projection of the liquidus surface of a system A-B-C. The binary subsystems A-B and C-A are simple eutectic systems. The binary phase diagram B-C is shown in the insert. All solid phases are assumed pure stoichiometric components or compounds. Small arrows show crystallization paths of alloys of compositions at points *a* and *b*.

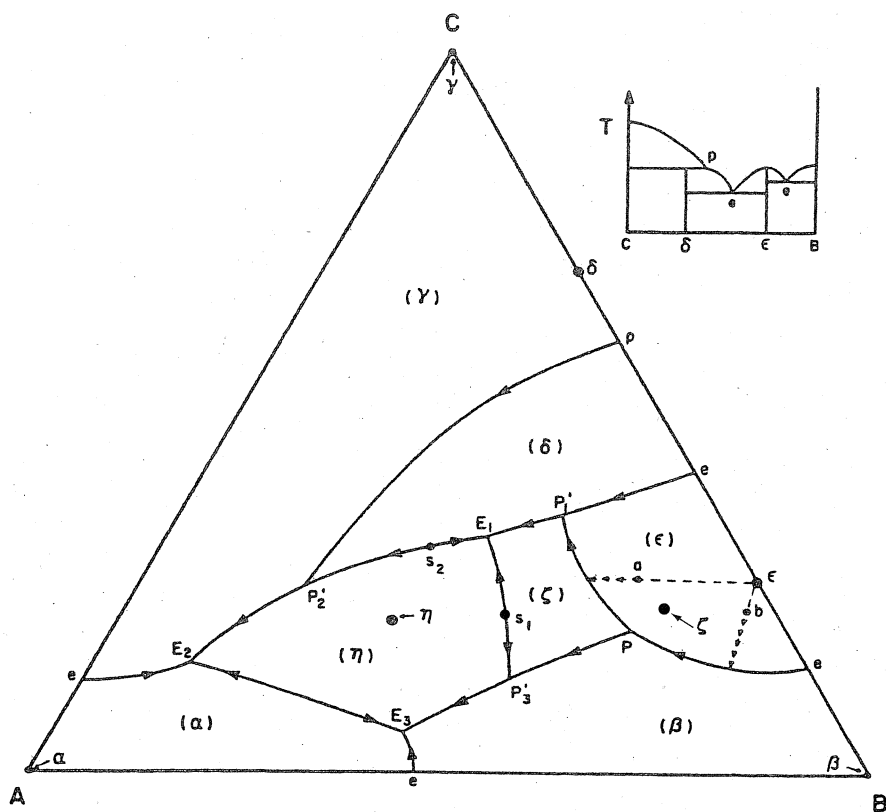


Figure 27. Polythermal projection of the liquidus surface of the Zn-Mg-Al system at  $P = 1$  bar (see FactSage).

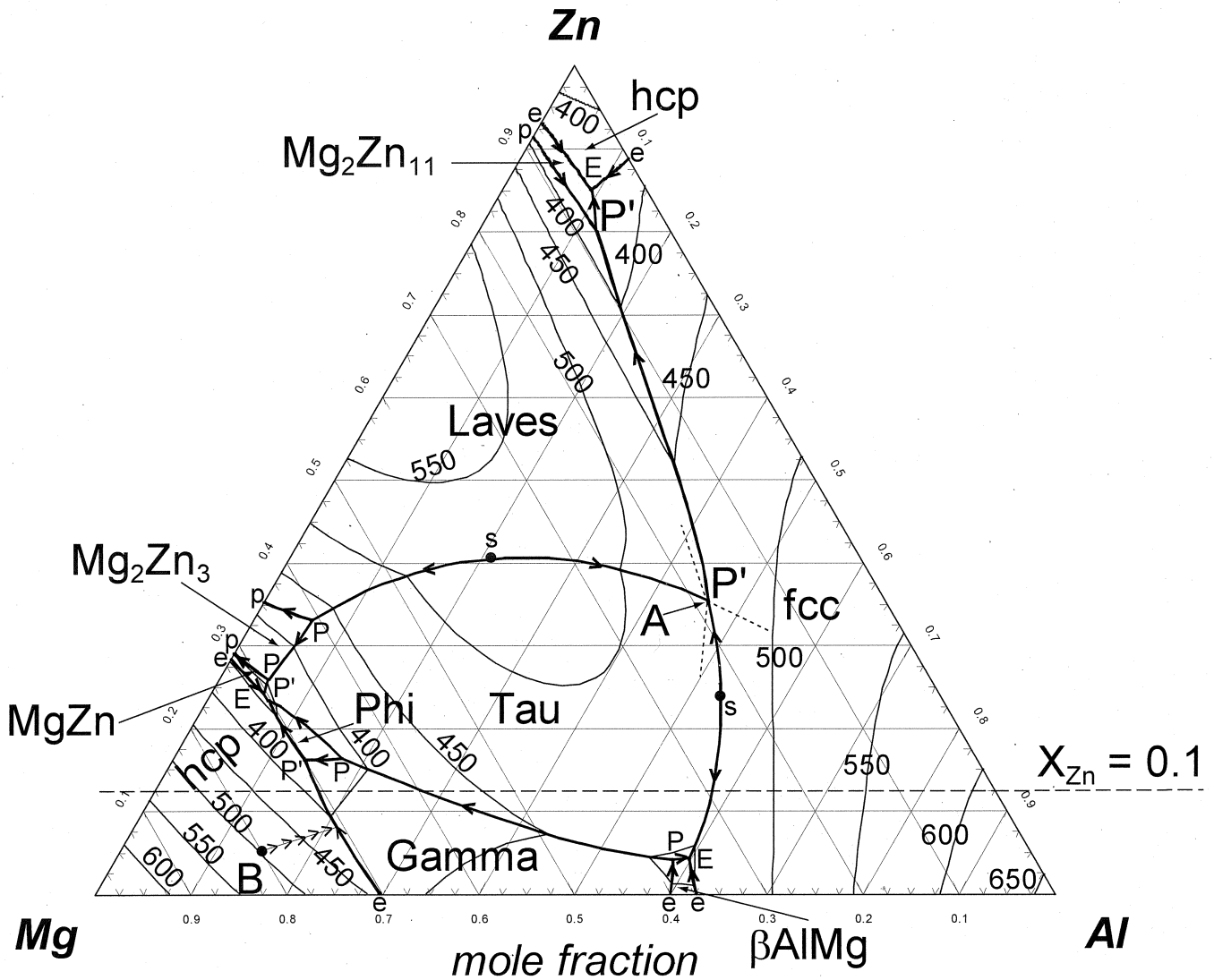


Figure 28. Isothermal section of the Bi-Sn-Cd system at 423 K at  $P = 1$  bar (after Bray et al., 1961-1962). Extents of solid solubility in Bi and Sn have been exaggerated for clarity of presentation.

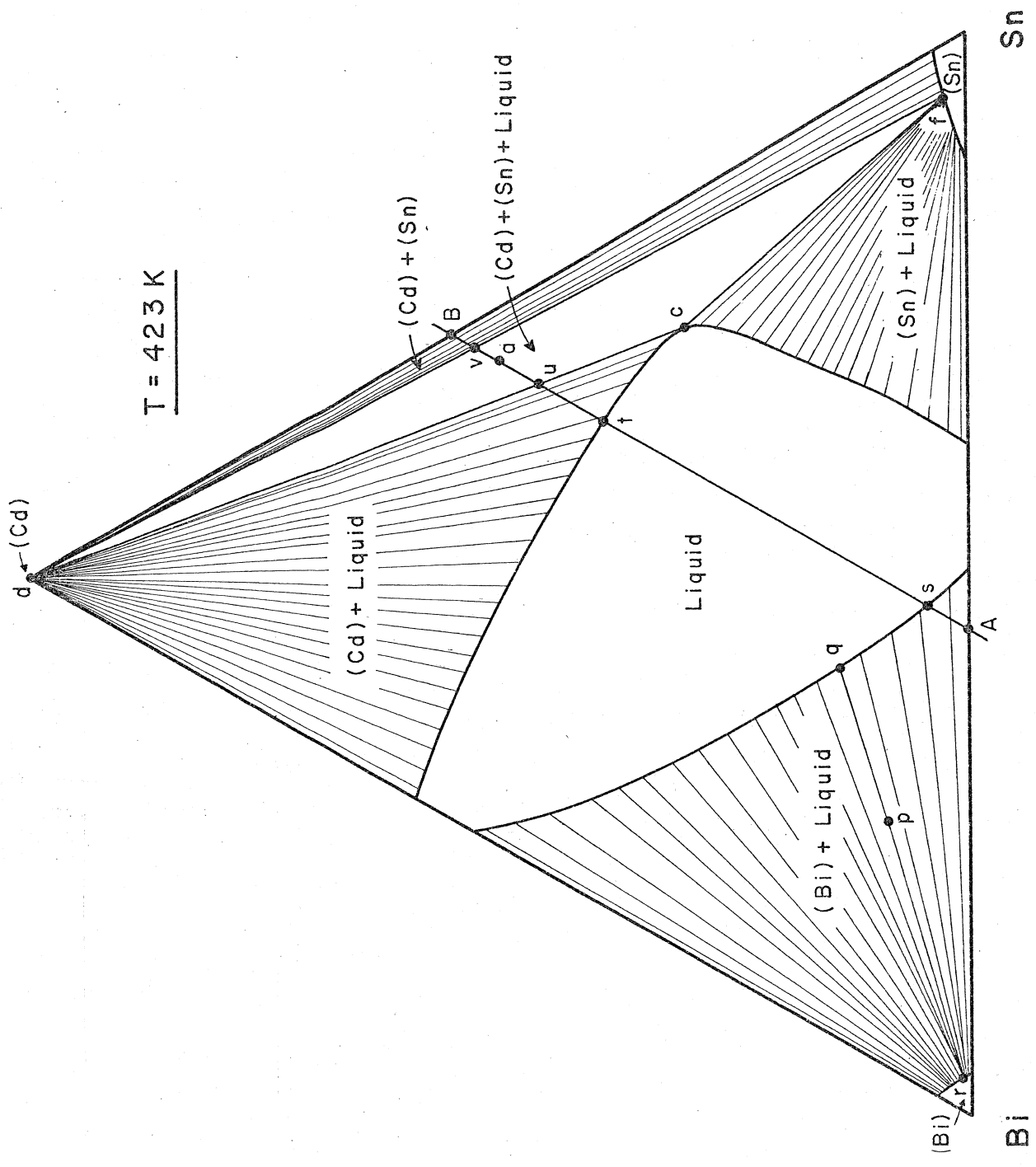


Figure 29. A tie-triangle in a ternary isothermal (and isobaric) section illustrating the lever rule and the extension rule (Schreinemakers' rule).

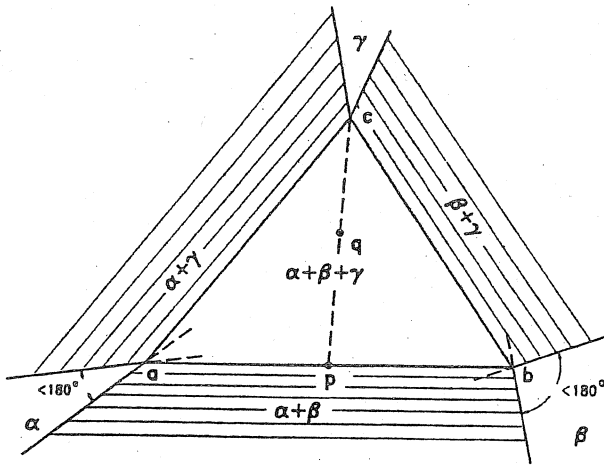


Figure 30. Isopleth (constant composition section) of the Bi-Sn-Cd system at  $P = 1$  bar following the line  $AB$  of Fig. 24. (Extents of solid solubility in the terminal solid solutions have been exaggerated for clarity of presentation.)

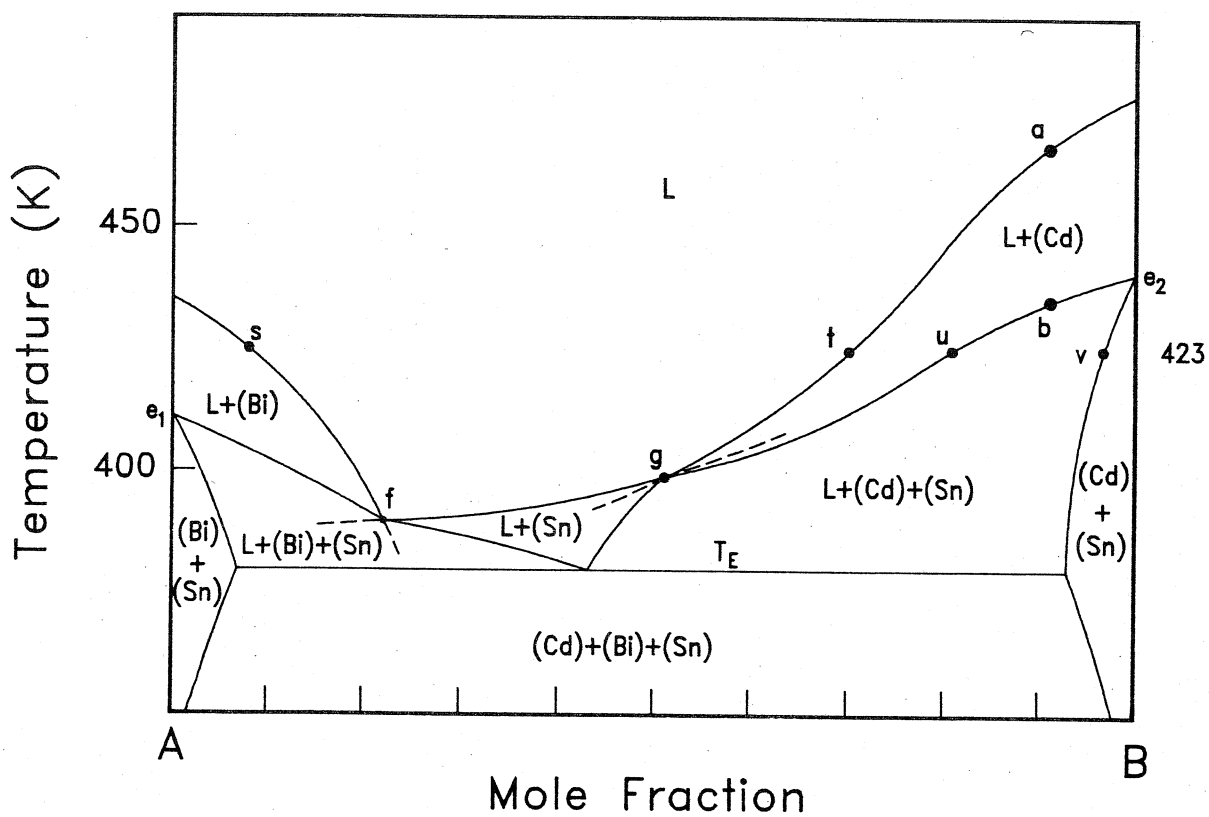


Figure 31. An isobaric temperature-composition phase diagram with the eutectic “opened up” to show that it is an infinitely narrow three-phase region (reprinted with permission from Pelton, 2001a).

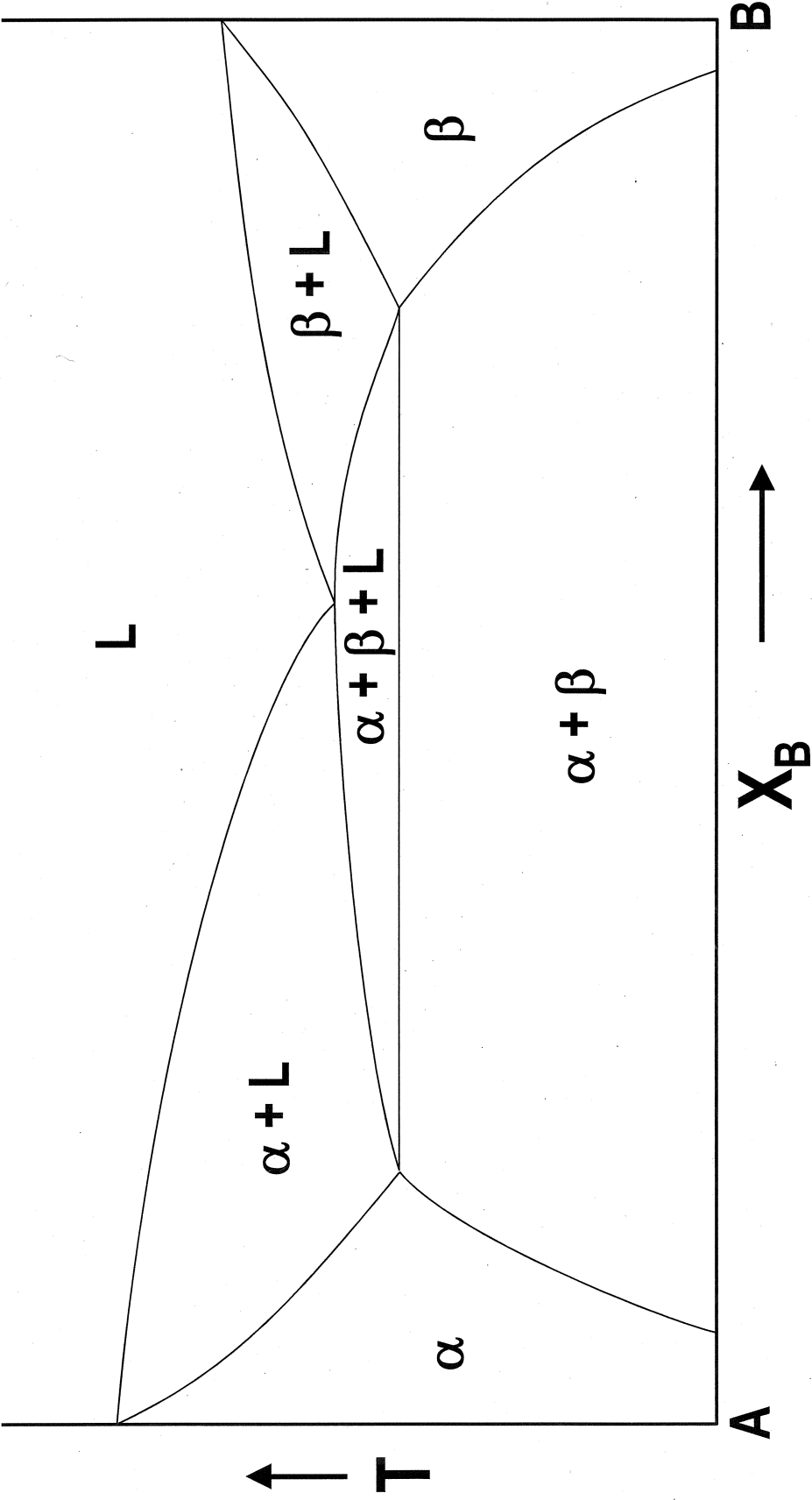


Figure 32. A  $P$ - $T$  diagram in a one-component system “opened up” to show that the two-phase lines are infinitely narrow two-phase regions (reprinted with permission from Pelton, 2001a).

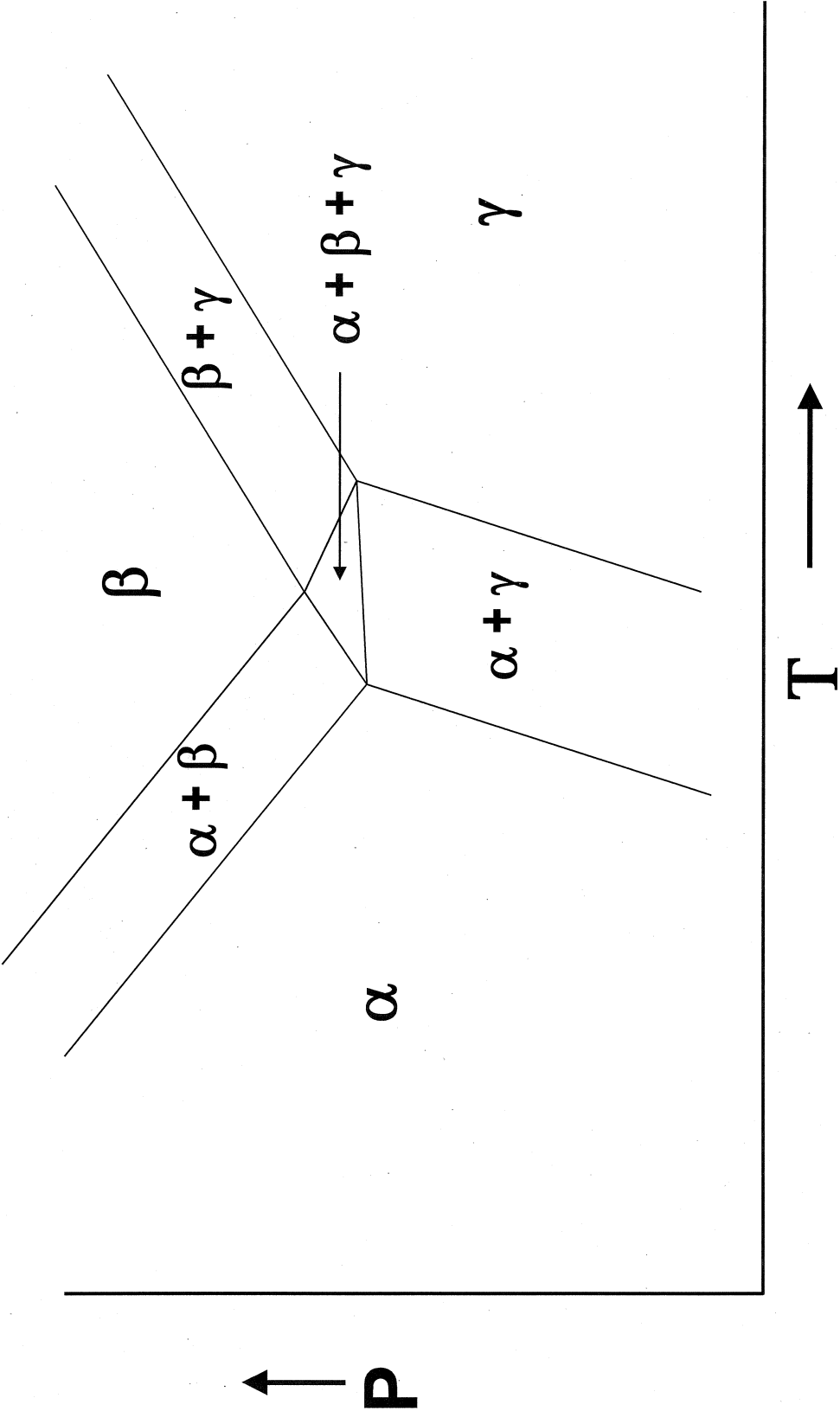


Figure 33. A node in a general phase diagram section. Schreinemakers' Rule is obeyed. Red and blue lines are Zero Phase Fraction (ZPF) lines of the  $\beta$  and  $\gamma$  phases respectively (reprinted with permission from Pelton, 2001a).

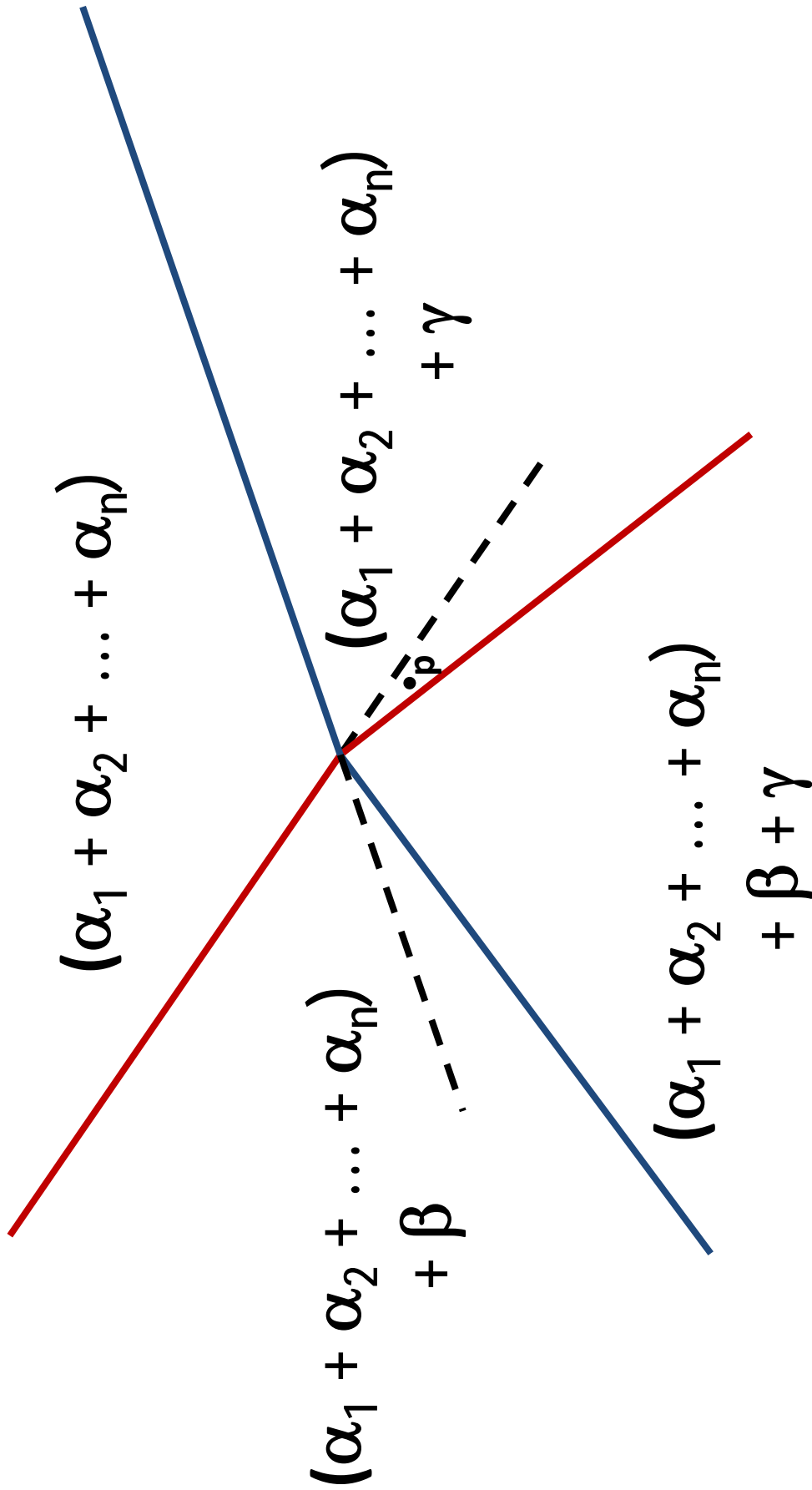


Figure 34. Binary  $T$  composition phase diagram at  $P = 1$  bar of the MgO-CaO system showing Zero Phase Fraction (ZPF) lines of the phases (see FactSage).

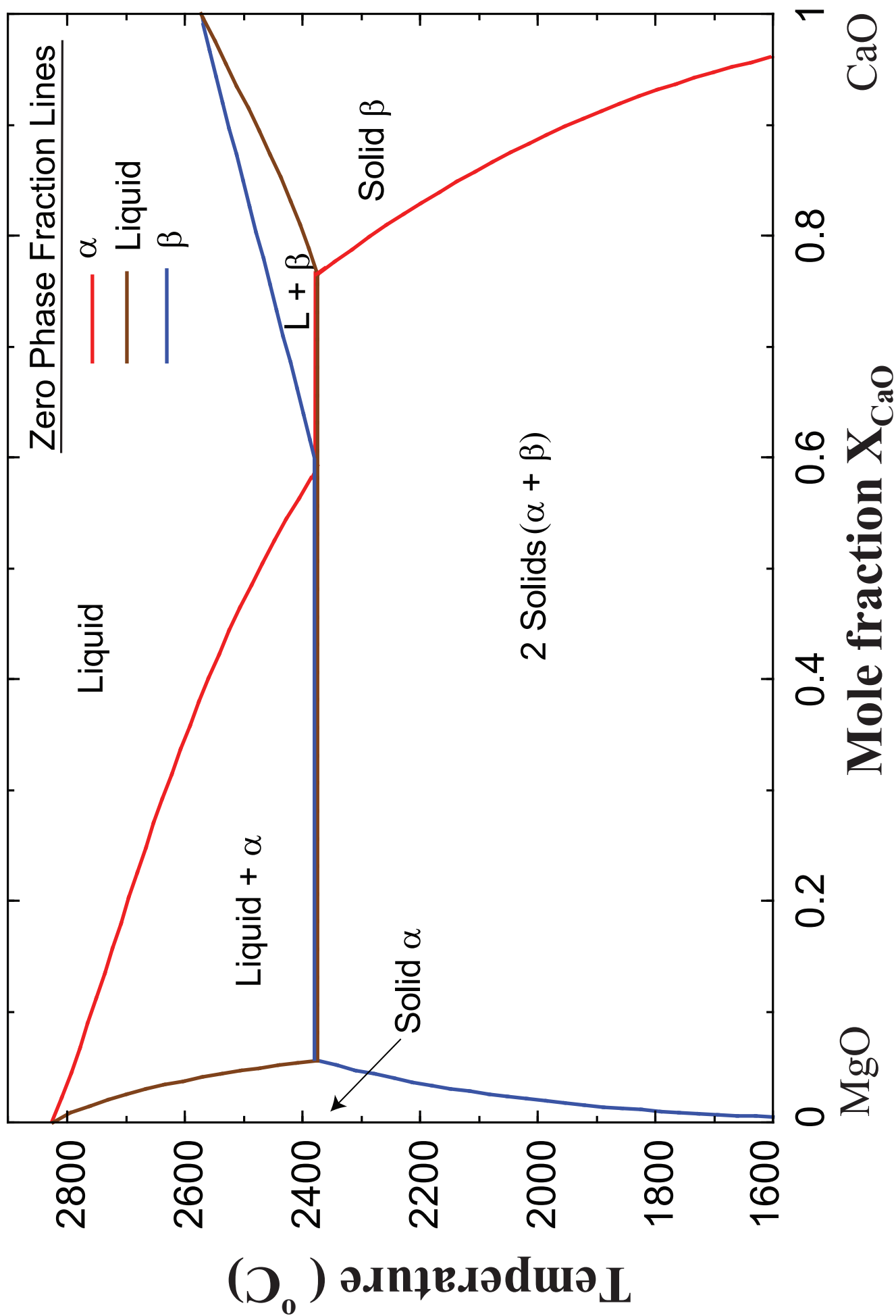


Figure 35. Schematic  $P$ - $V$  diagram for  $H_2O$ . This is not a single-valued phase diagram section (reprinted with permission from Pelton, 2001a).

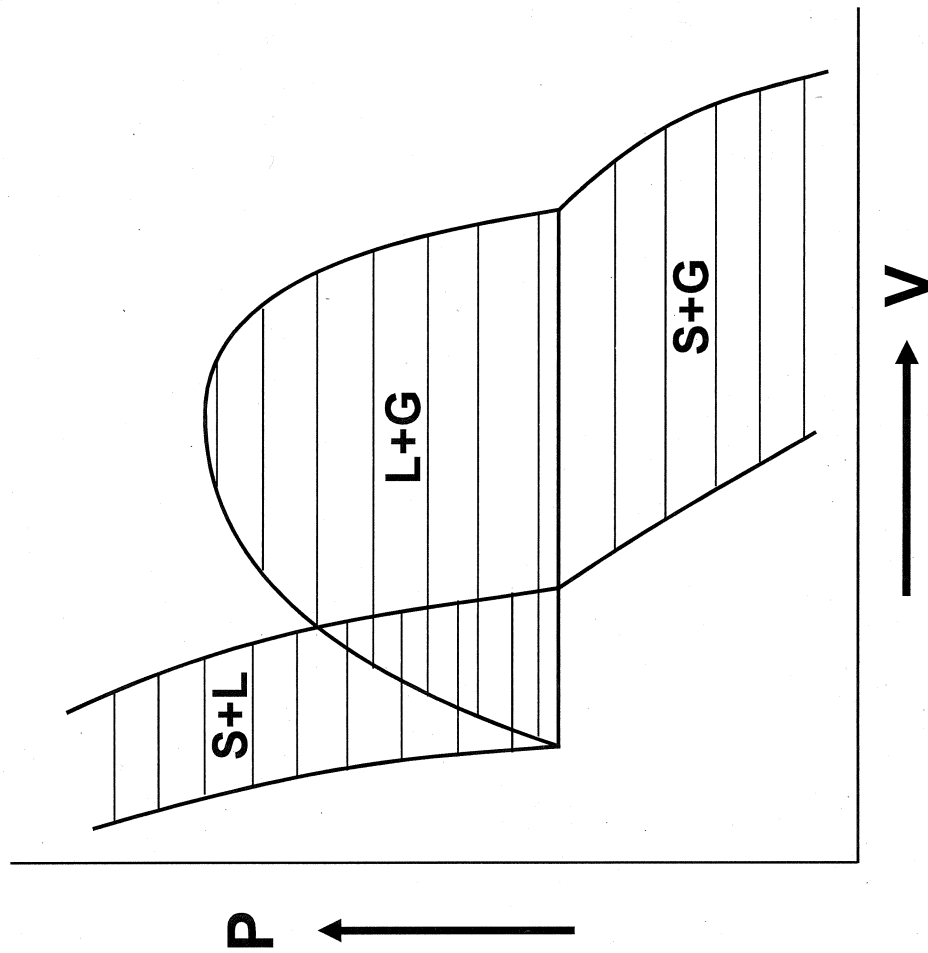


Figure 36. Equilibrium  $S_2$  pressure versus mole fraction of Ni in the Cu-Ni- $S_2$  system at  $427^\circ\text{C}$ . This is not a single-valued phase diagram (see FactSage).

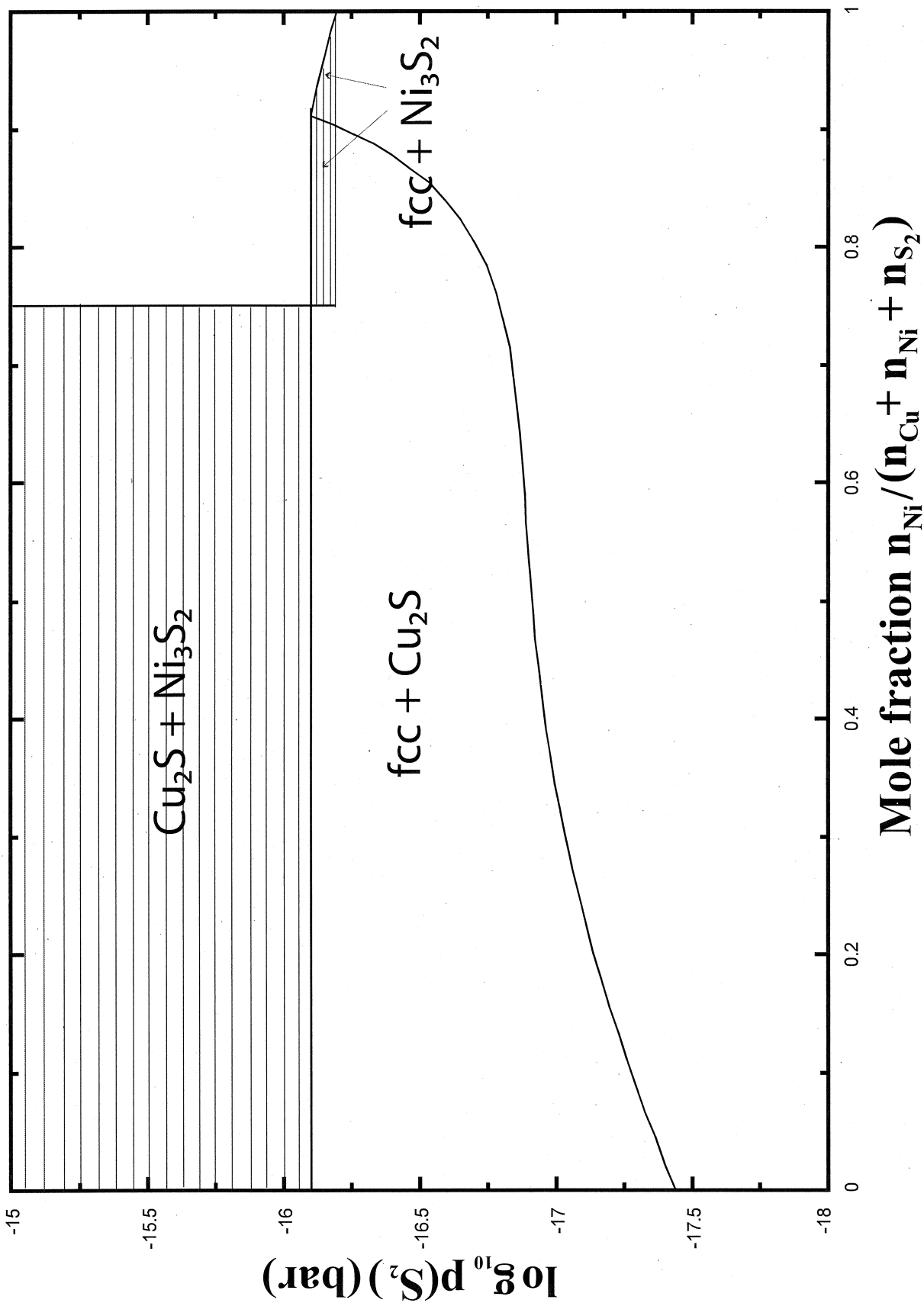


Figure 37. Equilibrium  $S_2$  pressure versus molar ratio  $n_{Ni}/(n_{Cu} + n_{Ni})$  in the Cu-Ni- $S_2$  system at  $427^\circ C$ . This is a single-valued phase diagram (see FactSage).

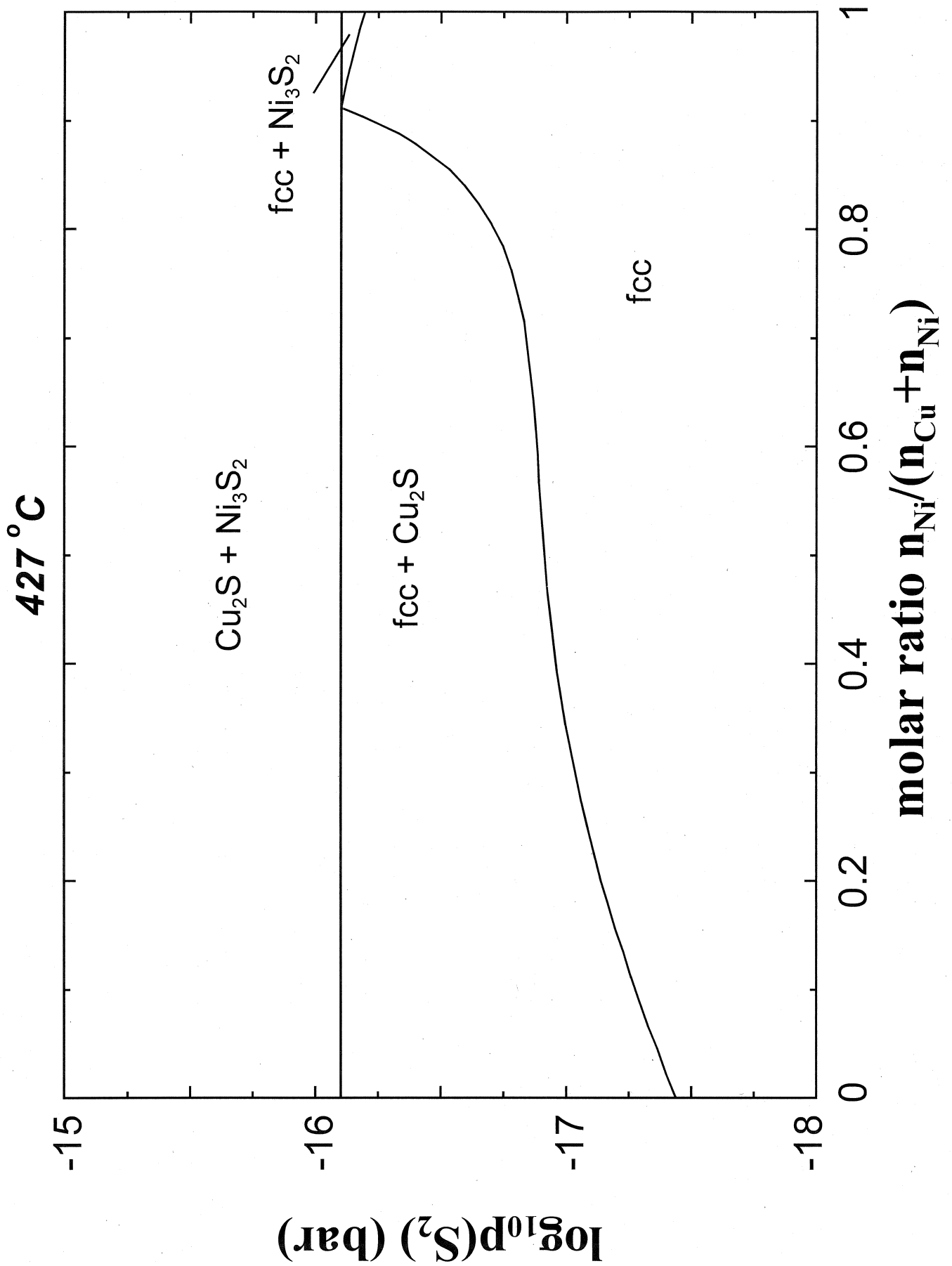


Figure 38. Corresponding  $T-X_O$  and  $T - (\mu_{O_2} - \mu_{O_2}^o)$  phase diagrams of the Fe-O system (after Muan and Osborn, 1965).

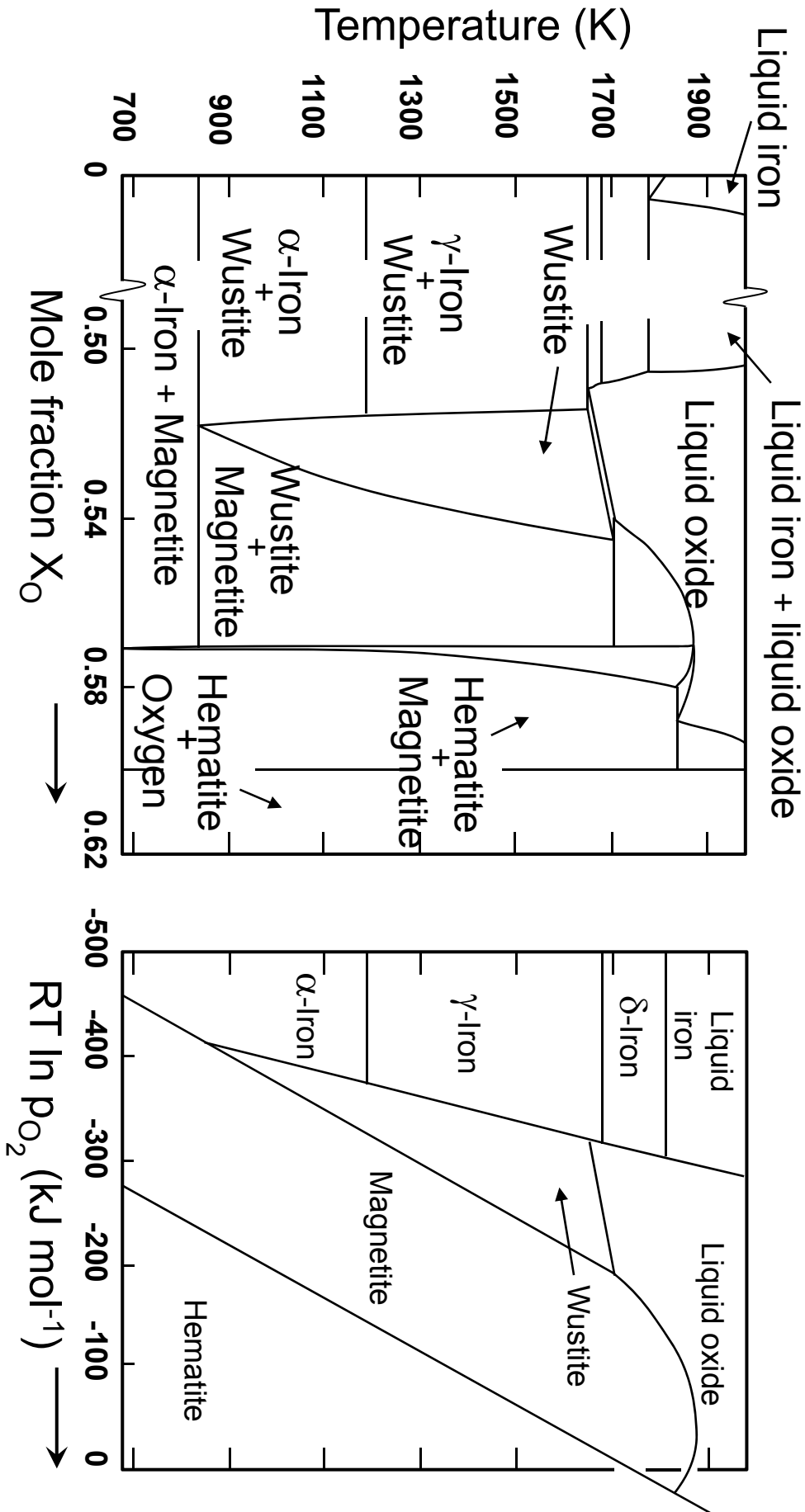


Figure 39. A corresponding set of phase diagrams for a C-component system when the potentials  $\phi_4, \phi_5, \dots, \phi_{C+2}$  are constant (Pelton and Schmalzried, 1973).

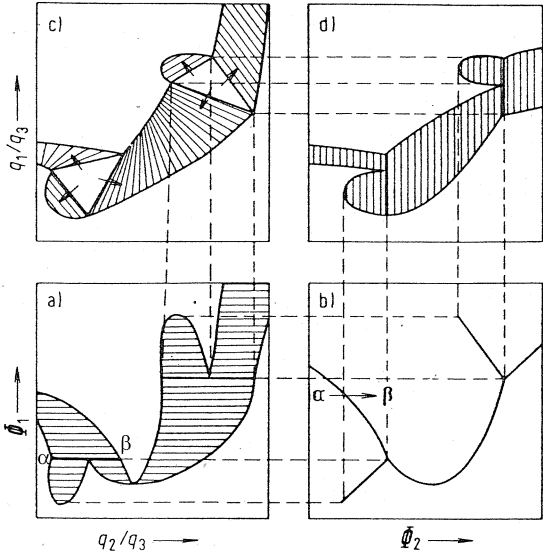


Figure 40. Corresponding phase diagrams of the Fe-Cr-O<sub>2</sub> system at 1300°C (Pelton and Schmalzried, 1973).

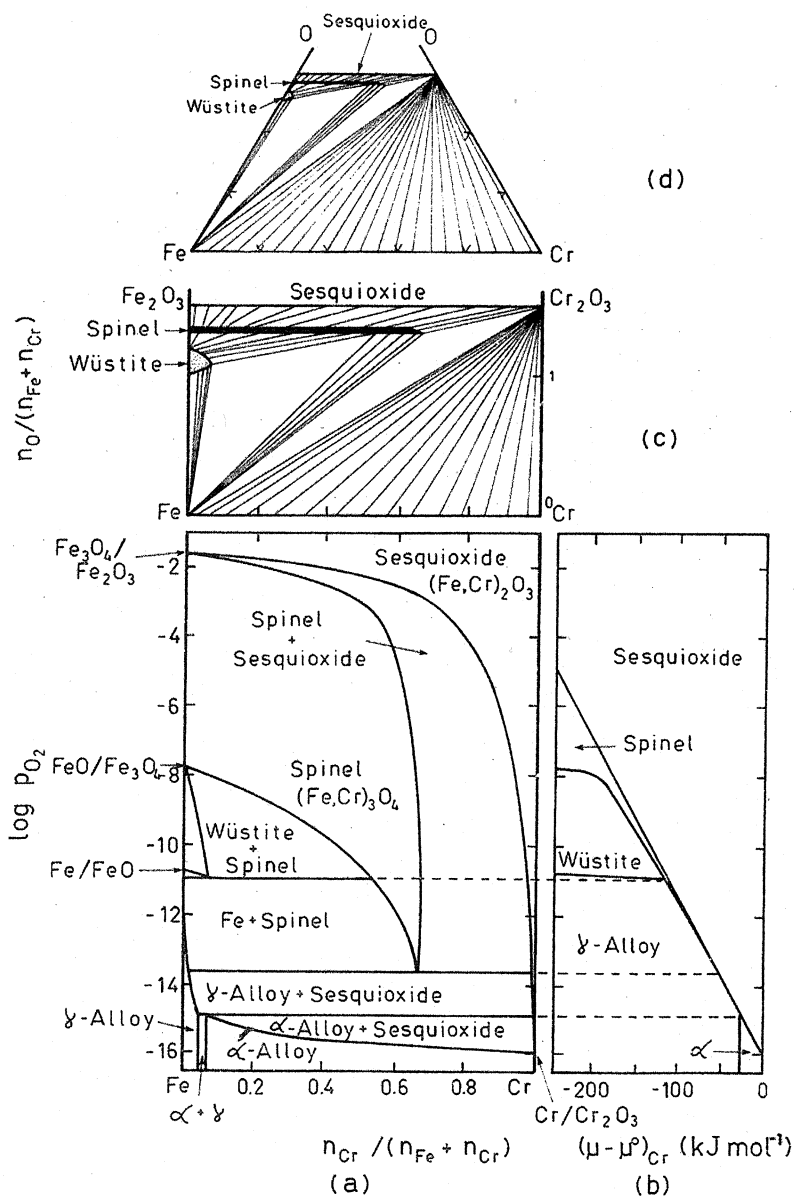


Figure 41. Corresponding  $T$ -composition and enthalpy-composition phase diagrams of the Mg-Si system at  $P = 1$  bar. The enthalpy axis is referred to the enthalpy of the system at equilibrium at  $25^\circ\text{C}$  (see FactSage).

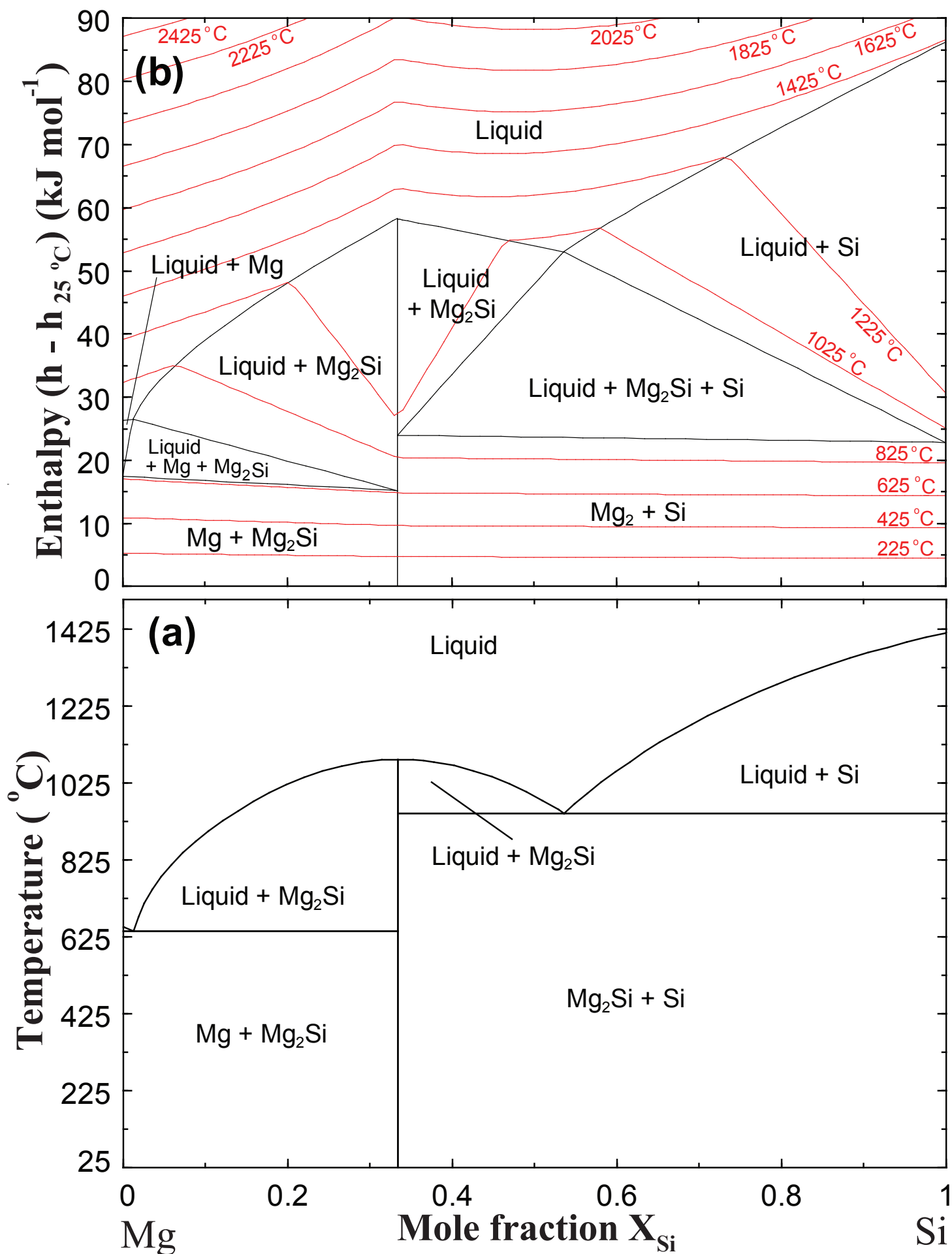


Figure 42.  $\phi_1$ - $\phi_2$ - $\phi_3$  surfaces of  $\alpha$  and  $\beta$  phases in a C-component system when  $\phi_4, \phi_5, \dots, \phi_{C+2}$  are constant (reprinted with permission from Hillert, 2008).

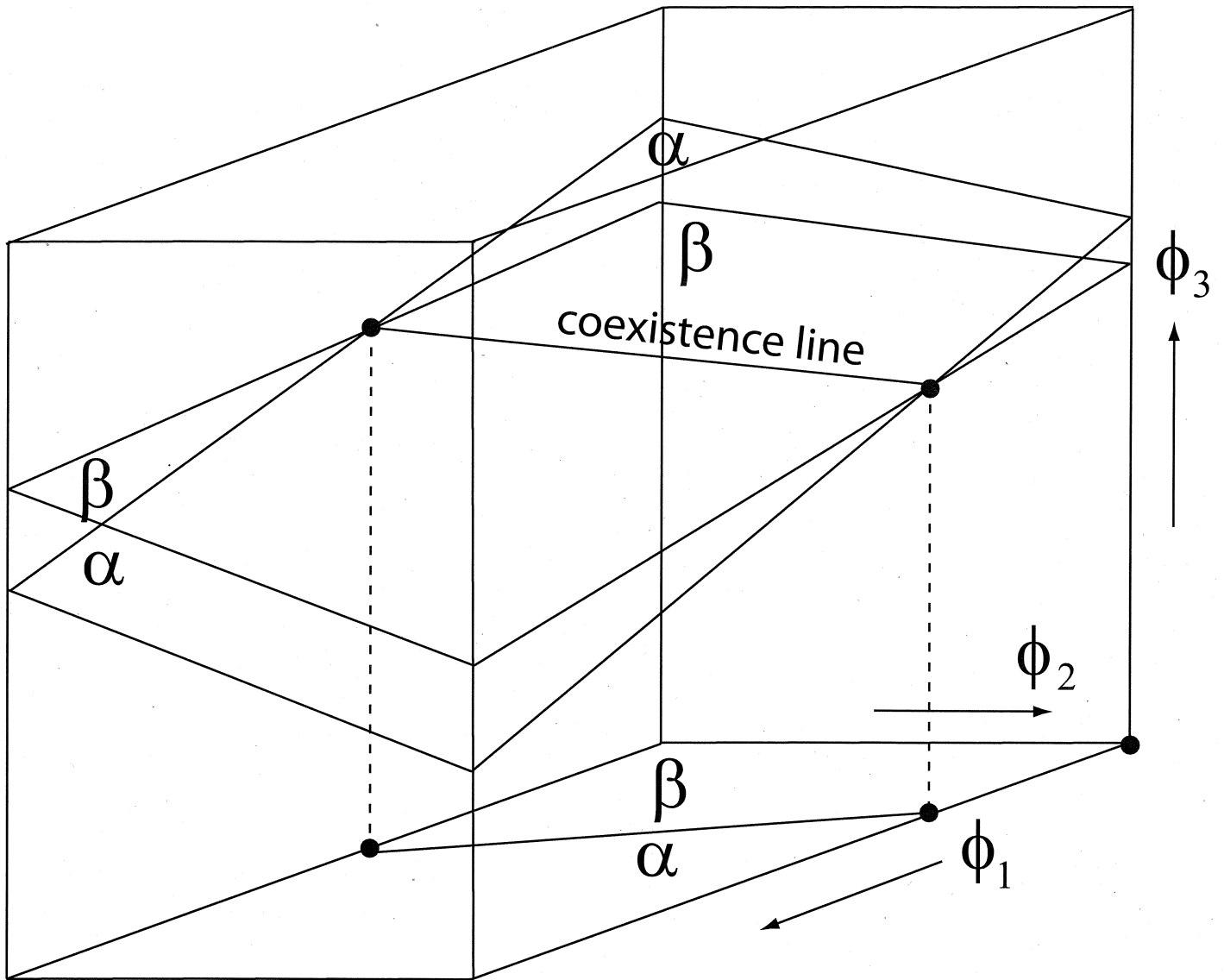


Figure 43. Isoplethal section across the  $\text{Fe}_3\text{O}_4\text{-SiO}_2$  join of the  $\text{Fe-Si-O}_2$  system. ( $P = 1$  bar) (see FactSage).

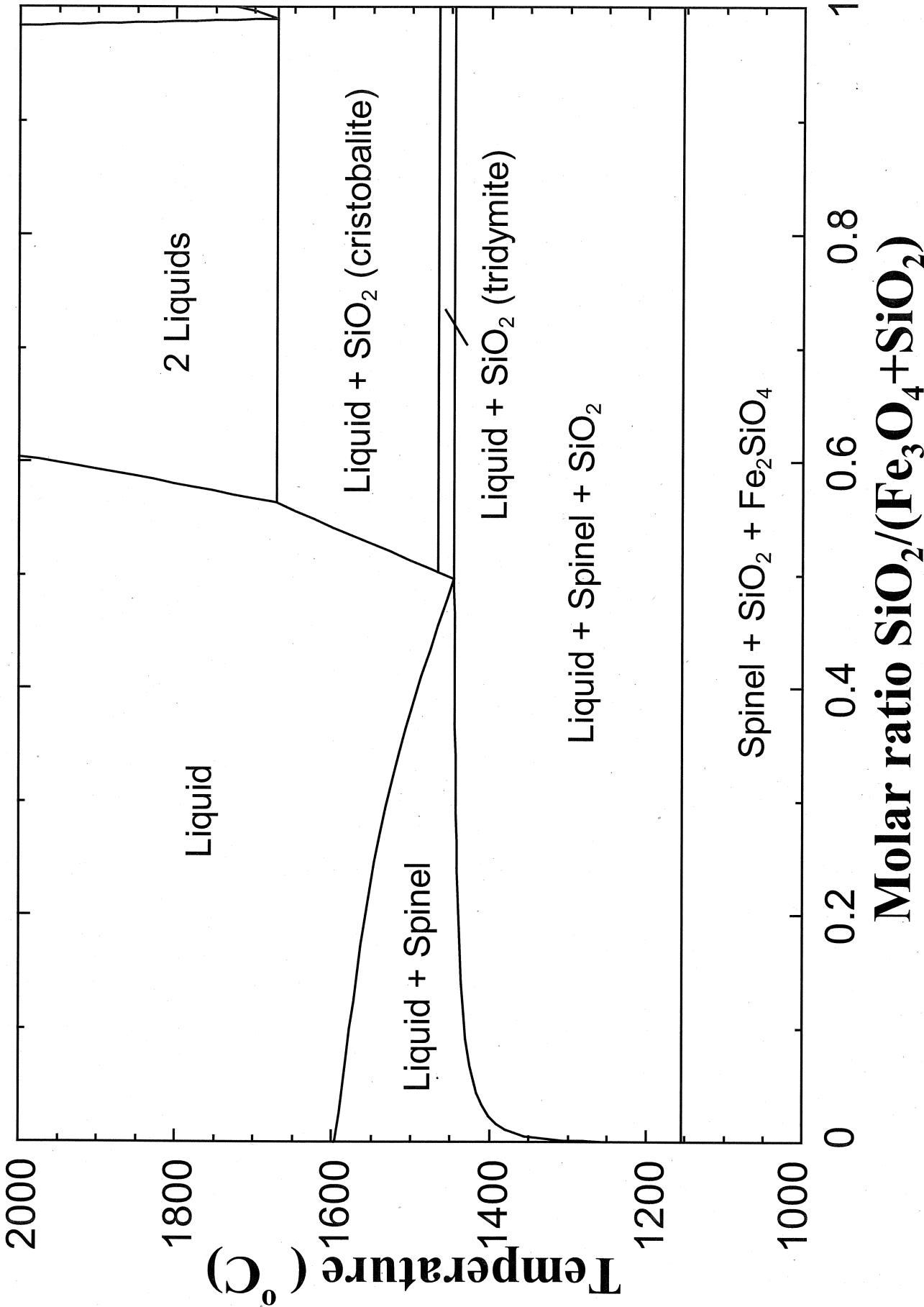


Figure 44. "Fe<sub>2</sub>O<sub>3</sub>-SiO<sub>2</sub> phase diagram in air (p<sub>O<sub>2</sub></sub> = 0.21 bar)" (see FactSage).

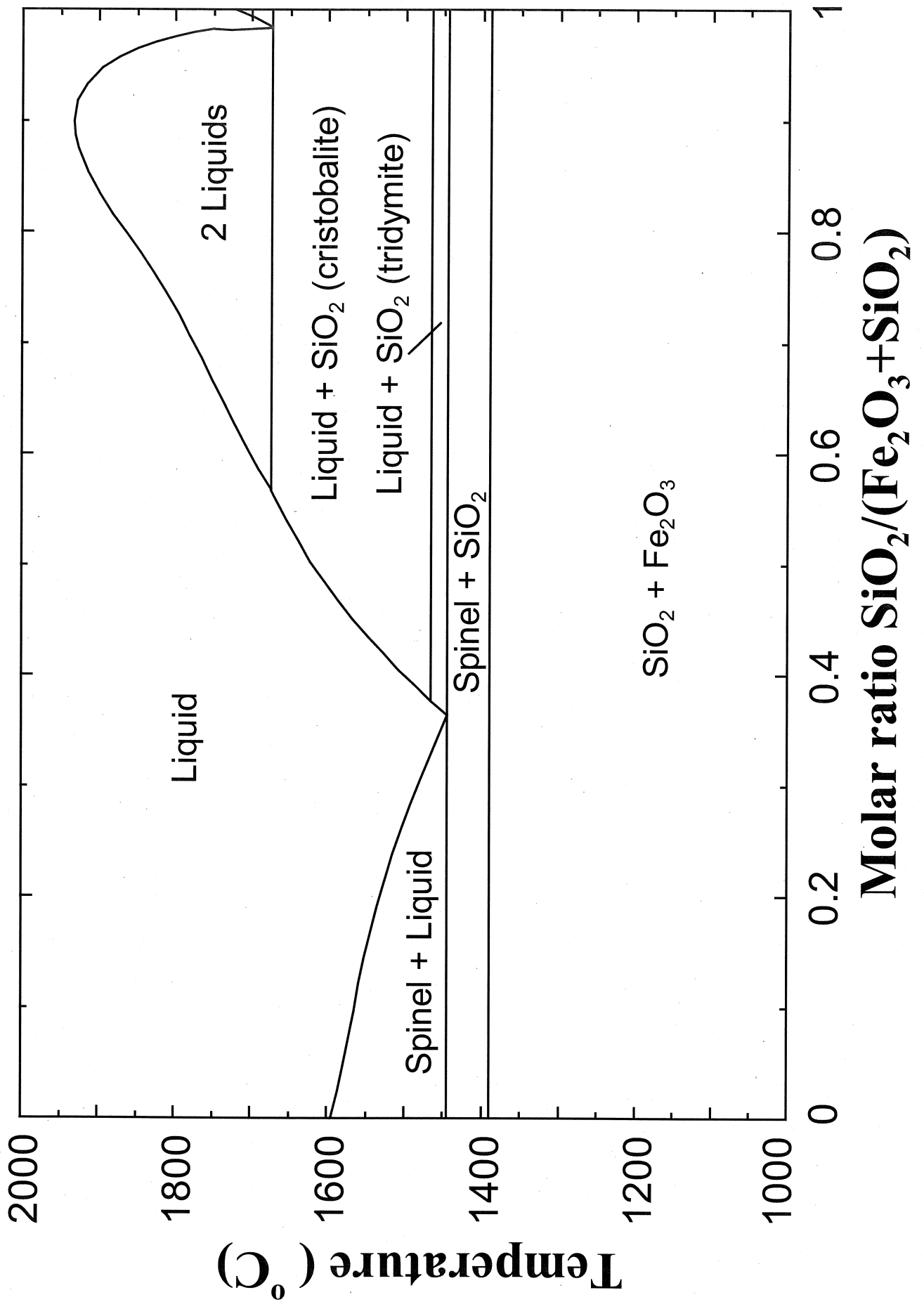


Figure 45. "FeO-SiO<sub>2</sub> phase diagram at Fe saturation" (see FactSage).

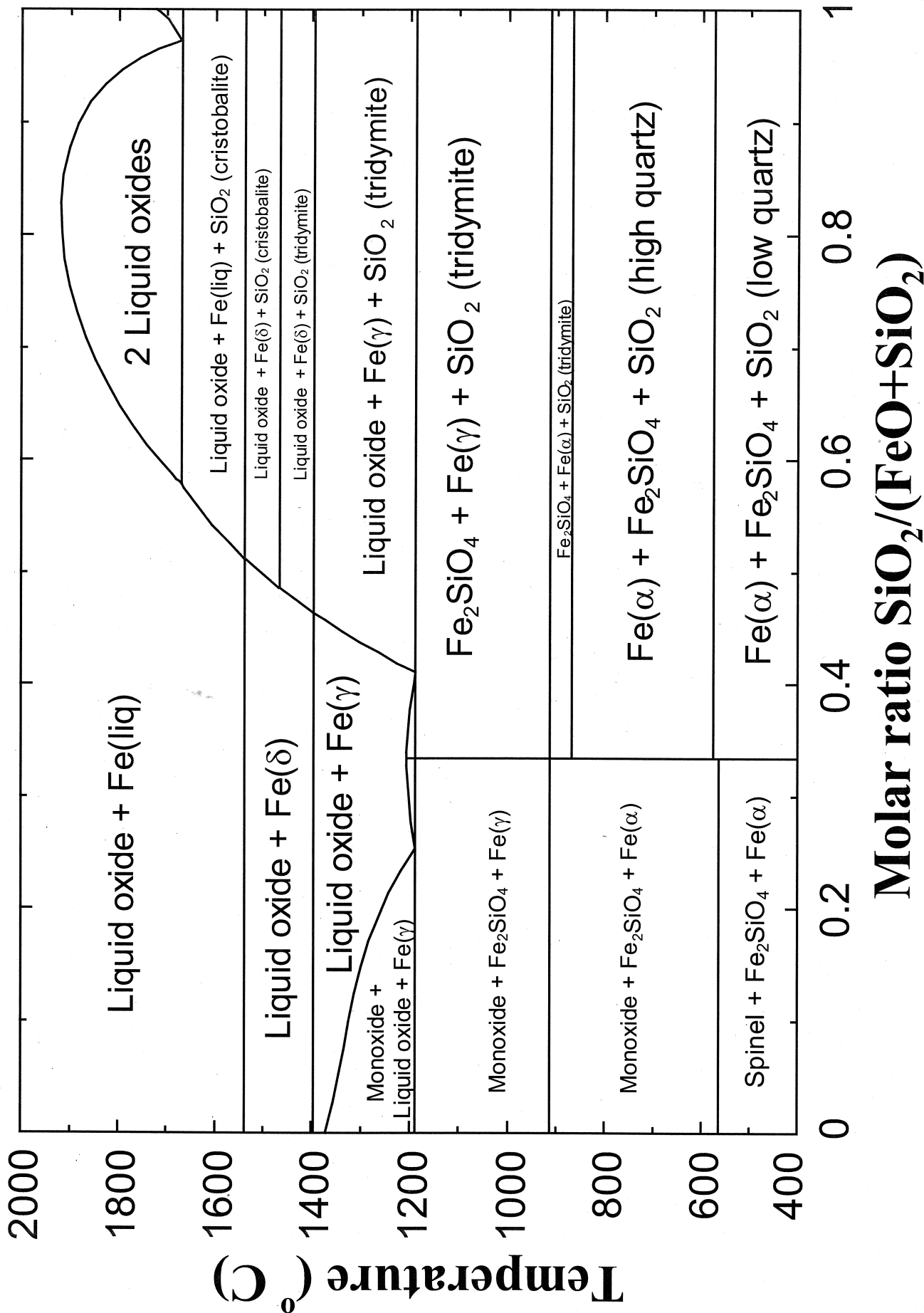


Figure 46. Constant  $p_{O_2}$  line in the Fe-Si-O<sub>2</sub> system illustrating the construction and interpretation Figure 44.

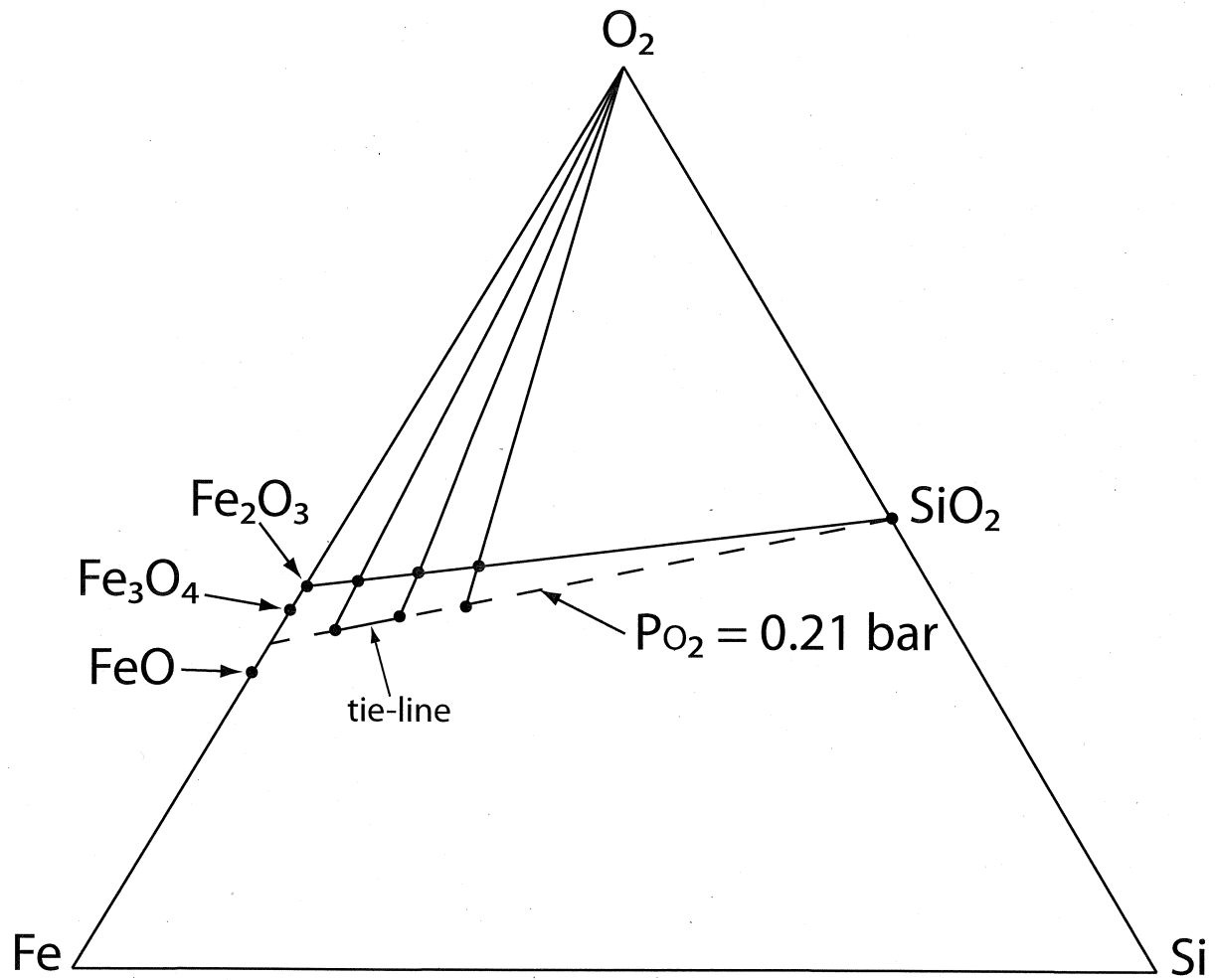
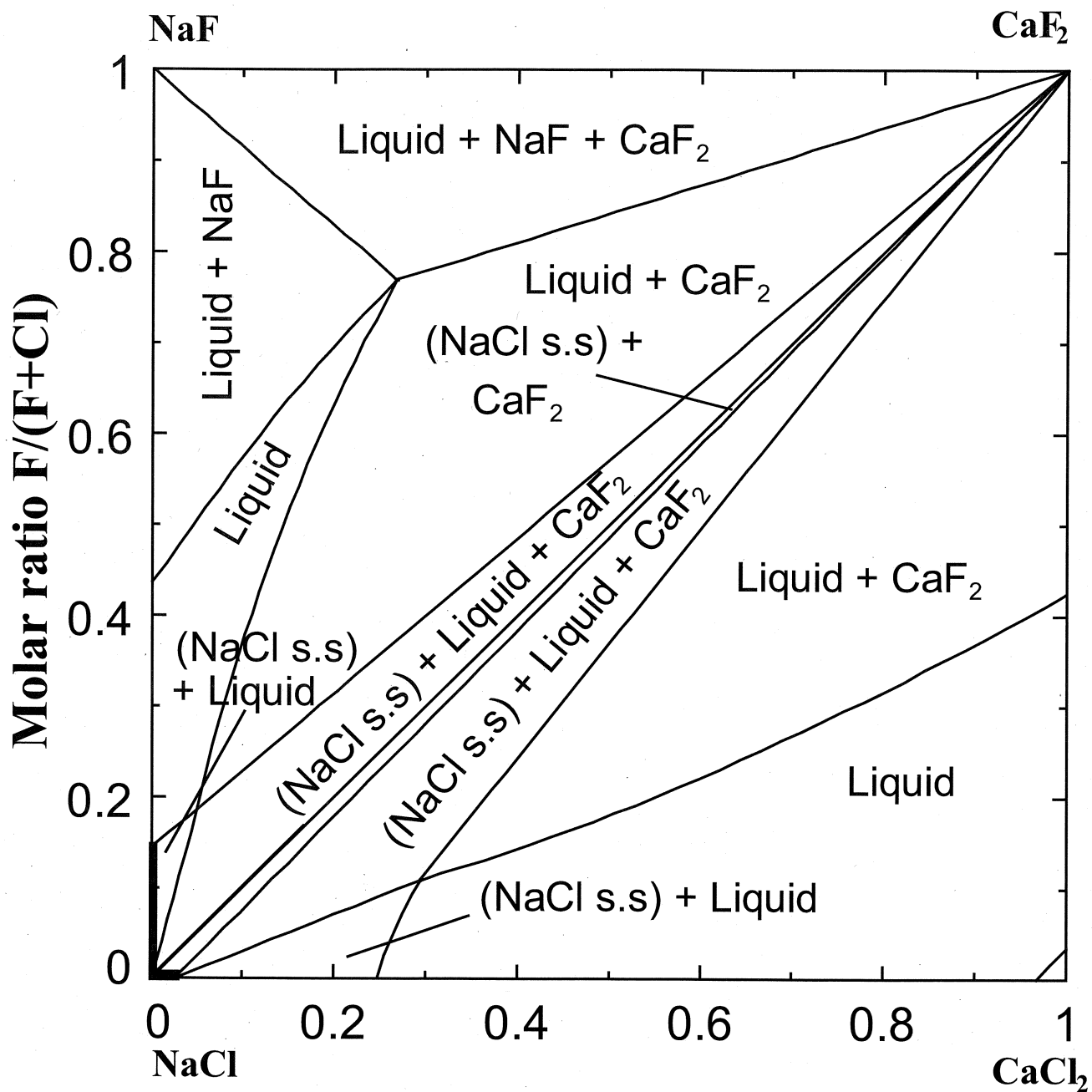


Figure 47. Phase diagram at  $T = 750^{\circ}\text{C}$  and  $P = 1$  bar of the reciprocal system NaCl-CaCl<sub>2</sub>-NaF-CaF<sub>2</sub> (see FactSage).



**Molar ratio  $2Ca/(F+Cl) = 2Ca/(2Ca + Na)$**

Figure 48. Isolethal section of the Mg-Al-Ce-Mn-Y-Zn system at 0.05% Ce, 0.5% Mn, 0.1% Y and 1.0% Zn (weight %) at  $P = 1$  bar (see FactSage).

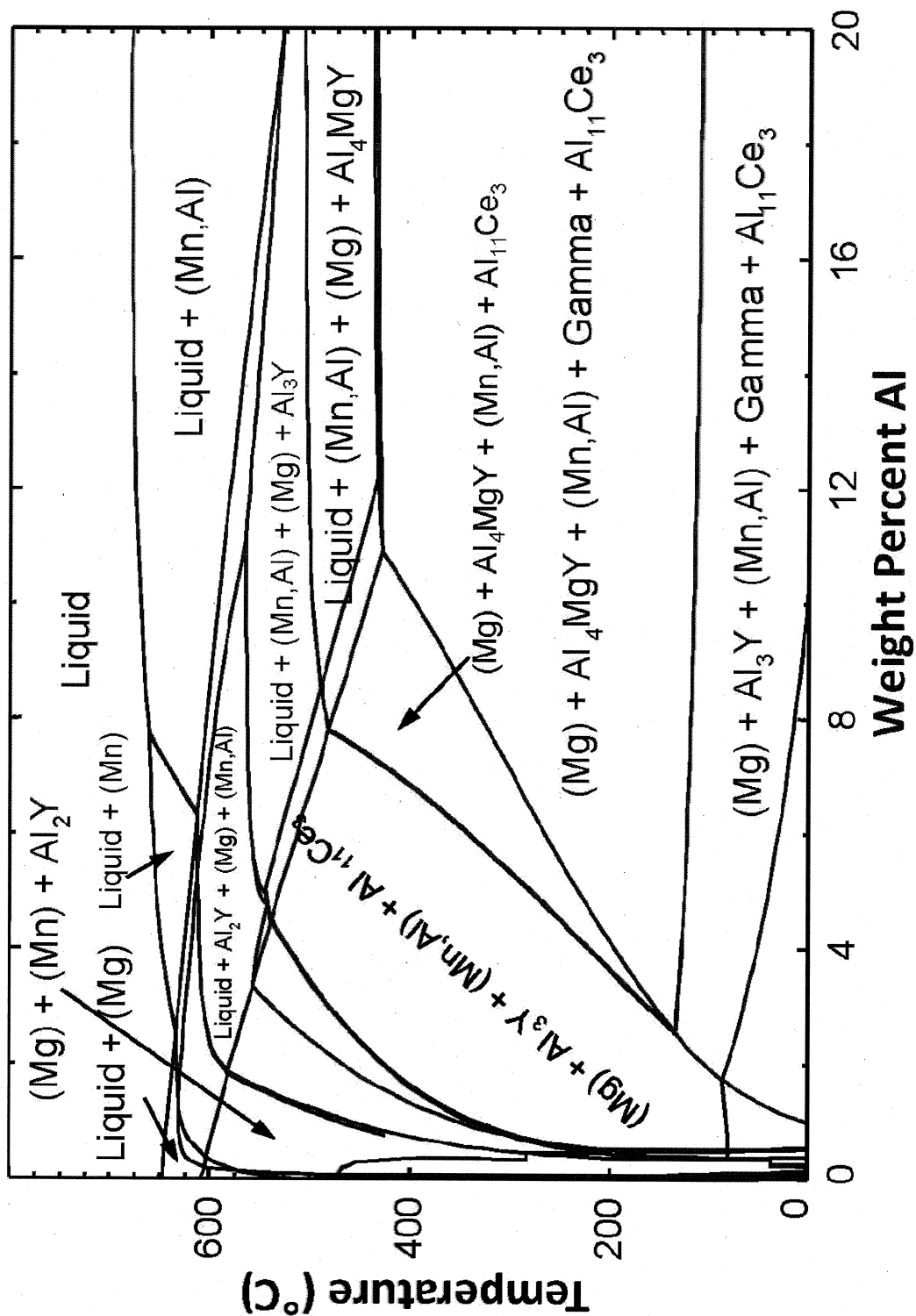


Figure 49. Cd-Na phase diagram at  $P=1$  bar calculated from optimized thermodynamic parameters showing experimental data points.  $\circ$  Kurnakow and Kusnetzow (1907),  $\triangle$  Mathewson (1906),  $\times$  Weeks and Davies (1964).

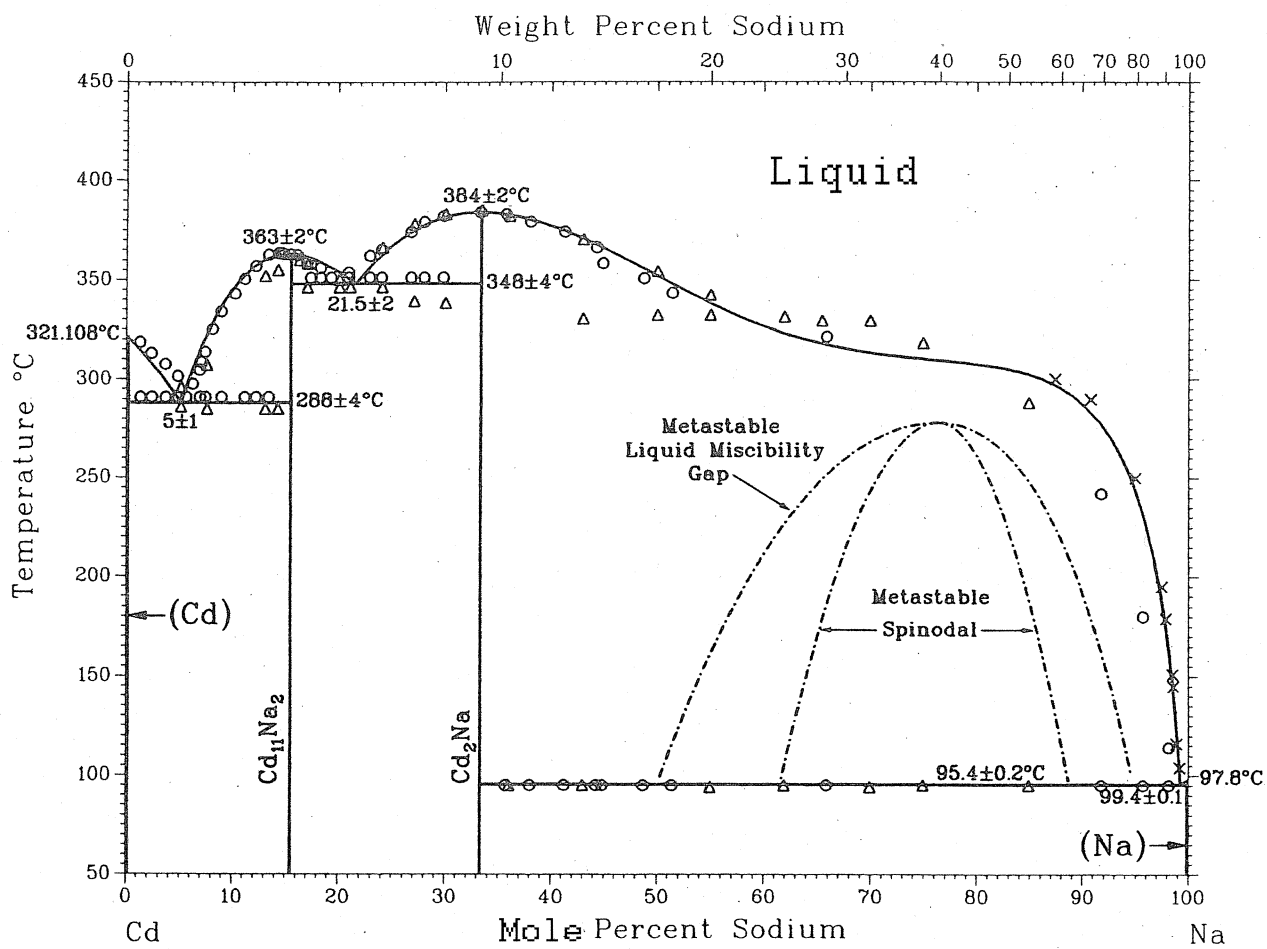


Figure 50. Sodium activity coefficient in liquid Cd-Na alloys at 400°C. Line is calculated from optimized thermodynamic parameters.  $\square$  Hauffe (1940),  $\bullet$  Lantratov and Mikhailova (1971),  $\triangle$  Maiorova et al. (1976),  $\blacktriangledown$  Alabyshev and Morachevskii (1957),  $\circ$  Bartlett et al. (1970).

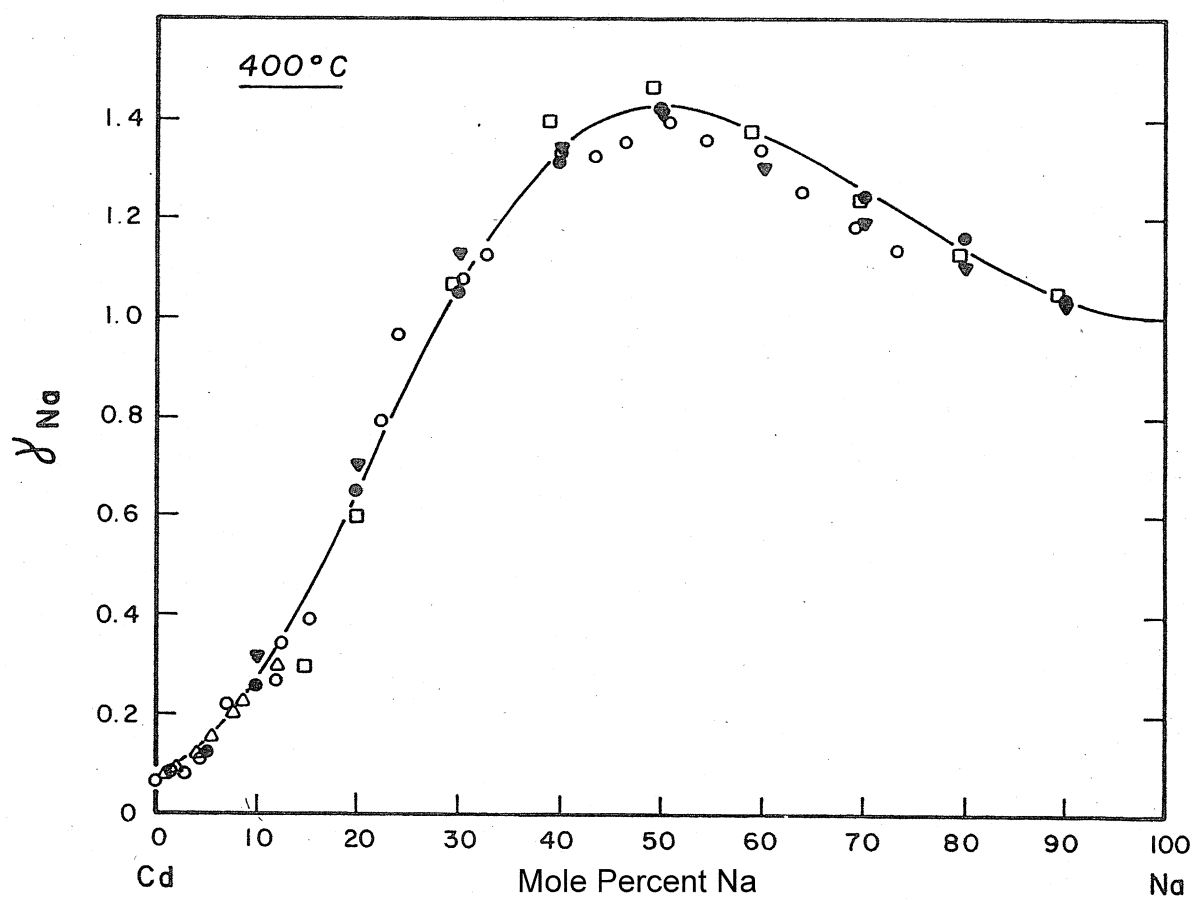


Figure 51. Partial excess enthalpy of sodium in liquid Cd-Na alloys. Line is calculated from optimized thermodynamic parameters. ● Lantratov and Mikhailova (1971), △ Maiorova et al. (1976), ○ Bartlett et al. (1970).

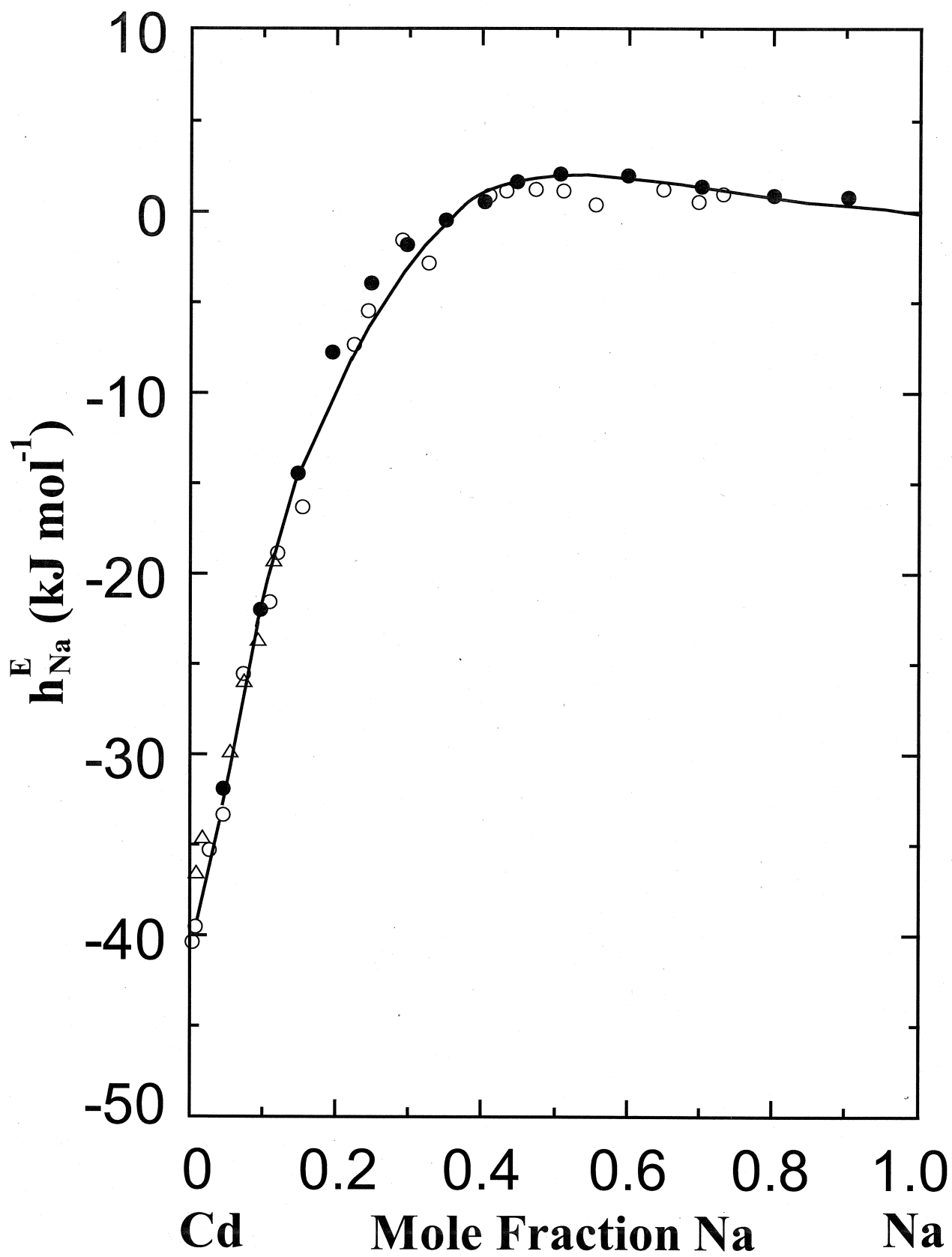


Figure 52. Calculated amounts of phases present during equilibrium cooling of an alloy of composition 85 mol% Mg, 15% Al, 5% Zn (point B on Fig. 27) (see FactSage).

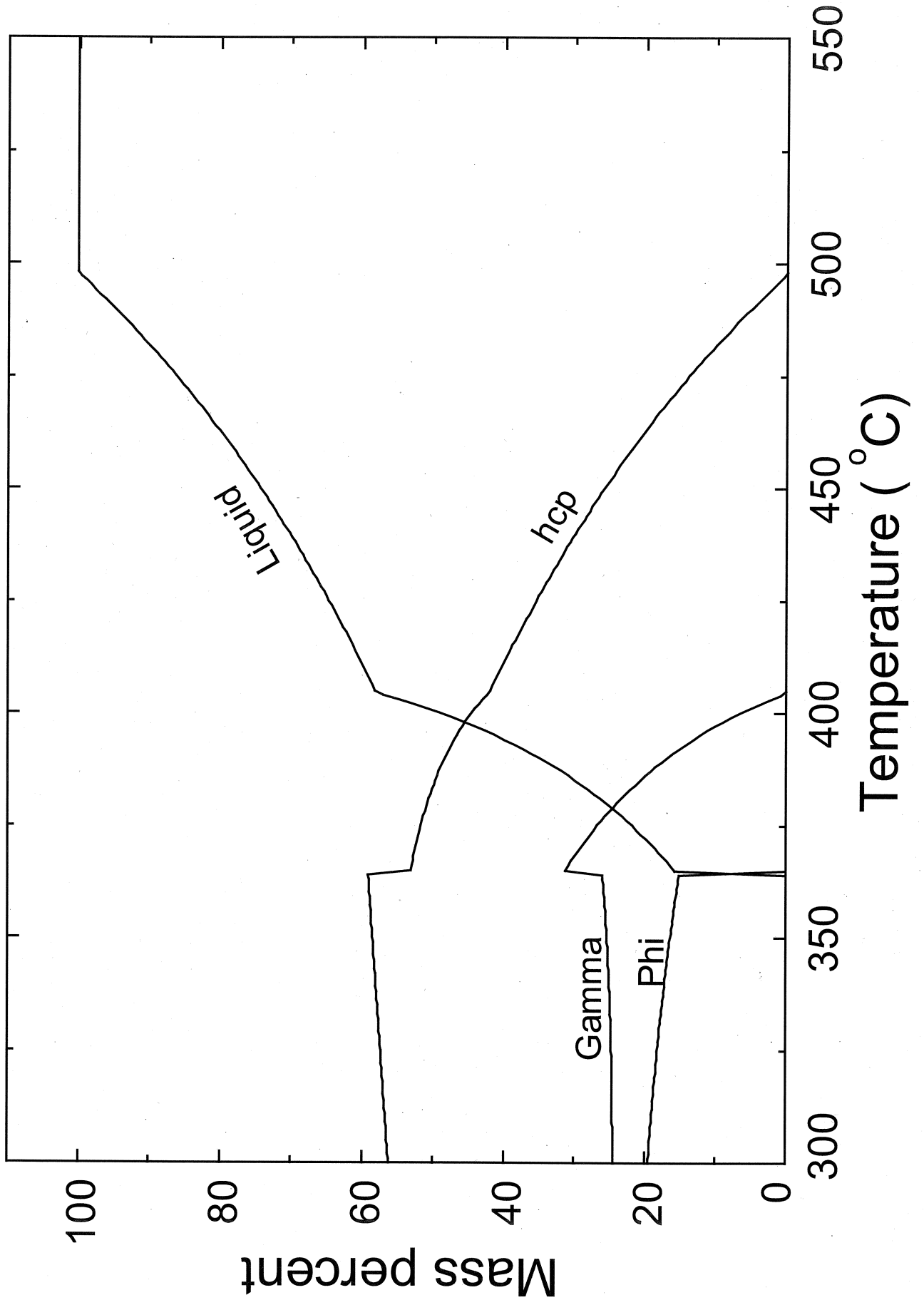


Figure 53. Liquidus projection of a system A-B-C with a minimum on the univariant line joining the binary eutectic points  $e_1$  and  $e_2$ . Solid phases are stoichiometric A and a binary solid solution B-C.

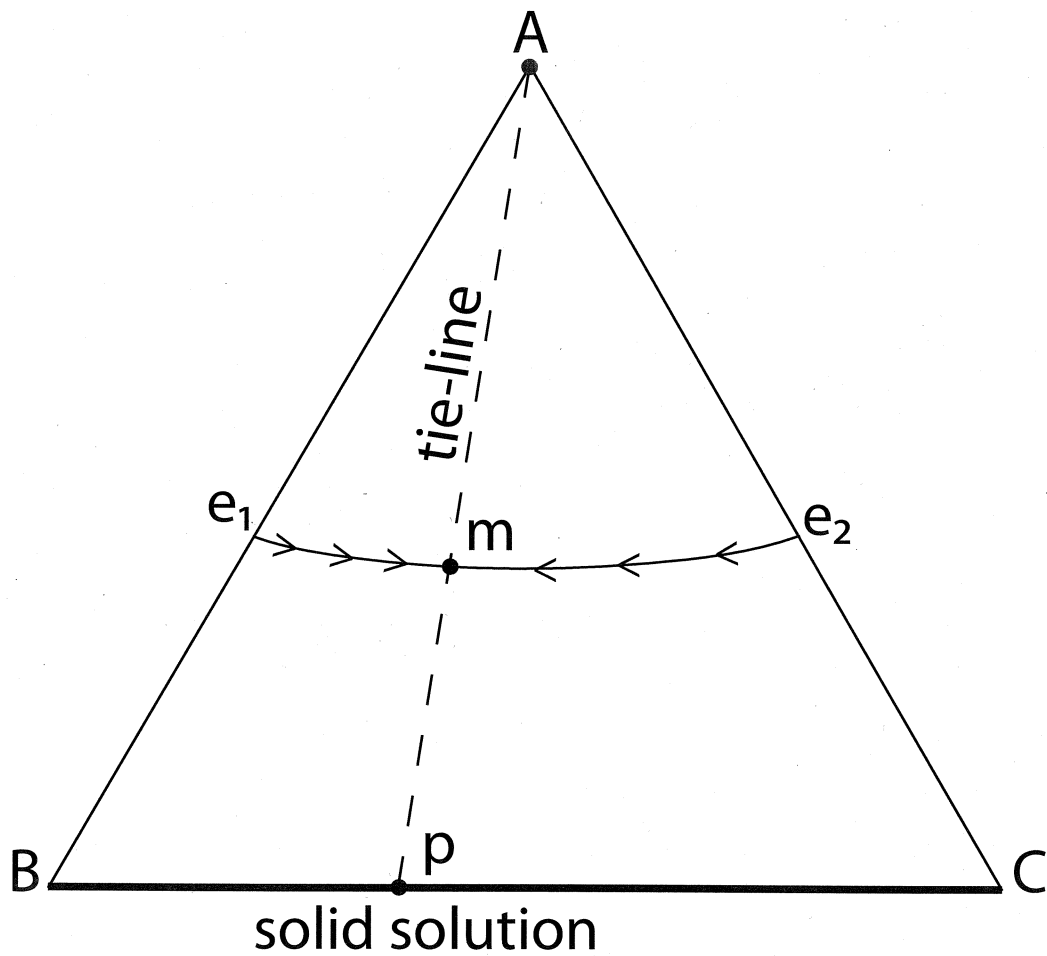


Figure 54. Temperature-composition phase diagram of the Fe-Ni system at  $P = 1$  bar showing the magnetic transformations (see FactSage; SGTE; Massalski et al., 2001).

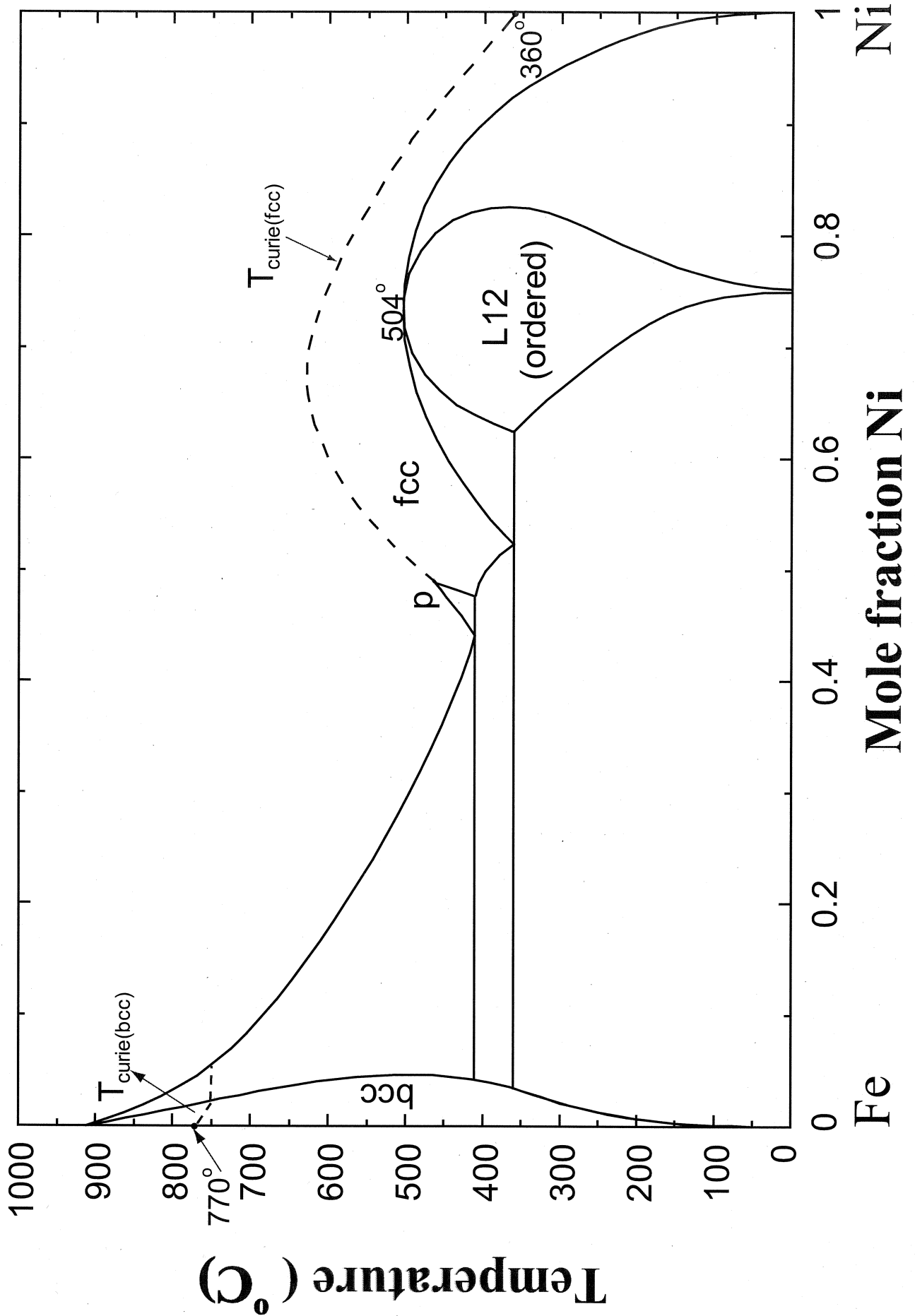


Figure 55. Temperature-composition phase diagram of the Al-Fe system at  $P = 1$  bar showing the B2  $\rightarrow$  A2 order-disorder transition (see FactSage; SGTE).

